Mathematics and Visualization

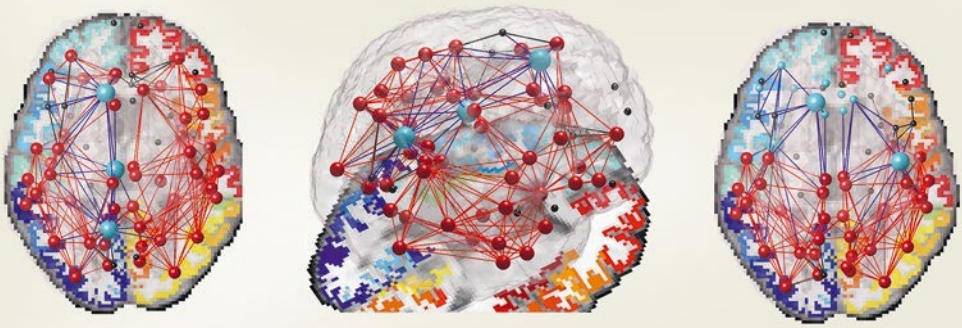

Lauren O'Donnell · Gemma Nedjati-Gilani
Yogesh Rathi · Marco Reisert
Torben Schneider *Editors*

Computational Diffusion MRI

MICCAI Workshop, Boston, MA, USA, September 2014

Springer

Mathematics and Visualization

The series *Mathematics and Visualization* is intended to further the fruitful relationship between mathematics and visualization. It covers applications of visualization techniques in mathematics, as well as mathematical theory and methods that are used for visualization. In particular, it emphasizes visualization in geometry, topology, and dynamical systems; geometric algorithms; visualization algorithms; visualization environments; computer aided geometric design; computational geometry; image processing; information visualization; and scientific visualization.
Three types of books will appear in the series: research monographs, graduate textbooks, and conference proceedings

More information about this series at
http://www.springer.com/series/4562

Lauren O'Donnell • Gemma Nedjati-Gilani •
Yogesh Rathi • Marco Reisert • Torben Schneider
Editors

Computational Diffusion MRI

MICCAI Workshop, Boston, MA, USA, September 2014

With 63 Figures, 51 in color

Springer

Editors
Lauren O'Donnell
Yogesh Rathi
Harvard Medical School
Boston, MA
USA

Marco Reisert
Department of Radiology
University Medical Center
Freiburg
Germany

Gemma Nedjati-Gilani
Department of Computer Science
University College London
London
United Kingdom

Torben Schneider
Queen Square Multiple Sclerosis Centre
UCL Institute of Neurology
Queen Square House
Queen Square
London
United Kingdom

ISSN 1612-3786 ISSN 2197-666X (electronic)
ISBN 978-3-319-11181-0 ISBN 978-3-319-11182-7 (eBook)
DOI 10.1007/978-3-319-11182-7
Springer Cham Heidelberg New York Dordrecht London

Library of Congress Control Number: 2014960246

Mathematics Subject Classification (2010): 68T10, 68U10, 42B10, 42B35

Cover design: Cover illustration from "Rich Club Network Analysis Shows Distinct Patterns of Disruption in Frontotemporal Dementia and Alzheimer's Disease" by M. Daianu, N. Jahanshad, J.E. Villalon-Reina, M.F. Mendez, G. Bartzokis, E.E. Jimenez, Simantini J Karve, J. Barsuglia and P.M. Thompson with kind permission

Printed on acid-free paper

Springer is part of Springer Science+Business Media (www.springer.com)

Preface

The 2014 MICCAI Workshop on Computational Diffusion MRI (CDMRI) was held on September 18 in Boston, MA, USA, under the auspices of the 17th International Conference on Medical Image Computing and Computer Assisted Intervention, MICCAI 2014. The sixth event in a successful series, CDMRI'14 followed the exciting and well-attended workshops in 2008, 2010, 2011, 2012, and 2013.

The 18 original research papers collected in this proceedings volume clearly demonstrate that the field remains as vibrant and diverse as ever. From fundamental theoretical work on mathematical diffusion modeling to the development of robust algorithms for tractography and connectivity mapping, diffusion MRI continues to provide mathematical and computational challenges. We are confident that the computational research presented at the CDMRI workshop will continue to provide a unique insight into the microstructure of living tissue, enable in vivo connectivity mapping of the brain, give fundamental new insights in neuroscience and neuroanatomy, and support a widespread transfer of diffusion MRI into the clinic.

We would like to express our gratitude to the members of the Program Committee for ensuring the quality of the presented work and to Carl-Fredrik Westin for serving as keynote speaker. It has been our distinct pleasure to welcome participants to CDMRI 2014 and to provide this record of the exciting work represented at the workshop.

London, UK — Gemma Nedjati-Gilani
Boston, MA, USA — Lauren J. O'Donnell
Boston, MA, USA — Yogesh Rathi
Freiburg, Germany — Marco Reisert
London, UK — Torben Schneider
September 2014

Workshop Organizers

Gemma Nedjati-Gilani	University College London, UK
Lauren J. O'Donnell	Harvard Medical School, USA
Yogesh Rathi	Harvard Medical School, USA
Marco Reisert	University Hospital Freiburg, Germany
Torben Schneider	University College London, UK

Program Committee

Nagesh Adluru	University of Wisconsin-Madison, USA
Sylvain Bouix	Harvard Medical School, USA
Emmanuel Caruyer	University of Pennsylvania, USA
Ai Wern Chung	St George's, University of London, UK
Moo K Chung	University of Wisconsin, USA
Jon Clayden	University College London ICH, UK
Philip Cook	University of Pennsylvania, USA
Fani Deligianni	University College London ICH, UK
Rachid Deriche	INRIA, France
Maxime Descoteaux	Sherbrooke University, Canada
Ivana Drobnjak	University College London, UK
Tim Dyrby	Copenhagen University Hospital, Denmark
Andrea Fuster	Technische Universiteit Eindhoven, The Netherlands
Aurobrata Ghosh	INRIA, France
Saad Jbabdi	University of Oxford, UK
Enrico Kaden	University College London, UK
Jan Klein	Fraunhofer MEVIS, Germany
Uwe Klose	University of Tuebingen, Germany
Klaus Meier-Hein	German Cancer Research Center, Germany
Dorit Merhof	University of Konstanz, Germany
Eleftheria Panagiotaki	University College London, UK
Ofer Pasternak	Harvard Medical School, USA
Xavier Pennec	INRIA, France
Matthew Rowe	University College London, UK
Benoit Scherrer	Harvard Medical School, USA
Thomas Schultz	University of Bonn, Germany
Stamatios Sotiropoulos	Oxford University, UK
Jacques-Donald Tournier	Brain Research Institute, Australia
Pew-Thian Yap	The University of North Carolina at Chapel Hill, USA
Anastasia Yendiki	Harvard Medical School, USA
Paul Yushkevich	University of Pennsylvania, USA
Liang Zhan	University of California at Los Angeles, USA
Hui Zhang	University College London, UK

Contents

Part I
Network Analysis

Vector Weights and Dual Graphs: An Emphasis on Connections in Brain Network Analysis

Peter Savadjiev, Carl-Fredrik Westin, and Yogesh Rathi

Abstract Graph theoretical representations of the brain as a complex network give a special emphasis to anatomical or functional units of the gray matter. These units are abstracted as the nodes of a graph and are pairwise connected by edges that embody a notion of connectivity. Graph theoretical operations in brain network analysis are typically employed to reveal organizational principles of the network nodes. At the same time, relatively little attention has been given to connection properties and the relations between them. Yet, various neuroscientific applications place an increased importance on connections and often require a characterization by multiple features per connection. It is not clear, however, how to incorporate vector edge weights in the standard graph representation. In this paper, we present a novel *Dual* graph formalism, in which the role of edges and vertices is inverted relative to the original (Primal) graph. This transformation shifts the emphasis of brain network analysis from gray matter units to their underlying connections in two important ways. First, it applies standard graph theoretical operations to discover the organization of connections, as opposed to that of gray matter centers. Second, it helps in removing the single scalar weight restriction and allows each connection to be characterized by a vector of several features. In this paper, we introduce the main concepts of this novel dual formalism and illustrate its potential in a population study on schizophrenia.

P. Savadjiev (✉)
Laboratory for Mathematics in Imaging, Brigham and Women's Hospital, Harvard Medical School, Boston, MA, USA

Psychiatry Neuroimaging Laboratory, Brigham and Women's Hospital, Harvard Medical School, Boston, MA, USA
e-mail: petersv@bwh.harvard.edu

C.-F. Westin
Laboratory for Mathematics in Imaging, Brigham and Women's Hospital, Harvard Medical School, Boston, MA, USA

Y. Rathi
Psychiatry Neuroimaging Laboratory, Brigham and Women's Hospital, Harvard Medical School, Boston, MA, USA

L. O'Donnell et al. (eds.), *Computational Diffusion MRI*, Mathematics and Visualization, DOI 10.1007/978-3-319-11182-7_1

1 Introduction

In recent years, the view that the functional and structural systems of the brain can be modeled as complex networks has motivated a large amount of research on the application of graph theoretical concepts to brain network analysis [3, 9].

The standard brain network model consists of a set of nodes, which represent a partitioning of the cortex and of other gray matter structures. These nodes are connected via a set of edges, or links, that represent structural and/or functional connections between gray matter partition units. Such a graph model of the brain's network organization can be constructed from a variety of imaging modalities such as structural MRI, diffusion MRI, functional MRI, or EEG/MEG. In this framework, a characterization of the organization of the different computational nodes and the functional or structural interaction between them is achieved via graph theoretical analysis [3, 9].

In this standard view of the brain network, a natural emphasis is placed on the nodes of the graph, which represent the computational units of the brain. While most graph theoretical measures do take edges into account, their ultimate goal is to describe the relationship between the computational centers, i.e. the nodes of the graph. The relationship between the edges themselves is often overlooked.

Yet, the study of the brain warrants a deeper investigation into the connections themselves. In our paper, we focus on structural connectivity networks derived from diffusion MRI data. In such networks, the graph edges represent white matter tracts. There is an extensive body of literature that implicates white matter tracts in a variety of psychiatric disorders such as schizophrenia, autism (and many others), where the tracts are seen not only as 'wires' that link computational nodes that may be lesioned in some way, but are also seen as lesion sites themselves, as revealed, for example, by changes in DTI measures such as FA, Trace etc. (see e.g. [6] for a review of DTI findings in schizophrenia).

The motivation behind our paper is thus to introduce a novel formalism for brain network analysis that shifts the emphasis from the nodes, which are typically gray matter structures, to edges, which are typically white matter structures (at least in the type of structural networks under consideration in this paper). Referring to the standard brain network graph as the *Primal* graph, we introduce (a type of) a *Dual* graph whose nodes correspond to the edges in the Primal graph. In the graph theory community, different authors have given to this construct several alternative names: the line graph, the edge-to-vertex dual, the interchange graph, the adjoint graph, and others (e.g. [4, 8]). Here, we use interchangeably the names *dual graph* and *line graph* for this construct which we describe in further detail below. It has previously been used in brain network analysis for wavelet smoothing of connectivity [5], but not explicitly as a descriptor of the organization of connections (to the extent of our knowledge).

1.1 Scalar vs. Vector Weights in Brain Network Analysis

In standard brain network analysis, the edges in the Primal graph may have a scalar weight associated with them in order to reflect connectivity strength, measured for example as functional or structural correlation between connected gray matter regions, or as mean track FA in structural networks based on diffusion MRI [3, 9]. While graph theoretic measures for networks with scalar weights are well-known and widely used [9], it is not clear how these measures can be extended to the case of *vector-weighted* networks. In fact, the analysis of vector weighted networks is still an open problem. Meanwhile, the ever-increasing abundance of measurements on white matter tracts in neuroscientific applications highlights further the need to remove the restriction to single scalar connection weights in traditional network analysis.

In this paper, we propose a two-step solution to this problem. First, we introduce a transformation from the Primal graph to a Dual graph, such that weights on edges in the Primal graph become feature vectors on nodes in the Dual graph. Then, we introduce a metric on vector weights associated to nodes in dual space. The Dual graph can then be analysed via standard graph measures, modified to take into account the metric on feature vectors associated with each node. With this approach, we achieve a solution to the vector weights problem while incorporating it into a novel graph formalism, which allows to stress novel aspects of network connectivity.

To summarize, working in the dual space makes it possible to explicitly model relations between connections in the Primal graph. Furthermore, these connections can now be characterized by a vector of relevant features as opposed to single scalar features. We test our approach on a small population study on schizophrenia, where we show that the dual graph can improve the separation between schizophrenia patients and normal controls. Of course, the goal of this study is certainly not to make clinical claims regarding schizophrenia. As a first study based on this novel methodology, with a small population sample, it is inherently preliminary and limited, and its purpose is to only illustrate the method and show how it could be applied in a future clinical study.

2 The Model

Before describing the dual graph model, we first formalize the notions of feature vectors and distances between them. We then incorporate these concepts into our novel dual graph formalism, which is designed to facilitate the analysis of network relations between connections associated with feature vectors.

2.1 Feature Vectors in Product Spaces

Consider the simple case of two feature vectors (x_1, y_1) and (x_2, y_2). If R_x and R_y are 2 metric spaces and $x_1, x_2 \in R_x$ and $y_1, y_2 \in R_y$, then the metric for the product space $R_x \times R_y$ is given by

$$d^2((x_1, y_1), (x_2, y_2)) = d^2(x_1, x_2) + d^2(y_1, y_2). \tag{1}$$

Please see [2] for details. This result can be used to formulate geodesic distances between two feature vectors.

In general, we will be working with m feature vectors $\mathbf{f}_i = (x_{i1}, x_{i2} \ldots, x_{in})$, $i \in [1 \,..\, m]$, each with n features. As a first step in computing (1), we need to define the metrics of each individual feature space. We can endow each of the feature metric spaces with either an Euclidean or a Riemannian metric. In the Euclidean case, the metric is simply $d(x_{i1}, x_{j1}) = |x_{i1} - x_{j1}|$. In the Riemannian case, one possible metric is $d(x_{i1}, x_{j1}) = \log(t(x_{i1})/t(x_{j1}))$, where $t : R_1 \rightarrow \mathbb{R}_+ \bigcup \{0\} \equiv \mathbb{R}_{0+}$ is a mapping of the feature value from its native space to the space of non-negative real numbers.

In this article, we use feature vectors with three features: x_{FA}, x_{Tr}, x_{Disp}, which are the mean values of FA, Trace and Dispersion, respectively, computed over each track. Dispersion is a measure of track geometry introduced in [10, 11]. The values of all these three features range from 0 to some maximum value. In the case of FA, this maximum value is 1. In the case of Trace, it is three times the maximum value of the diffusion coefficient of free water at normal body temperature, i.e. 0.009 s/mm^2. In the case of Dispersion, the maximum value is π radians. Thus, for these three features we define $t(x) = x/(x^{max} - x)$ where x^{max} is the maximum possible value for each feature, as given above.

These metrics, together with (1) allow us to define geodesic distance measures on the product space of our feature vectors $\mathbf{f}_i = (x_{iFA}, x_{iTr}, x_{iDisp})$:

$$d_R(\mathbf{f}_i, \mathbf{f}_j) = \sqrt{log\left(\frac{t(x_{iFA})}{t(x_{jFA})}\right)^2 + log\left(\frac{t(x_{iTr})}{t(x_{jTr})}\right)^2 + log\left(\frac{t(x_{iDisp})}{t(x_{jDisp})}\right)^2} \tag{2}$$

for the Riemannian case, or

$$d_E(\mathbf{f}_i, \mathbf{f}_j) = \sqrt{|x_{iFA} - x_{jFA}|^2 + |x_{iTr} - x_{jTr}|^2 + |x_{iDisp} - x_{jDisp}|^2} \tag{3}$$

for the Euclidean case. Note that these distances could also be used to compute other operations on the space F of feature vectors, for example the mean of a set of feature vectors $\{\mathbf{f}_1, \ \ldots \ , \mathbf{f}_m\}$, which can be defined as

$$\min_{\bar{\mathbf{f}} \in F} \sum_{i=1}^{m} d(\bar{\mathbf{f}}, \mathbf{f}_i), \tag{4}$$

where d can be one of d_R or d_E as defined above. However, in the present paper, we only focus on distance.

2.2 The Dual Graph

A network is represented as a graph $G = \{V, E\}$ where V is a set of vertices that are pairwise joined by a set of edges E. Our model is based on the concept of the *line graph*, borrowed from graph theory, which defines a dual form of the graph G [4, 8] and which we will denote as $D(G)$. Given a graph G, its line graph $D(G)$ is formed by interchanging the roles of V and E. In other words, the line graph $D(G) = \{V_D, E_D\}$ has a one-to-one correspondence between its vertex set V_D and the edge set E of G. Furthermore, two vertices in $D(G)$ are connected if and only if the corresponding edges in G share a common endpoint (vertex). More formally,

$$\begin{aligned} E_D = \{\, \{(v_1, v), (v, v_2)\} \mid \\ \{v, v_1, v_2\} \in V, \\ (v_1, v) \in E, (v, v_2) \in E \,\}. \end{aligned} \tag{5}$$

The transformation of the Primal graph G to the Dual graph $D(G)$ entails that each vertex of degree k in G results in $k(k-1)/2$ edges in $D(G)$. Isolated nodes in G, i.e. nodes of degree 0, are not represented in $D(G)$.

Figure 1 shows a simple example of a graph and its corresponding line graph.

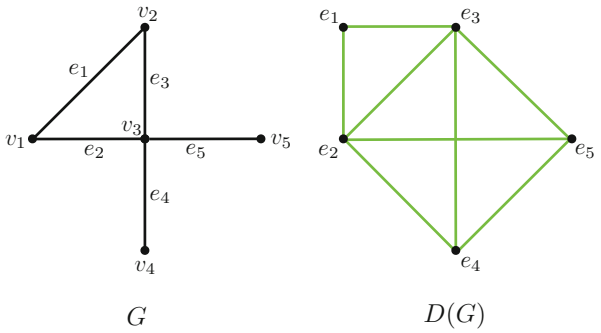

Fig. 1 A simple example of a graph G and it's corresponding dual graph $D(G)$

3 Experimental Methods

These theoretical tools are combined in a set of experiments designed to illustrate their application to neuroscientific studies. To this end, we performed a small scale population study on schizophrenia, where we computed the three features for a set of connections in each participant. We then used the above distance measures in computing the standard network measure of global efficiency on the dual graph [9]. This dual approach reveals between-group network differences that are not detected with a standard analysis on the Primal graph. The efficiency measure was picked as an example, others are possible as well.

3.1 Subjects and Data Acquisition

Our subject population consists of 14 adult male healthy control subjects and ten adult male chronic schizophrenia patients. In each subject, diffusion MRI data was acquired on a GE Signa HDxt 3.0T scanner using an echo planar imaging sequence with a double echo option, an 8 Channel coil and ASSET with a SENSE-factor of 2. The acquisition consisted of 51 directions with $b = 900\,s/mm^2$, and eight images with $b = 0\,s/mm^2$, with scan parameters TR = 17,000 ms, TE = 78 ms, FOV = 24 cm, 144 ×144 encoding steps, 1.7 mm slice thickness. Eighty five axial slices covering the whole brain were acquired. Structural MR T1 images at 1 mm resolution were acquired as well.

3.2 Network Construction and Analysis

In each subject, we computed whole-brain tractography with the filtered tractography method of [7], followed by a standard FreeSurfer parcellation of the cortex (http://surfer.nmr.mgh.harvard.edu), which was then registered to the subject's diffusion MRI space, specifically to the unweighted b0 volume. From the whole-brain tractography we extracted all existing connections between pairs of FreeSurfer-defined cortical areas. As the number of fibers per connection varies across subjects, we selected those connections that have at least 30 fibers in every subject. There were 218 such connections. Based on them, we constructed a structural network graph, our Primal graph G, a schematic view of which is shown in Fig. 2. By working with only these 218 connections, we ensure to have the same network representation in all 24 subjects. In this manner, the structural network topology is not a source of variability, and will not affect the observed between-group differences.

In each subject, we computed the mean values for FA and Trace along each of these 218 connections. Additionally, we applied the method of [10] to compute

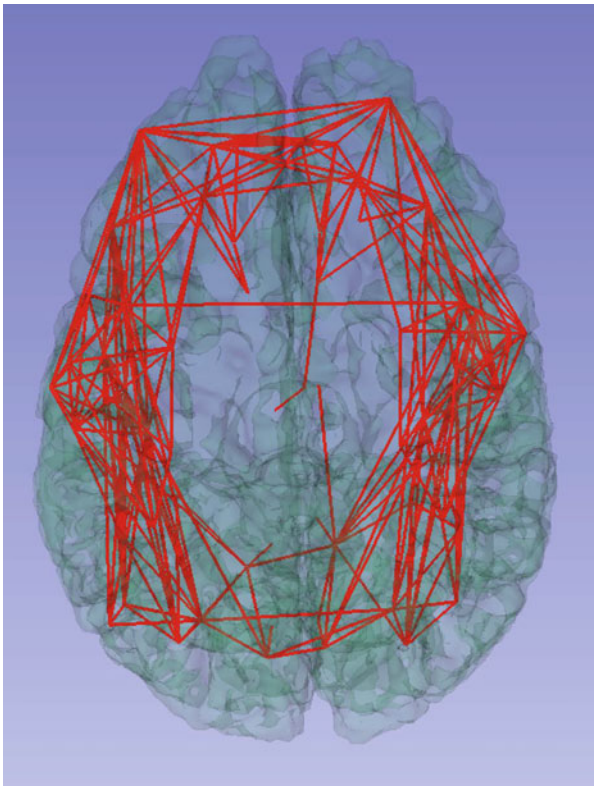

Fig. 2 An illustration of our structural network consisting of 218 connections, shown over a translucent rendering of the brain surface

mean fiber dispersion over each fiber bundle, using a spatial scale parameter $S = 8.5$ mm. We then computed $D(G)$, the Dual graph of our Primal brain network graph G, as described previously in Sect. 2.2. Each node in the Dual graph represents one of the 218 connections and is associated with a feature vector of three elements, i.e. the mean values of FA, Trace and Dispersion.

Using the distance measures defined in Sect. 2.1, we then computed the global efficiency measure on the dual graph using the implementation available in the Brain Connectivity Toolbox [9]. The global efficiency of a graph is a network theoretic measure commonly used in brain network analysis, defined as the average inverse shortest path length in the network [9]. In the case of our dual graph, path length between nodes translates to similarity between feature vectors. We chose global efficiency as one possible network measure that can be used to compare graphs. Of course, many other measures are available, and a future study should investigate several different network measures, not only one. Here, we restrict ourselves to one measure for brevity of exposition. Also, we note that previous network analysis studies have shown global efficiency in functional networks to be abnormal in schizophrenia [1]. Thus, we chose the global network efficiency as an example

measure to compare the primal graph vs. the dual graph approach in a population study in schizophrenia, with results presented next in Sect. 4.

4 Results

It is important to remember that the goal of our experiments is not to make clinical claims of significance in schizophrenia, but rather to simply illustrate the behavior of our method and to suggest ways in which it could be used in the future. At this stage, we only use a small population sample, and all our clinical findings remain preliminary.

We compared global network efficiency between our groups of schizophrenia patients and control subjects in a series of experiments, where the efficiency measure was computed on the Dual graph using either the Riemannian distance measure (2) or the Euclidean distance measure (3). We performed these comparisons using the full feature vectors. In addition, to explore the performance of single features in isolation, we considered modified feature vectors containing only one feature. The global efficiency measure computed with individual features on the Dual graph was also compared to the efficiency measure computed in the Primal graph, where the feature under consideration was used as weight in a classical weighted graph computation [9]. The results of all these experiments, in the form of p-values, are summarized in Table 1. We note that network efficiency in functional connectivity has previously been shown to be abnormal in schizophrenia [1]. Broadly, our results seem to fall in line with this finding.

Table 1 p-Values for the global network efficiency comparison between our schizophrenia and controls groups

	$D(G)$, d_E	$D(G)$, d_R	G
FA	0.92	0.83	0.58
Tr	**0.0075**	**0.0075**	0.65
Disp	0.15	**0.026**	0.19
(FA, Tr, Disp)	0.36	0.063	

Column heading $D(G)$ indicates efficiency was computed on the dual graph $D(G)$, with the Euclidean distance measure d_E (3) or the Riemannian distance measure d_R (2). Column heading G indicates efficiency was computed on the Primal graph G. FA, Tr, Disp indicate the features used in the feature vector when working with the Dual graph $D(G)$, or alternatively indicate the scalar weight used in the Primal graph G. Significant p-values (below 0.05) are indicated in *boldface*

5 Discussion

We wish to re-emphasize that the main conclusions to be drawn from our results do not rest in the specific p-values. Even when the p-value drops below the standard threshold of 0.05, it is still difficult to make claims of clinical significance given the small size of the subject population. Rather, we would like to steer the reader's attention to the overall pattern of the p-value change. First, we note that the choice of Euclidean vs. Riemannian distance measure may or may not influence the comparison result. When the comparison is made with the full feature vector with three features, the p-value drops to a nearly significant level when choosing the Riemannian metric over the Euclidean.

Second, our experiments demonstrate that working with the Dual graph, as opposed to the Primal graph, comes with a 'dual' benefit. First, we are no longer restricted to single scalar features (weights), we can now work with feature vectors—the equivalent of vector-valued edge weights in the Primal graph. Second, even when using single scalar features, the dual graph formalism appears to allow for a better discrimination between the control and schizophrenia groups. An exact mathematical derivation of why this may be the case is the topic of future work. At this point, we will point to the fact that in the Primal weighted graph, a path length is a sum of edge weights. In contrast, in the Dual graph formalism, a path length is the sum of distances between features. Thus, in some sense, the Dual graph represents a differential form of the Primal graph. Thus, in the case of the Dual graph, increased efficiency embodies the notion that along a path, connections have a smaller variation between their feature vectors, possibly denoting reduced local 'specialization'. In other words, increased efficiency implies that connections along a path are more homogeneous in terms of their feature vectors. If some of these features carry functional information (not in our present paper, but in our future work), then changes in such similarity could be important to reveal how functional and structural connection properties change together in a disease. Of course, a full theoretical analysis of the Dual graph measures is necessary, as well as an extended analysis of their implications. This will be done in future work.

We believe that this novel Dual graph formalism holds great promise for highlighting the importance of connections in brain network analysis. In terms of relevance to brain disorders such as schizophrenia, where white matter abnormalities are known to be important, the Dual graph approach is expected to reveal a novel view on the organization and distribution of white matter abnormalities in the brain, in a manner that cannot be directly accessed with traditional track-based studies, or with the traditional Primal graph approach to brain network analysis.

The present paper was aimed at introducing and illustrating the main concepts. Future work can proceed in several different directions. First, we showed how a distance measure between feature vectors can be used to compute a length-based network measure, namely efficiency. Other network measures, such as clustering and centrality need to be explored as well. Second, in this paper we worked with up to three features per connection. Future work will surely explore a wider variety

of connection features, not all of which need to be tied to DTI. Additionally, we kept network topology constant across subjects in the present work, in order to limit potential sources of variability. Future work needs to relax this constraint. In order to do this, however, first we must understand the effect of thresholding the network structure. In the present work, our network consisted of connections with at least 30 fibers in every subject. Future work needs to investigate how robust are the results relative to variation in this threshold value. In addition to answering all these methodological questions, the method's performance in clinical studies needs to also be further explored, in carefully designed studies with a larger population size.

Acknowledgements This work was supported by NIH grants R01 MH097979, R01 MH074794, R01 MH092862, R01 MH082918, P41 RR013218, P41 EB015902, and Swedish Research Council (VR) grant 2012-3682.

References

1. Alexander-Bloch, A.F., Vértes, P.E., Stidd, R., Lalonde, F., Clasen, L., Rapoport, J., Giedd, J., Bullmore, E.T., Gogtay, N.: The anatomical distance of functional connections predicts brain network topology in health and schizophrenia. Cereb. Cortex **23**(1), 127–138 (2013)
2. Amari, S., Nagaoka, H.: Methods of Information Geometry. AMS, New York (2000)
3. Bullmore, E.T., Sporns, O.: Complex brain networks: graph theoretical analysis of structural and functional systems. Nat. Rev. Neurosci. **10**, 186–198 (2009)
4. Gross, C.J.L., Yellen, J. (eds.): Handbook of Graph Theory. CRC Press, New Jersey (2004)
5. Kim, W.H., Adluru, N., Chung, M.K., Charchut, S., GadElkarim, J.J., Altshuler, L., Moody, T., Kumar, A., Singh, V., Leow, A.D.: Multi-resolutional brain network filtering and analysis via wavelets on non-Euclidean space. In: Mori, K., Sakuma, I., Sato, Y., Barillot, C., Navab, N. (eds.) MICCAI 2013, Part III. LNCS, vol. 8151, pp. 643–51. Springer, Heidelberg (2013)
6. Kubicki, M., McCarley, R., Westin, C.F., Park, H.J., Maier, S., Kikinis, R., Jolesz, F.A., Shenton, M.E.: A review of diffusion tensor imaging studies in schizophrenia. J. Psychiatr. Res. **41**, 15–30 (2007)
7. Malcolm, J.G., Michailovich, O., Bouix, S., Westin, C.F., Shenton, M.E., Rathi, Y.: A filtered approach to neural tractography using the Watson directional function. Med. Image Anal. **14**, 58–69 (2010)
8. van Rooij, A.C.M., Wilf, H.S.: The interchange graph of a finite graph. Acta Math. Hung. **16**, 263–269 (1965)
9. Rubinov, M., Sporns, O.: Complex network measures of brain connectivity: uses and interpretations. Neuroimage **52**, 1059–1069 (2010)
10. Savadjiev, P., Rathi, Y., Bouix, S., Smith, A.R., Schultz, R.T., Verma, R., Westin, C.F.: Fusion of white and gray matter geometry: a framework for investigating brain development. Med. Image Ana. **18**(8), 1349–1360 (2014)
11. Savadjiev, P., Rathi, Y., Bouix, S., Verma, R., Westin, C.F.: Multi-scale characterization of white matter track geometry. In: Ayache, N., Delingette, H., Golland, P., Mori, K. (eds.) MICCAI 2012, Part III. LNCS, vol. 7512, pp. 34–41. Springer, Heidelberg (2012)

Rich Club Network Analysis Shows Distinct Patterns of Disruption in Frontotemporal Dementia and Alzheimer's Disease

Madelaine Daianu, Neda Jahanshad, Julio E. Villalon-Reina, Mario F. Mendez, George Bartzokis, Elvira E. Jimenez, Simantini J Karve, Joseph Barsuglia, and Paul M. Thompson

Abstract Diffusion imaging and brain connectivity analyses can reveal the underlying organizational patterns of the human brain, described as complex networks of densely interlinked regions. Here, we analyzed 1.5-Tesla whole-brain diffusion-weighted images from 64 participants—15 patients with behavioral variant frontotemporal (bvFTD) dementia, 19 with early-onset Alzheimer's disease (EOAD), and 30 healthy elderly controls. Based on whole-brain tractography, we reconstructed structural brain connectivity networks to map connections between cortical regions. We examined how bvFTD and EOAD disrupt the weighted 'rich club'—a network property where high-degree network nodes are more interconnected than expected by chance. bvFTD disrupts both the nodal and global organization of the network in both low- and high-degree regions of the brain. EOAD targets the global connectivity of the brain, mainly affecting the fiber density of high-degree (highly connected) regions that form the rich club network. These rich club analyses suggest distinct patterns of disruptions among different forms of dementia.

1 Introduction

Rapid advances in neuroimaging have revolutionized the study of brain connectivity, also known as 'connectomics' [1], revealing organizational principles in fiber connections and how these contribute to the functional and structural integrity of

M. Daianu (✉) • N. Jahanshad • J.E. Villalon-Reina • P.M. Thompson
Imaging Genetics Center, Institute for Neuroimaging & Informatics, University of Southern California, Los Angeles, CA, USA
e-mail: madelaine.daianu@ini.usc.edu; neda.jahanshad@ini.usc.edu; julio-villalon@ini.usc.edu; pthomp@usc.edu

M.F. Mendez • G. Bartzokis • E.E. Jimenez • Simantini J Karve • J. Barsuglia
Alzheimer's Disease Research Center, Department of Neurology, UCLA School of Medicine, Los Angeles, CA, USA
e-mail: mmendez@ucla.edu; gbar@ucla.edu; elvira@ucla.edu; karves@smccd.edu; joseph.barsuglia@va.gov

L. O'Donnell et al. (eds.), *Computational Diffusion MRI*, Mathematics and Visualization, DOI 10.1007/978-3-319-11182-7_2

the brain. Structural and functional imaging can be used to create connectivity maps of the brain. To analyze these maps, advanced mathematical methods have been employed, such as graph theory, to better understand connectivity patterns in the healthy [2, 3] and diseased brain [4].

Diffusion weighted imaging (DWI) can be used in structural brain connectivity studies to assess the global and local breakdown of network integration in degenerative disease. Recent concepts that describe network properties—such as the "rich club" effect—can provide important information on the complexity and higher-order structure of the brain network. The rich club network is composed of densely interconnected components that are more heavily interconnected among themselves than would be expected by chance. Rich club components are highly central and interconnected regions of the brain [5] that have also been identified as "brain hubs" [2]. Studying the role and function of these hubs allows us to describe the brain in terms of a hierarchical ordering, specialization, and level of resilience [3]—identifying properties of brain networks in health and disease.

In this study we analyzed the nodal and global weighted rich club network in behavioral variant frontotemporal dementia (bvFTD) and early onset Alzheimer's disease (EOAD), as compared to the healthy brain. Prior work suggests that if in particular the rich club organization is altered, it can cause damage to the cortical synchronization of the brain [3, 6]. Here, we hypothesize that the rich club network may be disrupted in both forms of dementia, perhaps leading to disrupted communication among cognitive systems of the brain. We expected frontal cortical regions to be disrupted in bvFTD [7], while in EOAD, we hypothesized differences in the posterior cingulate and precuneus regions [8]. Overall, we aimed to detect distinct patterns of disruption in the nodal and global organization of the rich club network. We found, for the first time, severely disrupted global connectivity in bvFTD participants with lower fiber density in both low- and high-degree cortical regions. This was accompanied by altered connectivity across more than 60 % of the nodal connections of the brain. On the other hand, EOAD mainly affected the global connectivity of the network, and some of the high-degree cortical regions that form the rich-club. However, unlike in bvFTD, the overall organization of the brain network in EOAD was relatively preserved.

2 Methods

2.1 Participants and Diffusion-Weighted Brain Imaging

We analyzed diffusion-weighted images (DWI) from 30 healthy controls and 34 dementia patients—15 bvFTD subjects and 19 age-matched EOAD subjects (Table 1). All 64 subjects underwent whole-brain MRI scanning on 1.5-Tesla Siemens Avanto scanners, at the MRI Center at UCLA. Standard anatomical T1-weighted sequences were collected (256×256 matrix; voxel size $= 1 \times 1 \times 1$ mm^3;

Table 1 Demographic information for the 30 healthy controls, 15 bvFTD and 19 EOAD patients. The mean age and sex are listed for each diagnostic group

	CTL	bvFTD	EOAD	Total
Age	59.5 ± 9.6 SD	61.3 ± 10.8 SD	57.9 ± 4.3 SD	59.5 ± 8.7 SD
Sex	13M/17F	7M/8F	7M/12F	27M/37F

TI = 900, TR = 2,000 ms; TE = 2.89 ms; flip angle = 40°), and diffusion-weighted images (DWI) using single-shot multisection spin-echo echo-planar pulse sequence (144×144 matrix; voxel size: $2 \times 2 \times 3$ mm^3; TR = 9,800 ms; TE = 97 ms; flip angle = 90; scan time = 5 min 38 s). 31 separate images were acquired for each DTI scan: 1 T2-weighted images with no diffusion sensitization (b_0 image) and 30 diffusion-weighted images ($b = 1{,}000$ s/mm^2). Image preprocessing was performed as described in [4]. This was not included here due to space limitations.

2.2 *N* × *N* Connectivity Matrix Computation

We performed whole-brain tractography as described in [4]. We used a method based on the Hough transform to recover fibers, using a constant solid angle orientation distribution function to model the local diffusion propagator [9].

Each subject's dataset contained ~10,000 useable fibers (3D curves) in total. 34 cortical labels per hemisphere, as listed in the Desikan–Killiany atlas [10], were automatically extracted from all aligned T1-weighted structural MRI scans with FreeSurfer (http://surfer.nmr.mgh.harvard.edu/).

For each subject, a 68×68 connectivity matrix was created whereby each element represented the total number of detected fibers, in that subject, that passed through each pair of ROIs. The connectivity matrices were normalized by the total number of fibers extracted for each brain.

2.3 *Weighted Rich Club Networks*

Graph theory metrics were used to examine the topology of the connectivity matrices. We used the Brain Connectivity Toolbox measures as described previously [11].

The *weighted rich club coefficient* is a function of the nodal degree, k—the number of edges that connect to a node. At a particular k level the nodal degree is computed as:

$$\boldsymbol{k} = \sum\nolimits_{j \in N} \boldsymbol{a_{ij}} \tag{1}$$

where k_i is the degree of a node i, and a_{ij} is a connections status between nodes i and j ($a_{ij} = 1$ if nodes i and j are connected and $a_{ij} = 0$ otherwise) [4, 12].

We computed the rich club coefficient for each subject's anatomical network at a range of k value thresholds (i.e., $k = 1$–22). To do this, we examined subnetworks, $\boldsymbol{M}$, in the connectivity matrix, and computed the nodal degree by counting the links that interconnected each node i in the subnetwork with k other nodes. Nodes that had a nodal degree $\leq k$ were removed from the network. Then, we ranked all the connections in the network as a function of weight and stored them in a vector, $\boldsymbol{W}^{\boldsymbol{ranked}}$. Within $\boldsymbol{M}$, we selected the degrees larger than k; the number of links between the components of the subnetwork was counted, $\boldsymbol{E}_{>k}$, as well as the sum of their collective weight, $\boldsymbol{W}_{>k}$. Then, the weighted rich club, $\boldsymbol{\phi}^{\boldsymbol{w}}(\boldsymbol{k})$, was computed as the ratio between $\boldsymbol{W}_{>k}$ and the sum of the ranked weights from $\boldsymbol{W}^{\boldsymbol{ranked}}$ (from the whole network) given by the top strongest connections in $\boldsymbol{E}_{>k}$ [3].

$$\boldsymbol{\phi}^{\boldsymbol{w}}(\boldsymbol{k}) = \frac{\boldsymbol{W}_{>k}}{\sum_{\boldsymbol{l}=\boldsymbol{11}}^{\boldsymbol{E}_{>k}} \boldsymbol{w}_{\boldsymbol{l}}^{\boldsymbol{ranked}}} \tag{2}$$

To normalize the measures, we compared the observed values to a rich club coefficient computed on an average calculated from 100 randomized networks of equal size and similar connectivity distribution. This is an important step in the analysis, as the absolute values provide limited information on network integration in the brain [2] (Fig. 2a).

$$\boldsymbol{\phi}_{\boldsymbol{norm}}^{\boldsymbol{w}}(\boldsymbol{k}) = \frac{\boldsymbol{\phi}^{\boldsymbol{w}}(\boldsymbol{k})}{\boldsymbol{\phi}_{\boldsymbol{rand}}^{\boldsymbol{w}}(\boldsymbol{k})} \tag{3}$$

Rich club subnetworks, as described throughout the study, were set at a high-degree k-levels ($k > 15$), as previously reported [3]. As part of our nodal analysis, we investigated the rich club networks at $k = 16$ by thresholding the connectivity matrices at nodal degree, k. We computed the nodal degree on the rich club networks at $k = 16$ and compared it between bvFTD and controls, using a linear regression, with healthy coded at 0 and diseased coded as 1; we covaried for age, sex and brain volume. Similarly, we compared the EOAD group to controls and, separately, bvFTD to EOAD. For our global analyses, we tested how the unnormalized and separately, normalized, rich club coefficients at all 22 k-levels differed in bvFTD, relative to controls, using the same setup for the linear regression as described above. Then, we compared EOAD to controls and finally, bvFTD to EOAD. We used the false discovery rate procedure (FDR) to correct for the multiple tests performed at each cortical region and at each k level. In addition, we corrected for the three comparisons between diagnostic groups by adjusting the significance threshold to 0.05/3.

3 Results

3.1 Nodal Analysis

In our nodal analysis of the rich club network (at $k = 16$), over 60 % of the cortical regions in the bvFTD brain network were less interconnected (43 regions of 68), relative to healthy controls (FDR critical p-value $= 0.016$). Among these, the most affected regions (p-value $< 10^{-10}$) were the left and right hemisphere caudal and rostral anterior cingulate, lateral orbitofrontal, rostral middle frontal and superior frontal regions. In addition, the left hemisphere insula and *pars triangularis* were also less interconnected in bvFTD, as was the precentral gyrus in the right hemisphere (p-value $< 10^{-10}$) (Fig. 1). Not all regions are listed due to space limitations. On the other hand, 20 % of the cortical regions (14 regions of 68) in the rich club had a lower nodal degree in EOAD participants, relative to healthy controls (FDR critical p-value $= 0.010$) with most affected regions found in the left hemisphere posterior cingulate, precuneus and superior frontal region (p-value $< 10^{-4}$) (Fig. 1).

When compared to each other, the brain network of bvFTD participants was significantly less interconnected than the EOAD brain (FDR critical p-value $= 0.013$). The left and right hemisphere caudal and rostral anterior cingulate, lateral orbitofrontal, rostral middle frontal and superior frontal, *pars triangularis* had a lower nodal degree in bvFTD (p-value $< 10^{-5}$); furthermore, the left hemisphere lateral and medial orbitofrontal and insula were also more affected in bvFTD. Overall, the left hemisphere was most affected in both bvFTD and EOAD, indicating that it might be more vulnerable to network disruptions than the right.

3.2 Global Analysis

The unnormalized rich club coefficient was lower in the diseased groups, relative to healthy controls (Fig. 2). The unnormalized rich club coefficient was lower in bvFTD participants, relative to controls (FDR critical p-value $= 0.010$), but no difference was detected in EOAD. Furthermore, the bvFTD group had a lower unnormalized rich club coefficient than EOAD participants (FDR critical p-value $= 5 \times 10^{-4}$).

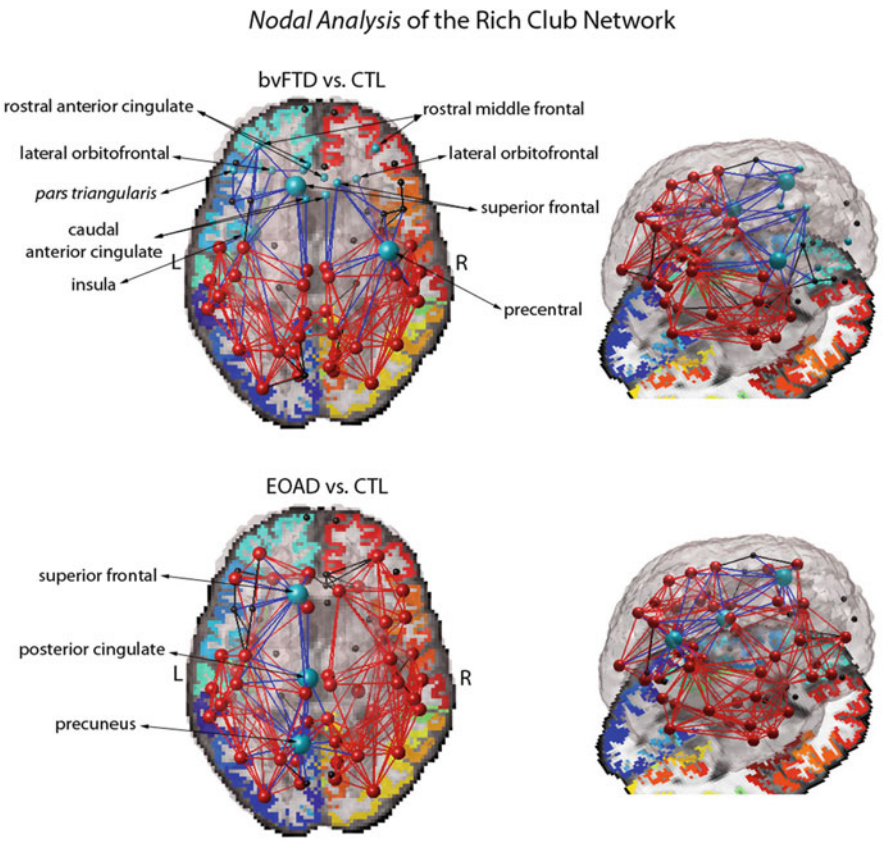

Fig. 1 Average pattern of network connections and group differences in the nodal degree (at $k = 16$) between bvFTD and controls (CTL) (*top*), and EOAD and CTL (*bottom*). Nodes and connections in *red* indicate the presence of rich club components (at $k = 16$) averaged across all subjects for bvFTD and EOAD participants; components in *black* are in the low-degree k-level regime ($k < 16$), not included in the rich club network. Most affected cortical regions in disease with a decrease in nodal degree are indicated in *blue* along with their connections to neighboring nodes; *blue large spheres* are part of the rich club network, but *small spheres* are not. The bvFTD network shows a visibly sparse organization, especially in the frontal lobe; EOAD targets the rich club components of the *left hemisphere*, but the overall organization of the rich club network is preserved

In a separate analysis, the normalized weighted rich club coefficient was higher in the diseased groups, relative to healthy controls (Fig. 2). The normalized rich club was significantly higher in bvFTD subjects across most of the k-value regime (FDR critical p-value $= 0.016$). Similarly, the normalized rich club coefficient was also higher in EOAD subjects, relative to healthy controls, but mostly in the high k-level network ($k > 13$) (FDR critical p-value $= 0.016$). When we compared the diseased global networks to each other, bvFTD participants had a significantly

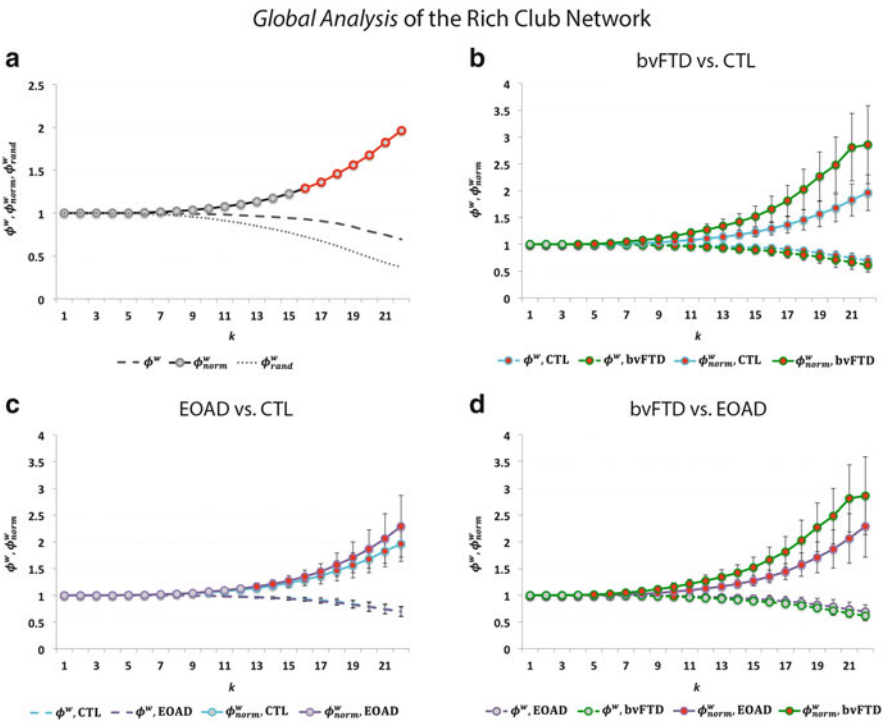

Fig. 2 (**a**) Shows the rich club *curves*, including the unnormalized (ϕ^w), normalized (ϕ^w_{norm}) and randomized rich club (ϕ^w_{rand}) as a function of nodal degree, k, for the weighted group average networks in healthy controls; a rich club is formed at $k > 15$. (**b**) Shows significant differences (*red*) in the normalized (FDR critical p-value $= 0.016$) and unnormalized rich club coefficient (FDR critical p-value $= 0.010$) between bvFTD (*green*) and controls (*blue*) across most of the k-value regime. (**c**) Shows significant differences in the normalized (FDR critical p-value $= 0.016$) rich club coefficient between EOAD (*purple*) and controls mostly in the high-level k-value regime. (**d**) Shows significant differences in the normalized (FDR critical p-value $= 0.016$) and unnormalized rich club coefficient (FDR p-value $= 5 \times 10^{-4}$) between bvFTD and EOAD participants. *Gray dots* on the *curves* indicate that no differences were detected. *Error bars* indicate standard error

higher normalized rich club coefficient than EOAD across the low and high k-level regime (FDR critical p-value $= 0.016$).

4 Discussion

Here we analyzed structural brain connectivity by examining the weighted rich club organization in cognitively healthy controls and participants with dementia (bvFTD and EOAD). The weighted rich club curves revealed distinct patterns of disruption in each disease group—bvFTD subjects showed severe nodal and global

network disruptions in fiber density across the entire *k*-value regime, while EOAD participants showed disruptions mainly in the rich club network (i.e., high *k*-value regime), suggesting an overall more robust network than bvFTD.

The rich club phenomenon describes the hierarchical "assortative" organization of the human brain where high degree nodes are more likely to be interconnected among themselves than expected by chance [3, 13]. The human brain, in both health and disease, exhibits networks with high connectivity density indicating that the communication hubs of the brain operate collectively, and not as individual entities [3]. The findings from our nodal analysis are in line with prior reports that the central hubs of the human and non-human brain, often called the 'central brain module', include the superior frontal regions, precuneus, posterior cingulate and insula [2, 5, 14]. We found that these rich club regions are disrupted in disease: bvFTD participants showed severe alterations in the left and right hemisphere frontal regions and insula, while EOAD participants showed greatest disruptions in the left hemisphere precuneus, posterior cingulate and superior frontal region (Fig. 1).

Failure of the central brain module may severely affect global network efficiency, and the communication among network components [3, 15]. Meanwhile, EOAD targets the rich club cortical regions of the left hemisphere, which is in line with some prior work suggesting that the left hemisphere structural connectivity might be more affected in late-onset AD than the right [4].

The global analysis of the weighted right club coefficient takes into account the interconnectivity of the densest subnetworks of the brain, as a function of weight (i.e., fiber density), at each *k*-level, relative to the top *k* ranked weights across of the whole network. Hence, the unnormalized rich club coefficient decreased with increasing *k*-value thresholds as nodes are "peeled off" (Fig. 2). When normalized, using random networks of the same size and degree distribution, this pattern inverts. The bvFTD brain network is more vulnerable to the erosive decomposition method of the rich club showing disruptions in fiber density throughout most of the *k*-value regime (Fig. 2b). This is indicated by a lower unnormalized rich club coefficient and higher normalized rich club coefficient, relative to healthy elderly. In contrast, the early stages of AD showed a more robust network, unaffected in the low *k*-value regime, but fiber density was disrupted among the rich club nodes of the EOAD network, relative to controls (Fig. 2c). Similarly, this is indicated by a higher normalized rich club coefficient while no differences were detected in the unnormalized rich club coefficient, compared to controls. Finally, among the two disease groups, bvFTD seemed to have a more drastically altered global connectivity, with lower fiber density compared to EOAD (Fig. 2d).

There is room for possible speculation regarding the biological origins of the low and high-degree *k*-value regime. It may be that the low-degree *k*-value regime, where low degree nodes are eliminated from the rich-club subnetwork, may reflect a high level of specialization of these nodes [3]. Meanwhile, the high-degree *k*-value regime may indicate the absence of a densely interconnected connectome, where low-degree connections between cortical regions are missing; this may also reflect levels of differentiation between the densely connected hubs of the network [3]. In our analyses, bvFTD participants had a severely impaired fiber density across

both the low- and high-degree k-value regime; the lower fiber density may have eliminated some of the potentially highly specialized low-degree nodes and reduced the connections among the high-degree nodes, leading to a more sparse rich club network. This may impair communication with neighboring nodes, and possibly function. Although EOAD affects the fiber density of major hubs in the network, the organizational integrity of the high-degree nodes in the rich club network is, however, relatively preserved.

One limitation of this study is the low spatial resolution of connectome—we represented the human brain as a network of 68 segmented cortical regions. This low network resolution may affect the topological properties of the recovered network [3]. In addition, the number of tractography fibers ($\sim$10,000) may also impact the detection of changes in complex structure and architecture of the white matter bundles. Overall, our analyses have successfully outlined distinct patterns of disruption in two different forms of dementia, providing insight into how damage to the human connectome may occur in degenerative brain disorders.

Acknowledgments Algorithm development and image analysis for this study was funded, in part, by grants to PT from the NIBIB (R01 EB008281, R01 EB008432) and by the NIA, NIBIB, NIMH, the National Library of Medicine, and the National Center for Research Resources (AG016570, AG040060, EB01651, MH097268, LM05639, RR019771 to PT). Data collection and sharing for this project was funded by NIH Grant 5R01AG034499-05. This work was also supported in part by a Consortium grant (U54 EB020403) from the NIH Institutes contributing to the Big Data to Knowledge (BD2K) Initiative, including the NIBIB and NCI.

References

1. Toga, A.W., Thompson, P.M.: Connectomics sheds new light on Alzheimer's disease. Biol. Psychiatry **73**(5), 390–392 (2013)
2. Sporns, O., Honey, C.J., Kötter, R.: Identification and classification of hubs in brain networks. PLoS ONE **2**, e1049 (2007)
3. van den Heuvel, M.P., Sporns, O.: Rich-club organization of the human connectome. J. Neurosci. **31**(44), 15775–15786 (2011)
4. Daianu, M., Jahanshad, N., Nir, T.M., Toga, A.W., Jack Jr., C.R., Weiner, M.W., Thompson, P.M.: Breakdown of brain connectivity between normal aging and Alzheimer's disease: a structural k-core network analysis. Brain Connect. **3**(4), 407–22 (2013)
5. Hagmann, P., Cammoun, L., Gigandet, X., Meuli, R., Honey, C.J., Wedeen, V.J., Sporns, O.: Mapping the structural core of human cerebral cortex. PLoS Biol. **6**, e159 (2008)
6. Honey, C.J., Sporns, O.: Dynamical consequences of lesions in cortical networks. Hum. Brain Mapp. **29**, 802–809 (2008)
7. Lu, P.H., Lee, G.J., Shapira, J., Jimenez, E., Mather, M.J., Thompson, P.M., Bartzokis, G., Mendez, M.F.: Regional differences in white matter breakdown between frontotemporal dementia and early-onset Alzheimer's disease. J. Alzheimers Dis. **39**(2), 261–269 (2014)
8. Thompson, P.M., Hayashi, K.M., de Zubicaray, G., Janke, A.L., Rose, S.E., Semple, J., Herman, D., Hong, M.S., Dittmer, S.S., Doddrell, D.M., Toga, A.W.: Dynamics of gray matter loss in Alzheimer's Disease. J. Neurosci. **23**(3), 994–1005 (2003)

9. Aganj, I., Lenglet, C., Sapiro, G., Yacoub, E., Ugurbil, K., Harel, N.: Reconstruction of the orientation distribution function in single and multiple shell Q-ball imaging within constant solid angle. Magn. Reson. Med. 64(2), 554–466 (2010)
10. Desikan, R.S., Segonne, F., Fischl, B., Quinn, B.T., Dickerson, B.C., Blacker, D., Buckner, R.L., Dale, A.M., Maguire, R.P., Hyman, B.T., Albert, M.S., Killiany, R.J.: An automated labeling system for subdividing the human cerebral cortex on MRI scans into gyral based regions of interest. Neuroimage **31**(3), 968–980 (2006)
11. Rubinov, M., Sporns, O.: Complex network measures of brain connectivity: uses and interpretations. Neuroimage **52**(3), 1059–1069 (2010)
12. Sporns, O.: The human connectome: a complex network. Ann. N. Y. Acad. Sci. **1224**, 109–125 (2011)
13. Bassett, D.S., Brown, J.A., Deshpande, V., Carlson, J.M., Grafton, S.T.: Conserved and variable architecture of human white matter connectivity. Neuroimage **54**, 1262–1279 (2011)
14. Zamora-López, G., Zhou, C., Kurths, J.: Cortical hubs form a module for multisensory integration on top of the hierarchy of cortical networks. Front. Neuroinform. **4**, 1 (2010)
15. Albert, R., Jeong, H., Barabasi, A.L.: Error and attack tolerance of complex networks. Nature **406**, 378–382 (2000)

Parcellation-Independent Multi-Scale Framework for Brain Network Analysis

M.D. Schirmer, G. Ball, S.J. Counsell, A.D. Edwards, D. Rueckert, J.V. Hajnal, and P. Aljabar

Abstract Structural brain connectivity can be characterised by studies employing diffusion MR, tractography and the derivation of network measures. However, in some subject populations, such as neonates, the lack of a generally accepted paradigm for how the brain should be segmented or parcellated leads to the application of a variety of atlas- and random-based parcellation methods. The resulting challenge of comparing graphs with differing numbers of nodes and uncertain node correspondences has yet to be resolved, in order to enable more meaningful intra- and inter-subject comparisons. This work proposes a *parcellation-independent multi-scale analysis* of commonly used network measures to describe changes in the brain. As an illustration, we apply our framework to a neonatal serial diffusion MRI data set and show its potential in characterising developmental changes. Furthermore, we use the measures provided by the framework to investigate the inter-dependence between network measures and apply an hierarchical clustering algorithm to determine a subset of measures for characterising the brain.

1 Introduction

The analysis of brain connectivity has many challenges and requires approaches dedicated to the analysis of complex systems of interacting components. Thus, graph theoretical applications are an attractive concept to analyse brain networks (see e.g. [15]). Brain networks can be defined over various scales, from synapses to entire brain regions, and a variety of imaging and sensing methods can be used to infer them, e.g. diffusion MRI (dMRI), functional MRI (fMRI) or EEG. The latter

M.D. Schirmer (✉) • G. Ball • S.J. Counsell • A.D. Edwards • J.V. Hajnal • P. Aljabar
Division of Imaging Sciences & Biomedical Engineering, King's College London, St. Thomas' Hospital, London, UK

Centre for the Developing Brain, King's College London, St. Thomas' Hospital, London, UK
e-mail: markus.schirmer@kcl.ac.uk

D. Rueckert
BioMedIA Group, Department of Computing, Imperial College London, London, UK

Centre for the Developing Brain, King's College London, St. Thomas' Hospital, London, UK

L. O'Donnell et al. (eds.), *Computational Diffusion MRI*, Mathematics and Visualization, DOI 10.1007/978-3-319-11182-7_3

two focus on functional networks, in which two brain regions are considered to have a connection if there exists a correlation in activation (see e.g. [5]). Diffusion MRI on the other hand infers the underlying structural network by identifying the probable pathways of white matter tracts connecting regions of interest [7].

Various network-theoretical aspects of brain connectivity have been investigated, such as segregation and integration [3] and rich club organisation [2, 6], alongside the study of conditions, such as Alzheimer's disease [9]. These approaches define a set of brain regions that act as nodes in a graph. In adults, these regions (parcels) are assumed to be functionally coherent or anatomically correspondent. For groups such as neonates, however, due to the significant changes in the developing brain in this early period, no such gold standard exists. In particular, the lack of such a standard parcellation and the unknown (and possibly varying) number of regions in the developing brain strongly motivates the use of random parcellation approaches, as they rely on fewer assumptions about the underlying anatomy [1]. The stochastic nature of random parcellation methods, however, can lead to varying number of nodes in the resulting network, either for the same brain or across different subjects. This can subsequently lead to artifactual variation in topological network measures obtained from the brain networks. Network normalisation has been proposed as a method of eliminating such dependency effectively on a local scale (see e.g. [14]). Figure 1 shows the dependence of the betweenness centrality as the number of regions varies over a range of 100–550.

Changes in global network measures have served as a basis to investigate differences in networks. However, the mentioned dependence on the network size hinders quantitative comparison of such measures across studies. As suggested in Fig. 1, determining which subject and which scan (baseline or follow-up) reveals a higher betweenness centrality is dependent on the number of regions/nodes and consequently might lead to different results when comparing subjects. Furthermore,

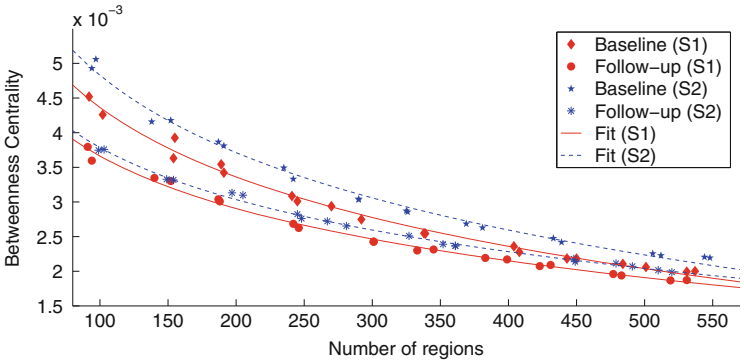

Fig. 1 Betweenness centrality taken from multiple brain networks defined over a range of 100–550 regions/nodes for two subjects S1 and S2, each with a baseline scan ($\sim$ 31 weeks gestational age (GA)) and a follow-up scan ($\sim$ 41 weeks GA). The fit for each subject at each scan is based on a logarithmic function

the trend of betweenness centrality suggests that the baseline scan may have a higher betweenness centrality than the follow-up scan at a number of regions higher than 550. This emphasises the potential bias of the results on the chosen parcellation scheme. It also emphasises that effects based on age or pathology may be difficult to detect, if a specific number of regions is chosen. This motivates the use of parcellations over a range of number of regions and subsequently the use of multi-scale analyses. Even though network normalisation methods may be able to eliminate this dependency on a local scale around a set number of regions, on a larger scale such dependencies might still exist [14].

It has been suggested that networks may undergo basic changes, such as subtle randomisation [13]. In particular in the early stages of brain development, during mid- to late-gestation when significant structural changes occur, it is reasonable to assume that such developmental changes are reflected in the structural network topology of the brain. This raises the question of how to quantify such changes in network structure.

In this work we propose the use of a parcellation-independent multi-scale framework for commonly used network measures in order to describe changes in the developing brain. This form of multi-scale analysis can use the dependence of the results of network measures on the number of regions for network characterisation. Furthermore, by using a reparametrisation, we are able to determine changes in structural brain networks independent of a specific parcellation scheme of the brain, with a given number of regions, which in turn allows us to investigate the clustering of network measures and propose a meaningful subset.

2 Methods and Data

2.1 Network Measures

There are various measures to describe properties of networks. For a more complete summary and detailed discussion, the reader is referred to [12]. Our analysis focuses mainly on three types of network measures, commonly thought to describe local segregation, global integration and prevalence of important nodes. Table 1 broadly subdivides the measures investigated into these three categories.

Table 1 Division of the measures investigated into three broad categories

Local segregation	Clustering coefficient (C), Transitivity (T), Modularity (Q)
Global integration	Characteristic path-length (λ), Efficiency (E), Diameter (dia), Eccentricity (ecc), Degree (k)
Node importance	Betweenness centrality (BC)

2.2 Parcellation-Independent Multi-Scale Analysis

The proposed approach begins by parcellating the brain of each subject at multiple scales, ranging from a coarse scale with larger regions ($\sim$ 100) to a fine scale ($\sim$ 550 regions). Structural networks at each scale are then estimated, based on probabilistic tractography of the dMRI data for each subject, and using each of its multiple parcellations. This provides a number of measures of network connectivity (see Table 1) at a variety of different scales. We use the complete set of values for each measure to fit a model and subsequently use the model parameters to represent the data across all scales. The model that is fitted can be determined by the user and our approach can readily accommodate different choices of models. We find that the function

$$m(G) = a \cdot \log(N(G)) + b, \tag{1}$$

where $m(G)$ is an individual measure obtained from a graph G defined over $N(G)$ nodes, can be used to reparametrise the network measure over the entire range, with parameters a and b. These parameters can be estimated with a standard fitting algorithm and serve as a summary measure for the subject as part of a group analysis. We emphasise that other functions may be used within this framework and that the choice of function acts as a parameter of our approach.

This process is repeated for each subject and the parameters a and b can be used as multi-scale measures to describe the brain networks of all subjects for each of the original network measures. Furthermore they can be used to compare brain networks across subjects and across ages in a parcellation-independent manner. The framework of the parcellation-independent multi-scale analysis is shown schematically in Fig. 2.

2.3 Correlation

In order to potentially determine a subset of independent parameters for characterising changes in the developing brain we conduct a correlation analysis among the calculated parameters. As it has been suggested that network measures may be non-linearly correlated [8], we base our analysis on Spearman's rank correlation coefficient.

2.4 Subject and Image Data

Ethical permission was granted by the Hammersmith and Queen Charlotte's and Chelsea Hospital (QCCH) Research Ethics Committee and written parental consent was obtained for each infant.

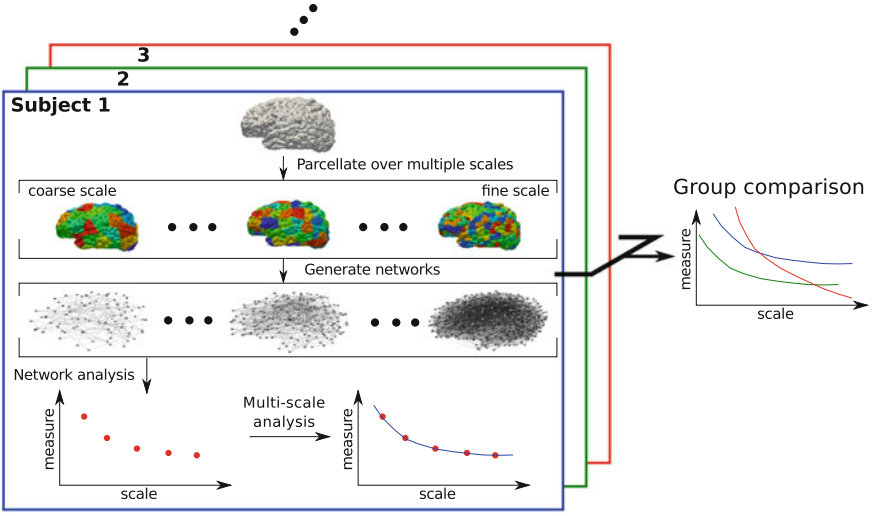

Fig. 2 A framework for parcellation-independent multi-scale analysis. Each brain image is parcellated at multiple scales from a coarse (larger regions) to a fine scale. Subsequent estimates of structural networks are based on the subjects' dMRI data. For each network, the fitted models for global network measures over multiple scales are used for group comparison

As part of studies at Queen Charlotte's and Chelsea Hospital, serial dMRI data were acquired from 28 recruited infants born at less than 32 weeks GA. Mean GA at birth was 28.0 ± 2.3 weeks and the mean age at scan was 30.8 ± 1.9 and 41.2 ± 1.2 weeks at the first and second scans respectively.

Each infant successfully underwent 32-direction dMRI at both time points on a Philips 3T scanner, using an eight channel phased array head coil. Single shot echo planar imaging dMRI was acquired in the transverse plane in 32-non-collinear directions using the following parameters: TR: 8, 000 ms; TE: 49 ms; slice thickness: 2 mm; field-of-view: 224 mm; matrix: 128×128 (voxel size: $1.75 \times 1.75 \times 2$ mm; b-value: 750 s/mm^2; SENSE factor of 2). The individual gradient directions of the diffusion-weighted images were assessed and 17 of 28 subjects had at least one gradient removed (maximum: 4, mean: 2.35) due to motion artefacts.

Twenty instances of random parcellations of the cortex into between 100 and 550 small regions were obtained for each subject using Poisson disk sampling [4]. We emphasise that the use of a probabilistic parcellation method is beneficial, as the optimal number and location of brain regions in neonates for the purpose of connectivity analysis is unknown. The approach allows distinct parcellations across a large number of regions to be readily generated, enabling stochastic analysis methods to be applied. Diffusion MRI data were pre-processed using the FSL's Diffusion Toolkit and corrected for geometric distortions. Subsequently a voxelwise, two compartment "ball-and-stick" diffusion model (implemented as BedpostX in FSL) was fit to the diffusion data, with a maximum of two fibre populations per voxel. A probabilistic diffusion tractography algorithm (modified version of

ProbtrackX [11]) was applied to each parcellation in order to generate structural networks, where the connections were weighted by the mean integrated anisotropy along the streamlines that reached their target. For more details the reader is referred to [2].

3 Results

3.1 Multi-Scale Analysis

In order to analyse our datasets, we fitted the model given by Eq. 1 to the global network measures generated by 20 parcellations over a range of 100–550 regions. The results for parameters a and b are given in Fig. 3. The values represent the group

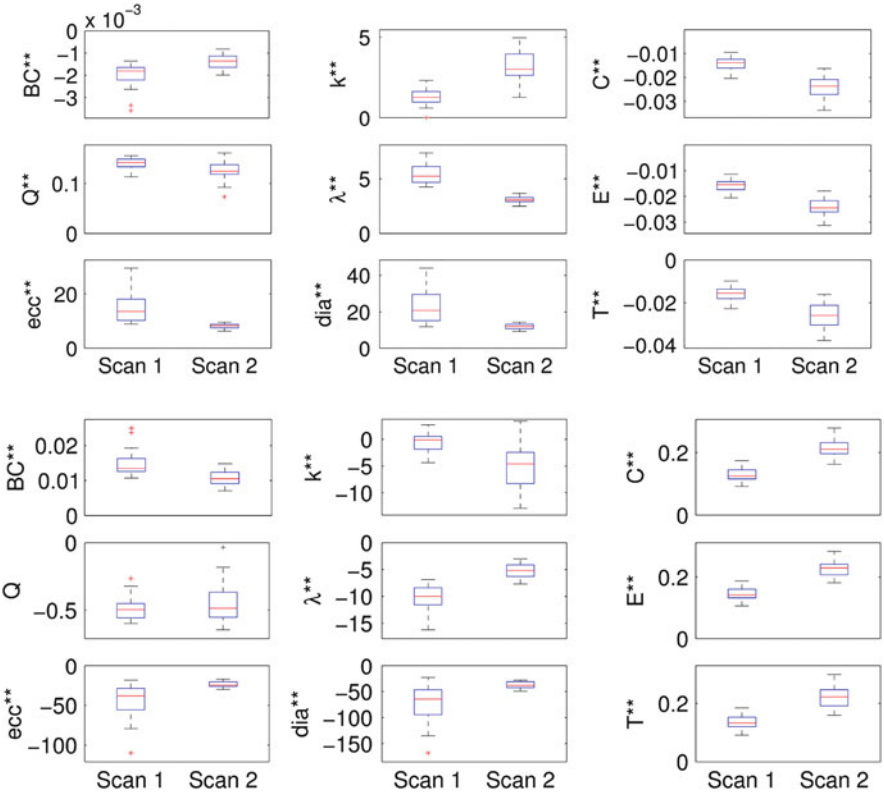

Fig. 3 Box-plots for the model parameters a (*top*) and b (*bottom*) for each measure at both time points. Values represent the group at each scan, where the subjects of scan one and two were 30.8 ± 1.9 and 41.2 ± 1.2 weeks old, correspondingly. One and two stars next to the measure name represents P-values of $P < 0.01$ and $P < 0.001$, correspondingly

Table 2 Coefficients of determination of a linear fitting model and the logarithmic fitting model (given by Eq. 1) for each network measure averaged over 56 subjects

	BC	k	C	Q	λ	E	ecc	dia	T
Linear model	0.919	0.748	0.904	0.923	0.976	0.929	0.881	0.872	0.903
Logarithmic model	0.986	0.894	0.989	0.988	0.982	0.992	0.894	0.881	0.990

The average standard deviation of the coefficients of determination over all measures for the linear and logarithmic model are 0.053 and 0.045, respectively

at each scan. The stars indicate P-values obtained from a paired t-test of $P < 0.01$ (*) and $P < 0.001$ (**).

Our results suggest that parameter a changes highly significantly with age for all network measures. Parameter b changes highly significantly for all measures, except modularity Q.

In order to assess the quality of fit, we calculated the coefficient of determination R^2 for each measure and each subject. $R^2 \in [0, 1]$ represents the amount of variation in the data explained by a given model and is equivalent to 1/0 if all/none of the variation in the data is captured by the model. We furthermore compared the results for R^2 for the logarithmic model given by Eq. 1 to a linear model. The results are given in Table 2.

Our results show that the logarithmic model explains on average 95 % of the variation within the data and outperforms a linear model for all network measures.

3.2 Determining an Independent Subset of Measures

In a further test we analysed the non-linear correlations between the model parameters across the network measures. Our results indicate a high correlation between the model parameters for all network measures, with an average absolute correlation coefficient of 0.68 and 0.58 for parameters a and b respectively. Our results support the suggestion that most network measures are highly correlated, as presented e.g. [10], suggests that the computation of all network measures may be unnecessary for the characterisation of the changes within brain networks.

In order to determine a comparatively independent subset of measures, we conducted a hierarchical cluster analysis using the absolute value of the correlations for each parameter individually and for the combination of both, where we calculated the combined correlation by taking the geometric mean of the corresponding individual absolute values for a and b. Figure 4 shows the results of the complete-linkage hierarchical cluster analysis.

In order to pick a number of clusters n_c, we analysed the dendrogram presented in Fig. 4 in terms of consistency. All three provided the same clustering for $n_c \in \{2, 4, \geq 6\}$. The choice of clusters, as it presents an open challenge, is user dependent and difficult to determine in a data driven analysis. For example, based on

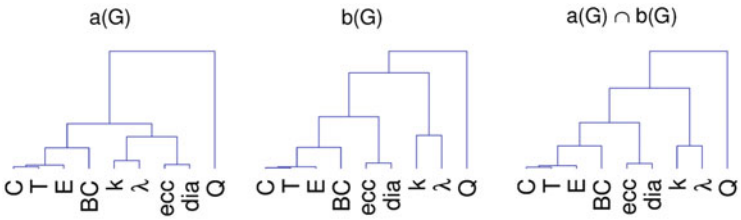

Fig. 4 Complete-linkage hierarchical cluster analysis performed on the pairwise measure correlations, based on the individual and combined correlations of parameter a and b

a choice of four clusters, our work suggests a grouping of $\{C, T, E, BC\}$, $\{ecc, dia\}$, $\{k, \lambda\}$ and $\{Q\}$, where any combination may be used to build a subset of measures to investigate changes in brain networks.

4 Conclusion

In this work, we introduced a multi-scale framework for analysing network measures that can be used to characterise changes in brain networks, circumventing the dependency on the parcellation scheme. Our approach allows for analysis of networks in two ways. First, the off-set parameter b may be used in a similar way to global network measure comparison, however, the benefit of our approach lies in the independence of changes in parcellation scale. The second model parameter, a, on the other hand may provide insight into the underlying network type. This has been suggested in the results of Zalesky et al., which show that clustering coefficient and characteristic path-length in complete random networks have a different slope than brain networks across a large number of regions [16]. Further investigation is needed to show in more detail if these changes can be used as biomarkers in order to assist in the early detection of mental and developmental diseases and their dependency on the dMRI and tractography model.

Interpreting the changes of b in our analysis in a similar way to global network measure comparison indicates that the brain develops towards a higher efficiency with respect to information flow on local scales. This reinforcement of local segregation is highlighted by the increase in clustering coefficient and transitivity. However, measures thought to reflect global integration appear to decrease with age (decreasing degree and increasing characteristic path-length, diameter and eccentricity), but with a contrasting increase in efficiency. These results differ from previously published studies which suggest an increase in both local segregation and global integration over this period [14]. Further analysis regarding the interpretation of b with respect to changing network topology is necessary. The aim of future work will be to determine if this approach is compatible with direct global network measure comparisons, which in turn might indicate an inherent bias on

the parcellation scheme of the latter. The change of parameters a may suggest a fundamental change of the underlying structural brain network, as one might expect in these early stages of brain development.

Our work highlights further the inter-measure dependence. It suggests that commonly used network measures are correlated and thus may reflect the same underlying topological features. In this work we showed their interdependence independent of the parcellation scheme, number of nodes and processing steps such as normalisation. Furthermore, we used our results to propose a subset of measures, which can be used to investigate changes in brain networks. We note that finding a maximally independent subset of measures would not only be beneficial for computational reasons, but also for second order analysis, where artefactual correlations are removed from the data.

Acknowledgements This research was supported by the National Institute for Health Research (NIHR) Biomedical Research Centre at Guy's and St Thomas' NHS Foundation Trust and King's College London. The views expressed are those of the author(s) and not necessarily those of the NHS, the NIHR or the Department of Health. Medical Research Council (MRC) Centre for Transplantation, King's College London, UK—MRC grant no. MR/J006742/1.

References

1. Ball et al.: The influence of preterm birth on the developing thalamocortical connectome. Cortex 1–11 (2012)
2. Ball et al.: Rich-club organization of the newborn human brain. Proc. Natl. Acad. Sci. **111**(20), 7456–7461 (2014)
3. Bassett, D.S., Bullmore, E.: Small-world brain networks. The neuroscientist **12**(6), 512–523 (2006)
4. Bridson, R.: Fast poisson disk sampling in arbitrary dimensions. In: ACM SIGGRAPH, vol. 2007. ACM (2007)
5. Bullmore, E., Sporns, O.: Complex brain networks: graph theoretical analysis of structural and functional systems. Nat. Rev. Neurosci. **10**(3), 186–198 (2009)
6. Collin et al.: Structural and functional aspects relating to cost and benefit of rich club organization in the human cerebral cortex. Cereb. Cortex (2013)
7. Dyrby et al.: Validation of in vitro probabilistic tractography. NeuroImage **37**(4), 1267–77 (2007)
8. Li et al.: The correlation of metrics in complex networks with applications in functional brain networks. J. Stat. Mech. **2011**(11), P11,018 (2011)
9. Lo et al.: Diffusion tensor tractography reveals abnormal topological organization in structural cortical networks in Alzheimer's disease. J. Neurosci. **30**(50), 16,876–85 (2010)
10. Lynall et al.: Functional connectivity and brain networks in schizophrenia. J. Neurosci. **30**(28), 9477–9487 (2010)
11. Robinson et al.: Identifying population differences in whole-brain structural networks: a machine learning approach. NeuroImage **50**(3), 910–9 (2010)
12. Rubinov, M., Sporns, O.: Complex network measures of brain connectivity: uses and interpretations. NeuroImage **52**(3), 1059–69 (2010)
13. Rubinov et al.: Small-world properties of nonlinear brain activity in schizophrenia. Hum. brain Mapp. **30**(2), 403–416 (2009)

14. Schirmer et al.: Normalisation of Neonatal Brain Network Measures Using Stochastic Approaches. In: Mori, et al. (ed.) MICCAI 2013, Lecture Notes in Computer Science, vol. 8149, pp. 574–581. Springer, Berlin (2013)
15. Sporns, O.: The human connectome: a complex network. Ann. N. Y. Acad. Sci. **1224**, 109–125 (2011)
16. Zalesky et al.: Whole-brain anatomical networks: does the choice of nodes matter? NeuroImage **50**(3), 970–83 (2010)

Part II
Clinical Applications

Multiple Stages Classification of Alzheimer's Disease Based on Structural Brain Networks Using Generalized Low Rank Approximations (GLRAM)

L. Zhan, Z. Nie, J. Ye, Y. Wang, Y. Jin, N. Jahanshad, G. Prasad, G.I. de Zubicaray, K.L. McMahon, N.G. Martin, M.J. Wright, and P.M. Thompson

Abstract To classify each stage for a progressing disease such as Alzheimer's disease is a key issue for the disease prevention and treatment. In this study, we derived structural brain networks from diffusion-weighted MRI using whole-brain tractography since there is growing interest in relating connectivity measures to clinical, cognitive, and genetic data. Relatively little work has used machine learning to make inferences about variations in brain networks in the progression of the Alzheimer's disease. Here we developed a framework to utilize generalized low rank approximations of matrices (GLRAM) and modified linear discrimination analysis for unsupervised feature learning and classification of connectivity matrices. We apply the methods to brain networks derived from DWI scans of 41 people with Alzheimer's disease, 73 people with EMCI, 38 people with LMCI, 47 elderly healthy controls and 221 young healthy controls. Our results show that this new framework can significantly improve classification accuracy when combining multiple datasets; this suggests the value of using data beyond the classification task at hand to model variations in brain connectivity.

L. Zhan (✉) • Y. Jin • N. Jahanshad • G. Prasad • P.M. Thompson
Department of Neurology, Imaging Genetics Center, Keck School of Medicine, University of Southern California, Los Angeles, CA 90089, USA
e-mail: zhan.liang@gmail.com

Z. Nie • J. Ye • Y. Wang
School of Computing, Informatics, and Decision Systems Engineering, Arizona State University, Tempe, AZ 85004, USA

G.I. de Zubicaray • K.L. McMahon
fMRI Laboratory, University of Queensland, Brisbane, QLD 4072, Australia

N.G. Martin • M.J. Wright
Berghofer Queensland Institute of Medical Research, Brisbane, QLD 4006, Australia

L. O'Donnell et al. (eds.), *Computational Diffusion MRI*, Mathematics and Visualization, DOI 10.1007/978-3-319-11182-7_4

1 Introduction

Alzheimer's disease is by far the leading form of dementia. There is no cure for the disease, which worsens as it progresses, and eventually leads to death. According to the studies of Alzheimer's Disease Neuroimaging Initiative (ADNI) and other large-scale multicenter studies, this disease has been described into four stages: health control (HC); early mild cognitive impairment (EMCI), late mild cognitive impairment (LMCI) and Alzheimer's disease (AD) [1–3]. HC means there is no sign/clue that subject have any cognition impairment, while EMCI and LMCI are the middle stages in time for disease detection. AD is the last stage when there is clearly clue that disease has been onset. Defining at-risk stages of this disease is crucial for predementia detection, which in turn is the requirement for future predementia treatment. In literature, the Alzheimer's disease multiple stages' classification is mainly based on subjective questionnaire [1, 4]. Here we adopted machine learning method to explore multiple stages' automatic classification using diffusion-weighted MRI (DW-MRI).

DW-MRI is a non-invasive brain imaging technique, sensitive to aspects of the brain's white matter microstructure that are not typically detectable with standard anatomical MRI [5]. With DWI, anisotropic water diffusion can be tracked along the direction of axons using tractography methods. When tractography is applied to the entire brain, one can reconstruct major fiber bundles and describe connectivity patterns in the brain's anatomical network [6]. Brain networks and topological measures derived from them have been shown to be highly associated with aspects of brain function and clinical measures of disease burden [7]. Some studies have begun to apply machine learning techniques to identify network features that differentiate people with various neurological and psychiatric disorders from matched HC [8]. However, most studies focus only on identifying abnormal connectivity patterns in a single disease, compared to controls, and not intermediate stages of the disease, using only using one dataset to do so. While this may improve our understanding of the outcome of the disease, when applying the same analysis to a new disease or a new dataset, the model must be re-trained and re-evaluated. Often, disease effects (or effects of other predictors on brain networks) are subtle and may not be detected in one dataset alone, or may show conflicting results across datasets. In this light, consortia such as Enhancing Neuro Imaging Genetics through Meta-Analysis (Enigma) have been formed to jointly analyze over 20,000 brain scans from patients and controls scanned at over 100 sites worldwide to meta-analyze effects on the brain [9]. This allows researchers to compare effect sizes obtained with different imaging protocols and scanners, but also across different diseases. The notion of who qualifies as a healthy control may also depend on the dataset and may not represent the healthy population at large. If multiple datasets are used to model normal variation, then arguably diagnostic classification may be improved without retraining new models for every disease and every new dataset.

When pooling scans from patients with a variety of diseases, or at different stages of disease progression, machine learning techniques can classify the data into diagnostic groups. This may involve feature extraction, dimension reduction,

model training and testing. For example, principal component analysis (PCA) uses an orthogonal linear transformation to convert observations of potentially correlated variables into a new set of linearly uncorrelated principal components (PC). New datasets can then be classified into groups based on PC-projected features. Linear discriminant analysis (LDA) can also be used for dimensionality reduction and classification. It finds a linear combination of features that optimally separates two or more classes. LDA and PCA both use linear combinations of variables to model the data. LDA models the differences between classes within the data, but PCA seeks components that have the highest variance possible under the constraint that they are orthogonal to (i.e., uncorrelated with) the preceding components [10]. These dimensionality reduction methods assume that the data form a vector space. Here, each subject's data is modeled as a vector and the collection of subjects is modeled as a single data matrix. Each column of the data matrix corresponds to one subject and each row corresponds to a feature. There are disadvantages of this vector model, as it overlooks spatial relations within the data. To overcome this, generalized low rank approximations of matrices (GLRAM) has been proposed to use a lower dimension 2D matrix to obtain more compact representations of original data with limited loss of information [11].

In this study, we combined two different datasets collected with both standard T1-weighted MRI and DW-MRI and created connectivity networks for all study participants. Both datasets had scanned healthy controls; one had also scanned patients with Alzheimer's disease and patients with early and advanced signs of mild cognitive impairment (early MCI and late MCI respectively). We merged this data hypothesizing that we could automatically classify the scans into four groups (HC, EMCI, LMCI, and AD) using brain networks as the raw features. We used GLRAM to first reduce the dimensionality, and then applied LDA in the PCA subspace to classify the data. Classification of data from multiple sites and scanners will help us to understand differences in disease progression, ideally unconfounded by scanner differences.

2 Subjects and Methods

2.1 Data Description

Table 1 summarizes the two datasets used in this study. For all datasets, participants were scanned with both DW-MRI and standard T1-weighted structural MRI.

The first dataset included 221 healthy young adults. Images were acquired with a 4T Bruker Medspec MRI scanner, using single-shot echo planar imaging with the following parameters: TR/TE = 6,090/91.7 ms, 23 cm FOV, and a 128×128 acquisition matrix. Each 3D volume consisted of 55 2-mm axial slices, with no gap, and 1.79×1.79 mm^2 in-plane resolution. Hundred and five image volumes were acquired per subject: 11 with T2-weighted b0 volumes and 94 diffusion-weighted volumes (b = 1,159 s/mm^2).

Table 1 Summary of data used in this study

	Dataset 1			Dataset 2		
Type	Number	Age	Sex	Number	Age	Sex (M)
HC	221	24.1±2.1	85M	47	72.6±6.2	21
EMCI	N/A			73	72.3±7.9	44
LMCI				38	72.6±5.6	24
AD				41	75.5±9.0	25

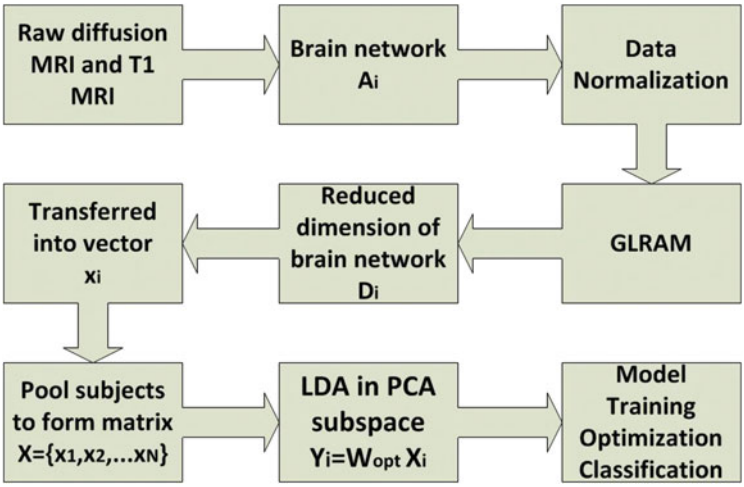

Fig. 1 Flowchart of proposed framework for connectivity based disease classification

The second dataset was from ADNI2, the second stage of the Alzheimer's disease neuroimaging initiative (ADNI), publically available online (http://adni.loni.usc.edu). This dataset has 199 subjects, which includes 47 healthy elderly controls, 111 with mild cognitive impairment (MCI) and 41 with Alzheimer's disease (AD). Images were acquired with 3T GE Medical Systems scanners at 14 sites across North America. Each 3D volume consisted of 2.7 mm isotropic voxels with a 128×128 acquisition matrix. Forty six image volumes were acquired per subject: 5 T2-weighted b0 images and 41 diffusion-weighted volumes (b = 1,000 s/mm^2).

2.2 Proposed Framework

First, we first used GLRAM to create dimensionality-reduced matrices for each subject. These new matrices were used as input to LDA on PCA for model training. Adaptive 1-nearest neighbor classification (A-1NNC) was used to label the test cases. The framework's flowchart is shown in Fig. 1.

2.2.1 Brain Network Computation

In this study, we used the subjects' structural networks as features for classification. To compute the brain networks, FreeSurfer (http://freesurfer.net/) was run on the T1-weighted images to automatically segment the cortex into 68 unique regions (34 per hemisphere). This segmentation was dilated with an isotropic box kernel of 5 mm to ensure cortical labels would intersect with the white matter tissue in areas of reliable tractography for the connectivity analysis. We registered the T1-weighted intensity image to the fractional anisotropy (FA) image from the DWI data. The resultant transformations were used to transform the dilated cortical segmentations into the DWI space.

DWI images were corrected for eddy current distortions using FSL [12]. Then we used an optimized global probabilistic tractography method [13] to generate whole brain tractography for each subject. We combined the cortical segmentation and tractography to compute a connectivity matrix for each subject. The matrices were 68×68 in dimension, corresponding to the 68 segmented cortical regions. Each cell value of the matrix represented the number of fibers that intersected pairs of cortical regions. We normalized the matrix by the total number of fibers per subject. This symmetric 68×68 matrix served as the input for our classification.

2.2.2 Data Normalization

Some form for data normalization is critical especially when working with data from different cohorts or projects, covering a wide age range. So directly pooling two datasets may introduce bias, if the proportion of controls depends on the scanner used or scanning site. To account for these confounds, we used generalized linear regression to adjust each value in the brain connectivity matrix for age, sex and scanning site. Then we further normalized the residual after regression to yield centered, scaled data, which served as the input for next step. This normalization used a Z-transformation based on the standardized statistic Z=(X-mean(X))/std(X), where X is one feature vector within each dataset. For our connectivity matrix, X is element (i,j) for all subjects in each dataset.

2.2.3 GLRAM

The purpose of GLRAM, proposed in [11], is similar to singular value decomposition (SVD) but has lower computational cost; it finds a lower rank 2D matrix D_i to approximate the original 2D matrix Ai, realizing the following function:

$$\min_{L,R,D} \sum_{i=1}^{N} \left\| A_i - L D_i R^T \right\|_F^2 \tag{1}$$

Here, A_i is each subject's raw brain network, N is the total number of subjects, Di is the reduced representation of A_i; and L and R are transformation matrices on the left and right side, respectively. F is the Frobenius norm. Details of how to solve this cost function optimization problem are in [11].

2.2.4 LDA on the PCA Subspace

PCA finds linear projections that maximize the scatter of all projected samples. Mathematically, given a set of N subjects $X = \{x_1, x_2, \ldots x_N\}$, where each subject belongs to one of C classes $X_1, X_2, \ldots X_C$, we plan to map x_i to y_i where $y_i \in R^m$ and m<n. To do this, we define a linear transformation W to satisfy $y_i = W^T x_i$ (i=1,2,...N). In PCA, the optimal projection $W_{opt-pca}$ is defined as:

$$\begin{cases} W_{opt-pca} = \arg\max_w \left| W^T S_T W \right| \\ S_T = \sum_{i=1}^{N} (x_i - \mu)(x_i - \mu)^T \end{cases} \tag{2}$$

Here $\mu \in R^n$ is the mean value of all samples. And $W_{opt-pca} = \{w_i \in R^n \,|i = 1..m\}$ is the set of eigenvectors of ST corresponding to the m largest eigenvalues. Once eigenvectors are determined, all data can be projected into this eigenspace for classification. However, PCA is not optimal for classification as the dimensions that model the greatest amount of variance in the data are not typically the ones that best differentiate groups. In other words, the discriminant dimensions could be thrown out or intermixed during PCA.

LDA seeks a projection to maximize the ratio of the determinant of the between-class scatter matrix (S_B) of the projected data to the determinant of the within-class scatter matrix (S_W) of the projected data. However, the within-class scatter matrix S_W in LDA is typically singular. This is because the number of subjects is often much smaller than the number of variables in the data. To overcome the complication of a singular S_W, we adopted the solution in [14]. In short, C is the number of classes, so we first adopted PCA to reduce the dimension of the feature space to N-C , and then we applied the standard LDA to reduce the dimension to C-1, so the transformation W_{opt} is given by:

$$\begin{cases} W_{opt} = W_{opt-pca} W_{opt-pca-lda} \\ W_{opt-pca-lda} = \arg\max_w \dfrac{\left| W^T W_{opt-pca}^T S_B W_{opt-pca} W \right|}{\left| W^T W_{opt-pca}^T S_W W_{opt-pca} W \right|} \\ S_B = \sum_{i=1}^{C} N_i (\mu_i - \mu)(\mu_i - \mu)^T \\ S_w = \sum_{i=1}^{C} \sum_{x_k \in X_i} (x_k - \mu_i)(x_k - \mu_i)^T \end{cases} \tag{3}$$

Where μ_i is the mean vector of class X_i, and N_i is the number of samples in class X_i. Also, $W_{opt-pca}$ can be computed using Eq. 2.

2.2.5 Adaptive 1-NNC

We classified the subject's class membership based on the Euclidean distance using 1-nearest neighbor classification (1-NNC). 1-NNC is designed to assign an object to the same class as its single nearest neighbor. Adaptive 1-NNC (A-1NNC) is a variation of 1-NNC. The test objects' class membership is still decided based on the class membership of the single nearest-neighbor used for training, but once a new test object's class membership has been determined, it is grouped into training group to enhance the membership class affinity.

2.3 Experimental Procedure

The detailed procedure is described as follows:

1. Construct the brain network for each subject in both datasets.
2. Data Normalization to get input matrix A.
3. Group subjects into four classes: HC, EMCI, LMCI and AD.
4. Divide each class into three parts by randomization: training (80 %), optimizing (10 %) and testing (10 %).
5. Pick up training dataset A_{train}
6. Set the initial dimension size to run GLRAM on A_{train} to get L_{train}, R_{train} and $D_{train}=D_1, D_2, \ldots D_N$ for each class (using Eq. 1)
7. Transfer D_{train} into vector x_i and form matrix $X_{train}=\{ x_1, x_2, \ldots x_N \}$
8. Run LDA in PCA subspace to get W_{opt} (using Eq. 3) and get the projected data $Y_{train}= y_1, y_2, \ldots y_N = W_{opt}X$
9. Then the projection of the optimizing dataset $A_{optimizing}$ can be generated using Eq. 4.
10. Use A-1NNC classification to assign $Y'_{optimizing}$s class based on Y_{train} and compute the accuracy by comparing the assigned membership to ground truth
11. Then adjust the parameter in **Step 6**, re-run steps 6–10 to find the optimal parameter for the dimension of L and R in Eq. 1 that achieves best accuracy
12. Use this optimal parameter achieved in **Step 11**, and use the test dataset to test our framework and get final grade
13. Repeat **steps 4–12** (100 times) and compute the area under the curve (AUC) for overall classification accuracy, as well as for the accuracy of each class. The higher the AUC, the better the model performance.

$$\begin{cases} D_{\text{optimizing}} = L_{train}^{T} A_{\text{optimizing}} R_{train} \\ D_{\text{optimizing}} \rightarrow X_{\text{optimizing}} \\ Y_{\text{optimizing}} = W_{opt} X_{\text{optimizing}} \end{cases} \tag{4}$$

3 Results and Discussion

Before we ran classification experiments, we first studied the effects of pooling datasets 1 and 2 together. A testable null hypothesis is that the feature set in the dataset 1 and dataset 2 are independent random samples drawn from Normal distributions with equal means and equal but unknown variances. As each subject's brain network is symmetric and has dimension 68×68, we have 68×67/2=2,278 features per subject. Thus we adopted false discovery rate (FDR) to account for the multiple comparisons (FDR q = 0.05). Figure 2 shows the FDR-corrected P map from a Student's t-test between dataset 1 (all HC) and HC from dataset 2. Our results showed that by using our proposed normalization methods, there are no detectable differences between the HCs in dataset 1 and dataset 2. Given this information, we pooled data bettering an effort to boost statistical power.

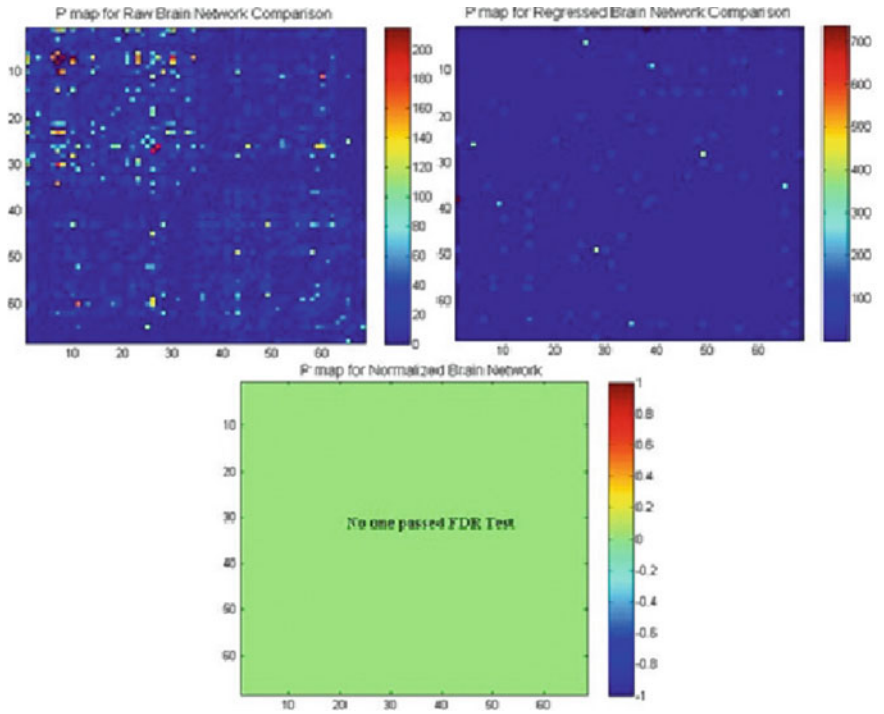

Fig. 2 An FDR-corrected P map (on a log scale) for the null hypothesis asserting that features in datasets 1 and 2 are independent random samples drawn from Normal distributions with equal means and equal but unknown variances. All P values larger than the critical FDR threshold have been set to zero. The *top left* map is for the raw brain networks (generated in Sect. 2.2.1). The *top right* map is for residual brain networks after the effects of age and sex are removed (regression on age, sex and data label, described in Sect. 2.2.2). The *bottom map* is for normalized brain networks generated as in Sect. 2.2.2

Table 2 Comparison of AUCs

	Overall	HC	EMCI	LMCI	AD
Dataset2 only					
Direct PCA	26.19	26.50	46.47	17.50	22.44
LDA in the PCA subspace	26.31	59	21.20	9.25	13.67
GLRAM only	26.74	53.1	14.38	12.38	21.22
Proposed method	40.48	40	53.33	37.50	22.22
Dataset1+Dataset2					
Direct PCA	65.43	82.36	5.25	5.75	14
LDA in the PCA subspace	66.48	90.14	5.2	2	5.11
GLRAM only	80.69	99.96	43.40	15	21.33
Proposed method	83.62	100	46.67	37.50	33.33

A higher value indicates greater accuracy

Then we compared our proposed method with the other three methods including: direct PCA, LDA in the PCA subspace, and GLRAM only. Table 2 shows the AUC comparison for the 4-class (HC, EMCI, LMCI and AD) classification results using dataset 2 only and then also using both datasets for defining the PCs. The results indicated that our proposed framework performed better than other methods. As shown in Table 2, PCA showed the poorest performance, which is reasonable as PCA emphasizes the data variance, which is not necessarily useful for classification. Also, GLRAM performed better than LDA. The possible explanation could be that our features were the full brain networks, which emphasized the connections between the nodes. So there may be some 2D spatial information in the features that are ignored in the vector space model (LDA). Moreover, HC classification accuracy improved when adding dataset 1, suggesting the advantage of pooling data, so long as appropriate normalization is applied.

4 Conclusion

Here we presented a novel framework using GLRAM and modified LDA to reduce the dimension of a 68×68 element structural brain connectivity network. We then used Adaptive-1NNC to classify patients with different stages of Alzheimer's disease versus healthy controls. Our proposed method outperformed classical classification methods, but incorporating healthy controls from additional datasets also improved classification.

As our proposed framework is based on some elementary approaches (such as PCA and LDA), we compared these methods to ours, instead of other more complex approaches. In future work, we will try more sophisticated approaches. As an innovation, most current studies focus on one type disease vs. HC, while our target is for a more complicated (realistic) situation and we know there are ways to improve the proposed framework. Our current results indicate that our approach is promising.

References

1. Jessen, F., Wolfsgruber, S., Wiese, B., et al.: AD dementia risk in late MCI, in early MCI, and in subjective memory impairment. Alzheimers Dement. **10**, 76–83 (2014)
2. Mitchell, A.J.: CSF phosphorylated tau in the diagnosis and prognosis of mild cognitive impairment and Alzheimer's disease: a meta-analysis of 51 studies. J Neurol. Neurosurg. Psychiatry **80**, 966–975 (2009)
3. Aisen, P.S., Petersen, R.C., Donohue, M.C., et al.: Clinical core of the Alzheimer's disease neuroimaging initiative: progress and plans. Alzheimers Dement. **6**, 239–246 (2010)
4. Winblad, B., Palmer, K., Kivipelto, M., et al.: Mild cognitive impairment–beyond controversies, towards a consensus: report of the international working group on mild cognitive impairment. J. Intern. Med. **256**, 240–246 (2004)
5. LeBihan, D.: IVIM method measures diffusion and perfusion. Diagn. Imaging (San Franc) **12**, 133–136 (1990)
6. Sporns, O.: The human connectome: a complex network. Ann. N.Y. Acad. Sci. **1224**, 109–125 (2011)
7. Ajilore, O., Lamar, M., Leow, A., et al.: Graph theory analysis of cortical-subcortical networks in late-life depression. Am. J. Geriatr. Psychiatry **22**, 195–206 (2014)
8. Zhang, J., Cheng, W., Wang, Z., et al.: Pattern classification of large-scale functional brain networks: identification of informative neuroimaging markers for epilepsy. PLoS One **7**, e36733 (2012)
9. Thompson, P.M., Stein, J.L., Medland, S.E., et al.: The ENIGMA consortium: large-scale collaborative analyses of neuroimaging and genetic data. Brain Imaging Behav. **8**, 153–162 (2014)
10. Wang, J., Zhou, L.:Research on magnetoencephalography-brain computer interface based on the PCA and LDA data reduction. Sheng Wu Yi Xue Gong Cheng Xue Za Zhi **28**, 1069–1074 (2011)
11. Ye, J.: Generalized low rank approximations of matrices. Mach. Learn. **61**, 167–191 (2005)
12. Jenkinson, M., Beckmann, C.F., Behrens, T.E., et al.: FSL. Neuroimage **62**, 782–790 (2012)
13. Aganj, I., Lenglet, C., Jahanshad, N., et al.: A Hough transform global probabilistic approach to multiple-subject diffusion MRI tractography. Med. Image Anal. **15**, 414–425 (2011)
14. Belhumeur, P.N., Hespanha, J.P., Kriegman, D.J.: Eigenfaces vs. fisherfaces: recognition using class specific linear projection. IEEE Trans. Pattern Anal. Mach. Intell. **19**, 711–720 (1997)

The Added Value of Diffusion Tensor Imaging for Automated White Matter Hyperintensity Segmentation

Hugo J. Kuijf, Chantal M.W. Tax, L. Karlijn Zaanen, Willem H. Bouvy, Jeroen de Bresser, Alexander Leemans, Max A. Viergever, Geert Jan Biessels, and Koen L. Vincken

Abstract Automated white matter hyperintensity (WMH) segmentation techniques for brain MRI often employ voxel-wise classifiers, trained on traditional features such as: multi-spectral MR image intensities, spatial location, texture, or shape. Recent studies show that diffusion tensor imaging (DTI) provides a measure for WMH, independent from the commonly used FLAIR images. Hence, we hypothesized that adding features derived from DTI to a voxel-wise classifier for WMH segmentation may have added value and improve segmentation results.

A k nearest neighbour (kNN) classifier was implemented and trained on various combinations of features. Manual delineations of WMH were available for 20 subjects. Classifiers trained with diffusion features, such as fractional anisotropy and mean diffusivity, are compared to an equivalent classifier without diffusion features. Evaluation measures are sensitivity and Dice similarity coefficient (SI).

Adding diffusion features to a kNN classifier significantly (Student's t-test, $p < 0.0001$) improved the quality of the segmentation. Depending on the chosen kNN parameters and features, improvements in sensitivity ranged from 2.4 to 13.5 % and in SI from 4.7 to 18.0 %.

In conclusion, adding diffusion features derived from DTI to a voxel-wise classifier for WMH segmentation significantly improves the quality of the segmentation.

1 Introduction

Vascular lesions in the brain, like white matter hyperintensities (WMH), are commonly encountered on MR images of elderly people and are associated with cognitive impairment, vascular risk factors, and an increased risk for future stroke, dementia, and death [8, 16, 23].

H.J. Kuijf (✉) • C.M.W. Tax • L.K. Zaanen • W.H. Bouvy • J. de Bresser • A. Leemans • M.A. Viergever • G.J. Biessels • K.L. Vincken
University Medical Center Utrecht, Utrecht, The Netherlands
e-mail: hugok@isi.uu.nl

L. O'Donnell et al. (eds.), *Computational Diffusion MRI*, Mathematics and Visualization, DOI 10.1007/978-3-319-11182-7_5

WMH are usually visualized on MRI with a FLAIR sequence, on which they appear as hyperintense regions in the white matter. The assessment of WMH can be performed manually, with visual rating scales such as the Age-Related White Matter Changes rating scale [23]. Manual delineations of WMH can be used to quantitatively assess volume, shape, or location. However, this task is tedious, time-consuming, and observer dependent, making it infeasible for use in large research studies or daily clinical practice.

Automated segmentation techniques for WMH have been proposed in the literature for many years [17]. Many of these techniques employ a voxel-wise classification (e.g. k nearest neighbours (kNN), neural networks, support vector machines, random forest), using features such as intensity, spatial location, texture, or shape [1, 2, 7, 20]. Such features are derived from the traditional MR sequences that are available, including T1-weighted, T2-weighted, PD-weighted, FLAIR, or IR sequences. Often, post processing routines are applied to improve the resulting segmentation.

Diffusion tensor imaging (DTI) can be used to study the microstructural organization of white matter by sensitizing the MR sequence to diffusion [4]. Measures derived from DTI, such as fractional anisotropy (FA) and mean diffusivity (MD), are known to detect changes in the white matter microstructure [5]. A recent study by Maillard et al. [16] showed that FLAIR and DTI signals are independent predictors of white matter hyperintensities [8, 16].

Based on these findings, we hypothesize that it can be beneficial to add DTI measures to a voxel-wise classification technique for WMH segmentation. In this study, we will use a popular classifier for WMH segmentation, the kNN classifier [2, 17, 20], and investigate the added value of DTI measures.

2 Methods and Materials

2.1 Participants and MRI

For the present study, 20 subjects (mean age: 71 years, sd: 4 years, ten men, ten women) were recruited at the University Medical Center Utrecht, the Netherlands. Subjects included patients with diabetes and matched controls, all with varying degrees of atrophy and WMH. The study was approved by the medical ethics committee of the University Medical Center Utrecht. All subjects gave written informed consent.

The subjects underwent a standardized MR exam on a 3.0 T Philips Achieva MR scanner using an eight-channel head coil, including, amongst others, a 3D T1-weighted turbo field echo sequence (TR: 7.9 ms, TE: 4.5 ms), a multi-slice FLAIR sequence (TR: 11,000 ms, TE: 125 ms, TI: 2,800 ms), a multi-slice IR sequence (TR: 4,416 ms, TE: 15 ms, TI: 400 ms), and a single-shot EPI DTI sequence with 45 directions at b = 1,200 s mm^{-2} and a b = 0 s mm^{-2} image (TR: 6,638 ms, TE: 73 ms).

Using the `elastix` toolbox for medical image registration [13], the 3D T1, IR, and b = 0 s mm^{-2} DTI images were aligned with the FLAIR image and resampled to a voxel size of 0.96 × 0.95 × 3.00 mm^3. This matched the voxel size of the FLAIR and established a voxel-wise correspondence between all the images. The diffusion weighted scans were corrected for subject motion, eddy current induced geometric distortions [19], and EPI distortions [12], including the required B-matrix adjustments [15]. These corrections were performed in one interpolation step to minimize blurring effects, using ExploreDTI [14]. A binary mask including all intracranial structures (the brain and cerebrospinal fluid) was available for all subjects.

WMH were delineated manually by an experienced human observer on the FLAIR image using a freehand spline drawing tool. All delineations were verified by a second experienced human observer and adapted if needed.

2.2 Classification

A *k*NN classifier, as implemented in scikit-learn [18], was used to perform a voxel-wise classification. Here, only two classes were considered: a voxel is either WMH or non-WMH (background, brain tissue, etc.). The *k*NN classifier is trained with labelled samples, where each sample is an individual voxel for which the true class is known from the manual delineations. Each sample has certain features, which are explained below.

To perform WMH segmentation for a new subject, each voxel in the image data of that subject is evaluated by the *k*NN classifier. It will find k training samples having features that are the most similar to the new voxel (the nearest neighbours). The most frequent class amongst the nearest neighbours is assigned to the new voxel.

A leave-one-out cross-validation strategy was used to classify the data of each subject. The *k*NN classifier was trained on the data of 19 subjects and then applied to segment the data of 1 subject. This procedure was repeated 20 times, so that the data of each individual subject was classified using the data of the other 19 subjects. The quality of the resulting segmentation could be assessed by comparing the results of the *k*NN classifier against the manual delineations.

Included in the training data were all voxels labelled as WMH and 10 % of the non-WMH voxels within the binary mask. A k-d tree with a leaf size of 30 was used to perform the nearest neighbour search, with an Euclidean distance metric. To determine the robustness of the technique, various settings for the number of neighbours k and the neighbour weighting function w were used, as explained below in Sect. 2.4.

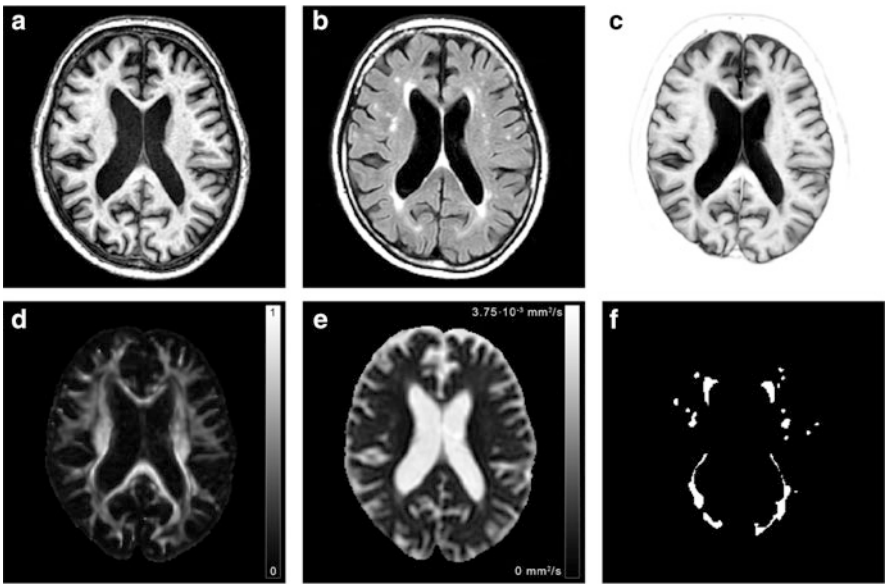

Fig. 1 Example image data of a subject with a high white matter hyperintensity (WMH) load (WMH volume: 34 ml). The *top row* shows the intensity features, where WMH appear *dark* on T1 and IR, and *bright* on FLAIR. *Bottom row* shows diffusion features, where WMH appear *dark* on FA and *bright* on MD, with the manual delineation of the WMH. (**a**) T1; (**b**) FLAIR; (**c**) IR; (**d**) FA; (**e**) MD; (**f**) Manual delineation

2.3 Features

A number of features was computed for each voxel in the image data of a subject, including: intensity, spatial, and diffusion features. All features were scaled to have values between 0 and 1, giving them equal weights within the kNN classification. Intensity and diffusion features for an example subject are shown in Fig. 1, together with the manual delineation of the WMH.

2.3.1 Intensity Features

The T1, FLAIR, and IR intensities were included as features. For each image, the intensities within the binary mask were normalized using the method proposed by Cocosco et al. [6], clipping the first and last percentile of the histogram and rescaling all intensities in between.

2.3.2 Spatial Features

As spatial features, the MNI-normalized spatial coordinates x, y, and z of each voxel were included. The T1 sequence of each subject was transformed to the MNI152

standard-space atlas by computing a linear registration using `elastix` [10,11,13]. By applying the inverse transformation, the MNI152 coordinates were "warped" to the coordinate space of the subject data and no interpolation or resampling of the original data was required. This approach is nicely demonstrated by Steenwijk et al. [20]. All values for x, y, and z within the binary mask were normalized.

By warping the MNI152 atlas, the spatial location of each voxel was comparable between all subjects and differences in, e.g., position in the scanner or head size were normalized.

2.3.3 Diffusion Features

Diffusion tensors were estimated using a weighted linear least squares approach [22]. The diffusion measures FA, MD, axial diffusivity (AD), radial diffusivity (RD) [3], and the Westin measures C_L, C_P, and C_S [24] were computed and subsequently normalized.

2.4 Experiments

Multiple settings for the kNN parameters k and w were applied. k is the number of neighbours used by the classifier and was set to 50, 75, or 100. w is the weighting function that was applied to the nearest neighbours to select a final class and was set to either 'uniform' or 'distance'. With uniform weighting, the class that occurs most amongst the nearest neighbours is assigned to the voxel being tested. With distance weighting, the inverse of the distance to each training sample is used as a weight: closer neighbours will have a greater influence in determining the final class than neighbours further away.

Various combinations of features were used, where combinations consisting of 'traditional' features will be compared to combinations with diffusion features. Selected combinations $f_i \in F$ included:

f_1: T1, IR, FLAIR
f_2: T1, IR, FLAIR, x, y, and z
f_3: T1, IR, FLAIR, with FA and MD
f_4: T1, IR, FLAIR, x, y, z, with FA and MD
f_5: T1, IR, FLAIR, x, y, z, with FA, MD, C_L, C_P, C_S, AD, and RD

In total, six different kNN classifiers will be evaluated for each $f_i \in F$. Each classifier employed a leave-one-out cross-validation approach. For each resulting segmentation, the sensitivity (percentage of true WMH voxels detected) and the commonly reported Dice similarity coefficient (SI, overlap between manual delineation and resulting segmentation) [9] will be assessed. Differences between the classifiers will be tested for significance using a paired samples two-tailed Student's t-test.

Table 1 *Left:* sensitivity and Dice similarity coefficient (SI) (higher is better) for the classifiers trained on combinations of features $f_i \in F$. *Right:* relative improvement between classifiers with diffusion features versus the equivalent classifier without diffusion features

F	Sensitivity (%)	SI			Relative improvement	
f_1	59.7 ± 0.2	0.349 ± 0.001				
f_2	73.4 ± 0.4	0.536 ± 0.005			Sensitivity (%)	Dice (%)
f_3	67.8 ± 0.3	0.411 ± 0.003		f_3 vs f_1	$13.5 \pm 0.2^*$	$18.0 \pm 0.6^*$
f_4	77.2 ± 0.4	0.565 ± 0.004		f_4 vs f_2	$5.1 \pm 0.1^*$	$5.4 \pm 0.2^*$
f_5	75.2 ± 0.6	0.561 ± 0.003		f_5 vs f_2	$2.4 \pm 0.3^*$	$4.7 \pm 0.5^*$

*The difference is statistically significant, using a paired samples two-tailed Student's t-test with $p < 0.0001$

3 Results

For each classifier trained on a combination of features $f_i \in F$, the reported results are the mean $\pm$ sd obtained by averaging the results for each setting of k and w. These results are reported in Table 1, together with the difference between classifiers using diffusion features versus the equivalent classifier without diffusion features.

Adding DTI measures as features to a kNN classifier results in statistically significant ($p < 0.0001$) improvements in both sensitivity and SI.

Including more diffusion features besides FA and MD, as is done with f_5, diminished the measured improvement, although the results are still significantly better than without these features.

The inclusion of spatial features (f_2 vs f_1 and f_4 vs f_3) resulted in a statistically significant ($p < 0.0001$) improvement in sensitivity and SI.

In cases where the sensitivity is high or approaches the inter observer variability, it is informative to inspect the false negative rate/type II error (defined as 1-sensitivity; the percentage of undetected WMH voxels). The relative reductions in false negative rate are: f_3 vs f_1: $-20.0 \pm 0.4\,\%$, f_4 vs f_2: $-14.2 \pm 0.2\,\%$, and f_5 vs f_2: $-6.5 \pm 1.0\,\%$. All reductions are statistically significant ($p < 0.0001$).

4 Discussion

It is clear that adding diffusion features to a voxel-wise classifier for WMH segmentation significantly improves the segmentation results. This is in line with the reports from literature that FLAIR and DTI are independent predictors and confirms our hypothesis that DTI has added value in automated WMH segmentation.

The kNN classifiers as presented herein do not have a high performance in terms of SI. However, the current classifiers are only used to demonstrate the added value of DTI measures. More advanced segmentation methods that are proposed in literature are also likely to benefit from diffusion features. Post processing steps

that reduce the number of false positive detections might increase the SI to a level comparable with literature, since SI is a measure that combines both sensitivity and specificity. However, adding these post processing routines is not relevant to demonstrate the added value of DTI.

Adding FA and MD features to the classifiers proved to be valuable. The addition of more DTI measures, such as C_L, C_P, C_S, AD, and RD, still improved the results with respect to an equivalent classifier without any DTI measures, but showed a diminished improvement with respect to the classifiers that only included FA and MD. A possible explanation for this can be found in the high correlation that exists between the DTI measures, since they are all derived from the eigenvalues of the diffusion tensor. Adding a feature to the classifier increases the dimensionality of the feature space and slightly reduces the influence of all other features. When a feature is added that (strongly) correlates with an existing feature, the influence of all other features is reduced. Therefore, only features that provide new information should be added and in the present situation, this is provided by FA and MD.

Future work will consist of improving the overall performance of the classifiers, by including more features and post processing routines that are known from literature to improve the segmentation quality. Possible improvements are the inclusion of tissue type priors [20], morphological operations to close segmentation gaps and remove too small hyperintensities, or optimize the probability threshold of the kNN classifier [2]. The latter option has the potential to further increase the sensitivity (by lowering the threshold), but will introduce more false positives that need to be removed by post processing. Increased involuntary head motion or altered cardiac pulsatile motion in these elderly patients may cause acquisition artefacts. This can result in large biases in the diffusion measures, which can be prevented by using robust tensor estimation procedures in future work [21].

5 Conclusion

Including DTI measures as features in a classification technique for WMH segmentation significantly improves the results of the final segmentation.

Acknowledgements We gratefully acknowledge the Utrecht Vascular Cognitive Impairment Study Group for recruiting the patients who were included as subjects in our study. This study was financially supported by the project Brainbox (Quantitative analysis of MR brain images for cerebrovascular disease management), funded by the Netherlands Organisation for Health Research and Development (ZonMw) in the framework of the research programme IMDI (Innovative Medical Devices Initiative); project 104002002.

References

1. Admiraal-Behloul, F., van den Heuvel, D., Olofsen, H., van Osch, M., van der Grond, J., van Buchem, M., Reiber, J.: Fully automatic segmentation of white matter hyperintensities in MR images of the elderly. NeuroImage **28**(3), 607–617 (2005). http://dx.doi.org/10.1016/j.neuroimage.2005.06.061
2. Anbeek, P., Vincken, K.L., van Osch, M.J., Bisschops, R.H., van der Grond, J.: Probabilistic segmentation of white matter lesions in MR imaging. NeuroImage **21**(3), 1037–1044 (2004). doi:http://dx.doi.org/10.1016/j.neuroimage.2003.10.012
3. Basser, P.J.: Inferring microstructural features and the physiological state of tissues from diffusion-weighted images. NMR Biomed. **8**, 333–344 (1995)
4. Basser, P.J., Mattiello, J., LeBihan, D.: Estimation of the effective self-diffusion tensor from the nmr spin echo. J. Magn. Reson. B **103**(3), 247–254 (1994)
5. Beaulieu, C.: The basis of anisotropic water diffusion in the nervous system - a technical review. NMR Biomed. **15**(7–8), 435–455 (2002). doi:http://dx.doi.org/10.1002/nbm.782
6. Cocosco, C.A., Zijdenbos, A.P., Evans, A.: A fully automatic and robust brain mri tissue classification method. Med. Image Anal. **7**(4), 513–527 (2003). doi:10.1016/S1361-8415(03)00037-9. [Medical Image Computing and Computer Assisted Intervention]
7. de Boer, R., Vrooman, H.A., van der Lijn, F., Vernooij, M.W., Ikram, M.A., van der Lugt, A., Breteler, M.M., Niessen, W.J.: White matter lesion extension to automatic brain tissue segmentation on mri. NeuroImage **45**(4), 1151–1161 (2009). doi:http://dx.doi.org/10.1016/j.neuroimage.2009.01.011
8. de Groot, M., Verhaaren, B.F., de Boer, R., Klein, S., Hofman, A., van der Lugt, A., Ikram, M.A., Niessen, W.J., Vernooij, M.W.: Changes in normal-appearing white matter precede development of white matter lesions. Stroke **44**(4), 1037–1042 (2013). doi:http://dx.doi.org/10.1161/STROKEAHA.112.680223
9. Dice, L.R.: Measures of the amount of ecologic association between species. Ecology **26**(3), 297–302 (1945). doi:10.2307/1932409
10. Fonov, V.S., Evans, A.C., McKinstry, R.C., Almli, C.R., Collins, D.L.: Unbiased nonlinear average age-appropriate brain templates from birth to adulthood. NeuroImage **47**(Suppl 1), S102 (2009). doi:10.1016/S1053-8119(09)70884-5. [Organization for Human Brain Mapping 2009 Annual Meeting]
11. Fonov, V.S., Evans, A.C., Botteron, K., Almli, C.R., McKinstry, R.C., Collins, D.L.: Unbiased average age-appropriate atlases for pediatric studies. NeuroImage **54**(1), 313–327 (2011). doi:10.1016/j.neuroimage.2010.07.033
12. Irfanoglu, M.O., Walker, L., Sarlls, J., Marenco, S., Pierpaoli, C.: Effects of image distortions originating from susceptibility variations and concomitant fields on diffusion mri tractography results. NeuroImage **61**(1), 275–288 (2012). doi:http://dx.doi.org/10.1016/j.neuroimage.2012.02.054
13. Klein, S., Staring, M., Murphy, K., Viergever, M.A., Pluim, J.P.W.: elastix: a toolbox for intensity-based medical image registration. IEEE Trans. Med. Imaging **29**(1), 196–205 (2010). doi:10.1109/TMI.2009.2035616
14. Leemans, A., Jeurissen, B., Sijbers, J., Jones, D.K.: Exploredti: a graphical toolbox for processing, analyzing, and visualizing diffusion mr data. In: Proceedings on International Society for Magnetic Resonance in Medicine, vol. 17, p. 3537 (2009)
15. Leemans, A., Jones, D.K.: The b-matrix must be rotated when correcting for subject motion in dti data. Magn. Reson. Med. **61**(6), 1336–1349 (2009). doi:http://dx.doi.org/10.1002/mrm.21890
16. Maillard, P., Carmichael, O., Harvey, D., Fletcher, E., Reed, B., Mungas, D., DeCarli, C.: Flair and diffusion mri signals are independent predictors of white matter hyperintensities. Am. J. Neuroradiol. **34**(1), 54–61 (2013). doi:http://dx.doi.org/10.3174/ajnr.A3146
17. Mortazavi, D., Kouzani, A., Soltanian-Zadeh, H.: Segmentation of multiple sclerosis lesions in mr images: a review. Neuroradiology **54**(4), 299–320 (2012). doi:http://dx.doi.org/10.1007/s00234-011-0886-7

18. Pedregosa, F., Varoquaux, G., Gramfort, A., Michel, V., Thirion, B., Grisel, O., Blondel, M., Prettenhofer, P., Weiss, R., Dubourg, V., Vanderplas, J., Passos, A., Cournapeau, D., Brucher, M., Perrot, M., Duchesnay, E.: Scikit-learn: Machine learning in python. J. Mach. Learn. Res. **12**, 2825–2830 (2011)
19. Rohde, G., Barnett, A., Basser, P., Marenco, S., Pierpaoli, C.: Comprehensive approach for correction of motion and distortion in diffusion-weighted mri. Magn. Reson. Med. **51**(1), 103–114 (2004). doi:http://dx.doi.org/10.1002/mrm.10677
20. Steenwijk, M.D., Pouwels, P.J., Daams, M., van Dalen, J.W., Caan, M.W., Richard, E., Barkhof, F., Vrenken, H.: Accurate white matter lesion segmentation by k nearest neighbor classification with tissue type priors (knn-ttps). NeuroImage: Clinical **3**(0), 462–469 (2013). doi:http://dx.doi.org/10.1016/j.nicl.2013.10.003
21. Tax, C.M., Otte, W.M., Viergever, M.A., Dijkhuizen, R.M., Leemans, A.: Rekindle: Robust extraction of kurtosis indices with linear estimation. Magn. Reson. Med. (2014, in press) doi:http://dx.doi.org/10.1002/mrm.25165
22. Veraart, J., Sijbers, J., Sunaert, S., Leemans, A., Jeurissen, B.: Weighted linear least squares estimation of diffusion mri parameters: Strengths, limitations, and pitfalls. NeuroImage **81**(0), 335–346 (2013). doi:http://dx.doi.org/10.1016/j.neuroimage.2013.05.028
23. Wahlund, L.O., Barkhof, F., Fazekas, F., Bronge, L., Augustin, M., Sjögren, M., Wallin, A., Ader, H., Leys, D., Pantoni, L., Pasquier, F., Erkinjuntti, T., Scheltens, P.: On behalf of the European Task Force on Age-Related White Matter Changes: A new rating scale for age-related white matter changes applicable to mri and ct. Stroke **32**(6), 1318–1322 (2001). doi:http://dx.doi.org/10.1161/01.STR.32.6.1318
24. Westin, C., Maier, S., Mamata, H., Nabavi, A., Jolesz, F., Kikinis, R.: Processing and visualization for diffusion tensor mri. Med. Image Anal. **6**(2), 93–108 (2002)

Algebraic Connectivity of Brain Networks Shows Patterns of Segregation Leading to Reduced Network Robustness in Alzheimer's Disease

Madelaine Daianu, Neda Jahanshad, Talia M. Nir, Cassandra D. Leonardo, Clifford R. Jack Jr., Michael W. Weiner, Matt A. Bernstein, and Paul M. Thompson

Abstract Measures of network topology and connectivity aid the understanding of network breakdown as the brain degenerates in Alzheimer's disease (AD). We analyzed 3-Tesla diffusion-weighted images from 202 patients scanned by the Alzheimer's Disease Neuroimaging Initiative—50 healthy controls, 72 with early- and 38 with late-stage mild cognitive impairment (eMCI/lMCI) and 42 with AD. Using whole-brain tractography, we reconstructed structural connectivity networks representing connections between pairs of cortical regions. We examined, for the first time in this context, the network's Laplacian matrix and its Fiedler value, describing the network's *algebraic connectivity*, and the Fiedler vector, used to partition a graph. We assessed algebraic connectivity and four additional supporting metrics, revealing a decrease in network robustness and increasing disarray among nodes as dementia progressed. Network components became more disconnected and segregated, and their modularity increased. These measures are sensitive to diagnostic group differences, and may help understand the complex changes in AD.

M. Daianu (✉) • N. Jahanshad • T.M. Nir • C.D. Leonardo • P.M. Thompson
Imaging Genetics Center, Institute for Neuroimaging & Informatics, University of Southern California, Los Angeles, CA, USA
e-mail: madelaine.daianu@ini.usc.edu; neda.jahanshad@ini.usc.edu; talia.nir@ini.usc.edu; cassandra.leonardo@loni.usc.edu; pthomp@usc.edu

C.R. Jack Jr. • M. A. Bernstein
Department of Radiology, Mayo Clinic, Rochester, MN, USA
e-mail: jack.clifford@mayo.edu; mBernstein@mayo.edu

M.W. Weiner
Department of Radiology, Medicine, and Psychiatry, University of California, San Francisco, CA, USA
e-mail: michael.weiner@ucsf.edu

L. O'Donnell et al. (eds.), *Computational Diffusion MRI*, Mathematics and Visualization, DOI 10.1007/978-3-319-11182-7_6

1 Introduction

Brain connectivity analyses are increasingly popular, and combine concepts from neuroscience and engineering to characterize the brain in terms of its structural and functional connections. Diffusion weighted imaging (DWI) and advanced tractography methods may offer new insights into how the brain changes in degenerative diseases such as Alzheimer's disease (AD), and its precursor, mild cognitive impairment (MCI). In addition, graph theory can be applied to study topological changes in the brain's networks using graphs—defined as a set of interconnected nodes and edges.

There is an increasing interest in analyzing the brain using graphs, which can be studied using network analysis toolboxes [1]. In a graph, network nodes are typically defined as regions of interest (ROIs)—in our case on the cortex, segmented from anatomical MRI. These nodes are linked by 'edges' that can be binary or weighed. However, as the field is still in its formative stages, we do not yet know which graph theoretic measures best differentiate disease states or change the most with disease progression.

Here, we applied ideas from algebraic graph theory—not previously examined in the context of AD using DWI derived measures. Specifically, we computed the second smallest eigenvalue of the Laplacian matrix (Fiedler value) for each subject to describe their algebraic connectivity—i.e., how difficult it is to tear a graph apart. A Fiedler value > 0 indicates that a graph is fully connected and the higher the magnitude of the Fiedler value, the more interconnected the graph is. The Fiedler value, accompanied by a measure of link density (interconnectedness of nodes) can further describe the robustness of a graph—the denser the connections, the less vulnerable the brain network is to being disconnected. Similarly, based on the set of eigenvalues, we determined the number of disconnected network components (ROIs that do not have connections to other ROIs, or where network connections are not detected). To expand our analysis of brain connectivity, we computed more standard measures of modularity—a measure that describes the degree to which a network may be subdivided to significantly delineated groups of nodes [1, 2].

To determine whether the network changes were behaviorally and clinical relevant, we related the network measures to the Mini Mental Status Examination score—a simple but widely-used test to evaluate patients and help in diagnosis of dementia. We hypothesized that with disease progression, the graph representation of the brain would become more modular (i.e., segregated), reducing the density of connections among its ROIs and eventually, leading to disconnections among its nodes. We expected to see changes predominantly in the entorhinal areas and temporal cortices, areas affected first by structural atrophy in Alzheimer's disease. In diagnostic group comparisons, we also aimed to show that the algebraic connectivity is disrupted. The overall goal of our work is to mathematically describe how the brain network changes in disease. Although all measures were sensitive to disease effects in the ADNI cohort, we found that the Fielder value was most sensitive to picking up topological effects among AD patients as well as lMCI patients.

2 Methods

2.1 Participants and Diffusion-Weighted Brain Imaging

We analyzed diffusion-weighted images (DWI) from 202 participants scanned as part of the Alzheimer's Disease Neuroimaging Initiative (ADNI). ADNI is a large multi-site longitudinal study to evaluate biomarkers of AD. Table 1 shows the demographics of the participants included here, including age, sex, and mini-mental state exam (MMSE) scores, broken down by diagnosis. All 202 participants underwent whole-brain MRI on 3-Tesla GE Medical Systems scanners, at 16 sites across North America. Standard anatomical T1-weighted IR-FSPGR (inverse recovery fast spoiled gradient recalled echo) sequences were collected (256×256 matrix; voxel size $= 1.2 \times 1.0 \times 1.0$ mm^3; TI $= 400$ ms, TR $= 6.984$ ms; TE $= 2.848$ ms; flip angle $= 11°$) in the same session as the DWI (128×128 matrix; voxel size: $2.7 \times 2.7 \times 2.7$ mm^3; scan time $= 9$ min). Forty six separate images were acquired for each scan: 5 T2-weighted images with no diffusion sensitization (b_0 images) and 41 diffusion-weighted images ($b = 1{,}000$ s/mm^2). Image preprocessing was performed as described previously in [3]. This was not included here due to space limitations.

2.2 N × N Connectivity Matrix Creation

We performed whole-brain tractography as described in [3]. We used a method based on the Hough transform to recover fibers, using a constant solid angle orientation distribution function to model the local diffusion propagator. Each subject's dataset contained ~10,000 useable fibers (3D curves) in total [4]. Thirty four cortical labels per hemisphere, as listed in the Desikan–Killiany atlas [5], were automatically extracted from all aligned T1-weighted structural MRI scans with FreeSurfer (http://surfer.nmr.mgh.harvard.edu/).

Table 1 Demographic information from 50 controls, 72 eMCI, 38 lMCI and 42 AD participants scanned with diffusion MRI as part of the ADNI project

	Controls	eMCI	lMCI	AD	Total
N	50	72	38	42	202
Age (mean ± SD in years)	72.6 ± 6.1	72.4 ± 7.9	72.6 ± 5.6	75.5 ± 8.9	73.1 ± 7.4
MMSE (mean ± SD)	28.9 ± 1.4	28.1 ± 1.5	26.9 ± 2.1	23.3 ± 1.9	27.1 ± 2.7
Sex	22M/28F	45M/27F	25M/13F	28M/14F	120M/82F

Their ages ranged from 55.2 to 90.4 years. The mean age and mini mental state exam (MMSE) scores are listed for each diagnostic group

For each subject, a 68×68 connectivity matrix was created whereby each element represented the total number of fibers, in that subject, that passes through each pair of ROIs. For simplicity, all connectivity matrices were binarized to describe whether any connection was detected between a pair of cortical ROIs (marked as 1), or otherwise (marked as 0). Weighted networks will be considered in future work.

2.3 Algebraic Connectivity and Supporting Network Metrics

Algebraic graph theory is a branch of mathematics that uses linear algebra and matrix theory to study the properties of graphs [4]. In algebraic graph theory, the Laplacian matrix is used to study the *spectrum* of a graph, which is the topic of study in another branch of mathematics known as *spectral graph theory* [5]. Recently, spectral theory has been applied to study the separability of brain networks in resting-state functional MRI data from ADHD participants [6]; also, it was employed to study the altered networks in AD using magnetoencephalography (MEG) data [7]. Other applications of algebraic graph theory are in the fields of circuit design, parallel and distributive computing, data representation [8] and the online web [9]. Here, we are the first to explore the application of algebraic graph theory to better understand the global structural changes in Alzheimer's disease using DWI derived networks.

Structural networks are usually modeled as undirected and symmetric graphs, $G(N,E)$ containing a set of nodes, N, and edges, E. Here we computed an adjacency matrix for each graph, $A(G) = a_{ij}$, where a_{ij} was 1 if a connection linked a pair of nodes and 0 otherwise. Next, we computed the Laplacian matrix of graph G (Fig. 1), $L(G) = l_{ij}$, where $L(G) = D(G) - A(G)$. $D(G)$ is the $N \times N$ diagonal degree adjacency matrix (i.e., diag(sum(G))). Then, the eigenvalues, λ_i, were computed on the Laplacian matrix, where $0 = det(L - \lambda I)$ and I is an $N \times N$ identity matrix. In this study, we were interested in the second smallest eigenvalue, also called the Fiedler value, and its corresponding eigenvector, $\boldsymbol{x}$, computed from $(L - \lambda I)\boldsymbol{x} = 0$ [10].

The magnitude of the Fiedler value describes the *algebraic connectivity* among the elements of a network; a Fiedler value of zero indicates that the network is

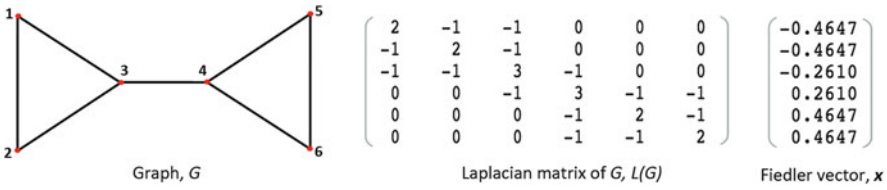

Fig. 1 Illustration of a graph G, its corresponding Laplacian matrix, $L(G)$, and the Fiedler vector, $\boldsymbol{x}$. The algebraic connectivity of G is approximately 0.43

disconnected [11]. The Fiedler value may be used in conjunction with the number of edges and nodes to further describe the robustness of a network [12]. To evaluate robustness, we also computed the number of edges in each brain network, E, and the link (edge) density defined as $d = 2E/N(N-1)$, because a decreasing edge density may indicate decreased robustness.

Another measure obtained from the eigenvalues of $L(G)$, the number of $\lambda_i = 0$, which reflects the number of disconnected components in the brain network [9]. The number of network components was further assessed with *modularity* computed using Newman's equations [2]. The algorithm efficiently defines an optimal community structure into non-overlapping sets of nodes such that the within group edges are maximized and the between-group edges are minimized. Essentially, modularity is a statistical evaluation of the degree to which the network may be subdivided to significantly delineated groups of nodes, $Q = \sum_{u \in M}(E_{uu} - (\sum_{v \in M} E_{uv})^2)$, where M is a nonoverlapping module that the network is subdivided into, and E_{uv} is the proportion of links that connects nodes in module u to nodes in modules v [1, 2]. If $Q < 0.3$, the community structure formed is not significant as the within-community edges are close or equal to what would be expected by chance; however, $Q \geq 0.3$ signifies significant community structures [2].

To plot the algebraic connectivity we sorted brain network nodes as a function of the Fiedler vector; components in the brain were assigned to groups based on the sorted magnitude of the eigenvector's corresponding component. This method is similar to *spectral partitioning* [5], however, in this study no partitions were added. Tools from the MIT Strategic Engineering website (http://strategic.mit.edu) were used for all calculations [9] excluding the modularity measure implemented from Newman [2] in the brain connectivity toolbox [1].

2.4 Statistical Analyses

First, we assessed if the graph metrics (Fiedler value, total number of nodes, link density, the number of disconnected components and modularity) related to Mini Mental State Examination (MMSE) scores across all 202 participants using a random-effects regression, covarying for sex and using site as a grouping variable. As we cannot assume statistical normality for the network measures, nonparametric methods may be more appropriate. We performed $m = 10{,}000$ permutations of the independent variable of interest (i.e., MMSE or disease status), while maintaining covariates (sex and age and imaging site) true to the subject. Next, we generated permutation-corrected p-values using the following formula: $p = (b+1)/(m+1)$, where b is the number of randomized test statistics t_{perm} found to have a greater magnitude than the observed test statistic t_{obs}. By performing 10,000 permutations, the smallest possible permutation corrected p-value is 10^{-4}, so even if the observed p-value was much less than 10^{-4}, the lowest corrected p-value was 10^{-4}.

Next, we tested if any of the graph theory metrics that closely describe algebraic connectivity (i.e., Fiedler value, link density and modularity) detected group

differences between controls and the diseased groups by running a random-effects regression with controls coded as 0 and diseased participants coded as 1, covarying for age and sex and using the imaging site as a random-effects grouping variable, to eliminate confounding effects of the scan site. Then, 10,000 permutations of the independent value were performed as described above.

3 Results

MMSE scores—a measure of clinical decline—were significantly related to five of the network measures across all 202 participants. To adjust for multiple statistical tests, the significance threshold was set to 0.05/5 when testing associations of MMSE with five network measures. MMSE scores declined with a decreasing Fielder value ($p_{perm} < 10^{-4}$) decreasing total number of edges ($p_{perm} < 10^{-4}$) and decreasing link density ($p_{perm} < 10^{-4}$). Meanwhile, as hypothesized, MMSE scores declined with an increasing number of disconnected components ($p_{perm} = 3.2 \times 10^{-3}$) in the network and increasing modularity among network communities ($p_{perm} = 3.4 \times 10^{-4}$). These disruptions led to a less robust and inefficient distribution of the brain's network components with advancing disease, and were sorted here as a function of the eigenvectors corresponding to the Fiedler eigenvalue (Fig. 1). Also, brain regions that showed most frequent disconnections (0 eigenvalues) among diseased participants were those of the entorhinal, temporal and frontal poles bilaterally, in line with the sites that typically show the earliest AD pathology.

For the group comparisons, AD participants showed a significantly decreasing algebraic connectivity and a topological organization of the brain network that was different overall, relative to controls. Here, the significance threshold was set to 0.05/3, to adjust for testing three network metrics in the group comparison. The Fiedler value ($p_{perm} < 10^{-4}$) and link density ($p_{perm} < 10^{-4}$) was lower in AD, than in controls. Meanwhile, modularity increased in AD, relative to healthy elderly ($p_{perm} < 10^{-4}$).

For group comparisons between lMCI and controls, the Fiedler value was the only measure to be significantly decreasing in lMCI, relative to healthy elderly (permuted p-value = 0.012). No significant differences were detected between eMCI and controls; this is not surprising as this group comparison is typically the most challenging among those we tested.

The average link density was 0.360 across all healthy elderly, 0.331 in eMCI and 0.333 in lMCI participants, and 0.304 in AD. This indicates that eMCI and lMCI had an 8.2–8.8 % "less" interconnected network, under this metric, while the AD patients had a 15.7 % less interconnected network.

4 Discussion

This study introduces the application of algebraic connectivity, with additional supporting neural metrics, to the analysis of brain connectivity. Here, we treated the networks as sets of nodes and edges and analyzed their interconnectedness based on associations with cognitive decline scores (i.e., MMSE) and diagnostic group differences. We fused all steps of analysis together and reported an overall assessment of how and where in the brain Alzheimer's strikes.

The decline in algebraic connectivity, as indicated by the decreased Fiedler values with disease progression (decreasing MMSE scores), accompanied by the reductions in the density of connections among brain regions, highlights the loss of interconnectedness within the brain network. The diseased brains may be more vulnerable to losses in connections that allow communication between cortical regions, leading to a less robust neural network, at least according to these mathematical metrics. If brain connections were to be purged (lost altogether), eMCI and lMCI brain networks would disconnect approximately 8–9 % more readily than healthy networks, while AD brain networks would disconnect approximately 16 % more readily than controls. Cortical regions that contributed the most to the loss of nodes were located in the entorhinal areas—regions that typically degenerate early in AD [11, 13], and the temporal pole progressing into the frontal pole in the more impaired—also supported by previous studies [11]. Disconnections in these nodes may in turn impair connected nodes, as information transfer may be reduced accordingly.

Modularity computed on the original graphs (not the Laplacian) was used to verify the goodness of component partitioning in the brain network [6]. Modularity increased with disease progression indicating that the brain networks became more segregated (formed more modular structures) with a loss in connections between modules, leading to a less efficient distribution of the network overall (Fig. 2). This

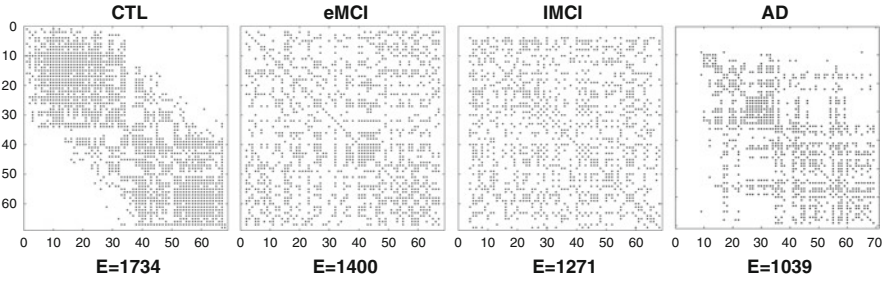

Fig. 2 Sorted connectivity matrix as a function of the sorted eigenvector, $\boldsymbol{x}$, corresponding to the Fiedler value (i.e., second smallest eigenvalue) in one participant from each diagnostic group. E is the number of edges within each network. The plots indicate patterns of disarray with increasing numbers of disconnected components with disease progression; no completely disconnected components are shown in controls (CTL) (no zero value rows/columns, i.e., missing dots), but there are 2 in eMCI, 4 in lMCI and 8 disconnected components in AD

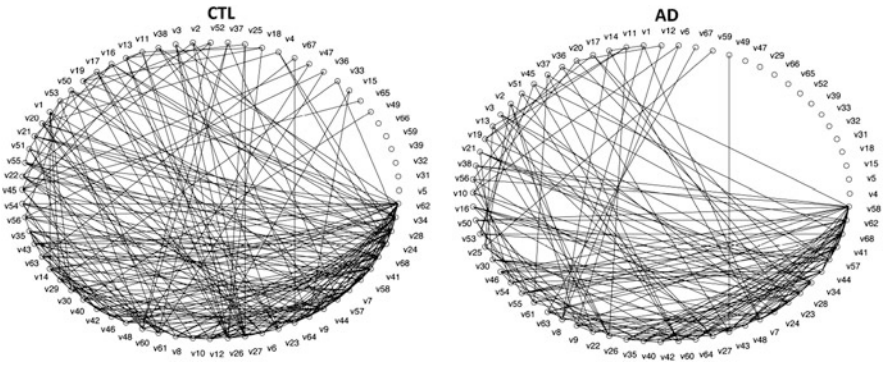

Fig. 3 Circle drawings of nodes (*v1* through *v68*) interconnected by averaged edges across 50 controls (CTL) and 42 AD participants. The loss in link (edge) density across the nodes indicates decreased interconnectedness

is complements the Fielder value, which defines the level of network integrity (i.e., connectedness) in the brain. Modular networks were less defined in controls at an average $Q = 0.34$, with $Q = 0.36$ in eMCI and lMCI and 0.39 in AD participants—leading to readily detectable disease differences.

The Fiedler value, link density, and modularity were sensitive to group differences in eMCI, lMCI and AD, versus controls (except for the Fiedler value that did not detect differences in eMCI, relative to controls). The direction of change for all these measures indicated an overall lower interconnectness for the diseased connectomes (Fig. 3).

Discovering changes in brain network organizational properties allows us to understand disease progression with additional detail. Most of these network algorithms have been successfully developed and applied for non-medical applications such as online social interactions [9] and functional imaging [6, 7]; our study used these properties to study disease progression using DWI. We found that measures such as the Fiedler value—a measure of algebraic connectivity—was the most sensitive measure to detecting differences between disease groups and controls. Supporting network metrics, such as the number of edges, link density, the number of disconnected components, and modularity, validate and strengthen the results indicating a less robust and more segregated brain with increased cognitive impairment. As a limitation, we acknowledge that future studies should compare these new metrics with standard DTI-derived measures such as FA and MD, and other non-DTI or non-imaging biomarkers of AD, to determine what added predictive value they contain. Also, for future works, weighted matrices (i.e., with measures of fiber density or FA) will be used and may provide additional information about network disruptions. Overall, the network disruptions in disease are so complex that the added mathematical descriptors are likely to enhance our understanding of network dysfunction in the living brain.

Acknowledgments Algorithm development and image analysis for this study was funded, in part, by grants to PT from the NIBIB (R01 EB008281, R01 EB008432) and by the NIA, NIBIB, NIMH, the National Library of Medicine, and the National Center for Research Resources (AG016570, AG040060, EB01651, MH097268, LM05639, RR019771 to PT). Data collection and sharing for this project was funded by ADNI (NIH Grant U01 AG024904). ADNI is funded by the National Institute on Aging, the National Institute of Biomedical Imaging and Bioengineering, and through contributions from the following: Abbott; Alzheimer's Association; Alzheimer's Drug Discovery Foundation; Amorfix Life Sciences Ltd.; AstraZeneca; Bayer HealthCare; BioClinica, Inc.; Biogen Idec Inc.; Bristol-Myers Squibb Company; Eisai Inc.; Elan Pharmaceuticals Inc.; Eli Lilly and Company; F. Hoffmann-La Roche Ltd and its affiliated company Genentech, Inc.; GE Healthcare; Innogenetics, N.V.; IXICO Ltd.; Janssen Alzheimer Immunotherapy Research & Development, LLC.; Johnson & Johnson Pharmaceutical Research & Development LLC.; Medpace, Inc.; Merck & Co., Inc.; Meso Scale Diagnostics, LLC.; Novartis Pharmaceuticals Corporation; Pfizer Inc.; Servier; Synarc Inc.; and Takeda Pharmaceutical Company. The Canadian Institutes of Health Research is providing funds to support ADNI clinical sites in Canada. Private sector contributions are facilitated by the Foundation for the National Institutes of Health. The grantee organization is the Northern California Institute for Research and Education, and the study is coordinated by the Alzheimer's Disease Cooperative Study at the University of California, San Diego. ADNI data are disseminated by the Laboratory for Neuro Imaging at the University of Southern California. This research was also supported by NIH grants P30 AG010129 and K01 AG030514 from the National Institute of General Medical Sciences. This work was also supported in part by a Consortium grant (U54 EB020403) from the NIH Institutes contributing to the Big Data to Knowledge (BD2K) Initiative, including the NIBIB and NCI.

References

1. Rubinov, M., Sporns, O.: Complex network measures of brain connectivity: uses and interpretations. Neuroimage **52**(3), 1059–1069 (2010)
2. Newman, M.E.: Fast algorithm for detecting community structure in networks. Phys. Rev. E: Stat. Nonlinear Soft Matter Phys. **69**(6 Pt 2), 066133 (2004)
3. Daianu, M., Jahanshad, N., Nir, T.M., Toga, A.W., Jack, C.R., Jr., Weiner, M.W., Thompson, P.M. and the Alzheimer's Disease Neuroimaging Initiative: Breakdown of brain connectivity between normal aging and Alzheimer's disease: a structural k-core network analysis. Brain Connect. **3**(4), 407–422 (2013)
4. Norman, B.: Algebraic Graph Theory, 2nd edn. Cambridge University Press, Cambridge (1993)
5. Mohar, B.: The Laplacian spectrum of graphs. Graph Theory, Combinatorics, and Applications. Alavi, Y., Chartrand, G., Oellermann, O.R., Schwenk, A.J.: Wiley vol. 2, pp. 871–898 (1991)
6. Bohland, J.W., Saperstein, S., Pereira, F., Rapin, J., Grady, L.: Network, anatomical, and non-imaging measures for the prediction of ADHD diagnosis in individual subjects. Front. Syst. Neurosci. **6**, 78 (2012). doi:10.3389/fnsys.2012.00078
7. de Haan, W., van der Flier, W.M., Wang, H., Van Mieghem, P.F., Scheltens, P., Stam, C.J.: Disruption of functional brain networks in Alzheimer's disease: what can we learn from graph spectral analysis of resting-state magnetoencephalography? Brain Connect. **2**(2), 45–55 (2012)
8. Chung, F.R.K., Faber, V., Manteuffel, T.A.: SIAM J. Discrete Math. **7**, 443 (1994)
9. Bounova, G., de Weck, O.L.: Overview of metrics and their correlation patterns for multiple-metric topology analysis on heterogeneous graph ensembles. Phys. Rev. E **85**, 016117 (2012)
10. Fiedler, M.: Algebraic connectivity of graphs. Czechoslov. Math. J. **23**, 298–305 (1973)
11. Thompson, P.M., Hayashi, K.M., de Zubicaray, G., Janke, A.L., Rose, S.E., Semple, J., Herman, D., Hong, M.S., Dittmer, S.S., Doddrell, D.M., Toga, A.W.: Dynamics of gray matter loss in Alzheimer's disease. J. Neurosci. **23**(3), 994–1005 (2003)

12. Jamakovic, A., van Mieghem, P.: On the robustness of complex networks by using the algebraic connectivity. Networking, network ad-hoc and sensor networks, wireless networks, next generation Internet. Lect. Notes Comput. Sci. **4982**, 183–194 (2008)
13. Devanand, D.P., Pradhaban, G., Liu, X., Khandji, A., De Santi, S., Segal, S., Rusinek, H., Pelton, G.H., Honig, L.S., Mayeux, R., Stern, Y., Tabert, M.H., de Leon, M.J.: Hippocampal and entorhinal atrophy in mild cognitive impairment: prediction of Alzheimer. Neurology **68**(11), 828–836 (2007)
14. Aganj, I., Lenglet, C., Sapiro, G., Yacoub, E., Ugurbil, K., Harel, N.: Reconstruction of the Orientation Distribution Function in Single and Multiple Shell Q-Ball Imaging within Constant Solid Angle: Magn Reson Med **64**(2), 554–466 (2010)
15. Desikan, RS., Segonne, F., Fischl, B., Quinn, BT., Dickerson, BC., Blacker, D., Buckner, RL., Dale, AM., Maguire, RP., Hyman, BT., Albert, MS., Killiany, RJ: An automated labeling system for subdividing the human cerebral cortex on MRI scans into gyral based regions of interest: Neuroimage **31**(3), 968–80 (2006)

Diffusion-Map: A Novel Visualizing Biomarker for Diffusion Tensor Imaging of Human Brain White Matter

Mohammad Hadi Aarabi and Hamid Saligheh Rad

Abstract Rich information about brain tissue microstructure and composition is yielded by MRI-based measurement of the local diffusion tensor (DT) of water molecules in neural fibers, whose axons are running in myelinated fiber tracts. Diffusion tensor imaging (DTI) possesses high-dimensional and complex structure, so that detecting available pattern information and its analysis based on conventional linear statistics and classification methods become inefficient. Classification, segmentation, compression or visualization of the data could be facilitated through dimension reduction. The previously proposed methods mostly rely on complex low dimensional manifold embedding of the high-dimensional space, which are not able to deal with complex and high dimensional data. The purpose of this paper is to propose a new method for meaningful visualization of brain white matter using diffusion tensor data to map the six-dimensional tensor to a three dimensional space, employing Markov random walk and diffusion distance algorithms, leading to a new distance-preserving map for the DTI data with lower dimension and higher throughput information.

1 Introduction

To gain a better insight into the disease effects on brain anatomy and physiology, a systematic pattern of anatomy must be detected in anatomical imaging of the brain. Diffusion tensor imaging (DTI) is a promising method, which yields fundamental information of the brain tissue microstructure and composition by means of magnetic resonance imaging (MRI)-based measurement of local diffusion tensor (DT) of water molecules in human brain [1]. In particular, DTI is used to characterize and map the three dimensional (3D) diffusion of water, as a function of spatial location and generate 3D quantitative maps like mean-diffusivity (MD) or fractional-anisotropy (FA), obtained from dominant orientation of water diffusion

M.H. Aarabi (✉) • H. Saligheh Rad
Quantitative MR Imaging and Spectroscopy Group, Research Center for Molecular and Cellular Imaging, Tehran University of Medical Sciences, Tehran, Iran
e-mail: m-aarabi@razi.tums.ac.ir; h-salighehrad@tums.ac.ir

L. O'Donnell et al. (eds.), *Computational Diffusion MRI*, Mathematics and Visualization, DOI 10.1007/978-3-319-11182-7_7

for each voxel in the image. Brain regions, such as cortical and subcortical gray matter and cerebrospinal fluid, have a vast isotropic diffusivity due to the lack of constraining process of diffusion by axons, running in myelinated fiber tracts [6]. The diffusion tensor can be used for characterizing magnitude, degree of anisotropy and orientation of directional diffusion. Therefore, mapping diffusion anisotropy and principal diffusion directions is one of the best ways to estimate white matter connectivity patterns in the brain obtained from white matter tractography. This could result in voxel-wise and tensor-wise analysis of diffusivity and anisotropic change in the white matter, which enables neuroscientists to chart the complex network of neural fiber tracts in the human brain. DTI possesses high dimension and complex structure, so that, detecting available pattern information and its analysis are mainly based on conventional linear statistics and classification methods become inefficient. In order to facilitate classification, segmentation, compression or visualization of the data, alleviating the undesirable properties of high-dimensional spaces, i.e. dimensionality reduction, is far-reaching. Dimensionality reduction is based on finding valid structures and geometric characterization of high dimensional data, to be realized with several techniques, which are categorized into linear and nonlinear methods. Linear methods are based on classic approaches, such as principal component analysis (PCA) and multi-dimensional scaling (MDS) [12]. Although they guarantee acquisition of real data structures lying on or near a linear subspace of high dimensional input space, they cannot deal with complex nonlinear data. This has led to development of nonlinear methods, such as Kernel PCA [9], and Isomap and diffusion-map (DM) techniques for biological data with highly nonlinear manifolds [2,7,8,10–13]. This paper seeks to address a technique for multiple valued DTI data visualization, based on images with pixels, sampled from underlying manifold, e.g. every single pixel may consist of a high dimensional vector as a positive semi-definite tensor in a DT-MRI acquisition. Diffusion map (DM) represents a dataset via a weighted graph of corresponding points to vertices and edges, in which, the spectral properties of the graph Laplacian would be used to map six-dimensional data to a 3D representation. Diffusion distance is applied by using a specific value, which is obtained for the proximity of each data point, performing the random walk for a number of time steps. Thus, pairwise diffusion distances in the low-dimensional representation of the data is maintained [4,5]. Differences between DT-MRI pixels are mainly evaluated using a diffusion distance metric with regard to rank 3, second-order positive semi-definite DTs, while the difference between DT pixels is approximated by DM. In this article, we evaluated case studies of high-dimensional phantom data, as well as normal clinical brain DT-MRI.

2 Method

To represent the underlying DTI data, high dimensional DT-MRI data are used. As long as the pixel dimensionality is greater than 3D space, dimensionality reduction must be employed in order to represent the low dimensional image pixels. To

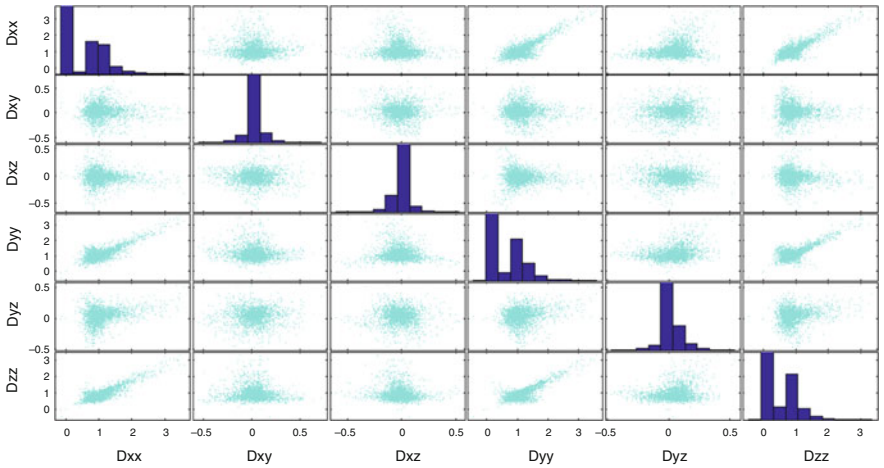

Fig. 1 Distribution of multi-dimensional DT-MR data

achieve this intention, pixel dissimilarities must be measured and pixels must be mapped to perceptually meaningful colors [3, 13]. It is assumed that high dimensional pixel values are sampled from underlying manifold acquired with distance metric. The manifolds are either learned using manifold learning techniques (e.g. DM), derived analytically or by approximation. Diffusion distance between two corresponding points on the manifold are the measured differences between any two high dimensional pixels. Similarities between DT pixels are evaluated by diffusion metric that scales the rank 3 manifold of DT pixels. DTs are symmetric 3×3 matrices, or second-order rank 3 diffusion tensors, with six unique elements. Furthermore, DTs must be positive semi-definite (PSD), in that six unique elements are defined in Diffusion tensors which are symmetric 3×3 matrices, i.e. $f(x) : x \in R^3 \rightarrow R^6$. An example of data distribution of a real data is shown in Fig. 1.

2.1 Dissimilarity Between High Dimensional Diffusion Tensor Imaging Data

Measuring dissimilarities between observations is an important step in handling high dimensional data. As far as the DT-MRI goes, estimation of DM and dissimilarity metrics are needed for the manifold learning structures, assuming $x^1, x^2, \ldots, x^k \in M$, M is the manifold embedded in R^3.

2.2 Implementation of Diffusion Map Algorithm in DT-MRI

The implemented algorithm proposed for DT-MRI of human brain is outlined in six steps as follows:

1. Constructing the similarity matrix, W, of the graph; the entries of W are the weights along the edges connecting corresponding nodes i and j, to be determined by the heat kernel as follows [13]:

$$W_{ij} = exp(-\frac{\|x_i - x_j\|^2}{\epsilon}) \tag{1}$$

where W is PSD and $\|.\|$ is the Euclidean norm. One should note that $W \in R^{k\times k}$ is a symmetric matrix. In the DM algorithm, the choice of the parameter ϵ is very important. Lafon in chose ϵ to be in the order of the average smallest non-zero value of $\|x_i - x_j\|^2$, that is:

$$\epsilon = \frac{1}{k}\sum_{i=1}^{k} min\|x_i - x_j\|^2; x_i \neq x_j \tag{2}$$

2. Formulating $k \times k$ normalization matrix of D; diagonal entries of D are row or column sum of W [11]:

$$D_{ii} = \sum_{i=1}^{n} W_{ij}, i \in 1, \ldots, n \tag{3}$$

The W matrix is then normalized as

$$P = D^{-1}W \tag{4}$$

Since DMs originate from dynamical systems theory, the resulting matrix P is considered to be a Markov matrix that defines the forward transition probability matrix of a data point.

3. Find the eigenvalues of P; the conjugate matrix of P is calculated as below:

$$\tilde{P} = D^{-\frac{1}{2}}WD^{\frac{1}{2}} \tag{5}$$

This so-called normalized graph Laplacian preserves the eigenvalues.

4. Singular value decomposition (SVD) of $\tilde{P}$ to be calculated by:

$$\tilde{P} = U\Lambda U^* \tag{6}$$

yielding the eigenvalues

$$\Lambda = diag([\lambda_1, \lambda_2, \ldots, \lambda_n]) \tag{7}$$

and eigenvectors in matrix

$$U = [u_1, u_2, \ldots, u_n] \tag{8}$$

[2]

5. Computing eigenvectors of $\tilde{P}$; one notes that eigenvalues of P and $\tilde{P}$ stay the same

$$V = D^{\frac{1}{2}}U \tag{9}$$

6. Creating low-dimensional coordinates in the embedded space Ψ using Λ and V, as follows:

$$\Psi = V\Lambda \tag{10}$$

Now, for each n-dimensional point x_i, there is a corresponding d-dimensional coordinate, where d < n. The coordinates for a single point can be expressed as:

$$\Psi_d : x_i \rightarrow [\lambda_1 v_1, \lambda_2 v_2, \ldots, \lambda_{d+1} v_{d+1}]. \tag{11}$$

Finally, diffusion map (DM) is defined as:

$$DM = \frac{[\lambda_1 v_1 + \lambda_2 v_2 + \lambda_3 v_3]}{3}. \tag{12}$$

An overview of all these steps is shown in Fig. 2.

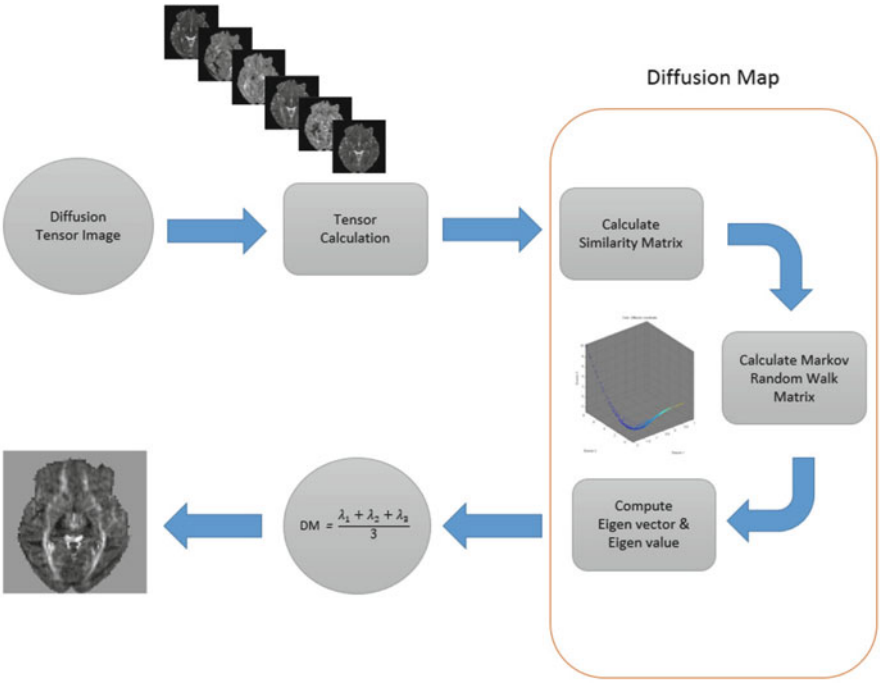

Fig. 2 Overview of proposed method

3 DT-MR Data

The idea of generating simulated MR images for this work are adopted from. The fibers were constructed based on streamline algorithm in ExploreDTI software [13]. The six tensor elements were calculated using linear fitting methods. MR acquisition on real data was performed on four normal subjects on a 1.5T clinical scanner MAGNETOM Avanto (Siemens Medical Solution, Erlangen, Germany) equipped with a maximum gradient strength of 40 mT/m and a slew rate of 200 mT/m/s. DT images were obtained with a single-shot echo-planar sequence with TR = 4,900 ms, TE = 85 ms, *b-value*= 1,000 s/mm^2, FOV = 230 mm, matrix size = 76×76, slice thickness = 3 mm, number of directions = 30, and NEX = 1.

4 Results and Discussion

4.1 Simulated MR Images

The implemented DM method was compared with fractional anisotropy (FA) and mean diffusivity (MD) maps (as shown in Fig. 3) on the simulated data. We quantitatively evaluated the image energy resulting from each method as indicated in Table 1, in terms of entropy, contrast, and correlation, which are defined as follows:

1. Entropy is a statistical measure of the randomness of data, representing the texture of the image:

$$Entropy = -\sum_{a}^{b} Plog_2 P \tag{13}$$

2. Contrast is a measure of intensity contrast, calculated between a pixel and its neighbor on the whole image:

$$Contrast = \sum_{i}^{j} |i - j|^2 p(i, j) \tag{14}$$

3. Correlation returns the amount of similarity between a pixel and its neighbor over the whole image:

$$Correlation = \sum_{i,j} \frac{(i - \mu i)(j - \mu j)p(i, j)}{\sigma_i \sigma_j} \tag{15}$$

The higher value of entropy and contrast, and lower correlation represent higher energy and more heterogeneity among the provided information. It can be inferred from Fig. 3 and Table 1 that DM technique yields higher amount of entropy and

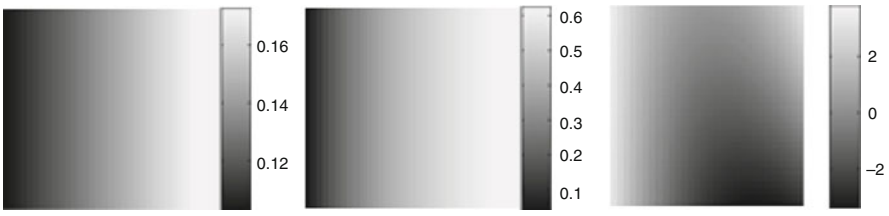

Fig. 3 Simulated data obtained using, mean diffusivity (MD) and fractional anisotropy (FA) maps in comparison with the proposed diffusion map (DM)

Table 1 Evaluation of the proposed diffusion map (DM), in comparison with mean diffusivity (MD) and fractional anisotropy (FA) maps, in terms of entropy, contrast, and correlation

Map	Entropy	Contrast	Correlation
DM	5.7014	0.2419	0.9690
MD	4.1800	0.2333	0.9827
FA	4.9542	0.2333	0.9827

Table 2 The amount of similarity between FA and DM

Correlation coefficient r	−0.5392
Significance level	P<0.0001
95 % confidence interval for r	−0.5573 to −0.5207

Table 3 The amount of similarity between MD and DM

Correlation coefficient r	0.5967
Significance level	P<0.0001
95 % confidence interval for r	0.5798–0.6130

contrast, and lower correlation value in comparison with FA and MD maps, meaning that it extracts more information from a DT-MR image.

4.2 Real MR Images

In Tables 2 and 3, the amount of similarity between DM and FA, MD are calculated in terms of correlation coefficient and the significance of this correlation is assessed by p-value. It can be observed that DM has high correlation with both FA and MD with a significant level ($p<0.0001$). This means that DM could contain essential information from both FA and MD, providing better visualization of the information in DT-MRI. Figure 4 illustrates the results of applying the proposed DM technique and calculated FA and MD maps on the real data. It is apparent that DM map contains more information than T1-weighted image, MD and FA maps. This suggests that DM could be reliably employed for further statistical analysis of human brain. Figure 4 demonstrates the values of DM, MD and FA on the region of interest (ROI), located on the hippocampus region in the coronal view of the T1-weighted image. For convenient analysis, MD values are multiplied by 1,000 to bring it into the same scale as FA and DM. The pixel intensity versus pixel number plot shows that when MD is high, FA and DM have reverse signs and when

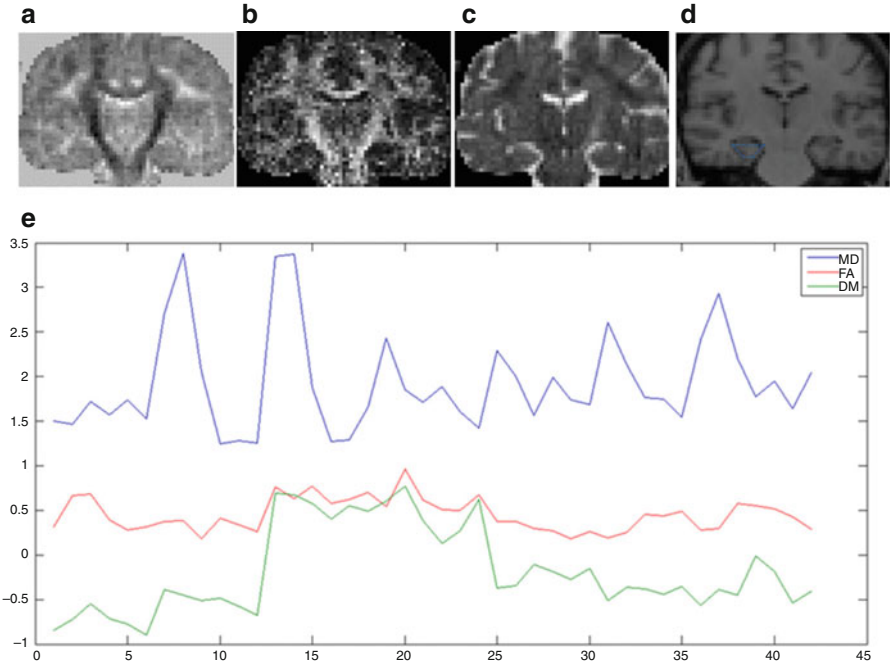

Fig. 4 The results on real data (**a**) T1-weighted image in a coronal view, with a region-of-interest (ROI) located on the hippocampal region; (**b**) the corresponding MD map; (**c**) fractional anisotropy (FA) map; (**d**) the proposed diffusion map (DM); and (**e**) the values of MD, FA, and DM on the selected ROI in part (**a**). The MD values are multiplied by 1,000 to be in the same scale as FA and DM

MD is low, their relationship is held with the similar sign. This suggests that DM has mutual information from both FA and MD, recommending a new visualization technique consisting of the necessary information of FA and MD, which could be used as a proper substitute for clinical applications. The visualization of DM, MD and FA are compared on several slices of a normal subject in axial, coronal and sagittal views in Figs. 5, 6, and 7.

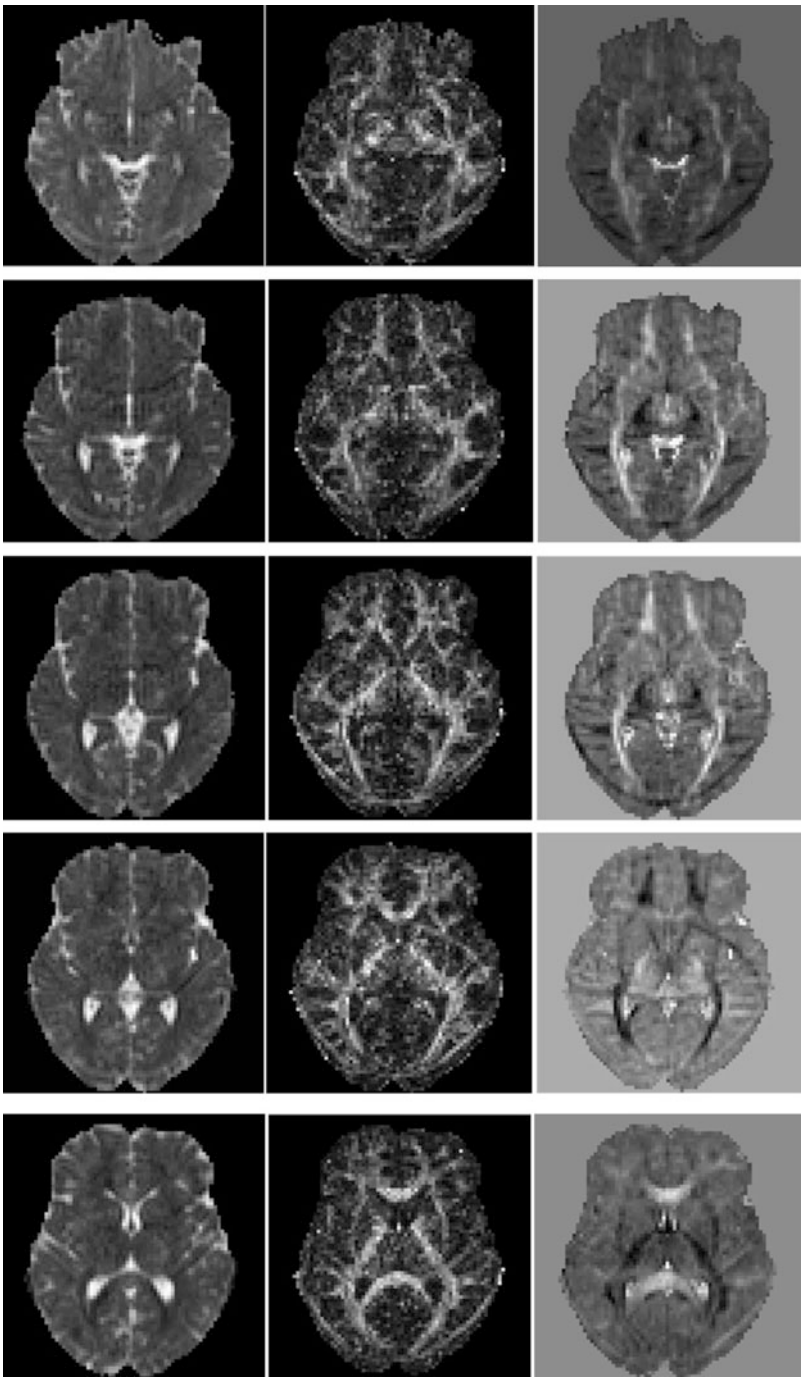

Fig. 5 Axial view of the results on real data: (*left column*) MD map, (*middle column*) FA map, and (*right column*) proposed diffusion map (DM)

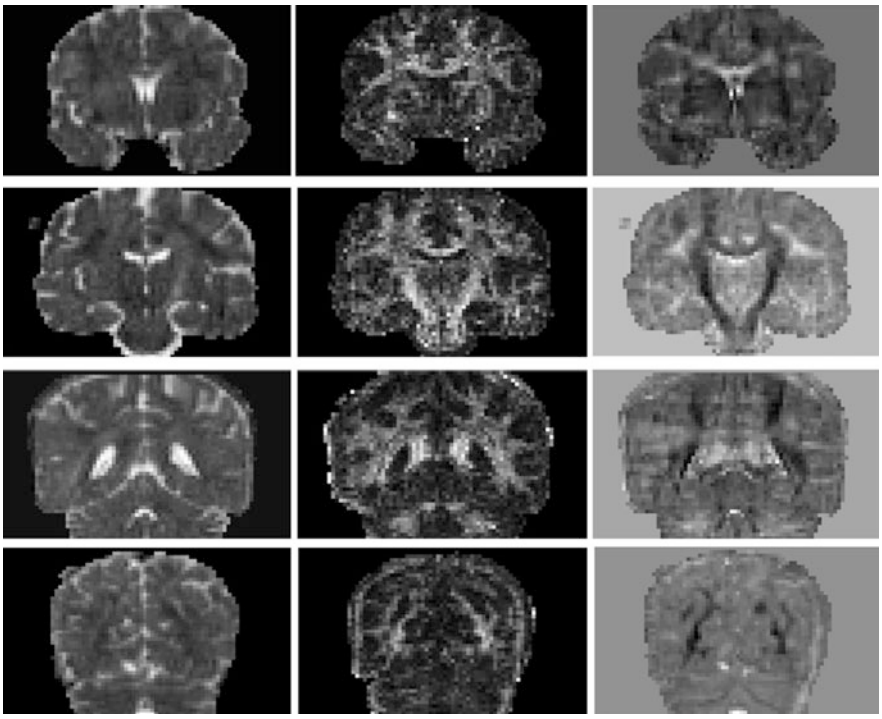

Fig. 6 Coronal view of the results on real data: (*left column*) MD map, (*middle column*) FA map, and (*right column*) proposed diffusion map (DM)

5 Conclusion

This study set out to propose a method for visualization of diffusion tensor (DT)-MRI as a robust method to noise, preserving distance in nonlinear data, while keeping low-dimensional space. The proposed analysis suggests that the diffusion map (DM) dimensionality reduction improves white matter segmentation and visualization, particularly in the low-SNR regimen of DT-MRI, while it stays an active research problem. Due to the wide range of research and clinical applications of DT-MRI, we hope that the proposed method will broaden new horizons for exploring the full richness of DTI to realize ways, in which such measurements are affected by pathologies and treatments. Manifold learning problems involve vector bundle on graphs providing the demand for vector diffusion mapping. Since vector diffusion mapping is an extended form of diffusion mapping, their properties and convergence behavior are similar. Besides, because the idea of vector diffusion mapping is a natural extended form of graph Laplacian operator combined with diffusion mapping on graphs, in the future, we are going to investigate the issues of smoothing and interpolation, as well as clustering of components of DTI datasets, leading to successful fiber clustering. In this work, it was indicated that DM could

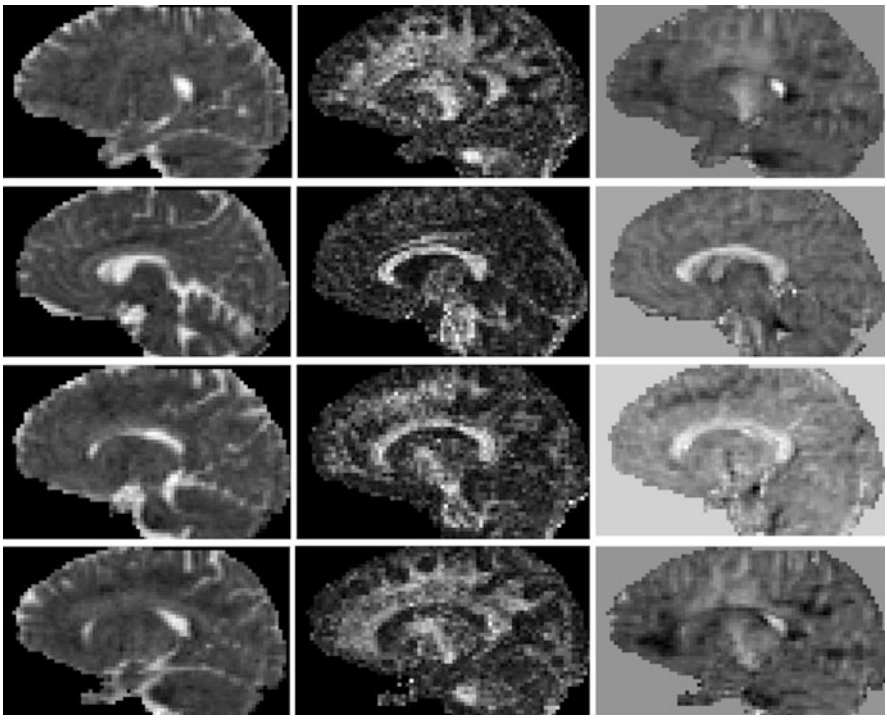

Fig. 7 Sagittal view of the results on real data: (*left column*) MD map, (*middle column*) FA map, and (*right column*) proposed diffusion map (DM)

provide information, which is present in both mean diffusivity (MD) and fractional anisotropy (FA) maps, as conventionally employed as quantitative maps in human brain. The exact mathematical relationship between DM and FA, MD along with the clinical applications of the proposed quantitative map will further be investigated in our future works.

References

1. Basser, P.J., Mattiello, J., LeBihan, D.: MR diffusion tensor spectroscopy and imaging. J. Biophys. **66**(1), 259–267 (1994). doi:10.1016/s0006-3495(94)80775-1
2. Mori, S., Zhang, J.: Principles of diffusion tensor imaging and its applications to basic neuroscience research. Neuron **51**(5), 527–539 (2006)
3. van der Maaten, L.J., Postma, E.O., van den Herik, H.J.: Dimensionality reduction: a comparative review. J. Mach. Learn. Res. 10(1–41), 66–71 (2009)
4. Schölkopf, B., Smola, A., Müller, K.-R.: Nonlinear component analysis as a kernel eigenvalue problem. Neural Comput. **10**(5), 1299–1319 (1998)
5. Tenenbaum, J.B., De Silva, V., Langford, J.C.: A global geometric framework for nonlinear dimensionality reduction. Science **290**(5500), 2319–2323 (2000)

6. Coifman, R.R., Lafon, S.: Diffusion maps. Appl. Comput. Harmon. Anal. **21**(1), 5–30 (2006)
7. Hamarneh, G., McIntosh, C., Drew, M.S.: Perception-based visualization of manifold-valued medical images using distance-preserving dimensionality reduction. IEEE Trans. Med. Imaging **30**(7), 1314–1327 (2011)
8. Khurd, P., Baloch, S., Gur, R., Davatzikos, C., Verma, R.: Manifold learning techniques in image analysis of high-dimensional diffusion tensor magnetic resonance images. Paper Presented at the IEEE Conference on Computer Vision and Pattern Recognition, 2007 (CVPR'07), pp. 1–7 (2007)
9. Goldberg, Y., Zakai, A., Kushnir, D., Ritov, Y.A.: Manifold learning: the price of normalization. J. Mach. Learn. Res. **9**, 1909–1939 (2008)
10. Nadler, B., Lafon, S., Coifman, R., Kevrekidis, I.G.: Diffusion Maps-A Probabilistic Interpretation for Spectral Embedding and Clustering Algorithms Principal Manifolds for Data Visualization and Dimension Reduction, pp. 238–260. Springer, New York (2008)
11. Nadler, B., Lafon, S., Coifman, R.R., Kevrekidis, I.G.: Diffusion maps, spectral clustering and reaction coordinates of dynamical systems. Appl. Comput. Harmon. Anal. **21**(1), 113–127 (2006)
12. Farup, I., Hardeberg, J.Y., Bakke, A.M., Kopperud, S., Rindal, A.: Visualization and interactive manipulation of color gamuts. Paper presented at the Color and Imaging Conference (2002)
13. Leemans, A., Jeurissen, B., Sijbers, J., Jones, D.: ExploreDTI: a graphical toolbox for processing, analyzing, and visualizing diffusion MR data. Paper Presented at the 17th Annual Meeting of International Society of Magnetic Resonance in Medicine, p. 3537 (2009)

A Multi-Parametric Diffusion Magnetic Resonance Imaging Texture Feature Model for Prostate Cancer Analysis

Farzad Khalvati, Amen Modhafar, Andrew Cameron, Alexander Wong, and Masoom A. Haider

Abstract In this work, we present a new multi-parametric magnetic resonance imaging (MP-MRI) texture feature model for automatic detection of prostate cancer. In addition to commonly used imaging sequences in conventional MP-MRI, namely T2-weighted MRI (T2w) and diffusion-weighted imaging (DWI), our proposed MP-MRI texture feature model uses computed high-b DWI (CHB-DWI) and a new diffusion imaging sequence called correlated diffusion imaging (CDI). A set of texture features was calculated for both the conventional MP-MRI and new MP-MRI texture feature model. We evaluated the performance of the proposed MP-MRI texture feature model via leave-one-patient-out cross-validation using a Bayesian classifier trained on cancerous and healthy tissue samples obtained from real clinical MP-MRI datasets. The proposed MP-MRI texture feature model outperformed the conventional model (i.e., T2w+DWI) with regard to cancer detection accuracy.

1 Introduction

Prostate cancer is the most common form of cancer and second leading cause of cancer death diagnosed in North American men, with more than 262,000 new cases and an estimated 33,660 deaths in 2013 [1,2]. Given that the median patient survival time for metastatic prostate cancer ranges from 12.2 to 21.7 months [3], early diagnosis of clinically significant prostate cancer would have significant benefits to patient care. This is particularly true given that the 5 year survival rate after diagnosis for patients with prostate cancer at the non-metastatic stage is 96 % in Canada [4].

F. Khalvati (✉) • A. Modhafar • M.A. Haider
Sunnybrook Research Institute, Toronto, ON, Canada
e-mail: farzad.khalvati@sri.utoronto.ca

A. Cameron • A. Wong
University of Waterloo, Waterloo, ON, Canada
e-mail: a28wong@uwaterloo.ca

L. O'Donnell et al. (eds.), *Computational Diffusion MRI*, Mathematics and Visualization, DOI 10.1007/978-3-319-11182-7_8

In the current clinical model, men with positive digital rectal exam (DRE) and elevated prostate-specific antigen (PSA) require multicore random biopsies for risk stratification. However, there is an ongoing controversy about the role of prostate PSA as a screening test in prostate cancer. Two recent major randomized clinical trials [5, 6] have demonstrated that PSA screening contains a significant risk of overdiagnosis for prostate cancer where it is estimated that 50 % of screened men are diagnosed with prostate cancer. This leads to painful needle biopsies and subsequent potential overtreatment [5, 6]. Moreover, it has become increasingly clear that prostate biopsies are harmful as they cause discomfort and possible sexual dysfunction and may result in increased hospital admission rates due to infectious complications [7]. Nevertheless, PSA testing has proven to reduce prostate cancer mortality by 20–30 % at long-term follow-ups [8]. Therefore, the PSA testing remains an important biomarker in diagnosing prostate cancers that are clinically significant. The remaining challenge is how to improve the prostate cancer diagnosis to reduce the overdiagnosis of clinically insignificant cancers.

Automatic detection of prostate cancer as part of a clinical decision support system can potentially help radiologists in interpreting images more accurately. Specifically, multi-parametric MR imaging (MP-MRI) which combines T2-weighted MRI (T2w), diffusion-weighted imaging (DWI), and dynamic contrast enhanced imaging (DCE) has been found to be a promising method for prostate cancer diagnosis and it has been used in different prostate cancer detection algorithms. By taking advantage of the unique information provided by each individual imaging technique, MP-MRI can exploit the different characteristics of prostate tissue to improve differentiation between cancerous and surrounding tissues. For example, cancerous tissue in the prostate gland may exhibit a moderate drop in signal in T2w [9] (which characterizes differences in transverse (spin-spin) relaxation time of tissue); restricted diffusion in DWI [9] (which characterizes diffusion of water in tissue); earlier onset time, higher peak, and shorter peak time in DCE [10] (which characterizes the concentration of an injected gadolinium contrast agent over time as it passes into the extracellular extravascular space of the tissue). Although DCE is considered as part of MP-MRI, T2w+DWI is the most common MP-MRI because it does not require invasive contrast agent as DCE does.

Radiologists' interpretations of MP-MRI have shown to achieve good prostate cancer detection rates, reaching accuracies of 80 % in the peripheral zone of the prostate gland. Similarly, several algorithms have been proposed for auto-detection of prostate cancer using MP-MRI setting [11–14]. These algorithms usually compute a set of low-level features from the MP-MRI data to construct feature vectors. Next, a supervised classifier is trained using the computed feature vectors from the training cases and their associated 'ground-truth' labels (e.g., labeled healthy or cancerous). Finally, the trained classifier is used to classify new cases. The reported values for accuracy of cancerous versus healthy tissue classification ranges from 64 to 89 %, depending on the feature sets and training/test data.

The underlying challenge in all these auto-detection algorithms is whether there is enough separability between the cancerous and healthy tissues in the feature

space. This means if the separability is poor, even sophisticated feature extraction algorithms may not have a significant effect on the accuracy of cancer detection. On the other hand, improving the separability of cancerous and healthy tissues in the images would have a significant impact on the performance of cancer auto-detection algorithms, potentially reducing the dependency on the feature extraction methods.

In this paper, we propose a new MP-MRI texture feature model that, in addition to T2w and conventional DWI, uses computed high-b diffusion-weighted imaging (CHB-DWI) [15] and the recently proposed correlated diffusion imaging (CDI) [16]. Compared to DWI, CHB-DWI and CDI have both shown initial promise to improve visual separability of cancerous and healthy tissues in prostate, which can lead to improved performance of the proposed MP-MRI texture feature model for detecting prostate cancer. To the authors' best knowledge, the proposed texture feature model is the first that utilizes all of the above-mentioned MP-MRI modalities.

This paper is organized as follows: in Sect. 2, the proposed MP-MRI texture feature model is presented. Section 3 presents the testing methodology which includes the description of image data and the evaluation metrics used in this research. Sections 4 and 5 present the experimental results and conclusions, respectively.

2 Proposed Multi-Parametric Magnetic Resonance Imaging Texture Feature Model

In this section, we present the proposed MP-MRI texture feature model for prostate cancer and discuss the imaging and feature extraction methods used in the model.

2.1 Imaging Methods

This subsection summarizes the imaging methods used in the proposed MP-MRI feature model.

2.1.1 T2-Weighted Imaging

T2w is a MR imaging modality in which the sensitivity of tissue is characterized by measuring the relaxation time (spin-spin) of the applied magnetic field. The T2w imaging of the prostate usually shows a small reduction in signal in the cancerous tissue [9].

2.1.2 Diffusion-Weighted Imaging

DWI is a promising imaging modality in which the sensitivity of tissue to Brownian motion of water molecules is measured by applying pairs of opposing magnetic field gradient pulses [17]. The diffusion-weighted signal, S is measured as:

$$S = S_0 e^{-bD} \tag{1}$$

where S_0 is the signal intensity without the diffusion weighting, b consists of amplitude and duration of the diffusion pulses, and the time between the two pulses as well as the gyromagnetic ratio, and D represents the strength of the diffusion. The diffusion-weighted image (S) is usually generated with different b values which can be used to estimate D in Eq. 1, called apparent diffusion coefficient map (ADC), using least-squares or maximum likelihood strategies [18]. The cancerous tissue in ADC is usually represented by a darker intensity compared to the surrounding tissue.

2.1.3 Computed High-b Diffusion-Weighted Imaging (CHB-DWI)

Previous research has shown that high b-value DWI images (e.g., b-values greater than 1,000 s/mm^2) allow for increased delineation between tumours and healthy tissues [15, 19] which makes the prostate cancer detection more robust. Nevertheless, due to hardware limitations, most MRI machines in practice do not produce DWI with b-values higher than 1,500 s/mm^2. CHB-DWI is an alternative approach to obtain high-b DWI in which a computational model is used to reconstruct DWI at high b-values using low b-value DWI acquisitions [15]. For our experiments, we constructed CHB-DWI with b-value at 2,000 s/mm^2 using the same least squares estimation technique used for ADC, extrapolating to the b-value of 2000 s/mm^2.

2.1.4 Correlated Diffusion Imaging (CDI)

CDI [16] is a new diffusion magnetic resonance imaging modality, which takes advantage of the joint correlation in signal attenuation across multiple gradient pulse strengths and timings to not only reduce the dependency on the way diffusion gradient pulses are applied, but also improve delineation between cancerous and healthy tissue. The local correlation of signal attenuation across all b-values within a local sub-volume is calculated to better represent the overall characterization of the water diffusion properties of the tissue. The CDI signal is calculated as follows [16]:

$$\begin{aligned} CDI(x) = \int \dots \int_{b_0}^{b_n} & S_0(x) \dots S_n(x) P(S_0(x), \dots, S_n(x) | V(x)) \\ & \times dS_0(x) \dots dS_n(x) \end{aligned} \tag{2}$$

where x denotes spatial location, S denotes the acquired signal, P denotes the conditional joint probability density function, and $V(x)$ denotes the local subvolume around x.

2.2 Texture Feature Model

In order to separate the cancerous tissue from the healthy one, a set of features is calculated on a given MR imaging sequence (i.e., T2w, DWI, CHB-DWI, CDI). As part of the proposed MP-MRI texture feature model, we incorporate the texture features used in separate studies to establish a relationship between these features and tumour glucose metabolism and stage [20] and to predict the response of metastatic renal cell cancer to treatment [21]. These features include mean grey-level intensity (M), entropy (En), and uniformity (U), which are calculated as follows:

$$M = \frac{1}{N} \sum_{x,y=0}^{N-1} pix(i, j) \tag{3}$$

$$En = -\sum_{l=1}^{k} p(l) log_2[p(l)] \tag{4}$$

$$U = \sum_{l=1}^{k} [p(l)]^2 \tag{5}$$

where $pix(i, j)$ is the gray-level intensity in the pixel window, N is the window size, p is the probability density function of pixels in the window, and k is the number of grey levels in the image.

In addition, the proposed MP-MRI texture feature model incorporates another set of texture features extracted from the gray-level co-occurrence matrix (GLCM) in 4 directions: 0°, 45°, 90°, and 135°. The GLCM texture features are calculated as follows:

1. Contrast (Con)—a measure of the intensity difference between a pixel and its neighbors:

$$Con = \sum_{x,y=0}^{N-1} |x - y|^2 p_{glcm}(x, y) \tag{6}$$

2. Energy (Eg)—the sum of squared elements in the GLCM;

$$Eg = \sum_{x,y=0}^{N-1} p_{glcm}(x, y)^2 \tag{7}$$

3. Homogeneity (H)—a value that measures the closeness of the distribution of elements in the GLCM to the GLCM diagonal.

$$H = \sum_{x,y=0}^{N-1} \frac{p_{glcm}(x, y)}{1 + (x - y)^2} \tag{8}$$

4. Correlation (Cor)—a measure of how correlated a pixel is to its neighbors:

$$Cor = \sum_{x,y=0}^{N-1} \frac{(x - \mu_x)(y - \mu_y) p_{glcm}(x, y)}{\sigma_x \sigma_y} \tag{9}$$

where p_{glcm} is the probability value from the GLCM, μ_x, μ_y, σ_x, and σ_y are the means and standard deviation values of p_{glcm} in horizontal and vertical directions, respectively.

As a result, the proposed MP-MRI texture feature model consists of a total of 19 features for each imaging modality: 16 from GLCM (4 in each direction) and 3 other texture features (i.e., mean gray level, entropy, and uniformity).

3 Testing Methodology

In the following, details about the image acquisition protocols and the performance measures are presented.

3.1 Image Data

MRI data of five patients were acquired using a Philips Achieva 3.0T machine at Sunnybrook Health Sciences Centre, Toronto, Ontario, Canada. All data was obtained under the local institutional research ethics board. For each patient, the following MP-MRI modalities were obtained (Table 1): T2w, DWI, and CDI. The patients' age ranged from 53 to 75.

Table 1 Description of the prostate T2w, DWI, and CDI images

Sequence	DFOV (cm^2)	Resolution (mm^2)	Resolution (pixels)	TE (ms)	TR (ms)
T2w	22 × 22	0.49 × 0.49 × 3	440 × 425 × 26	110	4,687
DWI	20 × 20	1.56 × 1.56 × 3	128 × 128 × 24	61	6,178
CDI	20 × 20	1.56 × 1.56 × 3	128 × 128 × 24	61	6,178

3.2 Evaluation Metrics

We evaluated the performance of the proposed MP-MRI texture feature model for detecting prostate cancer via a leave-one-patient-out cross-validation using a Bayesian classifier. First, the feature extraction function was applied to each MR imaging sequence (i.e., T2w, ADC, CHB-DWI, and CDI) separately across all patients' data. This generated four sets of features based on the proposed MP-MRI texture feature model. Next, a conventional MP-MRI setting was established by combining the features of T2w and ADC. As a new MP-MRI texture feature model, three configurations were realized: T2w+ADC+CHB-DWI, T2w+ADC+CDI, and CHB-DWI+ADC+CDI.

We used a Bayesian classifier to calculate sensitivity, specificity, and accuracy using leave-one-patient-out cross-validation approach. As ground-truth, all images were reviewed and marked as healthy and cancerous tissue by a radiologist with 18 and 13 years of experience interpreting body and prostate MRI, respectively.

4 Experimental Results

Table 2 shows sensitivity, specificity, and accuracy for all 8 MP-MRI modalities/models. For each modality, on average, 5,260 (5,110 healthy and 150 cancerous) and 1,315 (1,275 healthy and 40 cancerous) samples (i.e., pixel windows) were used as training and testing data, respectively for the leave-one-patient-out cross-validation. The results were averaged across all patients. In order to unify all three measures (sensitivity, specificity, and accuracy) for the purpose of comparison among different configurations, we also report the average of the three measures for each modality/configuration.

It is seen that CHB-DWI alone improves results compared to T2w and ADC (Sensitivity: 0.88 vs. 0.70 and 0.87, Specificity: 0.58 vs. 0.48 and 0.37, Accuracy: 0.58 vs. 0.49 and 0.38). Although CDI has a lower sensitivity compared to T2w (0.66 vs. 0.70), its specificity and accuracy is the highest among all individual

Table 2 Evaluation results for prostate cancer detection

Imaging modality	Sensitivity	Specificity	Accuracy	Average
T2w	0.7037	0.4815	0.4878	0.5577
ADC	0.8730	0.3659	0.3805	0.5398
CHB-DWI	0.8836	0.5751	0.5839	0.6809
CDI	0.6614	0.7998	0.7958	0.7523
T2w+ADC	0.8360	0.4096	0.4219	0.5558
T2w+ADC+CHB-DWI	0.8571	0.6350	0.6414	0.7112
T2w+ADC+CDI	0.6772	0.8125	0.8086	0.7661
CHB-DWI+ADC+CDI	0.7831	0.7867	0.7866	0.7854

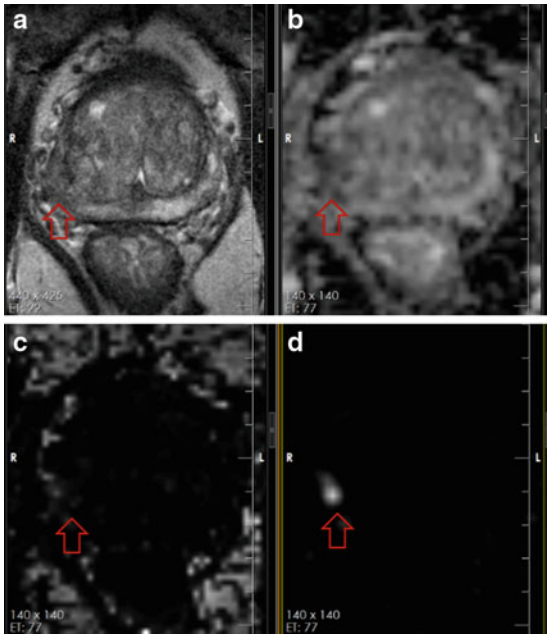

Fig. 1 (**a**) T2w does not clearly show a tumour although there is mild signal alteration in the left peripheral zone (*arrow*). (**b**) ADC does not clearly show a tumour (*arrow*). (**c**) CHB-DWI of 2,000 s/mm^2 shows no tumour (*arrow*). (**d**) CDI clearly shows a bright nodule (*arrow*) corresponding to tumour

modalities (0.80). This is due to the fact that CDI combines the information across b-values making it robust.

The first configuration of the new MP-MRI texture feature model, T2w+ADC+CHB-DWI, improves the results with regard to the conventional model, T2w+ADC, (Sensitivity: 0.86 vs. 0.84, Specificity: 0.63 vs. 0.41, Accuracy: 0.64 vs. 0.42). The second configuration of the new MP-MRI texture feature model, T2w+ADC+CDI, loses the sensitivity compared to the conventional model, T2w+ADC, (0.68 vs. 0.84) but outperforms it in both specificity (0.81 vs. 0.41) and overall accuracy (0.81 vs. 0.42). The third configuration of the proposed MP-MRI (CHB-DWI+ADC+CDI) only loses 5 % in sensitivity compared to the conventional MP-MRI (T2w+ADC) (0.783 vs 0.836). In return, it improves the specificity and accuracy by 38 and 37 %, respectively (Specificity: 0.79 vs. 0.41, Accuracy: 0.79 vs. 0.42). In other words, with a slight reduction in true positive cases, a significant amount of false positive cases can be avoided. The best result for average of all three measures (i.e., sensitivity, specificity, and produced by CHB-DWI+ADC+CDI (0.79).

Figure 1 shows an example for all four modalities which include T2w, ADC, CHB-DWI, and CDI. As it can be seen, CDI (Fig. 1d) is the only modality that clearly shows a bright nodule where a tumour is located (confirmed by histopathology data).

5 Conclusions

In this paper, we introduced a new multi-parametric MRI texture feature model for prostate cancer detection. Our new MP-MRI texture feature model adds two new image modalities, CHB-DWI and CDI, to the most commonly used MP-MRI, T2w+ADC. We calculated a set of texture features for both the conventional MP-MRI and new MP-MRI texture feature models. A Bayesian classifier was trained via leave-one-patient-out setting to classify the new cases. We evaluated the proposed MP-MRI texture feature model in three configurations. The first configuration (T2w+ADC+CHB-DWI) improved the results (sensitivity, specificity, and accuracy) compared to the conventional MP-MRI. The second configuration (T2w+ADC+CDI) improved specificity (40 %) and accuracy significantly (39 %) with a loss in sensitivity (16 %) with respect to the conventional MP-MRI. The best result was achieved by the third configuration (CHB-DWI+ADC+CDI); it improved specificity and accuracy significantly (38 and 37 %, respectively) with a rather small loss in sensitivity (5 %) with respect to the conventional MP-MRI. The proposed MP-MRI texture feature model showed promise to tackle the overdiagnosis problem in prostate cancer detection.

References

1. Canadian Cancer Society: Canadian Cancer Statistics (2013)
2. American Cancer Society: Cancer Facts and Figures (2013)
3. Ren, J., Wang, F., Wei, G., Yang, Y., Liu, Y., Wei, M., Huan, Y., Larson, A.C., Zhang, Z.: MRI of prostate cancer antigen expression for diagnosis and immunotherapy. PLoS ONE **7**(60), e38350 (2012)
4. Canadian Cancer Society: Canadian Cancer Statistics (2011)
5. Andriole, G.L., et al.: PLCO Project Team. Mortality results from a randomized prostate-cancer screening trial. N. Engl. J. Med. **360**, 1310–1319 (2009)
6. Schroder, F.H., et al.: ERSPC Investigators, screening and prostate-cancer mortality in a randomized European study. N. Engl. J. Med. **360**, 1320–1328 (2009)
7. Loeb, S., et al.: Systematic review of complications of prostate biopsy. Eur. Urol. **64**(6), 876–892 (2013)
8. Schroder, F.H., et al.: ERSPC Investigators. Prostate-cancer mortality at 11 years of follow-up. N. Engl. J. Med. **366**(11), 981–990 (2012)
9. Haider, M.A., van der Kwast, T.H., Tanguay, J., Evans, A.J., Hashmi, A.T., Lockwood, G., Trachtenberg, J.: Combined T2-weighted and diffusion-weighted MRI for localization of prostate cancer. AJR. Am. J. Roentgenol. 189(2), 323–328 (2007)
10. Langer, D.L., van der Kwast, T.H., Evans, A.J., Plotkin, A., Trachtenberg, J., Wilson, B.C., Haider, M.H.: Prostate tissue composition and MR measurements: investigating the relationships between ADC, T2, K-trans, v(e), and corresponding histologic features. Radiology **255**(2), 485–494 (2010)
11. Ozer, S., Haider, M.A., Langer, D.L., van der Kwast, T.H., Evans, A.J., Wernick, M.N., Trachtenberg, J., Yetik, I.S.: Prostate cancer localization with multispectral MRI based on relevance vector machines. In: 2009 IEEE International Symposium on Biomedical Imaging From Nano to Macro, IEEE, pp. 73–76 (2009)

12. Madabhushi, A., Feldman, M.D., Metaxas, D.N., Tomaszeweski, J., Chute, D.: Automated detection of prostatic adenocarcinoma from high-resolution ex vivo MRI. IEEE Trans. Med. Imaging **24**(12), 1611–1625 (2005)
13. Liu, X., Langer, D.L., Haider, M.A., Yang, Y., Wernick, M.N., Yetik, I.S.: Prostate cancer segmentation with simultaneous estimation of Markov random field parameters and class. IEEE Trans. Med. Imaging **28**(6), 906–915 (2009)
14. Ozer, S., Langer, D.L., Liu, X., Haider, M.A., van der Kwast, T.H., Evans, A.J., Yang, Y., Wernick, M.N., Miles, N., Yetik, I.S.: Supervised and unsupervised methods for prostate cancer segmentation with multispectral MRI. Med. Phys. **37**(4), 1873–1883 (2010)
15. Glaister, J., Cameron, A., Wong, A., Haider, M.A.: Quantitative investigative analysis of tumour separability in the prostate gland using ultra-high b-value computed diffusion imaging. In: EMBC'2012, IEEE pp. 420–423 (2012)
16. Wong, A., Glaister, J., Cameron, A., Haider, M.A.: Correlated diffusion imaging. BMC Med. Imaging **13**, 26 (2013)
17. Koh, D.M., Padhani, A.R.: Diffusion-weighted MRI: a new functional clinical technique for tumour imaging. Br. J. Radiol. **79**, 633–635 (2006)
18. Walker-Samuel, S., Orton, M., McPhail, L.D., Robinson, S.P.: Robust estimation of the apparent diffusion coefficient (ADC) in heterogeneous solid tumors. Magn. Reson. Med. **62**(2), 420–429 (2009)
19. Rosenkrantz, A.B., Chandarana, H., Hindman, N., Deng, F.M., Babb, J.S., Taneja, S.S., Geppert, C.: Computed diffusion-weighted imaging of the prostate at 3T: impact on image quality and tumor detection. Proc. Int. Soc. Magn. Reson. Med. **21**, 94 (2013)
20. Ganeshana, B., Abaleke, S., Young, R.C., Chatwin, C.R., Miles, K.A.: Texture analysis of non-small cell lung cancer on unenhanced computed tomography: initial evidence for a relationship with tumour glucose metabolism and stage. Cancer Imaging **10**, 137–143 (2010)
21. Goh, V., Ganeshan, B., Nathan, P., Juttla, J.K., Vinayan, A., Miles, K.A.: Assessment of response to tyrosine kinase inhibitors in metastatic renal cell cancer: CT texture as a predictive biomarker. Radiology **261**(1), 165–71 (2011)

Predicting Poststroke Depression from Brain Connectivity

J. Mitra, K.-K. Shen, S. Ghose, P. Bourgeat, J. Fripp, O. Salvado, B. Campbell, S. Palmer, L. Carey, and S. Rose

Abstract Depression is a common neuropsychological consequence of stroke. The ability to predict patients at high risk of developing depressive disorders using non-invasive neuroimaging strategies has the potential to help guide treatment programs aimed to enhance functional and cognitive recovery. In this study we hypothesize that modeling the disconnection of key cortical and subcortical brain networks due to ischemic brain injury may be used to predict poststroke depression. The loss in structural connectivity was measured using diffusion-weighted MRI (dMRI) and white matter fiber tracking for 25 stroke patients (acquired 12 months after stroke) and 41 age-matched control participant. Two connectivity matrices were generated for each control participant, one with and one without the use of a manually delineated stroke lesion of a patient as an exclusion mask. A paired t-test using network-based statistics (NBS) was then performed on these connectivity matrices to determine the neural networks affected by the ischemic injury. This procedure was repeated for all stroke patients, in an independent fashion, to generate 25 disconnectivity matrices that were subsequently used in regression forest to provide a probabilistic prediction of depression. The probabilistic scores obtained from

J. Mitra (✉) • K.-K. Shen • S. Ghose • P. Bourgeat • J. Fripp • O. Salvado • S. Rose
CSIRO (Digital Productivity Flagship), The Australian E-Health and Research Centre, Herston, QLD, Australia
e-mail: Jhimli.Mitra@csiro.au; Kaikai.Shen@csiro.au; Soumya.Ghose@csiro.au; Pierrick.Bourgeat@csiro.au; Jurgen.Fripp@csiro.au; Olivier.Salvado@csiro.au; Stephen.Rose@csiro.au

B. Campbell
Department of Medicine and Neurology, Melbourne Brain Centre at the Royal Melbourne Hospital, University of Melbourne, Parkville, VIC, Australia

S. Palmer
The Florey Institute of Neurosciences and Mental Health, University of Melbourne, Parkville, VIC, Australia
e-mail: smspalmer1@gmail.com

L. Carey
The Florey Institute of Neurosciences and Mental Health, University of Melbourne, Parkville, VIC, Australia

Department of Occupational Therapy, La Trobe University, Bundoora, VIC, Australia
e-mail: lcarey@unimelb.edu.au

L. O'Donnell et al. (eds.), *Computational Diffusion MRI*, Mathematics and Visualization, DOI 10.1007/978-3-319-11182-7_9

regression forests (in a leave-one-out manner) and the clinical depression scores for 25 stroke patients achieved a high positive Pearson's correlation with $\rho = 0.78$ ($p < 0.00001$). This methodology shows promise as a predictive tool of poststroke depression that maybe useful for optimizing rehabilitation strategies.

1 Introduction

Approximately one-third of stroke survivors exhibit depressive symptoms at some time following stroke [3]. Poststroke depression (PSD) has been associated with poor functional recovery, cognitive impairment, with individuals presenting with PSD twice as likely to experience poor long term functional outcomes [10]. Treatment and subsequent remission of PSD have been associated with improved physical and cognitive functional recovery [6]. Currently, there are no robust methods for identifying which stroke patients may go on to develop clinical depression. A number of assessment and screening tools exist for PSD [11], however many of these rely on self-reporting or observer-rating scales, applied well after the onset of depressive symptoms. The ability to identify stroke patients at high risk of developing PSD would enable the introduction of early interventions to improve functional recovery after stroke.

In this paper, we investigate the use of diffusion-weighted MRI (dMRI), probabilistic tractography and structural connectivity for predicting PSD. We hypothesize that white-matter (WM) fiber connections will be disrupted by the ischemic injury and that patients clinically identified with moderate or severe levels of PSD will have more disconnections within brain networks that are believed to be involved with depression compared to those patients who recover from stroke with little or no clinical symptoms of depression. Recent studies suggested that stroke lesions in limbic, cortical, striatal, pallidal and thalamic structures were associated with PSD [12, 14], with a prospective study suggesting little association between stroke location and onset of PSD [1]. Therefore, our hypothesis builds on the concept that not only is the anatomical location of the stroke important for assessing recovery, but the pronounced effect of the injury on key intra- and inter-hemispheric neural circuits is important for measuring the extent of injury and predicting functional recovery.

This hypothesis was tested and validated using a concept of network disconnectivity, where the impact of ischemic lesion on brain connectivity is measured using normative control data following [4]. This approach stems from the concept that fiber tracking may be more robust without the presence of significant pathology. Given a stroke patient, two sets of connectivity matrices were generated from dMRI data acquired from each age-matched control participants, one without the stroke lesion and the other with the lesion mask as an exclusion mask. The loss in connectivity associated with this stroke, assessed across the normative population, can then be determined using a network-based statistics (NBS) [15], employing a standard paired t-test design. The advantage of using a paired t-test approach in

a control population is that a simple measure of streamline number, although not quantitative in nature, can be used to infer information about cortical connectivity. Disconnectivity matrices for each stroke patient were used as features in a regression forest to provide a probabilistic prediction of depression. The novelties of our methodology are (1) measuring the impact of the stroke lesion on brain connectivity across a range of normative subjects using GLM based permutation testing and (2) using regression forest for continuous prediction of PSD from brain network disconnections. To the best of our knowledge this is the first attempt to predict PSD levels using a dMRI structural connectivity analysis.

2 Prediction of PSD Levels from Connectivity

In this study, we first identify the network connections that are affected by the ischemic lesion for each stroke patient when compared to a control population. The patterns of the disconnected networks are then used in the regression forests to predict the level of PSD. The schematic diagram of our method is shown in Fig. 1. The figure shows that two structural connectivity matrices are generated from dMRI data acquired from each of 41 age-matched control participant one with and without the stroke lesion as exclusion mask. The disconnectivity matrix obtained for each stroke patient using NBS, was passed into regression forest to predict PSD levels in a leave-one-out manner. The following sections explain our method in more details.

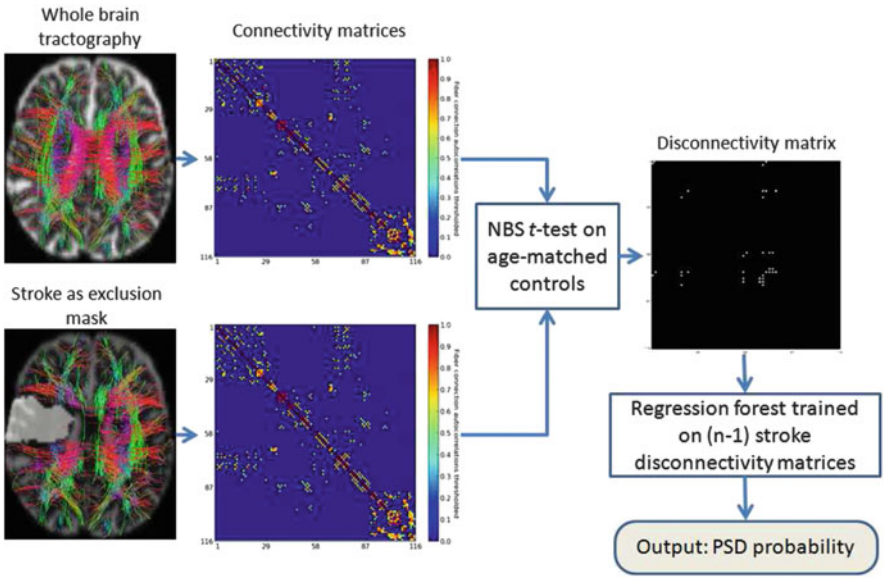

Fig. 1 Schema diagram of our proposed methodology

2.1 Connectivity with Network-Based Statistics (NBS)

The NBS is a non-parametric t-test using the generalized liner model (GLM), to isolate the components of a $l \times l$ undirected and symmetric connectivity matrix C that differ significantly between two distinct populations [15]. The number l depends on the number of parcellated regions of the brain. For DWI, usually the strengths of the fiber connections passing between a pair of regions is encoded into the C_{ij}^{th} and C_{ji}^{th} elements of the matrix C. Rather than using the raw fiber connection measures, we convert the connectivity matrix into an autocorrelation matrix C^H that ensures a unit diagonal and intensifies the stronger fiber connections while suppressing the noise in the estimation. The connectivity measures were further thresholded at τ to keep the significant network connections. Figure 2 shows a connectivity matrix with raw fiber connections and those with autocorrelation measures of fiber connections.

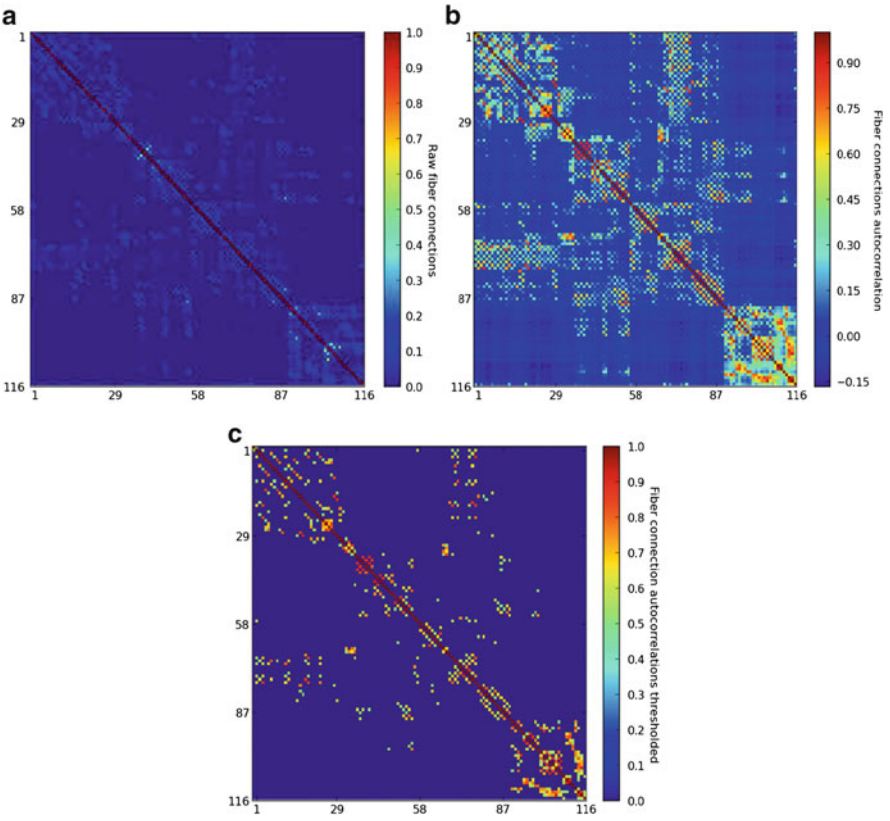

Fig. 2 Connectivity matrices. (**a**) Raw fiber connection measures encoded in connectivity matrix; (**b**) autocorrelation measures of the connectivity matrix in (**a**); and (**c**) connectivity matrix in (**b**) thresholded to keep the important connections

Given the connectivity matrices of whole brain connectivity C_w^H and with the manually segmented stroke masks as exclusion masks C_s^H as obtained from a tractography algorithm [13], the NBS controls the family-wise error-rate in a weak sense, when the null hypothesis is tested independently at each of the $l(l-1)/2$ edges comprising the connectivity matrix. It employs the GLM to perform a two-sample t-test at each edge independently to test the hypothesis that the connectivity between the two populations come from distributions with equal means. The GLM equation $\mathrm{y} = \mathrm{Xb} + \xi$ is defined by the data matrix y of size $n \times M$, where n is the total number of cases in both the populations and M is the size of the vectorized upper triangular connectivity matrix since C_w^H and C_s^H are symmetric; X is the design matrix of size $n \times k$ with independent predictor variables including a column of intercepts, and b of size $k \times M$ is a matrix of unknown parameters (regression coefficients) that need to be estimated. The error ξ is minimized to predict the optimized parameters of b using a least-square estimate as $\mathrm{b} = \left(\mathrm{X}^T\mathrm{X}\right)^{-1}\mathrm{X}^T\mathrm{y}$. To compute the differences in networks connections among the populations, a paired t-test is done in conjunction with permutation testing i.e. by randomly permuting the rows of the matrix y for s times, and is calculated as follows: $t = \frac{\mathrm{c}^T\mathrm{b}}{\sqrt{Var(\xi)\mathrm{c}^T\left(\mathrm{X}^T\mathrm{X}\right)^{-1}\mathrm{c}}}$, where, c is a $1 \times k$ contrast vector with the first element as 1 and remaining zeros that implies that network connections are more in C_w^H than C_s^H, and t is vector of size M. The t-statistic available at each edge are thresholded to form a set of suprathreshold edges and the size of the observed components defined by these edges are recorded for each permutation which yields an estimate of the null distribution of the maximal component size. A corrected p-value for each observed component is then calculated using this null distribution.

2.2 Prediction with Regression Forest

Given a labeled training set, a regression forest learns a general mapping which associates previously unseen independent test data with their correct continuous prediction [2]. In a regression forest training, each tree $\mathscr{T}$ in the forest receives the full multivariate training set V, along with the label at the root node and selects a test threshold along randomly chosen dimensions of the feature space to split V into two subsets in order to maximize the information gain. The left and the right child nodes receive their respective subsets V_i and the process is repeated at each child node to grow the next level of the tree. Each node in a decision tree also contains a class predictor $p^i{}_{\mathscr{T}}(\mathscr{C}|x)$, which is the probability of sample x belonging to class $\mathscr{C}$. Growth is terminated when either information gain is minimum or the tree has grown to maximum depth. At testing, a new multivariate data to be predicted is pushed through each tree $\mathscr{T}$ by applying the learned split functions. When reaching a leaf node $\mathscr{L}$, posterior probabilities $p^{\mathscr{L}}_{\mathscr{T}}(\mathscr{C}|x))$ are

gathered in order to compute the final posterior probability of the voxel defined by $p(\mathscr{C}|x) = \frac{1}{N}\sum_{\mathscr{T}=1}^{N} p_{\mathscr{T}}^{\mathscr{L}}(\mathscr{C}|x)$, where is the number of trees.

3 Experiments and Results

3.1 Data and Pre-Processing

Our study cohort involved 25 stroke patients at 12 month post-stroke stage and 41 age-matched normal subjects. High angular resolution diffusion imaging (HARDI), acquired using 60 diffusion encoding directions (b = 3,000 s/mm^2) were available for both stroke and normal cohort. Fractional anisotropy (FA) maps were generated using MRtrix [13] after preprocessing to reduce artifacts from involuntary head movement, cardiac pulstile motion and image distortions [8, 9]. 3D ROIs for the stroke lesions were manually delineated by an expert neurologist on fluid-attenuated inversion recovery (FLAIR) images. To ensure all connectivity measures were generated in dMRI space, intra-patient affine registrations [7] were performed to transform the stroke ROIs from FLAIR to FA co-ordinates. Non-rigid registrations [5] were performed between the FA maps of each stroke patient and each control subject to transform the ROIs into control co-ordinates. Additionally, the brain regions for each control subject were parcellated on the TIW images using the AAL atlas with 116 regions and the information was subsequently transferred into the dMRI space by affine registration. The depression scores for each stroke patient had been analyzed by a neuro-psychiatrist at 12 month chronic stage using the Montgomery-Åsberg depression scale (MADRS) which is an observer-rating scale.

3.2 Detecting Differences in Brain Networks Due to Stroke

Whole brain probabilistic diffusion tractography [13] with 5,000,000 tracks, and with each stroke ROI (used as exclusion mask) were performed respectively for each of the 41 control data sets. Connectivity matrices for each control participant were generated by hit-testing both terminal ends points of every streamline with every cortical and subcortical region (defined by the AAL atlas). For every possible link between brain regions, the number of connecting streamlines passing between each region was computed and their autocorrelation measures were encoded in each of the connectivity matrices. Although care should be taken when using streamline number as a measure of connectivity for group-wise analyses, to reduce any impact regarding quantitation, we employed a paired t-test analysis design of connectivity matrices in this study. The threshold τ for correlation measures of connectivity was set to 0.5 to consider significant connections. The data matrix y comprises of vectorized upper triangular matrices of the connectivity measures of 2×41

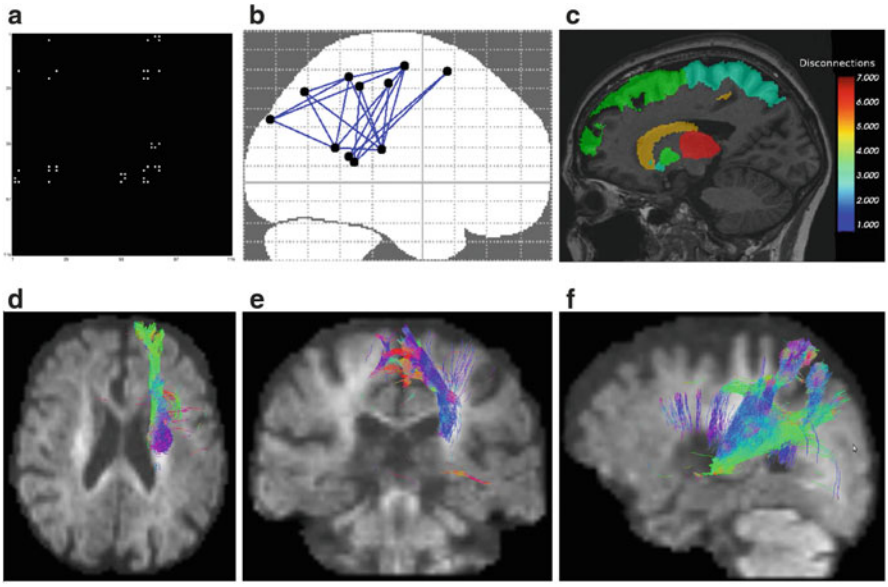

Fig. 3 An example of the network disconnections for a patient with stroke in the thalamus region. (**a**) Disconnectivity matrix showing the pattern of inter-AAL region disconnections; (**b**) network disconnectivity graph; (**c**) affected AAL regions due to stroke in thalamus. The regions are colored according to the number of inter-regional disconnections; (**d**), (**e**) & (**f**) show the probabilistic tracts of the connections between Superior_frontal_gyrus_dorsolateral_R & Thalamus_R, Supplementary_motor_area_R & Thalamus_R, and Superior_parietal_gyrus_R & Lenticular_nucleus_pallidum_R respectively

cases that includes the contrast group. The design matrix X consists of a column of intercepts to compare groups "with" and "without" stroke masks. Therefore for each row of the matrix X, the first regressor models the "with-without" stroke masks comparison and the other regressors model out each subjects mean separately. Pairwise comparison of the two groups (whole-brain connectivity and those with a stroke ROI as exclusion mask) was performed using the NBS permutation testing with 5,000 permutations, t-statistic threshold equal to 1.8 and $p < 0.05$. Figure 3 shows an example set of disconnections for a stroke patient. This patient had severe PSD and the stroke lesion was located in the thalamus region. The disconnections due to stroke were observed in the pallidal region; where both pallidal and thalamic regions are known to be associated with PSD [12]. Table 1 shows the list of significant disconnections with $p < 0.01$ for this patient that labelled according to the AAL regions.

Selecting the optimal values for τ and the t-statistic threshold of NBS were important since these indices influenced the inclusion/exclusion of certain connections in pairwise comparison and consequently the size of the networks that were significantly affected. Lowering τ below 0.5 would have resulted in the inclusion of more connections, however the robustness of these connectivity measures may

Table 1 Neural connections that are disconnected for a patient with severe depression due to stroke in the thalamus region

Region 1	Region 2
Superior_Frontal_gyrus_dorsolateral_R	Supplementary_motor_area_R
Supplementary_motor_area_R	Superior_frontal_gyrus_medial_R
Supplementary_motor_area_R	Paracentral_Lobule_R
Superior_frontal_gyrus_medial_R	Paracentral_Lobule_R
Superior_Frontal_gyrus_dorsolateral_R	Caudate_nucleus_R
Supplementary_motor_area_R	Caudate_nucleus_R
Superior_frontal_gyrus_medial_R	Caudate_nucleus_R
Paracentral_Lobule_R	Caudate_nucleus_R
Postcentral_gyrus_R	Lenticular_nucleus_putamen_R
Superior_parietal_gyrus_R	Lenticular_nucleus_putamen_R
Precentral_gyrus_R	Lenticular_nucleus_pallidum_R
Superior_parietal_gyrus_R	Lenticular_nucleus_pallidum_R
Paracentral_Lobule_R	Lenticular_nucleus_pallidum_R
Precentral_gyrus_R	Thalamus_R
Superior_Frontal_gyrus_dorsolateral_R	Thalamus_R
Supplementary_motor_area_R	Thalamus_R
Postcentral_gyrus_R	Thalamus_R
Paracentral_Lobule_R	Thalamus_R
Caudate_nucleus_R	Thalamus_R

have been impacted by the inclusion of false positive fiber tracts, or less well-defined connections through regions of complex WM architecture. The choice of the t-statistic threshold in our study was chosen empirically with the assumption that significant network disconnectivities due to stroke were associated with PSD. Regression forest was further used to predict the levels of PSD associated with such network disconnections obtained from NBS.

3.3 Depression Prediction with Regression Forest

The network disconnectivity matrices from NBS for each stroke patient were associated with training labels PSD and normal depending on the clinically assessed MADRS scores (MADRS score $>$ 6−PSD, else normal, while the range was between 0–29 for our cohort). The regression forest training/testing were performed in a leave-one-patient-out manner. The forest provided a posterior probability of prediction for a new test data at each tree leaf node that was learned form the trained split functions. The tree parameters were found optimally using a search space of tree-depth (D) in a range of 5–20 and number of trees (N) in a range of 10–300 in steps of 10, to avoid over-fitting and improve generalization while maximizing the correlation between the predicted and the clinical scores. The values N $=$ 190

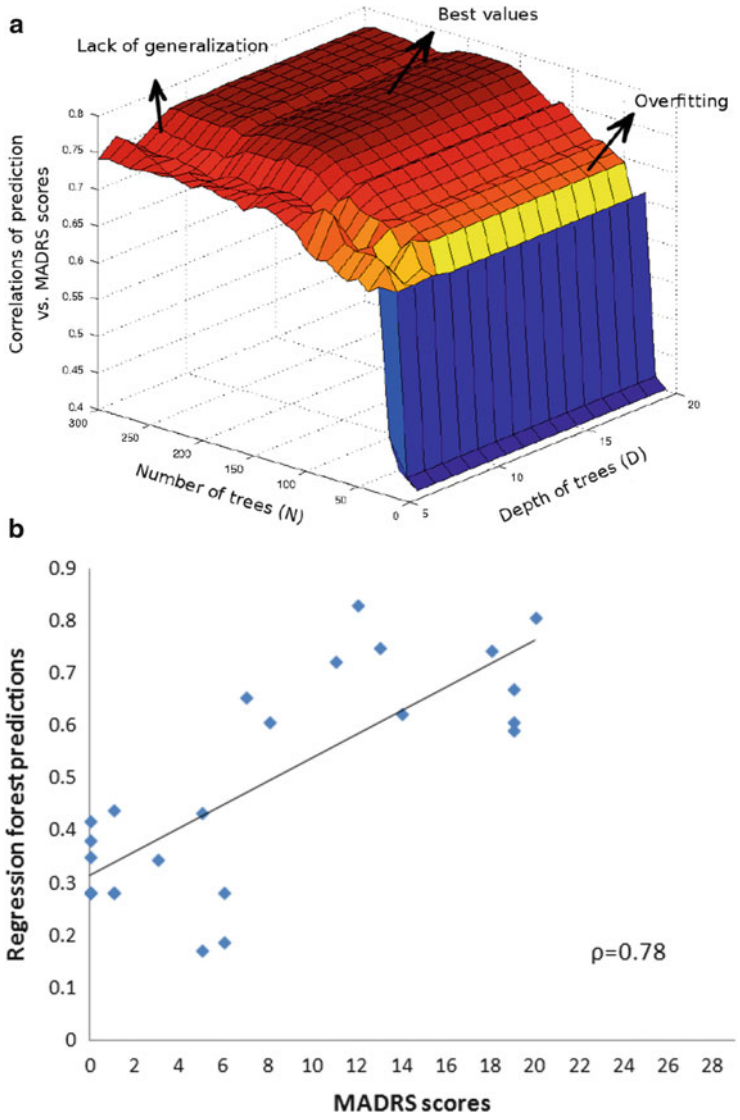

Fig. 4 Prediction accuracies of PSD for the stroke patient cohort. (**a**) Correlation of predicted scores vs. actual clinical scores plotted against varying number of trees and the depth of trees; (**b**) the correlation between predicted and clinical scores are shown for 25 patients with the optimal T and D values of regression forest

and D = 10 were found as the optimal parameters with a Pearson's correlation of $\rho = 0.78$ ($p < 0.00001$) between the predicted and clinical depression scores. Figure 4 shows the surface plot of PSD prediction & MADRS score correlations vs. N and D; and the regression line between the predicted and clinical MADRS scores

Table 2 Depression prediction accuracy with NBS and regression forest (NBS+RF)

Method	TP	TN	FP	FN	ACC (%)
NBS	9	5	9	2	56
NBS+RF	11	14	0	0	100

of PSD with the optimal parameters. It is known that higher values of D causes over-fitting while higher values of N does not necessarily overfit but too many trees may reduce generalization; a similar effect was observed in our study as shown in Fig. 4a [2]. Since the aim of this study is only to predict depression based on the network disconnectivity pattern of individual stroke patients, we do not measure the feature importance returned by regression forest for each stroke patient, where the significant connections were already obtained from NBS at a previous stage.

Although not a defined scope of this study, the binary prediction accuracies of PSD and normal with those obtained from NBS and regression forest are shown in Table 2. The ground truth for PSD and normal cases were obtained from the clinical MADRS scores as defined before. The accuracy for NBS was measured on the basis of the assumption defined before: presence of network difference & PSD—true positive (TP); absence of network difference & normal—true negative (TN); presence of network difference & normal—false positive (FP); and absence of network difference & PSD—true negative (FN). While, for the regression forest (RF), the TP, TN, FP and FN values were calculated after thresholding the prediction probabilities at $>= 0.5$ for PSD and normal otherwise. The accuracy (ACC) was measured as $(TP + TN)/(TP + TN + FP + FN)$. The table signifies that the number of false positives have reduced when regression forest was used in conjunction with NBS rather than NBS alone.

4 Conclusions

We have proposed a novel framework to quantify the level of PSD based on GLM-based permutation testing and regression forest from disconnections of structural connectivity due to stroke. The resulting algorithm involving NBS and regression forest showed high accuracies for the prediction of PSD levels and statistically significant correlations were shown with clinical depression scores. Future directions and works in progress include validating our method in a larger prospective study including a non-stroke patient group with depression and finding discriminative structural connections differentiating between the disease and control group. Our approach has the potential to identify stroke patients at high risk of developing depression, enabling early intervention strategies to improve long term outcome measures.

Acknowledgements We would like to acknowledge the Stroke Imaging Prevention and Treatment (START) program of research which is supported in part by the CSIRO of Australia through the Digital Productivity & Services Flagship cluster, the National Health and Medical Research

Council of Australia, and a Victorian Government Operational Infrastructure Support Grant. In particular, we wish to acknowledge the stroke patients, radiologists and START researchers who contributed to the data collected for this study. We would also like to thank the Brain Research Institute, Australia for providing the diffusion data of the normal controls used in this study. LC is supported by an Australian Research Council Future Fellowship [number FT0992299]. The funding sources had no role in conduct of the study or writing of the report.

References

1. Carson, A.J., et al.: Depression after stroke and lesion location: a systematic review. Lancet **356**, 122–126 (2000)
2. Criminisi, A., et al.: Decision forests for classification, regression, density estimation, manifold learning and semi-supervised learning. Technical Report, TR-2011-114, Microsoft Research Ltd., Cambridge (2011)
3. Hackett, M.L., et al.: Frequency of depression after stroke: a systematic review of observational studies. Stroke **36**(6), 1330–1340 (2005)
4. Kuceyeski, A., et al.: Linking white matter integrity loss to associated cortical regions using structural connectivity information in Alzheimer's disease and fronto-temporal dementia: the loss in connectivity (LoCo) score. NeuroImage **61**, 1311–1323 (2012)
5. Modat, M., et al.: Fast free-form deformation using graphics processing units. Comput. Methods Prog. Biomed. **98**(3), 278–284 (2010)
6. Narushima, K., et al.: Does cognitive recovery after treatment of poststroke depression last? a 2 year follow-up of cognitive function associated with poststroke depression. Am. J. Psychiatry **160**(6), 1157–1162 (2003)
7. Ourselin, S., et al.: Robust registration of multi-modal images: towards real-time clinical applications. In: MICCAI'02, pp. 140–147. Springer, Tokyo (2002)
8. Pannek, K., et al.: Homor: higher order model outlier rejection for high b-value MR diffusion data. NeuroImage **63**, 835–842 (2012)
9. Pannek, K., et al.: Diffusion MRI of the neonate brain: acquisition, processing and analysis technique. Pediatr. Radiol. **42**(10), 1169–1182 (2012)
10. Pohjasvaara, T., et al.: Depression is an independent predictor of poor long-term functional outcome poststroke. Eur. J. Neurol. **8**(4), 315–319 (2001)
11. Salter, K., et al.: The assessment of poststroke depression. Stroke Rehabil. **14**(3), 1–24 (2007)
12. Terroni, L., et al.: Stroke lesion in cortical neural circuits and post-stroke incidence of major depressive episode: a 4 month prospective study. World J. Biol. Psychiatry **12** 539–548, (2011)
13. Tournier, J.D., et al.: Robust determination of the fibre orientation distribution in diffusion MRI: non-negativity constrained super-resolved spherical deconvolution. NeuroImage **35**(4), 1459–1472 (2007)
14. Vataja, R., et al.: Poststroke depression and lesion location revisited. J. Neuropsychiatr. Clin. Neurosci. **16**(2), 156–162 (2004)
15. Zalesky, A., et al.: Network-based statistic: identifying differences in brain networks. NeuroImage **53**, 1197–1207 (2010)

Part III
Tractography

Fiber Bundle Segmentation Using Spectral Embedding and Supervised Learning

Dorothée Vercruysse, Daan Christiaens, Frederik Maes, Stefan Sunaert, and Paul Suetens

Abstract Diffusion-weighted imaging and tractography offer a unique approach to probe the microarchitecture of brain tissue noninvasively. Whole brain tractography, however, produces an unstructured set of fiber trajectories, whereas clinical applications often demand targeted tracking of specific bundles. This work presents a novel, hybrid approach to fiber bundle segmentation, using spectral embedding and supervised learning. Training data of 20 healthy subjects is labeled with a parcellation-based method, and used to train support vector machine and random forest classifiers. Cross-validation was used to avoid overfitting. Results on testing data of five independent subjects show a clear improvement over unsupervised methods. Moreover, estimating the label probabilities allows to reduce the effect of outliers.

1 Introduction

Diffusion-weighted magnetic resonance imaging (DWI) [1] is a unique approach to probe the microarchitecture of brain tissue noninvasively. Based on measurements of the local diffusion anisotropy, and assuming that diffusion is larger along the direction of neuronal fibers [3], numerous methods exist to estimate the local fiber orientation distribution function (fODF) [7, 17]. Tractography methods aim to reconstruct white matter (WM) pathways, usually by following the estimated fiber directions. Two distinct groups of stepwise tractography methods exist: deterministic methods, which select the most likely track direction in every step [2, 5, 12],

D. Vercruysse • D. Christiaens (✉) • F. Maes • P. Suetens
Department of Electrical Engineering, Medical Image Computing, KU Leuven, Leuven, Belgium

Medical Imaging Research Center, University Hospitals Leuven, Leuven, Belgium

iMinds, Medical IT Department, Belgium
e-mail: daan.christiaens@esat.kuleuven.be

S. Sunaert
Department of Imaging and Pathology, Translational MRI, KU Leuven, Leuven, Belgium

Medical Imaging Research Center, University Hospitals Leuven, Leuven, Belgium

L. O'Donnell et al. (eds.), *Computational Diffusion MRI*, Mathematics and Visualization, DOI 10.1007/978-3-319-11182-7_10

and probabilistic methods, which draw random samples from the fODF or a similar distribution [15, 18].

Whole brain tractography, however, produces an unstructured set of fiber trajectories, whereas clinical applications often demand targeted tracking of specific bundles. Generally, this requires manual delineation of regions-of-interest (ROI), which is tedious and subjective work. Therefore, a number of automated bundle segmentation methods have been presented, which can be categorized into fiber clustering methods and parcellation-based methods [14]. Fiber clustering methods aim to group neighbouring or similar tracks into clusters, which can then be assigned anatomically meaningful labels from an atlas [10, 11, 13]. Parcellation-based methods, on the other hand, employ carefully defined ROIs in atlas space, e.g., a cortical parcellation, to segment and label predefined WM bundles [21]. While this allows for highly specific labeling, tracts that do not intersect the ROIs are excluded from the analysis and may hence result in a low sensitivity.

This work presents a novel, hybrid approach to fiber bundle segmentation, using spectral embedding and supervised learning. The white matter query language (WMQL) [21], a parcellation-based method, is used to generate *ground-truth* labels to train the classifiers. The sensitivity and specificity of the proposed method is calculated using cross-validation, and results on unlabeled, whole brain tractography data are presented.

2 Methods and Materials

The proposed method is based on spectral embedding, a dimensionality reduction technique that allows to represent each track as a vector in the embedding space such that nearby tracks (provided some distance metric), are mapped onto nearby embedding vectors. O'Donnell et al. [13] were the first to use spectral embedding for fiber clustering, using the *unsupervised* k-means algorithm in the embedding space. Instead, we propose to use *supervised* learning, specifically support vector machines (SVM) and random forests, on the embedding vectors. The training data, required for this approach, is provided by the WMQL.

2.1 Spectral Embedding

The aim of spectral embedding is to find a meaningful representation of the input data in a lower dimensional space. When used for clustering, this representation should preferably group data points that score high for a certain similarity measure. As such, similarity relationships are represented spatially, i.e., every fiber is represented as a point and nearby points generally correspond to similar trajectories, which simplifies the clustering [13].

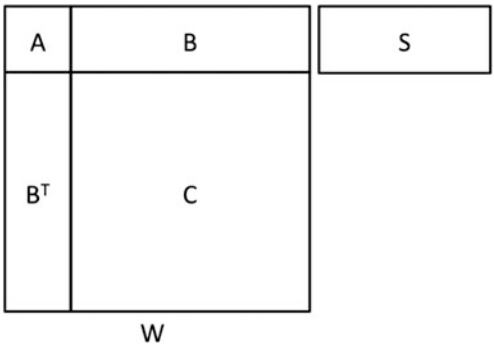

Fig. 1 Block structure of the normalized affinity matrix $\mathcal{W}$, used in the Nyström method. The regions in submatrices **A** and **B** denote the individual subjects. Submatrix **C** represents the part that does not need to be calculated when using the Nyström method. For the automatic segmentation of a new subject, matrix **S** contains the affinity values between the new tracks and the subset of matrix **A** (reproduced from [13])

Assuming that fibers following a similar trajectory belong to the same anatomical bundle, a pairwise fiber affinity w_{ij} between tracks i and j is calculated from the symmetrized mean closest point (MCP) distance $d_{ij} = d_{ji} = (\text{MCP}_{ij} + \text{MCP}_{ji})/2$ via a Gaussian kernel, i.e., $w_{ij} = e^{-\frac{d_{ij}^2}{\sigma^2}}$. These affinities are computed between all pairs of fibers, resulting in a symmetric affinity matrix **W**. Based on the Normalized Cuts algorithm by Shi and Malik [16], the embedding vectors are then computed using the eigenvectors **U** of the normalized affinity matrix $\mathcal{W} = \mathbf{D}^{-\frac{1}{2}}\,\mathbf{W}\,\mathbf{D}^{-\frac{1}{2}}$, where **D** is a diagonal matrix containing the row sums of **W**. The number of eigenvectors determines the dimension of the embedding space [13], and is fixed to $e = 25$ in our experiments.

In practice, the entire affinity matrix is too large to compute. Therefore, as described in Fowlkes et al. [8], its eigenvectors are approximated using the Nyström method [8]. Instead of calculating all pairwise fiber affinities, a random subset of tracks is chosen (containing an equal amount of fiber trajectories from each subject) and only the affinities from all subjects to this subset are computed. The layout of the entire affinity matrix is shown in Fig. 1. Submatrix **A** contains the pairwise affinities between the fibers of the subset and **B** those of the rest of the fibers to the subset. The largest submatrix **C** does not have to be calculated, reducing the computation time considerably.

Note that in order to make a multi-subject atlas, spectral clustering needs to be performed in all subjects together. Therefore, a registration step is required to transform the tracks to a common space, e.g., MNI space, using subject dependent deformation fields. As such, the fibers of all subjects are treated as if they originate from one brain for training, which results in one embedding space.

2.2 Supervised Classification

The proposition made is to cluster the embedding vectors into anatomically relevant bundles using supervised clustering instead of k-means. The training of the classifiers is performed on labeled WMQL output tracks. The WMQL is a parcellation based segmentation method developed by Wassermann et al. [21] which uses queries based on (1) *anatomical terms* that state if a fiber track traverses or ends in a certain anatomical region of the brain, (2) *relative position terms* that state if a track lies, for instance, lateral or frontal of a certain anatomical structure such as the amygdala and (3) *logical operations* that are for example conjunctions, disjunctions or exclusions of the previous two types of terms.

The supervised learning methods used in this study are support vector machines (SVM) and random forests. The basic principle of SVMs is to find a unique hyperplane by maximizing the margin between two classes [20]. Two different kernels are tested, linear SVMs and Gaussian radial basis function (RBF) kernels. The advantage of SVMs is that they are effective in high dimensional spaces. Furthermore, they employ only a subset of training points, the support vectors, in the decision function, which makes them memory efficient [6]. A drawback, however, is the slow training for large data sets. Random forests on the other hand, are classifiers developed by Breiman [4] which use the ensemble (forest) of decision trees, generated from random input vectors and using only a random subset of features for splitting nodes. Since the number of randomly selected features is much smaller than the number of input vectors, random forests learn fast on large datasets.

2.3 Automatic Segmentation

By training the classifiers, a white matter atlas is created which can be used for the automatic segmentation of fiber bundles from novel subjects. First, the new tracks must be registered or transformed to the atlas (MNI) space. Secondly, the affinity between the tracks of the new subject and the atlas is calculated. As illustrated in Fig. 1, a matrix $\mathbf{S}$ is calculated that contains the affinity values between the new tracks and the subset of tracks used for calculating $\mathbf{A}$. Note that $\mathbf{S}$ also has to be normalized [13]. Next, each new fiber will be embedded in the same embedding space as created for the original clustering. A detailed description of the eigenvector estimation of the novel subject is given by O'Donnell et al. [13]. The final step is the automatic segmentation itself, i.e., the cluster information from the atlas is applied to the new embedding vectors. In order to do this, the novel embedding vectors are used as input for the trained classifiers.

2.4 Materials

Data of 25 healthy subjects were provided by the Human Connectome Project (HCP), WU-Minn consortium [19]. DWI data consists of 3×90 gradient directions at b-values 1,000, 2,000, and 3,000 s/mm^2 and 18 non-diffusion weighted images ($b = 0$), at an isotropic voxel size of 1.25 mm, and was corrected for motion and EPI distortions as described in [9]. The fODF, and subsequent deterministic and probabilistic fiber tracks (50,000 each), were reconstructed with MRtrix [17] using default parameters. The tracks were segmented into 44 WM bundles using Wasserman's WMQL and the WM parcellation available in the HCP data set, resulting in approximately 4,500 labeled tracks for each subject. All tracks are warped to MNI space using the deformation fields provided by the HCP. The multisubject deterministic and probabilistic training sets to create the atlases consist of the labeled tracks of 20 subjects, the other five form the test set. For affinity calculation σ is set to 60 mm. The submatrix $\mathbf{A}$ contains a random sample of 4,000 tracks.

3 Validation

The proposed method was applied on the 20 training subjects, constructing the embedding space and training the SVM and random forest classifiers. To avoid overfitting, fivefold cross-validation is used for the training. The true positive rate, calculated on the test set of five novel subjects and assuming their WMQL labels as ground truth, is given in Table 1. For comparison, k-means is included, using 200 clusters (identical to [13]), and assigning labels based on majority voting.

The scores of the supervised classifiers are all in the same range of around 95 %, with a maximum of 95.78 % for the SVM with RBF-kernel on deterministic tracks. The true positive rate (TPR) for k-means, on the other hand, is below 85 %, hence the proposed method achieves over 10 % improvement.

To evaluate the performance of the models on finding each individual bundle, scores are determined following a *one-versus-the-rest* principle. The performance plots in Fig. 2 give an overview of the results on deterministic tracks. Results are preferably expected in the upper left quadrant of the plot, where the TPR (sensitivity) is high and the false positive rate (FPR, (1 − specificity)) is low.

Table 1 Validation scores (true positive rate, TPR)

	TPR (deterministic) (%)	TPR (probabilistic) (%)
K-means (K=200)	83.41	80.84
SVM, kernel=linear	94.90	93.75
SVM, kernel=RBF	95.78	95.63
Random forests	95.07	94.77

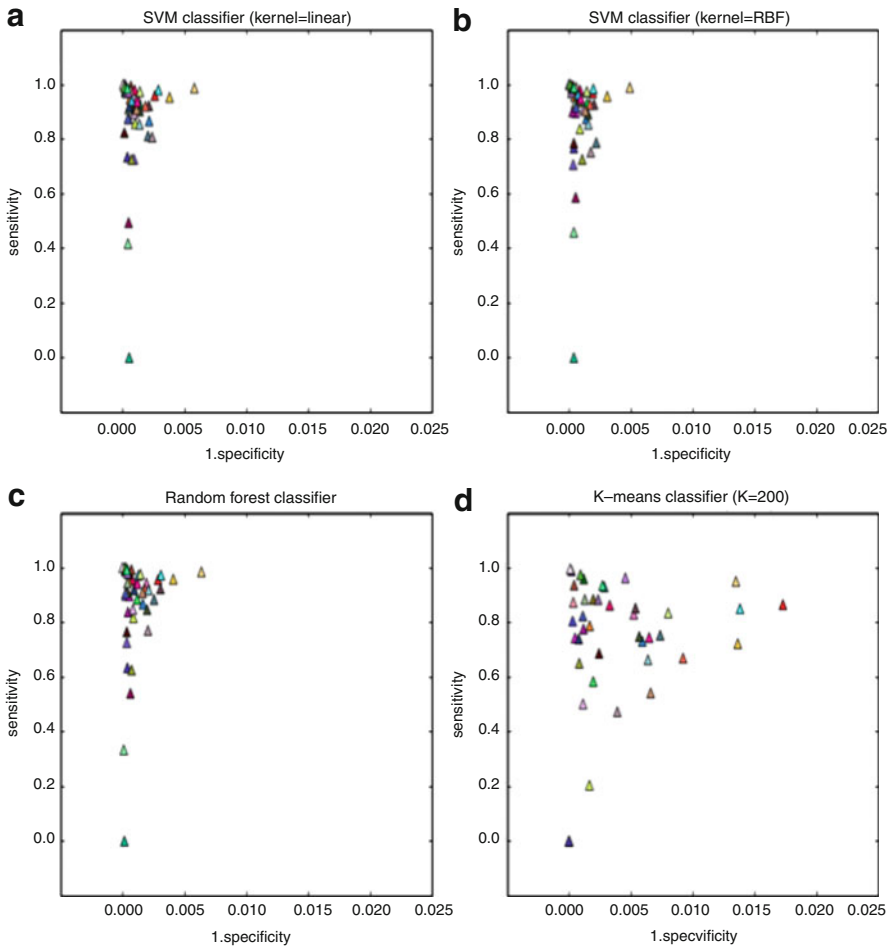

Fig. 2 Performance plots of the different classifiers for all 44 bundles (one-versus-the-rest) on deterministic WMQL output tracks, representing the true positive rate (sensitivity) versus the false positive rate (1 − specificity). The *marker colors* represent the bundle number. Note that the x-axis ranges from 0 to 0.025 to give a more detailed view

Since the negative class will always be very large (43 bundles, versus 1 bundle in the positive class), true negatives (TN) will be very high in comparison to false positives (FP). Therefore, the specificity will be high and the FPR low. Note that the x-axis in the plots only ranges from 0 till 0.025 instead of 1, to give a more detailed view. The sensitivity is spread over a wider range. The green bundle that scores very low with every supervised classifier (Fig. 2a–c), represents the right superior occipitofrontal fasciculus, a bundle that contains very little to no tracks in most subjects. This explains the bad training performance. The plot for the k-

means classifier (Fig. 2d) shows an overall larger spread, as was expected from the lower total clustering performance.

4 Results

The unsupervised and supervised classifiers that were trained as discussed above are now evaluated on the unlabeled whole brain track sets (deterministic and probabilistic, each containing 50,000 tracks) of the test subjects. The tracks are warped to atlas space and projected onto the embedding space of the training data. Afterwards, their labels are estimated by using the resulting embedding vectors as input for the trained classifiers. In case of the k-means classifier, each track receives the label of the closest centroid in embedding space.

Since the whole track set is used as input, including many spurious tracks (i.e., false positives) and interrupted tracks that were not labeled by the WMQL, it is no longer possible to use the labels generated by the WMQL as ground truth to calculate, e.g., the TPR. Therefore, the results can only be analyzed visually by comparing the resulting segmentation with the WMQL output bundles, and with basic neuroanatomical knowledge.

First, the results are studied without considering the label probability, i.e., using maximum-likelihood classification. This is shown in Figs. 3 and 4 for deterministic and probabilistic tractography respectively, in a single subject. The top row shows the segmentation of the corticospinal track (CST) in 1 subject. Notice the misclassified cerebellum (which is not defined in the WMQL queries) tracks in the k-means and linear SVM segmentation. Additionally, all classifiers label sagittal dispersions in the corona radiata as CST. The segmentation of the cingulum bundle (CB) contains misclassified tracks of the fornix (which is not labeled in the WMQL) and dispersing tracks from the corpus callosum.

In Fig. 5, a threshold is put on the labeling probabilities of the SVM with RBF-kernel and the random forest classifier, in order to try to ameliorate the results by excluding outlier tracks. For the CST, increasing the threshold results in the exclusion of the corona radiata tracks, while the cut off tracks of the left CST bundle are still correctly labeled, contrary to the WMQL segmentation. The CB segmentation contains a lot less dispersions into the CC with a high threshold and also the tracks from the fornix are eliminated.

5 Discussion

The high scores for validation on labeled WMQL output tracks show the potential of the proposed method for fiber bundle segmentation. The true positive rates (TPR) for the supervised classifiers are considerably higher than that obtained by the k-means classifier. The performance evaluation across individual bundles allows to

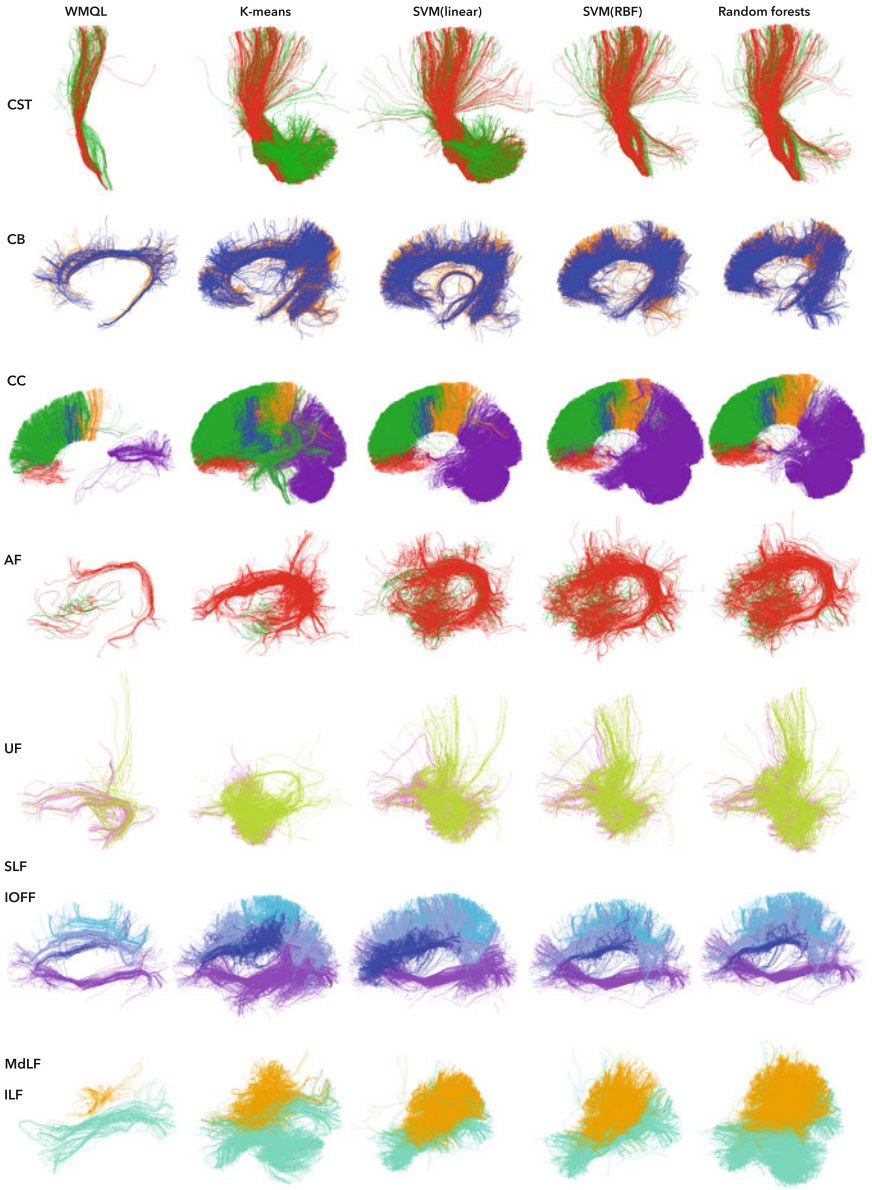

Fig. 3 Segmentation results on deterministic, whole brain tractography data, using the white matter query language (WMQL), k-means clustering, support vector classifiers (SVM) with linear and RBF-kernels, and random forests, shown for the corticospinal track (CST), cingulum bundle (CB), corpus callosum (CC), actuate fasciculus (AF), unicate fasciculus (UF), superior, middle, and inferior longitudinal fasciculus (SLF, MdLF, ILF), and inferior occipitofrontal fasciculus (IOFF)

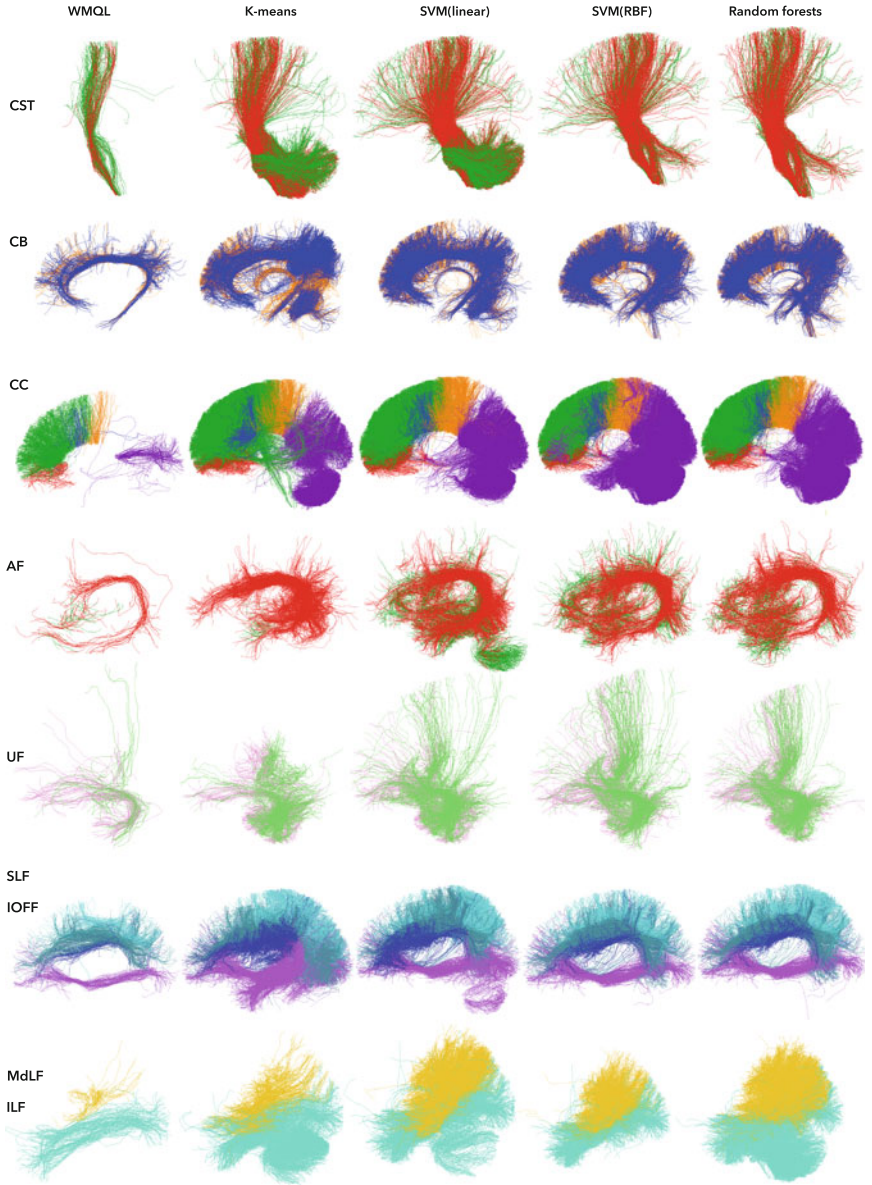

Fig. 4 Segmentation results on probabilistic, whole brain tractography data, using the white matter query language (WMQL), k-means clustering, support vector classifiers (SVM) with linear and RBF-kernels, and random forests, shown for the corticospinal track (CST), cingulum bundle (CB), corpus callosum (CC), actuate fasciculus (AF), unicate fasciculus (UF), superior, middle, and inferior longitudinal fasciculus (SLF, MdLF, ILF), and inferior occipitofrontal fasciculus (IOFF)

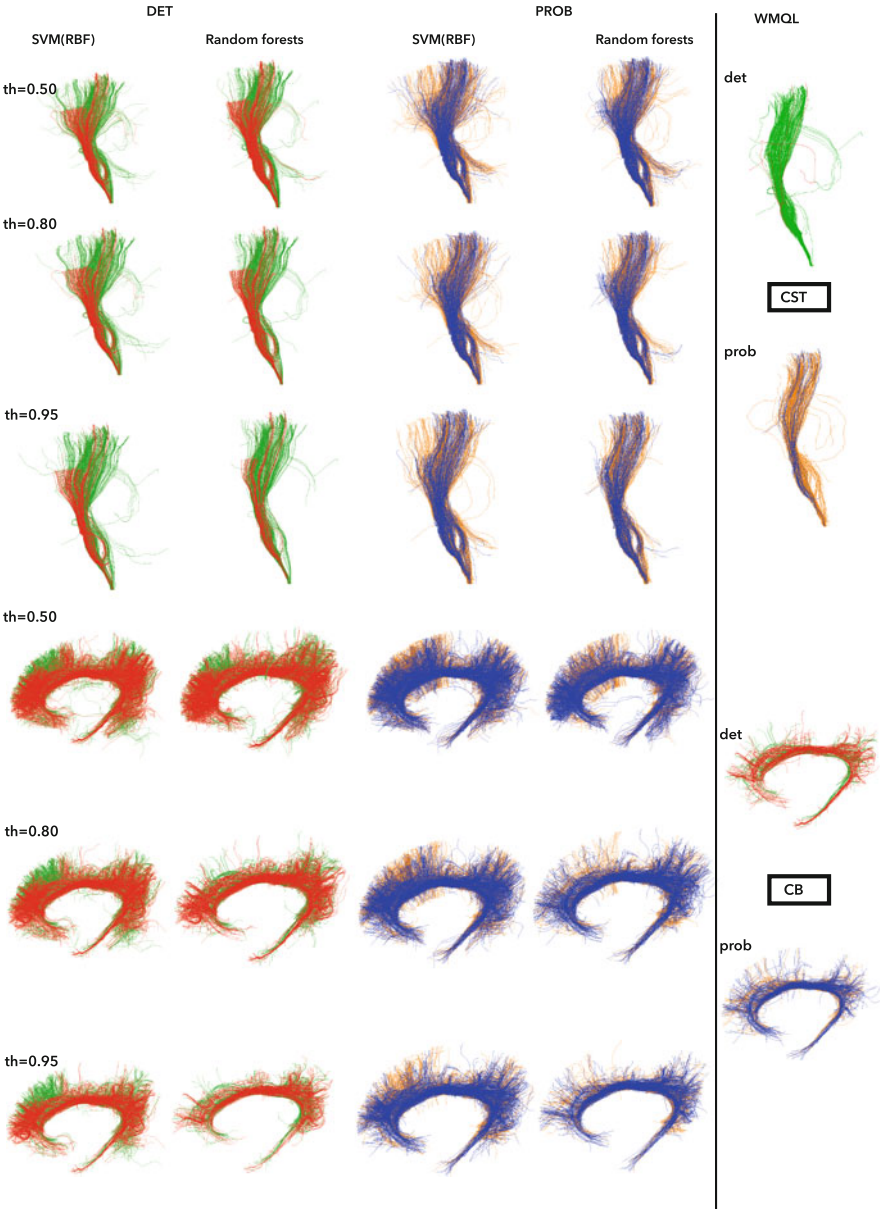

Fig. 5 Effect of different thresholds on the labeling probabilities for support vector machine (SVM) and random forest-based segmentation of the corticospinal track (CST, *top*) and the cingulum bundle (CB, *bottom*). The segmentation results of the white matter query language (WMQL) are shown for reference on the *right*

conclude that the results are in the same range for most bundles, except for three of them which contain little to no tracks in the training set. This could be solved by re-evaluating the WMQL queries for these specific bundles.

As expected, the results on complete whole brain tractography data sets, which include all outlier tracks (i.e., false positives), are not as good as those on validation data (WMQL output). This can be explained by the fact that the WMQL excludes most outliers due to the strict requirements of the queries, resulting in a cleaner segmentation. As demonstrated, setting a threshold on the labeling probabilities creates a *virtual* outlier class that can be used to eliminate such tracks. Since setting the threshold too high can lead to sparse bundles, a method for optimal threshold selection still has to be developed.

Since there is no real ground truth available for white matter structures, it would be useful to let a neuroanatomy expert revise the segmentations obtained by the atlas. Expert knowledge could also be used to extend the WMQL with known bundles such as the fornix which is not yet included in the queries.

6 Conclusion

This work introduced a new method for fiber bundle segmentation, based on spectral embedding and supervised learning. The proposed method outperforms existing unsupervised methods and is more robust to outlier tracks when the label probability is taken into account. Future work may extend the atlas to smaller, currently undefined fiber bundles.

Acknowledgements Data were provided by the Human Connectome Project, WU-Minn Consortium (Principal Investigators: David Van Essen and Kamil Ugurbil; 1U54MH091657) funded by the 16 NIH Institutes and Centers that support the NIH Blueprint for Neuroscience Research; and by the McDonnell Center for Systems Neuroscience at Washington University.

References

1. Basser, P.J., Mattiello, J., LeBihan, D.: Mr diffusion tensor spectroscopy and imaging. Biophys. J. **66**(1), 259–267 (1994)
2. Basser, P.J., Pajevic, S., Pierpaoli, C., Duda, J., Aldroubi, A.: In vivo fiber tractography using dt-mri data. Magn. Reson. Med. **44**(4), 625–632 (2000)
3. Beaulieu, C.: The basis of anisotropic water diffusion in the nervous system–a technical review. NMR Biomed. **15**(7–8), 435–455 (2002)
4. Breiman, L.: Random forests. Mach. Learn. **45**(1), 5–32 (2001)
5. Conturo, T.E., Lori, N.F., Cull, T.S., Akbudak, E., Snyder, A.Z., Shimony, J.S., McKinstry, R.C., Burton, H., Raichle, M.E.: Tracking neuronal fiber pathways in the living human brain. Proc. Natl. Acad. Sci. **96**(18), 10422–10427 (1999)
6. Cristianini, N., Shawe-Taylor, J.: An Introduction to Support Vector Machines and Other Kernel-Based Learning Methods. Cambridge University Press, Cambridge (2000)

7. Descoteaux, M., Deriche, R., Knosche, T., Anwander, A.: Deterministic and probabilistic tractography based on complex fibre orientation distributions. IEEE Trans. Med. Imaging **28**(2), 269–286 (2009)
8. Fowlkes, C., Belongie, S., Chung, F., Malik, J.: Spectral grouping using the nystrom method. IEEE Trans. Pattern Anal. Mach. Intell. **26**(2), 214–225 (2004)
9. Glasser, M.F., Sotiropoulos, S.N., Wilson, J.A., Coalson, T.S., Fischl, B., Andersson, J.L., Xu, J., Jbabdi, S., Webster, M., Polimeni, J.R., Van Essen, D.C., Jenkinson, M.: The minimal preprocessing pipelines for the human connectome project. NeuroImage **80**, 105–124 (2013)
10. Guevara, P., Duclap, D., Poupon, C., Marrakchi-Kacem, L., Fillard, P., Le Bihan, D., Leboyer, M., Houenou, J., Mangin, J.F.: Automatic fiber bundle segmentation in massive tractography datasets using a multi-subject bundle atlas. Neuroimage **61**(4), 1083–1099 (2012)
11. Maddah, M., Grimson, W.E.L., Warfield, S.K., Wells, W.M.: A unified framework for clustering and quantitative analysis of white matter fiber tracts. Med. Image Anal. **12**(2), 191–202 (2008)
12. Mori, S., van Zijl, P.: Fiber tracking: principles and strategies—a technical review. NMR Biomed. **15**(7–8), 468–480 (2002)
13. O'Donnell, L.J., Westin, C.F.: Automatic tractography segmentation using a high-dimensional white matter atlas. IEEE Trans. Med. Imaging **26**(11), 1562–1575 (2007)
14. O'Donnell, L.J., Golby, A.J., Westin, C.F.: Fiber clustering versus the parcellation-based connectome. NeuroImage **80**, 283–289 (2013)
15. Parker, G.J.: Probabilistic fiber tracking. In: Jones, D.K. (ed.) Diffusion MRI: Theory, Methods, and Applications, pp. 396–408. Oxford University Press, Oxford (2010)
16. Shi, J., Malik, J.: Normalized cuts and image segmentation. IEEE Trans. Pattern Anal. Mach. Intell. **22**(8), 888–905 (2000)
17. Tournier, J., Calamante, F., Connelly, A.: Robust determination of the fibre orientation distribution in diffusion MRI: non-negativity constrained super-resolved spherical deconvolution. NeuroImage **35**(4), 1459–1472 (2007)
18. Tournier, J.D., Mori, S., Leemans, A.: Diffusion tensor imaging and beyond. Magn. Reson. Med. **65**(6), 1532–1556 (2011)
19. Van Essen, D.C., Smith, S.M., Barch, D.M., Behrens, T.E., Yacoub, E., Ugurbil, K.: The WU-Minn human connectome project: an overview. NeuroImage **80**, 62–79 (2013)
20. Vapnik, V.: The Nature of Statistical Learning Theory. Springer, New York (2000)
21. Wassermann, D., Makris, N., Rathi, Y., Shenton, M., Kikinis, R., Kubicki, M., Westin, C.F.: On describing human white matter anatomy: the white matter query language. In: Mori, K., Sakuma, I., Sato, Y., Barillot, C., Navab, N. (eds.) Medical Image Computing and Computer-Assisted Intervention–MICCAI 2013. Lecture Notes in Computer Science, vol. 8149, pp. 647–654. Springer, Berlin (2013)

Atlas-Guided Global Tractography: Imposing a Prior on the Local Track Orientation

Daan Christiaens, Marco Reisert, Thijs Dhollander, Frederik Maes, Stefan Sunaert, and Paul Suetens

Abstract Since its introduction over a decade ago, diffusion tractography has come a long way from local, deterministic methods, over probabilistic approaches, towards global tractography. Yet, the development of tractography methods has been largely focused on single subject data, and very little on cross-population analysis and inter-subject variability. In this work, we extend global tractography with a prior on the local track orientation distribution (TOD), derived from 20 normal subjects. The proposed method is evaluated in five independent subjects. Results show that adding such prior regularizes the reconstructed track distribution, although registration errors can induce local artefacts. We conclude that atlas-guided global tractography can improve the fibre reconstruction and ultimately detect and quantify inter-subject differences in tractography.

1 Introduction

Since its introduction over a decade ago, diffusion tractography has come a long way from local, deterministic methods, over probabilistic approaches, towards global tractography [10, 12], steadily gaining importance for in vivo neuroanatomy studies and neurosurgical planning. Deterministic streamline approaches [14] are highly sensitive to local estimation errors, leading to low accuracy, sensitivity and specificity of the reconstructed tracks in the presence of noise, modelling errors,

D. Christiaens (✉) • T. Dhollander • F. Maes • P. Suetens
Department of Electrical Engineering, Medical Image Computing, KU Leuven, Leuven, Belgium,

Medical Imaging Research Center, University Hospitals Leuven, Leuven, Belgium,

iMinds, Medical IT Department, Belgium
e-mail: daan.christiaens@esat.kuleuven.be

M. Reisert
Department of Radiology, Medical Physics, University of Freiburg Medical Center, Freiburg Germany

S. Sunaert
Department of Imaging & Pathology, Translational MRI, KU Leuven, Leuven, Belgium,

Medical Imaging Research Center, University Hospitals Leuven, Leuven, Belgium

L. O'Donnell et al. (eds.), *Computational Diffusion MRI*, Mathematics and Visualization, DOI 10.1007/978-3-319-11182-7_11

and partial volume effects [10, 16]. Probabilistic fibre tracking can accommodate for this uncertainty [16], but won't improve the quality of each individual streamline. Moreover, streamline tractography is inherently difficult to quantify due to its dependence on the seeding distribution. Global fibre tracking methods [6, 11, 13, 18] aim to reconstruct the ensemble of fibres that best explain the measured DWI data [12]. By addressing the problem at a global scale, these methods can be less sensitive to local estimation errors and maintain a quantifiable correspondence to the data.

Yet, the development of tractography methods has been largely focused on single subject data, and very little on cross-population analysis and inter-subject variability. Indeed, while atlases are at the core of state-of-the-art segmentation and label fusion methods [1], their use in diffusion tractography is mostly limited to automated and consistent delineation of regions of interest for seeding, inclusion, and exclusion in streamline tractography, and for clustering and labelling of the resulting fibre tracks [15]. In regard to streamline tractography, Cook et al. [3] have demonstrated the use of a diffusion tensor atlas as a prior distribution for the fibre orientation. Yap et al. [22] have similarly used a distribution of the maxima of the fibre orientation distributions (FOD) in different subjects, as a means of improving tractography of the average atlas. Finally, Yendiki et al. [23] imposed a shape prior on specific pathways connecting segmented end regions.

In this work, we extend the global tractography framework of Reisert et al. [18] with a prior on the local track orientation distribution (TOD) [5]. This prior is derived from 20 normal subjects and represented as an atlas in the basis of spherical harmonics (SH), that captures both the expected fibre directions and their support by the local neighbourhood. We expect this atlas to guide the global tractography towards a more targeted reconstruction, due to its higher angular contrast. In contrast to the current state of the art, our method finds the globally optimal tractogram without restrictions to specific pathways.

2 Methods

2.1 Global Tractography in the SH Basis

2.1.1 Generative Model

The set of tracks we aim to reconstruct, i.e., the fibre model $\mathscr{M}$, is represented as a set of segments $\{(\mathbf{r}_i, \mathbf{n}_i)\}$, with position $\mathbf{r}_i$, direction $\mathbf{n}_i$, and fixed length 2ℓ, and a set of connections between their endpoints. Ultimately, we wish to maximize the posterior probability of $\mathscr{M}$ given the data D, which, according to Bayes' rule and assuming an exponential model, equals

$$P(\mathscr{M}|D) \propto P(D|\mathscr{M})\, P(\mathscr{M}) = e^{-E_{\text{ext}}(\mathscr{M},D)/T}\, e^{-E_{\text{int}}(\mathscr{M})/T}\,. \tag{1}$$

As such, the problem becomes finding the global minimum of $E(\mathscr{M}) = E_{\text{int}}(\mathscr{M}) + E_{\text{ext}}(\mathscr{M}, D)$. The internal energy E_{int} promotes connectivity and smoothness of the reconstructed tracks, and is defined identically as in [18]. The external energy E_{ext} measures the similarity to the data, defined as the mean squared error $\lambda_{\text{ext}} \| D(b, \mathbf{g}) - D'(b, \mathbf{g}) \|^2$ between the measured data D and the predicted data D' given the fibre model, for all b-values and gradient directions $\mathbf{g}$.

Given the model $\mathscr{M}$, we simulate the data D' by assuming that each segment has an equal contribution to the predicted signal D' in the form of a fibre response kernel $K_b(\theta)$, as used in spherical deconvolution techniques [4, 19]. $K_b(\theta)$ is a spherical function depending only on the elevation, that models the expected diffusion signal for a single fibre direction along the z-axis. The data is then simulated by rotating this kernel along all segments, and integrating over all segments in a voxel $V(\mathbf{r})$, i.e., $D'_b(\mathbf{u}) = \sum_{i \in V(\mathbf{r})} K_b(\arccos(\mathbf{u} \cdot \mathbf{n}_i))$. Cast into the real, symmetric SH basis [4], this becomes $D'_b(\mathbf{u}) = \sum_i K_b * \delta_{\mathbf{n}_i}(\mathbf{u}) = K_b * \Psi(\mathbf{u})$ where $\delta_{\mathbf{n}_i}(\mathbf{u})$ is the SH Dirac delta function along direction $\mathbf{n}_i$, $*$ is the spherical convolution operator, and $\Psi(\mathbf{u}) = \sum_i \delta_{\mathbf{n}_i}(\mathbf{u})$ models the orientation distribution of the segments in that voxel. In addition, we introduce one or more isotropic kernels $c(b)$ that account for partial volume contamination of other tissue types and depend only on the b-value. In summary, the predicted DWI signal in every voxel equals

$$D'(b, \mathbf{g}) = K_b * \Psi(\mathbf{g}) + \sum_j f_j \, c_j(b) \, , \tag{2}$$

where f_j are the respective isotropic fractions, estimated in each voxel as the least-squares solution of the external energy, given the current segment configuration.

The intermediary representation $\Psi(\mathbf{u})$ of the fibre model is related to the recently introduced TOD [5] by convolution with an apodized point spread function (aPSF), defined as the sharpest non-negative function that can be represented in the SH basis of order $\ell_{\max}$. We denote the resulting TOD as $\tilde{\Psi}(\mathbf{u}) = \text{aPSF} * \Psi(\mathbf{u})$, a non-negative distribution that is more robust to SH aliasing effects. Note that for global tractography, the TOD closely resembles the FOD obtained from constrained spherical deconvolution [19], as the reconstructed track distribution is optimized for maximal correspondence to the data.

2.1.2 Optimization

The optimization of (1) relies on the Metropolis-Hastings (MH) algorithm, a Markov Chain Monte Carlo technique, to obtain random samples from the posterior distribution [9]. As in simulated annealing methods, the temperature T is gradually cooled down to increase the likelihood of sampling from the maximum of $P(\mathscr{M}|D)$ (or the minimum of $E(\mathscr{M})$). At each iteration, the MH sampler proposes a new state $\mathscr{M}'$, obtained as a random perturbation of the current state $\mathscr{M}$, and evaluates the Green's ratio

$$R = \min\left(1, \frac{e^{-E(\mathscr{M}')/T}}{e^{-E(\mathscr{M})/T}} \frac{p^{\text{prop}}(\mathscr{M}|\mathscr{M}')}{p^{\text{prop}}(\mathscr{M}'|\mathscr{M})}\right) \, , \tag{3}$$

where $p^{\text{prop}}(y|x)$ is the transition probability from state x to state y. The proposed state $\mathscr{M}'$ is then accepted with probability R, or discarded otherwise. Transition proposals include birth/death of segments, random and optimal shifts, and creation/deletion of connections [11, 18].

2.2 Atlas Prior

Given an atlas A of the local track orientation, the posterior probability of the fibre model equals $P(\mathscr{M}|D, A) \propto P(D|\mathscr{M}, A)\, P(\mathscr{M}|A) \propto P(D|\mathscr{M})\, P(A|\mathscr{M})\, P(\mathscr{M})$, using Bayes' rule and assuming the subject data is independent of the atlas. Assuming the usual exponential model, the new energy function becomes

$$E(\mathscr{M}) = E_{\text{ext}}(\mathscr{M}, D) + E_{\text{atlas}}(\mathscr{M}, A) + E_{\text{int}}(\mathscr{M})\ . \tag{4}$$

Hence, the atlas prior is a direct extension of the global tractography framework explained in the previous section, and can be optimized in the same way.

We define the atlas energy $E_{\text{atlas}}(\mathscr{M}, A)$ as the L_2-distance between the reconstructed TOD $\tilde{\Psi}(\mathbf{u})$ and the atlas TOD $\tilde{\Psi}_a(\mathbf{u})$, which, according to Parseval's theorem, equals the sum of squared differences between the corresponding SH coefficients. In the spirit of [5], we propose to use a minimum track length threshold for the atlas TOD, which emphasizes the neighbourhood support of the local track orientation. Note that by imposing such length threshold, the distinction between the TOD, which is a direct representation of *any* tractogram, and the FOD, which relates to the data, becomes important.

3 Experiments and Results

3.1 Data

Data of 25 neurologically healthy subjects between ages 22 and 35 years old were provided by the WU-Minn Human Connectome Project (HCP) Q3 data release [20]. The diffusion data consists of 3×90 gradient directions at b-values 1,000, 2,000, and 3,000 s/mm^2 and 18 non-diffusion weighted images ($b = 0$), at an isotropic voxel size of 1.25 mm, and was corrected for motion and EPI distortions as described in [8]. In each subject, the white matter (WM) response function was estimated in a fractional anisotropy (FA ≥ 0.75) mask using standard techniques for all shells [19]. Isotropic grey matter (GM) and cerebrospinal fluid (CSF) kernels were estimated as the average signal in manually delineated regions. Finally, the kernels of all subjects were averaged to obtain one mean WM, GM and CSF kernel.

3.2 Atlas Construction

The atlas was constructed out of 20 randomly selected subjects, using our global tractography method without atlas prior in each of them individually. The segment length was set to 2 mm, the maximal order of the SH basis to $\ell_{\max} = 10$, and the weight of each segment to 0.1, such that on average ten segments per white matter voxel are reconstructed. We ran the MH sampler for 10^9 iterations, which took around 10 h on a standard desktop computer.

The resulting fibre segments were normalized to MNI space, using the non-linear warps provided by the HCP and originally obtained from FSL FNIRT [8]. The centre point of each segment is transformed to atlas space and its direction is reoriented according to the Jacobian of the local deformation field. Next, we imposed a minimum track length threshold, such that only tracks consisting of at least ten segments remained. These segments were subsequently transformed and reoriented to the space of the five remaining subjects for testing. Finally, the set of transformed and filtered segments of all subjects was converted to a TOD representation using aPSFs as described in Sect. 2.1. Conceptually, this is identical to existing methods for FOD/TOD reorientation and atlas construction [2,17], except that those methods first fit a weighted sum of uniformly oriented aPSFs to the data in every voxel. The segment representation, used in global tractography, allows to avoid this fitting step.

3.3 Evaluation

The effect of the proposed atlas prior was evaluated in the five remaining subjects, using identical parameter settings as for the initial global tractography. First of all, the mean track length, reported in Table 1, is exponentially distributed and increases significantly with the atlas prior (F-test, p-value 10^{-6}) by about 25 %. Simultaneously, the imposed atlas prior reduces the number of tracks by approximately 50 %. These observations indicate that while the overall density decreases, mostly the number of short, incomplete or interrupted tracks is reduced by the atlas prior.

Table 1 Mean track length and the total number of reconstructed tracks for the five test subjects

	Uniform prior		Atlas prior	
Subject	Average length (mm)	No. tracks	Average length (mm)	No. tracks
1	16.05	281,403	19.27	131,196
2	17.04	211,759	21.93	112,591
3	16.16	249,838	20.48	119,286
4	16.79	199,610	21.93	109,324
5	16.98	221,455	21.57	116,499

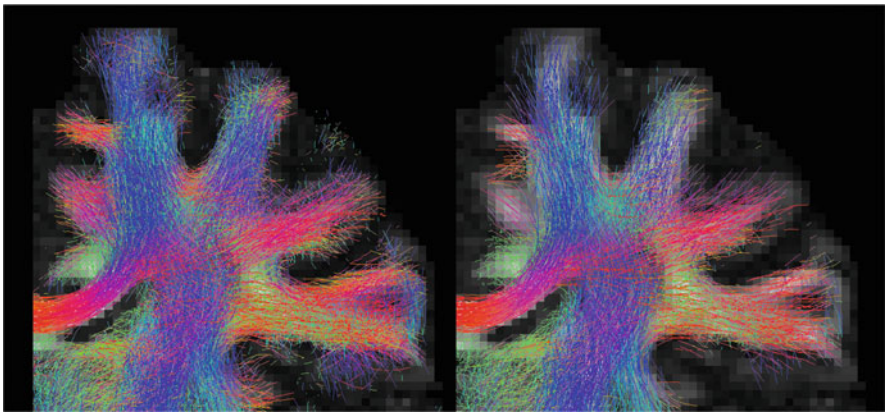

Fig. 1 Coronal slab (5 mm) of the reconstructed tractogram in the cerebrum, overlaid on a fractional anisotropy map, without atlas prior (*left*), and with atlas prior (*right*)

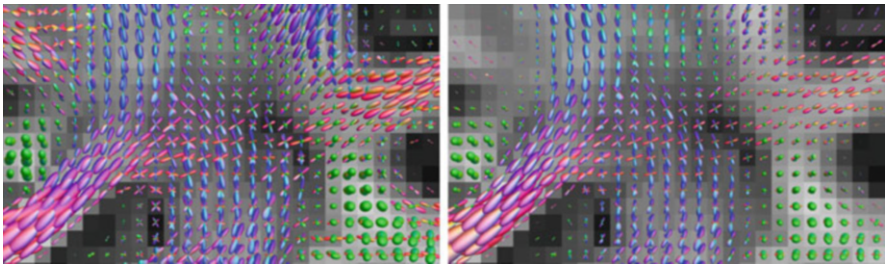

Fig. 2 Track orientation distribution (TOD) in the centrum semiovale, obtained without atlas prior (*left*), and with atlas prior (*right*). With atlas prior, the track orientations are more consistent across neighbouring voxels

Figure 1 shows a cross-section of the reconstructed tractogram of test subject 1, and illustrates that the density decrease with the atlas prior is mainly located in the distal gyri. All major WM bundles are present in the reconstruction, and the crossing of the corpus callosum, the corona radiata, and the superior longitudinal fasciculus, sometimes challenging for tractography, is successfully recovered in both global tractography reconstructions, with and without the atlas prior. However, a close-up of the TOD in this region, as shown in Fig. 2, illustrates that the main fibre directions are more consistent across neighbouring voxels when using the atlas prior. Similar results were observed in the remaining test subjects (not shown).

Finally, we segmented the left cingulate track in both reconstructions based on a WM parcellation obtained with FreeSurfer [7] following the protocol described in [21]. As shown in Fig. 3, the atlas prior strongly reduces the amount of spurious tracks that run from the cingulum into the corpus callosum. Hence, incorporating the atlas prior improves the specificity of the track reconstruction.

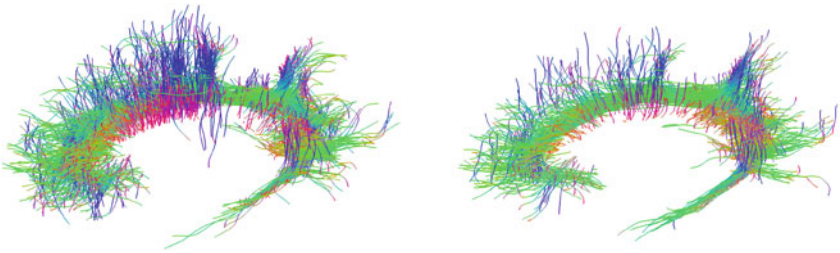

Fig. 3 Sagittal view of the left cingulate track, segmented from the global fibre reconstruction without atlas prior (*left*), and with atlas prior (*right*). Notice that with the prior, the number of false positive connections to the corpus callosum is reduced

4 Discussion

At a conceptual level, there are many analogies between tractography and segmentation. Both aim to delineate structures of interest, both rely on neighbourhood information for doing so, and both aim to reconstruct shapes with remarkable similarity across subjects. As such, we can expect that tractography, like segmentation, can benefit from inter-subject information in the shape of an atlas that captures the expected anatomy.

The global tractography framework is well suited for the inclusion of such atlas prior, as it aims to reconstruct the optimal fibre configuration in the whole image volume. Indeed, we have shown that a prior of the local track orientation can be elegantly included as an additional energy term in the optimization. Selecting the weight of this atlas energy allows to set the reliance on the atlas relative to the subject data, whereas the internal energy ensures spatial continuity.

While the atlas contains only local information, the imposed minimum track length ensures "track-like local support" in the neighbouring voxels [5], which can be a powerful prior for guiding the fibre reconstruction. This is particularly evidenced by our results in Figs. 2 and 3, in which we observed more consistent track orientations and fewer spurious connections. An alternative application of the presented method could be to use a high-resolution atlas, built from HCP data, in conjunction with data of lower spatial and angular resolution. As such, the reconstruction of clinical data with fast acquisition schemes may be improved.

Nevertheless, our proposed atlas-guided tractography method also suffers from some of the limitations of atlas-based segmentation methods. Foremost, the required atlas-to-subject registration can introduce misalignment artefacts that make for a fuzzy prior at best, and a plain wrong one at worst. We noticed the effect of such artefacts in some of the distal gyri, where a "null prior" was mapped onto the gyrus, disabling any track reconstruction in that area. Secondly, the robustness of the current setup to pathology is in question, as registration in the presence of (tumorous) lesions is still an open issue.

5 Conclusions

This work is, to the best of our knowledge, the first to include a track orientation prior in a global tractography framework. Our method has a beneficial effect on the reconstructed tractogram, although its success depends on the quality of the registration. Future work can focus on alternative atlas measures and multi-atlas approaches, which may perform better in this regard.

Acknowledgements D. Christiaens is supported by a Ph.D. grant of the Agency for Innovation by Science and Technology (IWT). Data were provided by the Human Connectome Project, WU-Minn Consortium (Principal Investigators: David Van Essen and Kamil Ugurbil; 1U54MH091657) funded by the 16 NIH Institutes and Centers that support the NIH Blueprint for Neuroscience Research; and by the McDonnell Center for Systems Neuroscience at Washington University.

References

1. Cabezas, M., Oliver, A., Lladó, X., Freixenet, J., Bach Cuadra, M.: A review of atlas-based segmentation for magnetic resonance brain images. Comput. Meth. Prog. Biomed. **104**(3), e158–e177 (2011)
2. Christiaens, D., Dhollander, T., Maes, F., Sunaert, S., Suetens, P.: Groupwise deformable registration of fiber track sets using track orientation distributions. In: Schultz, T., Nedjati-Gilani, G., Venkataraman, A., O'Donnell, L., Panagiotaki, E. (eds.) Computational Diffusion MRI and Brain Connectivity, Mathematics and Visualization, pp. 151–161. Springer, New York (2014)
3. Cook, P.A., Zhang, H., Awate, S.P., Gee, J.C.: Atlas-guided probabilistic diffusion-tensor fiber tractography. In: 5th International Symposium on Biomedical Imaging: From Nano to Macro—ISBI 2008, pp. 951–954. IEEE (2008)
4. Descoteaux, M., Deriche, R., Knosche, T., Anwander, A.: Deterministic and probabilistic tractography based on complex fibre orientation distributions. IEEE Trans. Med. Imaging **28**(2), 269–286 (2009)
5. Dhollander, T., Emsell, L., Van Hecke, W., Maes, F., Sunaert, S., Suetens, P.: Track orientation density imaging (TODI) and track orientation distribution (TOD) based tractography. NeuroImage **94**, 312–336 (2014)
6. Fillard, P., Poupon, C., Mangin, J.F.: A novel global tractography algorithm based on an adaptive spin glass model. In: Yang, G.Z., Hawkes, D., Rueckert, D., Noble, A., Taylor, C. (eds.) Medical Image Computing and Computer-Assisted Intervention—MICCAI 2009, LNCS, vol. 5761, pp. 927–934. Springer, Berlin (2009)
7. Fischl, B.: Freesurfer. NeuroImage **62**(2), 774–781 (2012)
8. Glasser, M.F., Sotiropoulos, S.N., Wilson, J.A., Coalson, T.S., Fischl, B., Andersson, J.L., Xu, J., Jbabdi, S., Webster, M., Polimeni, J.R., Van Essen, D.C., Jenkinson, M.: The minimal preprocessing pipelines for the human connectome project. NeuroImage **80**, 105–124 (2013)
9. Hastings, W.K.: Monte Carlo sampling methods using Markov chains and their applications. Biometrika **57**(1), 97–109 (1970)
10. Jbabdi, S., Johansen-Berg, H.: Tractography: where do we go from here? Brain Connect. **1**(3), 169–183 (2011)
11. Kreher, B., Mader, I., Kiselev, V.: Gibbs tracking: a novel approach for the reconstruction of neuronal pathways. Magn. Reson. Med. **60**(4), 953–963 (2008)

12. Mangin, J.F., Fillard, P., Cointepas, Y., Le Bihan, D., Frouin, V., Poupon, C.: Toward global tractography. NeuroImage **80**, 290–296 (2013)
13. Mangin, J.F., Poupon, C., Cointepas, Y., Riviere, D., Papadopoulos-Orfanos, D., Clark, C., Régis, J., Le Bihan, D.: A framework based on spin glass models for the inference of anatomical connectivity from diffusion-weighted MR data—a technical review. NMR Biomed. **15**(7–8), 481–492 (2002)
14. Mori, S., van Zijl, P.: Fiber tracking: principles and strategies—a technical review. NMR Biomed. **15**(7–8), 468–480 (2002)
15. O'Donnell, L.J., Golby, A.J., Westin, C.F.: Fiber clustering versus the parcellation-based connectome. NeuroImage **80**, 283–289 (2013)
16. Parker, G.J.: Probabilistic fiber tracking. In: Jones, D.K. (ed.) Diffusion MRI: Theory, Methods, and Applications, pp. 396–408. Oxford University Press, Oxford (2010)
17. Raffelt, D., Tournier, J., Crozier, S., Connelly, A., Salvado, O.: Reorientation of fiber orientation distributions using apodized point spread functions. Magn. Reson. Med. **67**(3), 844–855 (2012)
18. Reisert, M., Mader, I., Anastasopoulos, C., Weigel, M., Schnell, S., Kiselev, V.: Global fiber reconstruction becomes practical. NeuroImage **54**(2), 955–962 (2011)
19. Tournier, J., Calamante, F., Connelly, A.: Robust determination of the fibre orientation distribution in diffusion MRI: non-negativity constrained super-resolved spherical deconvolution. NeuroImage **35**(4), 1459–1472 (2007)
20. Van Essen, D.C., Smith, S.M., Barch, D.M., Behrens, T.E., Yacoub, E., Ugurbil, K.: The WU-Minn human connectome project: an overview. NeuroImage **80**, 62–79 (2013)
21. Wassermann, D., Makris, N., Rathi, Y., Shenton, M., Kikinis, R., Kubicki, M., Westin, C.F.: On describing human white matter anatomy: The white matter query language. In: Mori, K., Sakuma, I., Sato, Y., Barillot, C., Navab, N. (eds.) Medical Image Computing and Computer-Assisted Intervention – MICCAI 2013, Lecture Notes in Computer Science, vol. 8149, pp. 647–654. Springer, Berlin (2013)
22. Yap, P.T., Gilmore, J.H., Lin, W., Shen, D.: PopTract: population-based tractography. IEEE Trans. Med. Imaging **30**(10), 1829–1840 (2011)
23. Yendiki, A., Panneck, P., Srinivasan, P., Stevens, A., Zöllei, L., Augustinack, J., Wang, R., Salat, D., Ehrlich, S., Behrens, T., Jbabdi, S., Gollub, R., Fischl, B.: Automated probabilistic reconstruction of white-matter pathways in health and disease using an atlas of the underlying anatomy. Front. Neuroinformatics **5** (2011)

Part IV
Q-space Reconstruction

Magnitude and Complex Based Diffusion Signal Reconstruction

Marco Pizzolato, Aurobrata Ghosh, Timothé Boutelier, and Rachid Deriche

Abstract In Diffusion Weighted Magnetic Resonance Imaging (DW-MRI) the modeling of the magnitude signal is complicated by the Rician distribution of the noise. It is well known that when dealing instead with the complex valued signal, the real and imaginary parts are affected by Gaussian distributed noise and their modeling can thus benefit from any estimation technique suitable for this noise distribution. We present a quantitative analysis of the difference between the modeling of the magnitude diffusion signal and the modeling in the complex domain. The noisy complex and magnitude diffusion signals are obtained for a physically realistic scenario in a region close to a restricting boundary. These signals are then fitted with the Simple Harmonic Oscillator based Reconstruction and Estimation (SHORE) bases and the reconstruction performances are quantitatively compared. The noisy magnitude signal is also fitted by taking into account the Rician distribution of the noise via the integration of a Maximum Likelihood Estimator (MLE) in the SHORE. We discuss the performance of the reconstructions as function of the Signal to Noise Ratio (SNR) and the sampling resolution of the diffusion signal. We show that fitting in the complex domain generally allows for quantitatively better signal reconstruction, also with a poor SNR, provided that the sampling resolution of the signal is adequate. This applies also when the reconstruction is compared to the one performed on the magnitude via the MLE.

1 Introduction

Diffusion Weighted Magnetic Resonance Imaging (DW-MRI) measures the signal attenuation due to the loss of spin phase coherence caused by particles subject to Brownian motion. DW-MRI thus is inherently a low Signal to Noise Ratio (SNR) technique. Indeed, increasing the diffusion-weighting measured by the b-value or

M. Pizzolato (✉) • A. Ghosh • R. Deriche
Athena, Inria Sophia Antipoles-Méditerranée, Antibes, France
e-mail: pizzolato.marco@gmail.com; aurobrata.ghosh@gmail.com; rachid.deriche@inria.fr

T. Boutelier
Olea Medical, La Ciotat, France
e-mail: timothe.boutelier@olea-medical.com

L. O'Donnell et al. (eds.), *Computational Diffusion MRI*, Mathematics and Visualization, DOI 10.1007/978-3-319-11182-7_12

decreasing the voxel size can further reduce the SNR, causing the signal to be close to the background noise level [7]. This is particularly problematic when characterizing the non-Gaussianity of the diffusion signal profile, associated to restricted diffusion, since a high b-value is generally required [1]. Indeed a nonlinear dependence between the log-transformed DW intensity and the diffusion-weighting (b-value), as the sole result of noise, has been previously reported [7]. This can lead to misinterpretations of the underlying diffusion process which, for instance, can be erroneously thought as restricted, thus ascribing to the tissue more structural complexity than exists. However, one of the major sources of error in Magnetic Resonance Imaging (MRI), and even more accentuated in DW-MRI due to the inherent low SNR, is the noise.

In MRI the signal, acquired for each coil in quadrature, is complex with an additive thermal noise that can be considered to be derived from a bivariate normal distribution $N(0, \sigma)$ [6]. However, when the magnitude of the complex signal is computed, the noise becomes Rician distributed [5] and a not-negligible noise floor, the minimum signal measurable, appears. The bias introduced by the Rician distribution leads to the distortion of estimated quantitative diffusion parameters. For instance, the noise floor causes the DW signal to be overestimated, leading to underestimation of the Apparent Diffusion Coefficient (ADC) [4]. Other noise-related issues have also been reported, such as orientationally dependent deviation from Gaussianity of the ADC profile, underestimation of diffusion anisotropy indices and correlation between mean diffusivity and diffusion anisotropy [7]. Hence, denoising is essential in DW-MRI.

To properly denoise magnitude signals, the noise distribution should be taken into account. However, the distribution of the noise affecting magnitude DW images (DWIs) changes depending on the number of coils used for the acquisition and on the employed reconstruction method. For instance, when magnitude images are obtained from multiple coils after sum-of-squares reconstruction, the noise follows a non-central χ distribution [3]. Nevertheless, the complex diffusion signal is still affected by noise with a Gaussian distribution, which can be exploited via any Gaussian-based denoising technique or fitting procedure.

In this paper we analyze the theoretical performance gain given by considering the complex signal instead of just using the magnitude. The complex signal is synthetically generated, according to [8], by considering a voxel located close to a boundary, where the underlying diffusion process is restricted. In fact, by exploiting the asymmetry, due to the presence of the boundary, of the displacement density probability of the water molecules, also known as Ensemble Average Propagator (EAP) [2, 13], it is possible to obtain a complex valued signal. The complex signal is generated along one gradient direction and for a voxel located in the proximity of a single infinite plate. The noisy complex and magnitude signals are then obtained and the reconstruction of the magnitude diffusion signal is performed from each of them. The reconstructed signal, as the linear combination of basis functions, leads to an effective characterization of the diffusion properties and is a useful tool for measuring noise-related performances. In this respect we employ the Simple Harmonic Oscillator based Reconstruction and Estimation (SHORE) [9]. Within

this framework, a Maximum Likelihood Estimator (MLE), for the reconstruction based on the Rician magnitude signal, is also proposed for performance comparison.

2 Methods

In this section we present the theoretical framework. First, we present the diffusion signal equation for a voxel in a position close to a single infinite plate. Then we recapitulate the SHORE formulation for the signal fitting. Finally we describe the integration of the MLE in the SHORE.

2.1 Signal in the Proximity of a Single Infinite Plate

When considering a voxel located in the proximity of a restricting boundary such as an infinite plate, with voxel's dimensions significantly smaller than the separation distance between the plate and any other boundary, the magnetization in the voxel is influenced only by the boundary in the vicinity [8]. A graphical representation of this scenario is shown in Fig. 1a, where an infinite plate is represented with its normal aligned with the z-axis, and a voxel with height $z_2 - z_1$ is located at a distance z_1 from the plate itself. Using the notation in [8] it is convenient to define the dimensionless position variable

$$\zeta = \frac{z}{u} \tag{1}$$

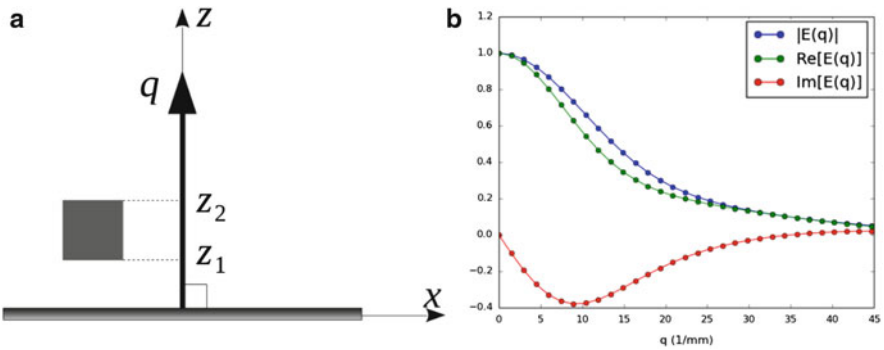

Fig. 1 (**a**) An infinite plate lies along the x-axis, with normal along the z-axis. A voxel is located at a distance z_1 from the infinite plate and has a height given by $z_2 - z_1$. The gradient vector **q** makes a right angle with the x-axis toward the positive z-axis; adapted from [8]. (**b**) Magnitude, real and imaginary parts of the signal generated according to Eq. 3 for a voxel with $z_1 = 0$ and dimensionless height of 0.25; $\delta = 3$ ms, Δ=100 ms, $D_0 = 2.299 \times 10^{-9}$ m^2/s and $G_{max} = 350$ mT/m

where u is the characteristic diffusion length given by

$$u = \sqrt{4D_0\Delta} \tag{2}$$

with D_0 being the free diffusion coefficient and Δ the diffusion time. Figure 1a also shows the gradient vector which, in this case, is assumed to be aligned with the positive z-axis. The gradient vector magnitude is then given by $q = \gamma\delta G/2\pi$ where γ is the gyromagnetic ratio, δ is the diffusion pulse duration and G is the diffusion gradient strength. The considered experiment is the pulsed gradient spin echo (PGSE) sequence with pulse duration δ small compared to Δ. Finally, after defining the dimensionless wave-number $\kappa = \pi q u$, the complex signal is given by [8]

$$E([\zeta_1, \zeta_2], \kappa) = e^{-\kappa^2} \frac{F(\zeta_2) - F(\zeta_1)}{2(\zeta_2 - \zeta_1)} \tag{3}$$

where ζ_1 and ζ_2 are the dimensionless coordinates of the voxel corresponding to z_1 and z_2 via Eq. 1, and $F(\zeta)$ is

$$\begin{aligned} F(\zeta) =& \zeta + \frac{1}{\sqrt{\pi}} e^{-(\zeta - i\kappa)^2} + \frac{e^{i4\kappa\zeta}}{i4\kappa} [1 - \mathrm{erf}(\zeta + i\kappa)] \\ & - \left[\zeta - i\left(\kappa + \frac{1}{4\kappa}\right)\right] \mathrm{erf}(-\zeta + i\kappa). \end{aligned} \tag{4}$$

2.2 Signal Reconstruction

The signal fitting is performed with SHORE [9], a promising signal reconstruction method suitable for q-space magnetic resonance. Within this framework the signal is represented as the linear combination of orthogonal basis functions, result of the multiplication between a Gaussian and an Hermite polynomial

$$\phi_n(u, q) = i^{-n} \sqrt{\frac{u\sqrt{\pi}}{2^{n-2} n!}} e^{-2\pi^2 q^2 u^2} H_n(2\pi q u) \tag{5}$$

where n is the order of the basis, $H_n(x)$ is the nth-order Hermite polynomial and u is the characteristic data dependent diffusion length or scaling factor to be determined, for instance by fitting the signal to a Gaussian according to $E(q) = \exp(-2\pi^2 q^2 u^2)$. Our formulation of the basis functions in Eq. 5 differs from the one given in [9] with the introduction of the normalizing factor $2\sqrt{u\sqrt{\pi}}$, which renders the bases orthonormal. The bases are well suited for representing the signal in the complex domain: the even order basis functions are real valued and evenly symmetric whereas the odd order basis functions are imaginary and show odd symmetry, which

is precisely the case of the real and the imaginary parts of the diffusion signal. The normalized diffusion signal in the SHORE representation can thus be expressed by

$$E(q) = \sum_{n=0}^{N-1} a_n \phi_n(u, q) \tag{6}$$

where N is the maximum allowed order in the reconstruction and a_n are the coefficients corresponding to the respective bases. The choice of N directly affects the signal reconstruction: in the case of noisy data, a high order will potentially cause the reconstruction to follow the noise, whereas a low order will inherently enforce a smoothing effect. For a given order N the signal reconstruction in the complex domain is performed by considering the even and odd coefficients for the real and imaginary parts respectively. In the case of the magnitude signal reconstruction, only the even coefficients are taken into account. In any case, a fitting procedure with a Linear Least Squares (LLS) approach is used to estimate the coefficients.

2.2.1 Maximum Likelihood Estimation

To better take into account the Rician distribution of the noise affecting the magnitude diffusion signal, the estimation of the coefficients can be performed with the Maximum Likelihood Estimator (MLE). In the case of Rician noise, the MLE has been introduced in [12]. Normally several noisy realizations of each signal sample are required to properly estimate via the MLE. However in the case of one noisy realization per sample, the signal samples can be interpreted as noisy realizations of a function, thus the likelihood is given by

$$L = \prod_{i=1}^{n} \frac{M_i}{\sigma^2} e^{-\frac{M_i^2 + [Ac]_i^2}{2\sigma^2}} \mathrm{I}_0\left(\frac{[Ac]_i M_i}{\sigma^2}\right) \tag{7}$$

where n is the number of samples of the magnitude signal, M_i is the i-th sample, σ^2 is the noise variance, A is the real SHORE design matrix, c is the even coefficients vector and I_0 is the modified zeroth order Bessel function of the first kind. The MLE is then defined as the estimator maximizing L or equivalently $\log L$

$$\hat{c}_{ML} = \underset{c}{\operatorname{argmax}} \left(\log L\right). \tag{8}$$

The performance of the estimator is expected to increase with the increasing number of samples of the signal. It should then be noticed that the MLE requires σ^2 to be given. Thus a prior estimation of the signal noise variance is necessary.

3 Experimental Results

This section describes the parameters adopted for the generation of the complex signal (see Sect. 2.1) and how the noisy complex and magnitude signals are obtained from this. Then, the reconstruction of the magnitude signal with SHORE, starting from both the complex and the magnitude signals (with both LLS and MLE), i discussed. Finally we present the way the performances of the magnitude signal reconstructions are compared.

We generated the complex diffusion signal, according to Eq. 3, for a voxel adjacent to an infinite plate and with dimensionless height of 0.25 (Fig. 1b). A total of n equally spaced samples of the signal, with $n \in \{2, 3, \ldots, 100\}$, is generated along the direction normal to the infinite plate (Fig. 1a). The sequence parameters are fixed to $G_{max} = 350\,\mathrm{mT/m}$, $\delta = 3\,\mathrm{ms}$, $\Delta = 100\,\mathrm{ms}$ and the physical quantities to $\gamma = 2.675 \times 10^8\,\mathrm{rad/sT}$ and $D_0 = 2.299 \times 10^{-9}\,\mathrm{m^2/s}$. Uncorrelated Gaussian noise with equal variance is added on the real and imaginary parts of the signal, obtaining the noisy complex signal. From this the magnitude is computed, obtaining the noisy magnitude signal. The standard deviation of the noise is calculated for several different SNR values as $\sigma = SNR^{-1}$ relatively to the non-weighted signal sample ($G = 0$).

The noisy complex and magnitude signals are then fitted via SHORE according to Eq. 6. The even (real) and odd (imaginary) SHORE bases are used for the complex signal fitting whereas only the even bases are used in the case of the magnitude signal fitting. Moreover the magnitude signal is also fitted with the MLE, obtaining the vector of the SHORE coefficients according to Eq. 8. To observe the influence of the maximum allowed order in the SHORE reconstruction N (see Sect. 2.2 and Eq. 6), two orders are tested: one relatively low order $N = 6$ and one relatively high order $N = 10$. However the following discussion is referred to $N = 6$ and a comparison with $N = 10$ will be given later in Sect. 4. In order to render the fitting of the complex and magnitude signals independent from the estimation of the scaling factor u, in every case the u estimated on the noisy magnitude is also used for the complex fitting.

After the complex signal fitting a real and an imaginary vectors of coefficients are obtained, leading to a real and an imaginary reconstructions respectively. These reconstructions are then used to compute the magnitude reconstruction from the complex signal fitting ($\mathscr{M}_C$), which is then compared to the one reconstructed from the noisy magnitude signal via both LLS ($\mathscr{M}_M$) and MLE ($\mathscr{M}_{M_{ML}}$) based fittings.

We performed the comparison by calculating the Root Sum of Squares (RSS) value of the residuals between the magnitude reconstructions ($\mathscr{M}_C$, $\mathscr{M}_M$,$\mathscr{M}_{M_{ML}}$) and the ground truth $\mathscr{M}_{GT} = |E(q)|$. The whole procedure is performed with 1,000 different noise realizations for each couple of SNR and number of samples n (sampling resolution). Hence a triple of averaged RSS values, $RSS_C \pm SD_{RSS_C}$, $RSS_M \pm SD_{RSS_M}$ and $RSS_{M_{ML}} \pm SD_{RSS_{M_{ML}}}$ ($RSS_{ML}, SD_{RSS_{ML}}$ from now on and in the figures) is obtained for each pair (SNR, n). For each value of n, the RSS values and

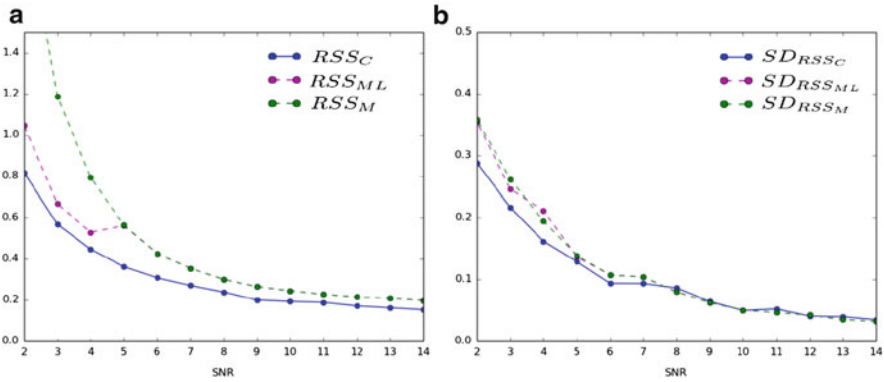

Fig. 2 Root sum of squares values RSS_C, RSS_M and RSS_{ML} (**a**), and standard deviations SD_{RSS_C}, SD_{RSS_M} and $SD_{RSS_{ML}}$ (**b**), as functions of the SNR. Each point represents the averaged value over 1,000 noise realizations with the corresponding SNR. $G_{max} = 350\,\mathrm{mT/m}$, with $n = 31$

their standard deviations can be represented as functions of the SNR, obtaining the curves $\{RSS\}$ and $\{SD_{RSS}\}$ as shown in Fig. 2a and b respectively ($n = 31$).

We also compared the reconstruction performances as function of the signal sampling resolution, i.e. as function of the number of samples n. In the following several numbers of samples n will be tested. However, when estimating the SHORE coefficients, if the number of unknown coefficients is higher than the number of samples considered for the signal, then the estimation is under determined. This happens for $n < N/2$. Figure 3 shows the integral of the difference between the RSS (light blue) and SD_{RSS} (magenta) curves of different techniques, as function of the number of samples n. Precisely, it shows the integral values of $\{RSS_M\} - \{RSS_C\}$ and $\{SD_{RSS_M}\} - \{SD_{RSS_C}\}$ (Fig. 3a), $\{RSS_{ML}\} - \{RSS_C\}$ and $\{SD_{RSS_{ML}}\} - \{SD_{RSS_C}\}$ (Fig. 3b), and finally $\{RSS_M\} - \{RSS_{ML}\}$ and $\{SD_{RSS_M}\} - \{SD_{RSS_{ML}}\}$ (Fig. 3c). Thus a positive value globally indicates a better reconstruction (less overall reconstruction error) for $\mathscr{M}_C$ compared to $\mathscr{M}_M$ (Fig. 3a), $\mathscr{M}_C$ compared to $\mathscr{M}_{M_{ML}}$ (Fig. 3b) and $\mathscr{M}_{M_{ML}}$ compared to $\mathscr{M}_M$ (Fig. 3c). It should be noticed that Fig. 3c substantially describes the difference between Fig. 3a and b.

Figure 4 shows the inter-technique comparisons of the mean RSS values (a,b,c) and their standard deviations (d,e,f), as function of both the SNR and the sampling resolution (i.e. n). In detail it shows the differences $RSS_M - RSS_C$ (Fig. 4a) and $SD_{RSS_M} - SD_{RSS_C}$ (Fig. 4d), $RSS_{ML} - RSS_C$ (Fig. 4b) and $SD_{RSS_{ML}} - SD_{RSS_C}$ (Fig. 4e), and finally $RSS_M - RSS_{ML}$ (Fig. 4c) and $SD_{RSS_M} - SD_{RSS_{ML}}$ (Fig. 4f). Thus a positive value (red) indicates a better reconstruction $\mathscr{M}_C$ compared to $\mathscr{M}_M$ (Fig. 4a,d), $\mathscr{M}_C$ compared to $\mathscr{M}_{M_{ML}}$ (Fig. 4b,e) and $\mathscr{M}_{M_{ML}}$ compared to $\mathscr{M}_M$ (Fig. 4c,f). It should be noticed that the range of values in the color bars are different. For instance the amplitude of the range of the performance gain for the complex reconstruction, compared to the magnitude based one, is higher when the comparison is made with respect to the LLS fitting (Fig. 4a) than when the MLE is considered (Fig. 4b). The opposite holds for the performance loss. On the contrary we observe that the range of

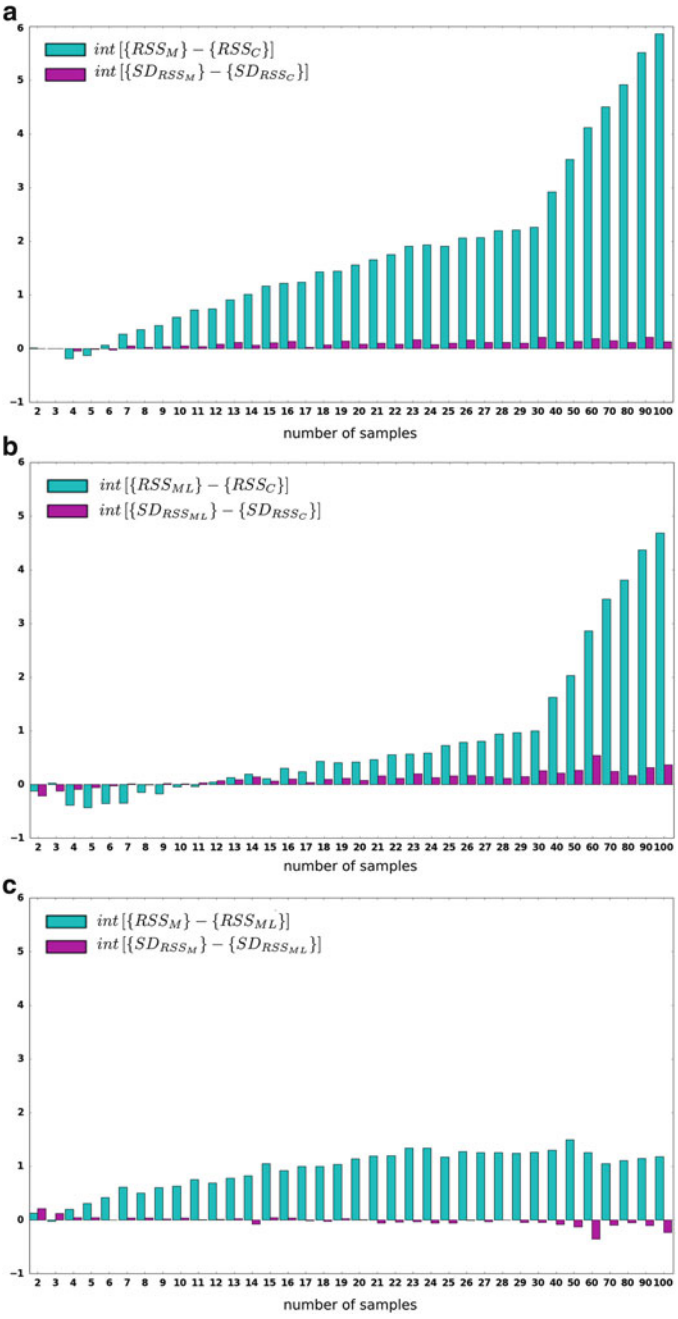

Fig. 3 In *light blue* the differences between the areas under the *RSS* curves of two different compared techniques (i.e. the curves in Fig. 2a); in *magenta* the differences between the areas under the SD_{RSS} curves (i.e. the curves in Fig. 2b). Values are shown as a function of the number of samples n. A positive value indicates a globally better reconstruction (less overall reconstruction error) for $\mathscr{M}_C$ over $\mathscr{M}_M$ (**a**), $\mathscr{M}_C$ over $\mathscr{M}_{M_{ML}}$ (**b**) and $\mathscr{M}_{M_{ML}}$ over $\mathscr{M}_M$ (**c**). $G_{max} = 350\,\mathrm{mT/m}$

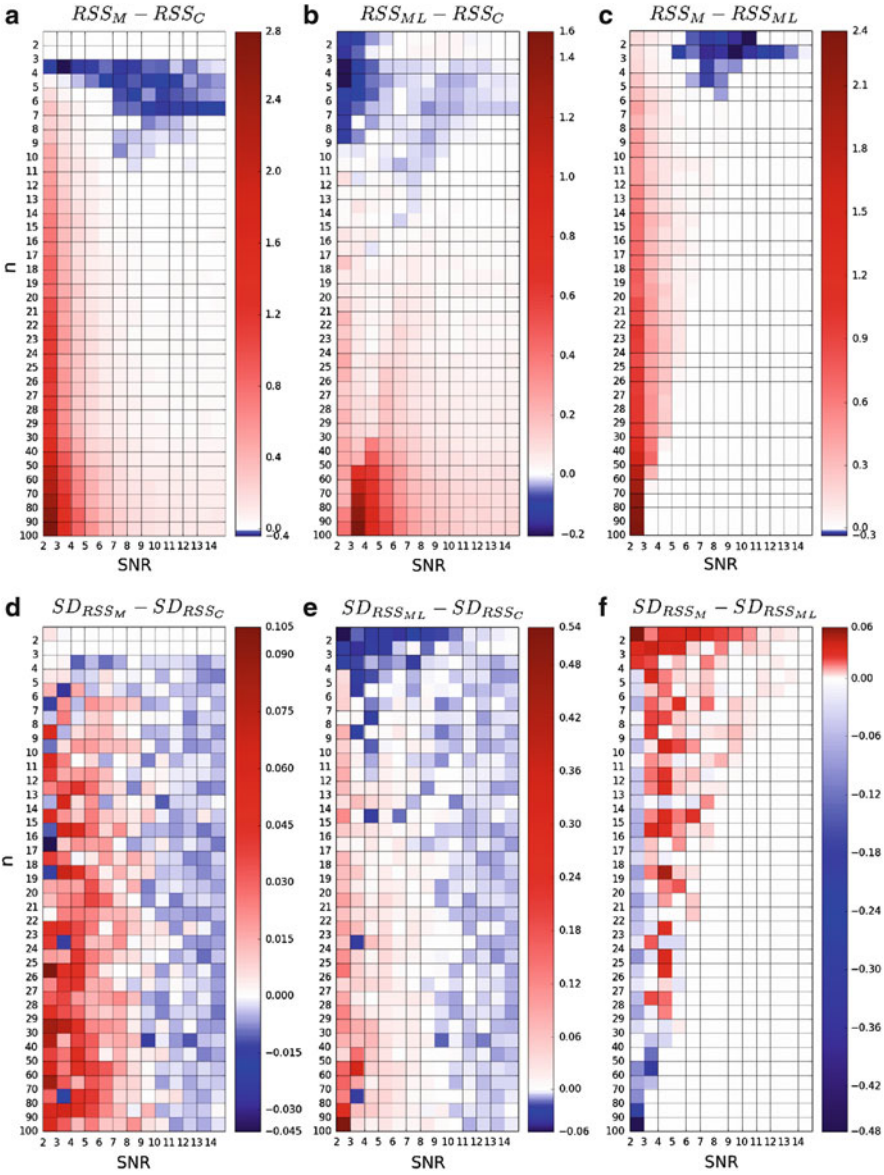

Fig. 4 Differences between *RSS* values (**a,b,c**) and correspondent SD_{RSS} (**d,e,f**) for different compared techniques, as function of the SNR and of the number of samples n. A positive value (*red*) indicates a better reconstruction for $\mathscr{M}_C$ compared to $\mathscr{M}_M$ (**a**), $\mathscr{M}_C$ compared to $\mathscr{M}_{M_{ML}}$ (**b**) and $\mathscr{M}_{M_{ML}}$ compared to $\mathscr{M}_M$ (**c**), or less error variance (**d,e,f**). Each *pixel* represents the average value over $1,000$ noise realizations for the corresponding SNR and number of samples n. $G_{max} = 350\,\mathrm{mT/m}$

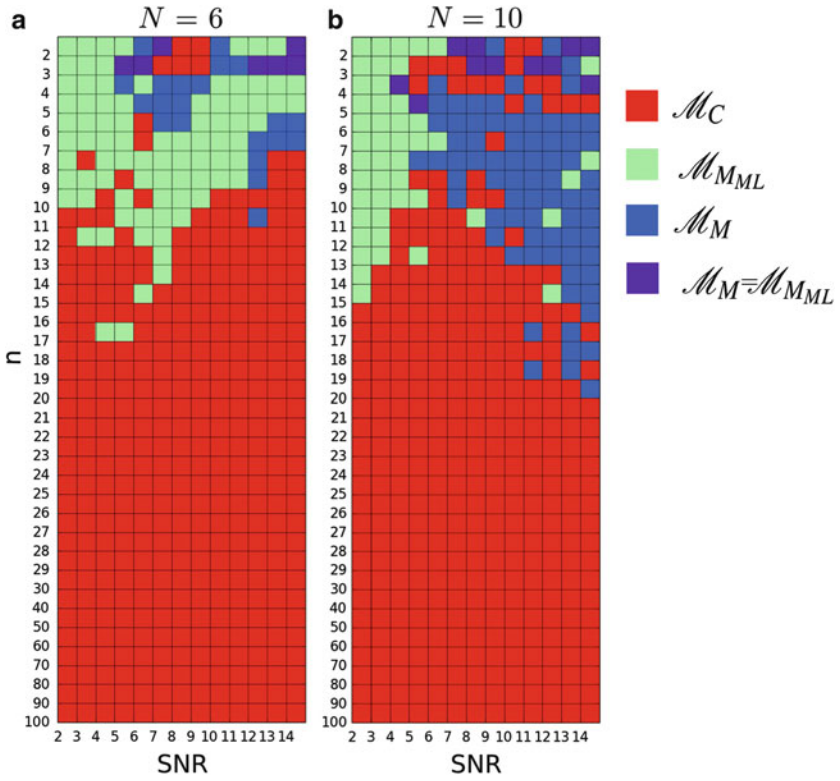

Fig. 5 The best reconstruction technique as a function of the SNR and the number of samples n, for a maximum reconstruction order $N = 6$ (**a**) and $N = 10$ (**b**), see Sect. 2.2 and Eq. 6 for reference. *Red, green* and *blue* colors indicate that the signal reconstruction showing less error is the one performed by fitting the noisy complex signal, $\mathscr{M}_C$, the noisy magnitude signal with the Maximum Likelihood Estimator (MLE), $\mathscr{M}_{M_{ML}}$, and with Linear Least Squares (LLS), $\mathscr{M}_M$, respectively. A *purple* color indicates that the best reconstruction is based on the noisy magnitude signal fitting, without any preference regarding the estimation technique

the performance gain/loss in the standard deviation is higher when the comparison refers to the MLE (Fig. 4e) rather than the LLS (Fig. 4d). Finally Fig. 5 shows the map of the best reconstruction technique for each pair of *SNR* and n, that is the technique giving less mean reconstruction error (RSS value). In order to show the influence of the maximum reconstruction order of SHORE N on the results, maps are generated for $N = 6$ (Fig. 5a) and $N = 10$ (Fig. 5b).

We performed the reconstructions also for a signal generated with a set of parameters closer to that achievable in experimental conditions. In detail the voxel size is set to 50 µm, $G_{max} = 60\,\text{mT/m}$, $\delta = 15\,\text{ms}$ and $\Delta = 50\,\text{ms}$. Results are shown in Fig. 6 for $N = 6$. More precisely it shows the comparison between the RSS value of the complex based reconstruction and that of the magnitude based reconstruction obtained with LLS (Fig. 6a) and MLE (Fig. 6b) respectively. The

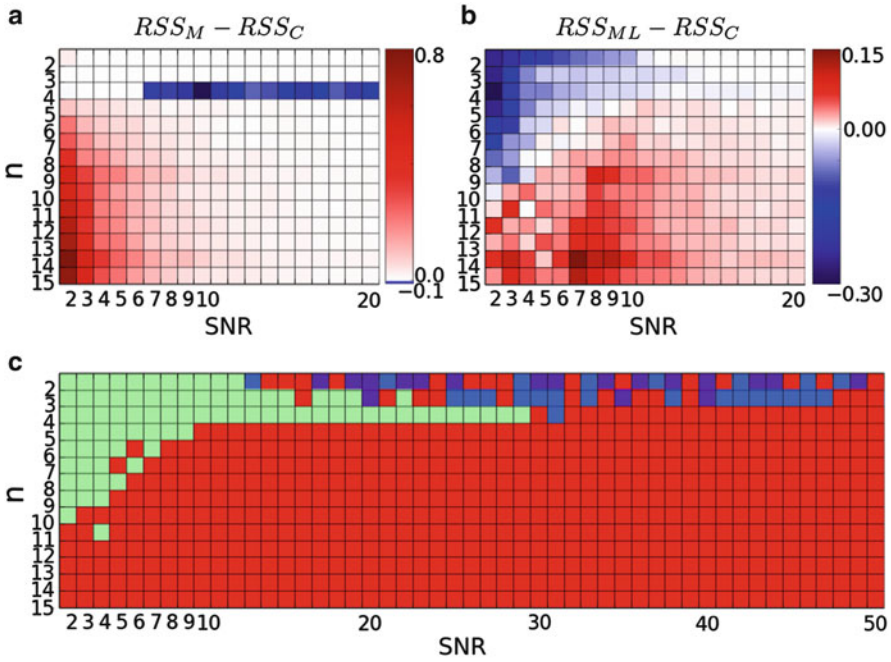

Fig. 6 Differences between *RSS* values for different compared techniques (**a**,**b**) and best reconstruction technique (**c**), as function of n and *SNR*. Results reported for a voxel with side 50 μm and with $G_{max} = 60\,\mathrm{mT/m}$, $\delta = 15\,\mathrm{ms}$, $\Delta = 50\,\mathrm{ms}$. A positive value (*red*) indicates a better reconstruction for $\mathscr{M}_C$ compared to $\mathscr{M}_M$ (**a**) and for $\mathscr{M}_C$ compared to $\mathscr{M}_{M_{ML}}$ (**b**). (**c**). *Red, green* and *blue* colors indicate that the signal reconstruction showing less error is the one performed by fitting the noisy complex signal, $\mathscr{M}_C$, the noisy magnitude signal with the Maximum Likelihood Estimator (MLE), $\mathscr{M}_{M_{ML}}$, and with Linear Least Squares (LLS), $\mathscr{M}_M$, respectively. A *purple* color indicates that the best reconstruction is based on the noisy magnitude signal fitting, without any preference regarding the estimation technique

range of SNR values $[2, 20]$ in the figures is set to that showing major differences (values different from zero) in the results and corresponds to that generally adopted [7]. The number of samples n range has been focused to $[2, 15]$, in fact at higher values the trend is similar to that shown in Fig. 4a and 4b. Figure 6c finally shows the best reconstruction technique for SNR values up to 50 and is representative also for higher SNR up to 100.

4 Discussion of the Results

The noisy complex and magnitude signals have been fitted with the SHORE obtaining the complex $\mathscr{M}_C$ and the magnitude based $\mathscr{M}_M$ reconstructions respectively. The magnitude has also been fitted via MLE, $\mathscr{M}_{M_{ML}}$. In each of the three cases

$\mathscr{M}_C$, $\mathscr{M}_{M_{ML}}$ and $\mathscr{M}_M$ the reconstruction error has been calculated and compared as function of the SNR and the number of samples n.

The magnitude reconstruction performed by fitting the complex domain signal, $\mathscr{M}_C$, globally shows a better performance (less reconstruction error) compared to the one based on the LLS fitting on the magnitude, $\mathscr{M}_M$, for $n > 5$ (Fig. 3a). The performance gain for the complex reconstruction is particularly evident for $SNR \leq 5$ (Fig. 4a), as expected. Indeed at higher SNR values the Rician distribution is well approximated by a Gaussian [10, 11], thus the performances of magnitude and complex based reconstructions should be equivalent. However an opposite trend is registered in case of $n = 4, 5$.

Moreover a performance dependence with the sampling resolution is observed. Indeed, by increasing the sampling resolution (n) the complex reconstruction $\mathscr{M}_C$ shows less error compared to the magnitude based one $\mathscr{M}_M$ also at $SNR > 5$; with this regard the range of SNR values in which the performance gain is observed also increases (Fig. 4a). In addition, the amount of error reduction in the case of $\mathscr{M}_C$ with respect to $\mathscr{M}_M$ increases with n.

Similar observations apply when the complex based reconstruction $\mathscr{M}_C$ is compared to that obtained via MLE on the magnitude $\mathscr{M}_{M_{ML}}$, but in this case for $n > 11$ (Fig. 3b). Indeed the MLE for the magnitude based fitting, sensibly improves the overall performance with respect to LLS at any sampling resolution, specially for low SNR values (Fig. 3c). However it should be noticed that the MLE requires an estimation of the noise variance, and in the present case the exact value was supplied. The reconstruction improvement given by the MLE over the LLS also occurs for $SNR < 5$ (Fig. 4c), as clearly represented in the example of Fig. 2a. In addition the amplitude of the error reduction obtained with MLE over LLS increases with the sampling resolution (n), whereas the range of SNR within which a performance gain is observed reduces (Fig. 4c).

Moreover, a performance loss for the MLE on the magnitude when compared to the LLS is observed within a region with $n \leq 6$ and $SNR \in [6, 13]$ at different grades (Fig. 4c). However the limits of this region seem to be dependent on the maximum reconstruction order N allowed in the SHORE, as shown in Fig. 5a for $N = 6$ and b for $N = 10$. In fact when $N = 10$ the range of the SNR values within which the performance gain of the MLE over the LLS is observed reduces. On the other hand the range of the number of samples n within which $\mathscr{M}_{M_{ML}}$ shows less error than $\mathscr{M}_C$, at very low SNR, slightly increases. Otherwise, the region in which the complex based reconstruction is the most performing do not seems to be affected by the choice of N. However the region where the SHORE estimation is under determined increases according to $N(n = 3$ for $N = 6$ and $n = 5$ for $N = 10)$.

Finally the complex based fitting leads to a reconstruction with an error standard deviation SD_{RSS_C} lower than SD_{RSS_M} for $n > 6$ (Figs. 3a and 4d). Similar observations apply when SD_{RSS_C} is compared to $SD_{RSS_{ML}}$ for $n > 8$ (Fig. 3b), although at low SNR the MLE shows a lower standard deviation (Fig. 4e and f).

Very similar considerations apply when the reconstructions are performed and evaluated for the case of signal generated with different voxel and pulse sequence parameters as shown in Fig. 6. However in this case the region in which the

magnitude based reconstruction shows better performances (Fig. 6c) is almost entirely defined by the performance of the MLE (Fig. 6b). Indeed almost everywhere in this region the performance of the LLS is comparable or inferior to that of the complex based reconstruction (Fig. 6a). Finally at higher SNR values the complex based reconstruction is generally the one showing the best performance (Fig. 6c).

Hence, as shown in Figs. 3b, 5a and 6c, at low SNR values it might be better to perform a reconstruction on the noisy magnitude signal when $n \leq 10$ with order $N = 6$ and $n \leq 15$ with order $N = 10$ (Fig. 5b). Within this region the MLE generally shows better performances for $SNR \leq 5$. However in the rest of the cases a reconstruction performed in the complex domain generally leads to less reconstruction error.

5 Conclusions

We have presented a comparative analysis between the magnitude diffusion signal reconstruction obtained by fitting the complex signal or magnitude signal directly. For the magnitude signal reconstruction we relied on the SHORE bases for both the noisy complex and magnitude fittings. In the case of the noisy (Rice distributed) magnitude fitting we introduced the maximum likelihood coefficients estimation (MLE) for the SHORE, as an alternative to the Linear Least Squares approach (LLS). We compared the performance of the reconstructions as a function of both the SNR and the number of samples in the signal n (sampling resolution).

Our results show that the choice of which reconstruction technique to adopt mainly depends on the SNR and on the number of samples of the signal, as shown in Figs. 5a,b and 6c. Depending on these parameters, the best magnitude signal reconstruction can be achieved for any of the compared techniques. However the complex based reconstruction reveals to be the most performing at any SNR with the increasing total number of samples of the diffusion signal. To further improve its performance, regularization constraints could also be implemented. This would be beneficial for the estimation of the diffusion parameters.

Despite the difficulty that may be encountered in clinical conditions in achieving an acquisition setup such as the one here adopted, the presented results might be directly useful and potentially validated in experimental setups.

Acknowledgements The authors would like to express their thanks to Olea Medical and to the Provence-Alpes-Côte d'Azur (P.A.C.A.) Regional Council for providing grant and support for this work. The authors also thank Demian Wassermann for the careful reading.

References

1. Basser, P. J.: Relationships between diffusion tensor and q-space MRI. Magn. Res. Med. **47**(2), 392–397 (2002)
2. Callaghan, P.T., MacGowan, D., Packer, K.J., Zelaya, F.O.: High-resolution q-space imaging in porous structures. J. Magn. Reson. **90**(1), 177–182 (1990, 1969)
3. Constantinides, C.D., Atalar, E., McVeigh, E.R.: Signal-to-noise measurements in magnitude images from NMR phased arrays. Magn. Res. Med. **38**(5), 852–857 (1997)
4. Dietrich, O., Heiland, S., Sartor, K.: Noise correction for the exact determination of apparent diffusion coefficients at low SNR. Mag. Res. Med. **45**(3), 448–453 (2001)
5. Gudbjartsson, H., Patz, S.: The Rician distribution of noisy MRI data. Magn. Reson. Med. **34**(6), 910–914 (1995)
6. Henkelman, R.M.: Measurement of signal intensities in the presence of noise in MR images. Med. Phys. **12**(2), 232–233 (1985)
7. Jones, D.K., Basser, P.J.: Squashing peanuts and smashing pumpkins: How noise distorts diffusion weighted MR data. Magn. Reson. Med. **52**(5), 979–993 (2004)
8. Özarslan, E., Nevo, U., Basser, P. J.: Anisotropy induced by macroscopic boundaries: surface-normal mapping using diffusion-weighted imaging. Biophys. J. **94**(7), 2809–2818 (2008)
9. Özarslan, E., Koay, C.G., Basser, P.J.: Simple harmonic oscillator based estimation and reconstruction for one-dimensional q-space MR. Proc. Intl. Soc. Mag. Reson. Med. **16**, 35 (2008)
10. Pajevic, S., Basser, P. J.: Parametric and non-parametric statistical analysis of DT-MRI data. J. Magn. Reson. **161**(1), 1–14 (2003)
11. Salvador, R., Pena, A., Menon, D.K., Carpenter, T.A., Pickard, J.D., Bullmore, E.T.: Formal characterization and extension of the linearized diffusion tensor model. Hum. Brain Mapp. **24**(2), 144–155 (2005)
12. Sijbers, J., den Dekker, A.J., Scheunders, P., Van Dyck, D.: Maximum-likelihood estimation of Rician distribution parameters. IEEE Trans. Med. Imaging **17**(3), 357–361 (1998)
13. Stejskal, E.O.: Use of Spin Echoes in a Pulsed Magnetic-Field Gradient to Study Anisotropic Restricted Diffusion and Flow. J. Chem. Phys. **43**, 3597–3603 (1965)

Diffusion Propagator Estimation Using Gaussians Scattered in q-Space

Lipeng Ning, Oleg Michailovich, Carl-Fredrik Westin, and Yogesh Rathi

Abstract The ensemble average diffusion propagator (EAP) obtained from diffusion MRI (dMRI) data captures important structural properties of the underlying tissue. As such, it is imperative to derive accurate estimate of the EAP from the acquired diffusion data. Taking inspiration from the theory of radial basis functions, we propose a method for estimating the EAP by representing the diffusion signal as a linear combination of 3D anisotropic Gaussian basis functions centered at the sample points in the q-space. This is in contrast to other methods, that always center the Gaussians at the origin in q-space. We also derive analytical expressions for the estimated diffusion orientation distribution function (ODF), the return-to-the-origin probability (RTOP) and the mean-squared-displacement (MSD). We validate our method on data obtained from a physical phantom with known crossing angle and on in-vivo human brain data. The performance is compared with the 3D-SHORE method of [4, 9] and radial basis function based method of [15].

1 Introduction

A classical method in dMRI is Diffusion tensor imaging (DTI) [3] which assumes the EAP to be a single Gaussian centered at the origin. However, this over-simplified assumption has limitations in voxels where there are more complicated structures. To resolve this issue, Diffusion spectrum imaging (DSI) was proposed in [17]. However, a large number of measurements and a long acquisition time makes it

L. Ning (✉) • C.-F. Westin • Y. Rathi
Brigham and Women's Hospital, Harvard Medical School, Boston, MA, USA
e-mail: lning@bwh.harvard.edu; westin@bwh.harvard.edu; yogesh@bwh.harvard.edu

O. Michailovich
University of Waterloo, Waterloo, ON, Canada
e-mail: olegm@uwaterloo.ca

L. O'Donnell et al. (eds.), *Computational Diffusion MRI*, Mathematics and Visualization, DOI 10.1007/978-3-319-11182-7_13

impractical to use DSI in clinical setting. To this end, many imaging methods have been proposed, which reduce the number of measurements by using suitable signal models or by using compressed sensing techniques. For example, Hybrid diffusion imaging (HYDI) [18], Diffusion Propagator Imaging (DPI) [5], the SHORE basis [9, 11], the Bessel Fourier basis [6], the Spherical Polar Fourier (SPF) basis [2, 4] and the spherical ridgelet basis [14] extend the spherical representation of the signal on a single shell to multiple shells with a continuous radial term. On the other hand, MAP-MRI [12] represents the diffusion signal using Hermite polynomials. Finally, the method of [19] (NODDI) estimates axonal dispersion while the CHARMED model [1] uses very high b-value to estimate the axon diameter distribution.

2 Our Contributions

In this work, we use 3D Gaussian functions for representing the diffusion signal and computing the EAP. The diffusion signal is expressed as a linear combination of Gaussian basis functions centered at several locations in the q-space at which measurements are available. This is in contrast to other mixture models, which typically center the basis functions at the origin in q-space [7, 13]. The present work is a generalization of the radial basis functions method in [15], incorporating directional anisotropic (non-radial) Gaussians for continuous representation of the diffusion signal and the propagator. Since the Fourier transform of a Gaussian is another Gaussian, one obtains simple analytical expressions for the EAP, the ODF, the return-to-the-origin probability (RTOP) and the mean-squared-displacement (MSD). We validate our method on a physical phantom data set with known fiber crossing and on in-vivo human brain data set. We also compare our method to the one using radial basis functions (RBF) [15], 3D-SHORE [9], and show that adding constraints helps in improving the performance of 3D-SHORE.

3 Signal Representation

Accurate reconstruction of high dimensional continuous functions from finite number of samples can be achieved using as a linear combination of radial basis functions centered around the given data points [8]. We use a similar methodology to represent the dMRI signal continuously in the q-space. Given a sampling of diffusion signal $E(\boldsymbol{q})$ at N data locations $\{\boldsymbol{q}_1, \ldots, \boldsymbol{q}_N\}$ in q-space, we consider its reconstruction using

$$\hat{E}(\boldsymbol{q}) = \sum_{n=0}^{N} w_n \phi_n(\boldsymbol{q} - \boldsymbol{q}_n), \text{ with } \phi_n(\boldsymbol{q} - \boldsymbol{q}_n) = \exp(-(\boldsymbol{q} - \boldsymbol{q}_n)^T D(\boldsymbol{q} - \boldsymbol{q}_n)), \tag{1}$$

$\boldsymbol{q}_0 = 0$ and $\phi_0(\boldsymbol{q}) = e^{-\boldsymbol{q}^T D_0 \boldsymbol{q}}$. The tensor D is assumed to have a cylindrical shape with eigenvalues $\sigma_0, \sigma_1, \sigma_2$ such that $\sigma_1 = \sigma_2$. The interpolation weights w_n's can then be computed by solving the following linear system: $E(\boldsymbol{q}_i) = \sum_{n=0}^{N} w_n \phi_n(\boldsymbol{q}_i - \boldsymbol{q}_n)$ for $i = 0, \ldots, N$ with $E(0) = 1$. Due to antipodal symmetry, we enforce equal coefficients for $\phi_n(\boldsymbol{q} - \boldsymbol{q}_n)$ and $\phi_n(\boldsymbol{q} + \boldsymbol{q}_n)$.

3.1 Closed Form Expressions for EAP and ODF

The EAP is given by the Fourier transform of $\hat{E}(\boldsymbol{q})$. Since the constructed $\hat{E}(\boldsymbol{q})$ is a linear combination of Gaussian functions, its Fourier transform is given by a linear combination of the Fourier transforms of the individual basis functions. Hence, the estimated EAP is of the form $P(\boldsymbol{r}) = \mathscr{F}(\hat{E}(\boldsymbol{q})) = \sum_{n=0}^{N} w_n \Phi_n(\boldsymbol{r})$ with $\Phi_0 = \mathscr{F}(\phi_0(\boldsymbol{q}))$ and $\Phi_n = \mathscr{F}(\phi_n(\boldsymbol{q} - \boldsymbol{q}_n) + \phi_n(\boldsymbol{q} + \boldsymbol{q}_n))$. In particular, Φ_0 is given by

$$\Phi_0(\boldsymbol{r}) = \int_{\mathbb{R}^3} e^{-i2\pi \boldsymbol{r}^T \boldsymbol{q}} e^{-\boldsymbol{q}^T D_0 \boldsymbol{q}} d\boldsymbol{q} = \pi^{\frac{3}{2}} |D_0|^{-\frac{1}{2}} e^{-\pi^2 \boldsymbol{r}^T D_0^{-1} \boldsymbol{r}}. \tag{2}$$

A translation of a basis function leads to a phase shift of its Fourier transform, i.e. $\mathscr{F}(\phi_n(\boldsymbol{q} + \boldsymbol{q}_n)) = e^{i2\pi \boldsymbol{r}^T \boldsymbol{q}_n} \mathscr{F}(\phi_n(\boldsymbol{q}))$. Hence, for $n \geq 1$,

$$\Phi_n(\boldsymbol{r}) = 2\pi^{\frac{3}{2}} |D|^{-\frac{1}{2}} \cos(2\pi \boldsymbol{r}^T \boldsymbol{q}_n) e^{-\pi^2 \boldsymbol{r}^T D^{-1} \boldsymbol{r}}. \tag{3}$$

The ODF is computed from the EAP by evaluating the integral $\Psi(\boldsymbol{u}) = \int_0^\infty P(r\boldsymbol{u}) r^2 dr$ [17], where $\boldsymbol{u}$ is a unit vector and r is the radial co-ordinate. From the propagator $P(\boldsymbol{r})$, $\Psi(\boldsymbol{u})$ is given analytically as $\Psi(\boldsymbol{u}) = \sum_{n=0}^{N} w_n \Psi_n(\boldsymbol{u})$ with

$$\Psi_0(\boldsymbol{u}) = \frac{1}{4\pi |D_0|^{\frac{1}{2}} (\boldsymbol{u}^T D_0^{-1} \boldsymbol{u})^{\frac{3}{2}}} \tag{4}$$

and

$$\Psi_n(\boldsymbol{u}) = \frac{1}{2\pi |D|^{\frac{1}{2}} (\boldsymbol{u}^T D^{-1} \boldsymbol{u})^{\frac{3}{2}}} \left(1 - \frac{2(\boldsymbol{u}^T \boldsymbol{q}_n)^2}{\boldsymbol{u}^T D^{-1} \boldsymbol{u}}\right) e^{-\frac{(\boldsymbol{u}^T \boldsymbol{q}_n)^2}{\boldsymbol{u}^T D^{-1} \boldsymbol{u}}}, \; n \geq 1. \tag{5}$$

3.2 Expressions for RTOP and MSD

Similarly, closed form expressions for RTOP and MSD can be computed. RTOP, which is given by $\int_{\mathbb{R}^3} \hat{E}(\boldsymbol{q}) d\boldsymbol{q}$, is simply $P(0) = \pi^{\frac{3}{2}} (w_0 |D_0|^{-\frac{1}{2}} + 2|D|^{-\frac{1}{2}} \sum_{n=1}^{N} w_n)$. Similarly, the MSD, which is given by $\int_{\mathbb{R}^2} P(\boldsymbol{r}) \|\boldsymbol{r}\|^2 d\boldsymbol{r}$, can be

computed from $\int_{\mathbb{R}^2} \Phi_0(\boldsymbol{r})\|\boldsymbol{r}\|^2 d\boldsymbol{r} = \frac{1}{2\pi^2}\text{trace}(D_0)$, and

$$\int_{\mathbb{R}^2} \Phi_n(\boldsymbol{r})\|\boldsymbol{r}\|^2 d\boldsymbol{r} = \frac{1}{\pi^2}\left(\text{trace}(D) - 2\boldsymbol{q}_n^T D^2 \boldsymbol{q}_n\right) e^{-\boldsymbol{q}_n^T D \boldsymbol{q}_n}.$$

3.3 The Relation to Radial Basis Functions Method

The radial basis functions method [15] is a special case of the proposed framework where radially symmetric Gaussian functions centered at the sample locations are used to represent diffusion measurement. The basis function is of the form $\phi_n^{\text{rbf}} = e^{-\sigma\|\boldsymbol{q}-\boldsymbol{q}_n\|^2}$ which corresponds to an isotropic tensor $D = \sigma I_{3\times 3}$. The corresponding EAP is expressed as $P(r) = \sum_{n=1}^{N} w_n \Phi_n^{\text{rbf}}(\boldsymbol{r})$ with

$$\Phi_n^{\text{rbf}}(\boldsymbol{r}) = 2\left(\frac{\pi}{\sigma}\right)^{\frac{3}{2}} \cos(2\pi \boldsymbol{r}^T \boldsymbol{q}_n) e^{-\frac{\pi^2\|\boldsymbol{r}\|^2}{\sigma}}.$$

The ODF is given by $\Psi(\boldsymbol{u}) = \sum_{n=1}^{N} w_n \Psi_n^{\text{rbf}}(\boldsymbol{u})$ with

$$\Psi_n^{\text{rbf}}(\boldsymbol{u}) = \frac{1}{2\pi}\left(1 - 2\sigma(\boldsymbol{u}^T\boldsymbol{q}_n)^2\right) e^{-\sigma(\boldsymbol{u}^T\boldsymbol{q}_n)^2}.$$

3.4 Estimation Procedure

We discuss different methods for estimating the coefficients w_n. From the samples at N locations in the q-space, we obtain an $N+1$ dimensional vector e with the first entry being the measurement at the origin. The tensor D_0 is computed as in standard DTI [3], while the tensor D is chosen to have the same eigenvectors as D_0. One constructs an $(N+1)\times(N+1)$ dimensional matrix A with

$$A(i,1) = \phi_0(\boldsymbol{q}_{i-1}) \text{ and } A(i,j) = \phi_j(\boldsymbol{q}_{i-1} - \boldsymbol{q}_{j-1}) + \phi_j(\boldsymbol{q}_{i-1} + \boldsymbol{q}_{j-1})$$

for $j \geq 1$ and $i = 1, \ldots, N+1$. We denote by w, an $N+1$ vector whose entries are the coefficients w_n to be estimated. A simple method to estimate w is $w = A^{-1}e$. However, to avoid ill conditioned matrices A, a Tikhonov regularized solution is given by $w_{\ell_2} = (A^TA + \lambda I)^{-1}A^Te$ where $\lambda > 0$ is a regularization parameter.

This method, however, does not account for the fact that the diffusion measurements are monotonically decreasing with increasing b-values. Moreover, the diffusion propagator should be positive and the value of the measurement at the origin is known to be one. Thus, one could numerically enforce these constraints while estimating the vector of weight w. The corresponding function then becomes: $\min_w \|Aw - e\|^2 + \lambda\|w\|^2$, s.t. $Bw \geq 0, c^Tw = 1$. The matrix B is of the form

$B = [B_1^T, B_2^T]^T$ with each column of B_1 being the difference of a Gaussian basis functions ϕ_n along a given set of gradient directions at several b-value shells and each column of B_2 being the evaluation of Φ_n at given set of locations for $\boldsymbol{r}$. The vector c contains the values of the basis functions at the origin. We note that these constraints are always feasible and a trivially feasible element is given by $w = [1, 0, \ldots, 0]^T$.

4 Experiments

We tested our method on a data set acquired from a spherical physical phantom with a crossing angle of 45 degree [10]. We acquired ten separate scans of the phantom with the 5 different b-values $b = \{1{,}000, 2{,}000, 3{,}000, 4{,}000, 5{,}000\}\,\mathrm{s/mm^2}$ and each b-value shell consisted of 81 gradient directions. The ten scans were averaged to obtain the "gold-standard" data. The test data set was acquired as follows: For each of the following number of gradient directions $K = \{16, 20, 24, 26, 30, 36, 42, 60, 81\}$ we acquired the diffusion measurement over 2 b-shells corresponding to $b = \{1{,}000, 3{,}000\}\,\mathrm{s/mm^2}$. Further, five repetitions were acquired for each of these data samples to test the effect of noise on signal reconstruction quality. Each acquisition had an average SNR of about 8.5.

4.1 Comparison Metrics

We used several quantitative metrics to test the ability of the proposed algorithm. Let $\hat{E}_{\boldsymbol{x}}$ denote the reconstructed signal in the voxel at location $\boldsymbol{x}$ and $E_{\boldsymbol{x},\mathrm{gold}}$ be the "gold-standard" signal. The Normalized mean squared error (NMSE) in signal reconstruction was computed as

$$\mathrm{NMSE} = \frac{1}{|\Omega|} \sum_{\boldsymbol{x} \in \Omega} \frac{\|\hat{E}_{\boldsymbol{x}} - E_{\boldsymbol{x},\mathrm{gold}}\|^2}{\|E_{\boldsymbol{x},\mathrm{gold}}\|^2}$$

where Ω denotes the set of locations for all voxels. The estimated angle between the two principal diffusion directions (in case of crossing) was computed as the average estimated angle (EA) given by

$$\mathrm{EA} = \frac{1}{|\Omega_2|} \sum_{\boldsymbol{x} \in \Omega_2} |\arccos(\boldsymbol{u}_{\boldsymbol{x},1}^T \boldsymbol{u}_{\boldsymbol{x},2})|$$

where $\boldsymbol{u}_{\boldsymbol{x},1}$ and $\boldsymbol{u}_{\boldsymbol{x},2}$ denote the direction of the two peaks in the voxel at location $\boldsymbol{x}$ and Ω_2 denote the set of locations for voxels that have two peaks. The estimated angle was computed only in the voxels where only two peaks are detected. In order to know if the recovered signal missed or exaggerated the number of peaks, we

computed the percentage of false peaks (PF) given as

$$\mathrm{PF} = \frac{1}{|\Omega_{\mathrm{gold}}|} \sum_{x \in \Omega_{\mathrm{gold}}} \mathscr{B}(n_x - n_{\mathrm{gold}})$$

where Ω_{gold} denotes the set of locations for voxels that have n_{gold} peaks in gold standard data which equals to 2 in this case, $\mathscr{B}$ is an indicator function whose value is 1 if $n_x = n_{\mathrm{gold}}$ and 0 otherwise.

We used all of these metrics to quantify the reconstruction quality of the data using Gaussian basis function. We used two methods to estimate the vector w. For the first one, w was chosen as w_{ℓ_2} where the ℓ_2 regularization coefficient λ is chosen such that the condition number of $A^T A + \lambda I$ is bounded by 10^7. The second estimate of w was computed by solving a constrained quadratic programming problem. We compared the proposed methods with the ℓ_1 3D-SHORE method [4], the ℓ_2 3D-SHORE method [9], the ℓ_2 3D-SHORE method with constraint of monotonic decrease of the signal along gradient directions and the radial basis functions (RBF) method [15].

4.2 Phantom Results

Results on the "gold standard" data (where the actual angle = 45°) with different methods are summarized in Table 1. For the test data set, the estimated angle (averaged over the five acquisitions) with different number of gradient directions are shown in Fig. 1. The percentage of false peaks and NMSE are shown in Fig. 1b, c respectively. The parameters $\sigma_0 = 0.002$ and $\sigma_1 = 0.001$ were used for all the Gaussian basis functions and for all experiments done on the test data set. The estimated ODF's with 42 gradient directions (two b-values, so a total of 84 measurements) with constrained Gaussians, constrained ℓ_2 3D-SHORE, ℓ_1 3D-SHORE and radial basis functions are shown in Fig. 2a–d, respectively.

Note that, the proposed method produces much sharper ODF's compared to the 3D-SHORE method. Further, from the error metrics shown in Fig. 1, it becomes clear that the proposed method, while having a slightly higher error in terms of the estimated angle, is yet very successful in detecting the two peaks (i.e. significantly lower percentage of false negatives) compared to 3D-SHORE (see Fig. 1b). Further, the method of 3D-SHORE itself does much better if constraints are added, which was not done in the method presented in [4, 9].

Table 1 Gold standard error metrics

Method	NMSE (%)	EA (°)	Method	NMSE (%)	EA (°)
Gauss no constraints	0.2	43.8	Gauss with constraints	0.4	42.4
ℓ_2 3D-SHORE	0.3	48.8	ℓ_2 3D-SHORE with constraints	0.4	48.8
ℓ_1 3D-SHORE	0.3	45.8	RBF	0.2	46.5

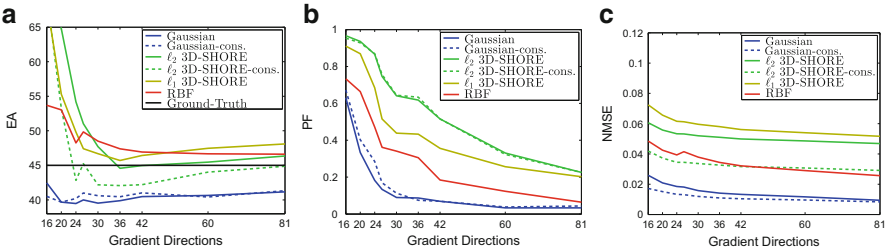

Fig. 1 (**a**) Estimated angle vs. gradient directions. (**b**) Percentage of false peaks vs. gradient directions. (**c**) NMSE vs. gradient directions

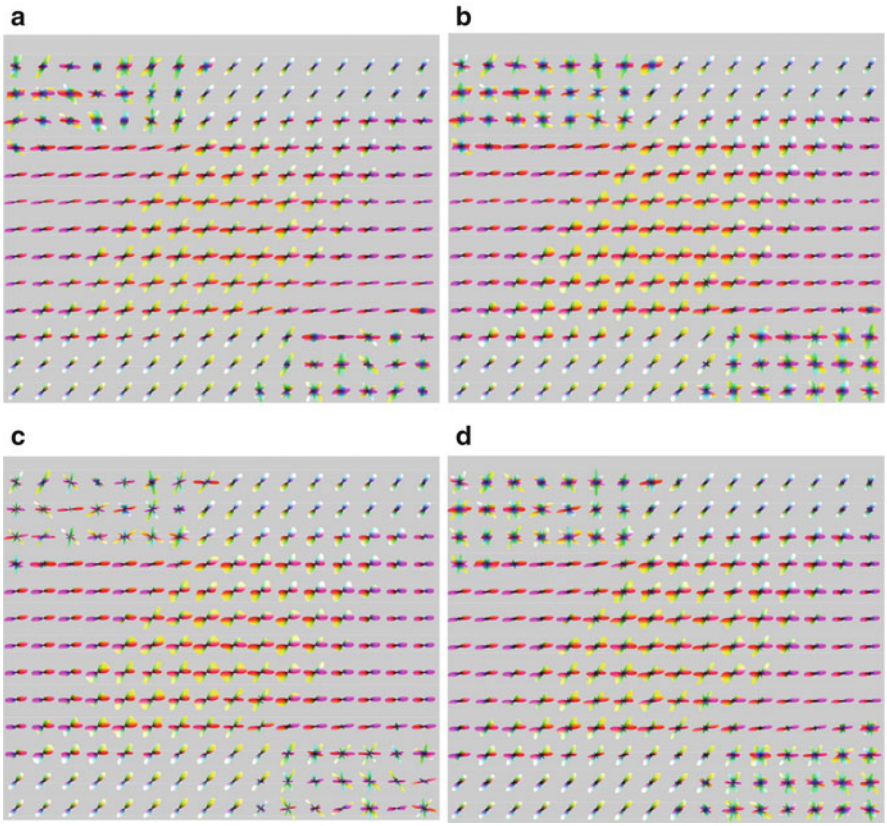

Fig. 2 Estimated ODF from measurements on 2 b-value shells with 42 gradient directions each using: (**a**) Gaussian basis functions with constraints, (**b**) ℓ_2 3-D SHORE with constraints, (**c**) ℓ_1 3-D SHORE, (**d**) radial basis functions

4.3 *In Vivo Results*

We tested our method on in-vivo human brain data with scan parameters: b-values of $\{900, 2{,}000, 3{,}600, 5{,}600\}\,\mathrm{s/mm^2}$ with each b-value shell having 60 gradient directions. This data set was considered as the "gold-standard" data. To obtain the test data, we used two subsets of this data. The first set consisted of data with b-values $b = \{900, 3{,}600\}\,\mathrm{s/mm^2}$ and 60 gradient directions on each shell, while the second set had the same b-values but 30 gradient directions per shell. For the rectangular region (white box) shown in Fig. 3c, the NMSE for these two sets compared to the "gold standard" are given in Table 2. The estimated ODF for the data set with 2 b-value shells and 60 gradient directions using the constrained Gaussians (proposed) and the constrained ℓ_2 3D-SHORE are shown in Fig. 3a and b.

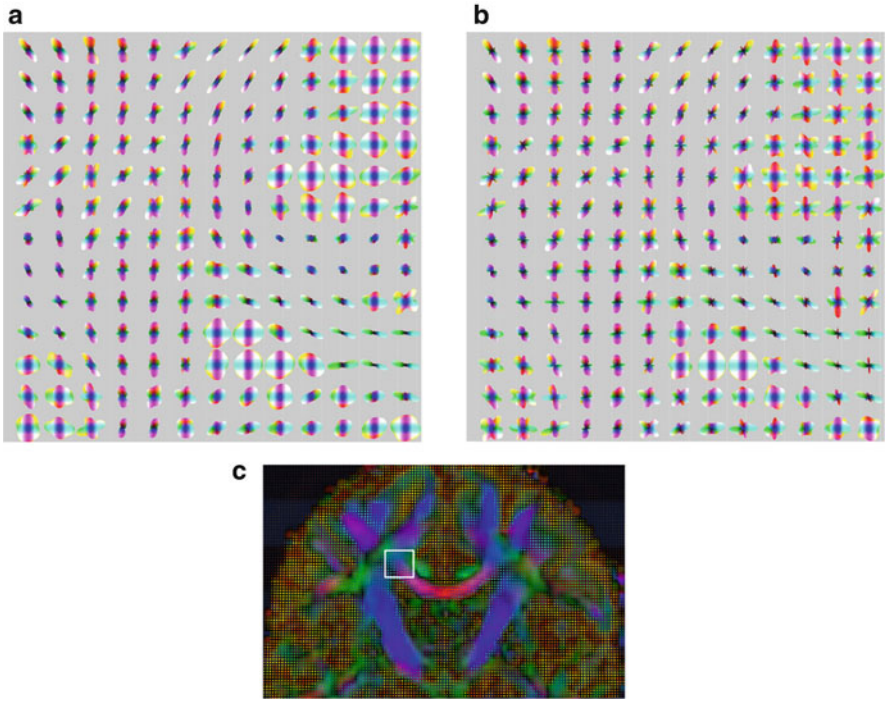

Fig. 3 Estimated ODF for the rectangle region in the color FA image (**c**) from measurements on 2 b-value shells with 60 gradient directions using: (**a**) Gaussian basis functions with constraints; (**b**) ℓ_2 3-D SHORE with constraints; (**c**) color FA image

Table 2 NMSE compared to "gold standard"

Test set	Gauss (%)	Gauss-cons (%)	ℓ_2 3D-SHORE (%)	ℓ_2 3D-SHORE-cons (%)	ℓ_1 3D-SHORE (%)	RBF (%)
1	3.6	3.5	6.5	4.5	7.2	4.3
2	5.6	3.9	7.4	5.4	7.9	7.8

5 Conclusion

In this work, we proposed a novel method of using anisotropic Gaussian functions centered at several locations in q-space to represent the diffusion signal and derive analytical expressions for the EAP, the MSD and RTOP. By using the same set of parameters, we showed the robustness of the proposed method to different number of gradient directions on a physical phantom data with very high noise (SNR = 8.5). We also showed that the 3D-SHORE method works better if it is constrained to ensure monotonic decrease of the signal with increasing b-value. Quantitatively, the proposed method seems to have lower error in detecting the crossing peaks compared to 3D-SHORE and RBF. A limitation of the current method is that the user has to choose the eigenvalues of the tensor for the Gaussian basis functions, which can be also be chosen by minimizing the fitting error in a leave-one-out cross-validation scheme [16].

Acknowledgements This work has been supported by NIH grants: R01MH097979 (Rathi), R01MH074794 (Westin), P41RR013218, P41EB015902 (Kikinis, Core PI: Westin), and Swedish research grant VR 2012-3682 (Westin).

References

1. Assaf, Y., Freidlin, R.Z., Rohde, G.K., Basser, P.J.: New modeling and experimental framework to characterize hindered and restricted water diffusion in brain white matter. Magn. Reson. Med. **52**(5), 965–978 (2004)
2. Assemlal, H.E., Tschumperlé, D., Brun, L.: Efficient and robust computation of PDF features from diffusion MR signal. Med. Image Anal. **13**(5), 715–729 (2009)
3. Basser, P., Mattiello, J., LeBihan, D.: Estimation of the effective self-diffusion tensor from the NMR spin echo. J. Magn. Reson., Ser. B **103**(3), 247–254 (1994)
4. Cheng, J., Ghosh, A., Jiang, T., Deriche, R.: Model-free and analytical EAP reconstruction via spherical polar Fourier diffusion MRI. In: Medical Image Computing and Computer-Assisted Intervention–MICCAI 2010, pp. 590–597. Springer (2010)
5. Descoteaux, M., Deriche, R., Le Bihan, D., Mangin, J.F., Poupon, C.: Multiple q-shell diffusion propagator imaging. Med. Image Anal. **15**(4), 603–621 (2011)
6. Hosseinbor, A.P., Chung, M.K., Wu, Y.C., Alexander, A.L.: Bessel fourier orientation reconstruction (bfor): an analytical diffusion propagator reconstruction for hybrid diffusion imaging and computation of q-space indices. NeuroImage **64**, 650–670 (2013)

7. Jian, B., Vemuri, B.C.: A unified computational framework for deconvolution to reconstruct multiple fibers from diffusion weighted MRI. IEEE Trans. Med. Imaging **26**(11), 1464–1471 (2007)
8. Lanczos, C.: Applied Analysis. Courier Dover Publications (1988)
9. Merlet, S.L., Deriche, R.: Continuous diffusion signal, EAP and ODF estimation via compressive sensing in diffusion MRI. Med. Image Anal. **17**(5), 556–572 (2013)
10. Moussavi-Biugui, A., Stieltjes, B., Fritzsche, K., Semmler, W., Laun, F.B.: Novel spherical phantoms for Q-ball imaging under in vivo conditions. Magn. Reson. Med. **65**(1), 190–194 (2011)
11. Özarslan, E., Koay, C., Shepherd, T., Blackb, S., Basser, P.: Simple harmonic oscillator based reconstruction and estimation for three-dimensional q-space MRI. In: ISMRM 17th Annual Meeting and Exhibition, Honolulu, p. 1396 (2009)
12. Özarslan, E., Koay, C.G., Shepherd, T.M., Komlosh, M.E., İrfanoğlu, M.O., Pierpaoli, C., Basser, P.J.: Mean apparent propagator (MAP) MRI: A novel diffusion imaging method for mapping tissue microstructure. NeuroImage **78**, 16–32 (2013)
13. Rathi, Y., Gagoski, B., Setsompop, K., Michailovich, O., Grant, P.E., Westin, C.F.: Diffusion propagator estimation from sparse measurements in a tractography framework. In: Medical Image Computing and Computer-Assisted Intervention–MICCAI 2013, pp. 510–517. Springer (2013)
14. Rathi, Y., Michailovich, O., Setsompop, K., Bouix, S., Shenton, M.E., Westin, C.F.: Sparse multi-shell diffusion imaging. In: Medical Image Computing and Computer-Assisted Intervention–MICCAI 2011, pp. 58–65. Springer (2011)
15. Rathi, Y., Niethammer, M., Laun, F., Setsompop, K., Michailovich, O., Grant, P.E., Westin, C.F.: Diffusion propagator estimation using radial basis functions. In: Computational Diffusion MRI and Brain Connectivity, pp. 57–66. Springer (2014)
16. Rippa, S.: An algorithm for selecting a good value for the parameter c in radial basis function interpolation. Adv. Comput. Math. **11**(2–3), 193–210 (1999)
17. Wedeen, V.J., Hagmann, P., Tseng, W.Y.I., Reese, T.G., Weisskoff, R.M.: Mapping complex tissue architecture with diffusion spectrum magnetic resonance imaging. Magn. Reson. Med. **54**(6), 1377–1386 (2005)
18. Wu, Y., Alexander, A.: Hybrid diffusion imaging. NeuroImage **36**(3), 617–629 (2007)
19. Zhang, H., Schneider, T., Wheeler-Kingshott, C.A., Alexander, D.C.: NODDI: Practical *in vivo* neurite orientation dispersion and density imaging of the human brain. Neuroimage **61**(4), 1000–1016 (2012)

An Analytical 3D Laplacian Regularized SHORE Basis and Its Impact on EAP Reconstruction and Microstructure Recovery

Rutger Fick, Demian Wassermann, Gonzalo Sanguinetti, and Rachid Deriche

Abstract In diffusion MRI, the reconstructed Ensemble Average Propagator (EAP) from the diffusion signal provides detailed insights on the diffusion process and the underlying tissue microstructure. Recently, the Simple Harmonic Oscillator based Reconstruction and Estimation (SHORE) basis was proposed as a promising method to reconstruct the EAP. However, the fitting of the basis is sensitive to noise. To solve this we propose to use the Laplacian of the SHORE basis as a natural regularization functional. We provide the derivation of the Laplacian functional and compare its effect on EAP reconstruction with that of separated regularization of the radial and angular parts of the SHORE basis. To find optimal regularization weighting we use generalized cross-validation and validate our method quantitatively on synthetic and qualitatively on human data from the Human Connectome Project. We show that Laplacian regularization provides more accurate estimation of the signal and EAP based microstructural measures.

1 Introduction

In diffusion MRI, the acquisition and reconstruction of the diffusion signal in 3D **q**-space allows for the reconstruction of the water displacement probability, known as the Ensemble Average Propagator (EAP) [6, 16]. This EAP describes the probability density that a particle will move along a certain direction in a given diffusion time Δ. The EAP, or $P(\mathbf{r})$, is related to the diffusion signal by a Fourier transform.

$$P(\mathbf{r}) = \int_{\mathbb{R}^3} E(\mathbf{q}) e^{-2i\pi \mathbf{q}\cdot\mathbf{r}} d\mathbf{q} \tag{1}$$

where $\mathbf{r}$ is a displacement vector in $\mathbf{r}$-space and $E(\mathbf{q})$ is the measured diffusion signal at wave vector $\mathbf{q}$ sampled in $\mathbf{q}$-space. Here $\mathbf{q}$ is related to the applied magnetic field gradient magnitude, direction and duration [6, 16]. Historically, the diffusion

R. Fick (✉) • D. Wassermann • G. Sanguinetti • R. Deriche
Athena, Inria Sophia Antipolis – Méditerranée, France
e-mail: rutger.fick@inria.fr; demian.wassermann@inria.fr; gsangui@gmail.com; rachid.deriche@inria.fr

L. O'Donnell et al. (eds.), *Computational Diffusion MRI*, Mathematics and Visualization, DOI 10.1007/978-3-319-11182-7_14

tensor (DT) [4] was the first model to describe the EAP by assuming it lies within the family of Gaussian distributions, though this assumption also limits its ability to describe complex tissue structures. To overcome this limition, so-called high angular resolution diffusion imaging (HARDI) methods such as Q-ball imaging [18] and constrained spherical deconvolution [17] were developed that are able to resolve the directionality of more complicated fiber bundle configurations. However, these models still make restricting assumptions on the shape of the EAP, which limits their ability to describe the full 3D EAP in an unbiased way. It is possible to reconstruct the EAP without any prior knowledge or restrictions using acquisition schemes such as Diffusion Spectrum Imaging (DSI) [20]. Though, DSI's need for a numerical inverse Fourier transform of $E(\mathbf{q})$, which requires a dense and lengthy sampling of $\mathbf{q}$-space, limits its clinical applicability. Indeed, an important research topic has been the accurate reconstruction of the EAP with a reduced number of samples. As a solution, models that involve analytical representations of the signal have been proposed as they provide compact representation of the 3D $\mathbf{q}$-space signal and are less sensitive to noise. Such models include the Spherical Polar Fourier (SPF) basis [2], the Solid Harmonic (SoH) basis [10] and the Simple Harmonic Oscillator based Reconstruction and Estimation (SHORE) basis [12]. These bases capture the radial and angular properties of the diffusion signal by fitting a linear combination of orthogonal dual basis functions. With a dual basis, the coefficients describing the contribution of every basis function to the signal can also be used to describe the EAP. In this way $E(\mathbf{q})$ and $P(\mathbf{r})$ are represented as

$$E(\mathbf{q}) = \sum_{n=0}^{\infty} c_n \Xi_n(\mathbf{q}) \qquad P(\mathbf{r}) = \sum_{n=0}^{\infty} c_n \Upsilon_n(\mathbf{r}) \tag{2}$$

where coefficients c_n describe the contribution of dual basis functions Ξ_n to the signal and Υ_n to the EAP. However, the fitting of the basis is sensitive to noise and appropriate regularization is required. In literature several regularization methods have been developed for such bases, most of which try to enforce smoothness in the reconstructed signal. For example, in the SoH basis only an angular Laplace Beltrami regularization term was used [10]. For the SPF basis, the combination of a radial low-pass filter and an angular Laplace Beltrami regularizer was proposed [2] (which we will now call separated regularization). Later, it was shown that the Laplacian functional for the SPF basis outperformed separated regularization [7]. For the SHORE basis, a regularization using the Laplacian functional was proposed only for 1D-SHORE [14], while for 3D-SHORE separated regularization [11] and later quadratic programming [15] was used. As for a choice of basis, an advantage of SHORE over the others is that its elements are eigenvectors of the Fourier transform, a property that ensures rapid convergence in both real and Fourier spaces [19]. For this reason, in this work we focus on regularization for the SHORE basis. Inspired by what was proposed in [7] for the SPF basis, we propose to use the full 3D Laplacian regularization of the SHORE basis as it is well suited for the smooth nature of the diffusion signal. We validate our approach in three steps: First we

simulate the intra-axonal signal for a single white matter (WM) bundle and quantify signal reconstruction based on the estimation of microstructural measures known as the Return-To-Axis and Return-To-Origin probability (RTAP and RTOP). Secondly, we generate fiber crossings and compare signal and EAP reconstruction with respect to similarity to the ground truth, and finally we compare EAP projections and ODF visualizations on human data from the Human Connectome Project.

2 Theory

The SHORE basis [12, 15] was designed to reconstruct the diffusion signal and the EAP in the complete 3D space. In this basis the diffusion signal is given by

$$\Xi_{jlm}(u_0, \mathbf{q}) = \sqrt{4\pi} i^{-l} (2\pi^2 u_0^2 q^2)^{l/2} e^{-2\pi^2 u_0^2 q^2} L_{j-1}^{l+1/2}(4\pi^2 u_0^2 q^2) Y_l^m(\mathbf{u}_q) \quad (3)$$

where $j = (n + 2 - l)/2$ is related to the radial order n and angular order l where $j \geq 1, l \geq 0$ and $\mathbf{q} = q \cdot \mathbf{u}_q$ is the $\mathbf{q}$-space vector with q its magnitude and $\mathbf{u}_q$ its normalized orientation. The real spherical harmonic basis Y_l^m was introduced in [9] with angular order l and phase factor m such that $-l \leq m \leq l$. Here $L_{j-1}^{l+1/2}$ is the generalized Laguerre polynomial and u_0 is the isotropic scale factor related to the diffusivity of the measured data. The basis functions Υ_{jlm} of the EAP are obtained by the three-dimensional inverse Fourier transform of Ξ_{jlm} resulting in

$$\Upsilon_{jlm}(u_0, \mathbf{r}) = \frac{(-1)^{j-1}}{\sqrt{2}\pi u_0^3} \left(\frac{r^2}{2u_0^2}\right)^{l/2} e^{-r^2/2u_0^2} L_{j-1}^{l+1/2}\left(\frac{r^2}{u_0^2}\right) Y_l^m(\mathbf{u}_r) \quad (4)$$

where $\mathbf{r} = r \cdot \mathbf{u}_r$ is the r-space vector with r its magnitude and $\mathbf{u}_r$ its normalized orientation. When the propagator is assumed symmetric, as is a consequence of the acquisition protocol in diffusion MRI, the number of coefficients is given by $N_{\text{coef}} = 1/6(F + 1)(F + 2)(4F + 3)$ with $F = \lfloor n_{\max}/2 \rfloor$. Note that for both bases the angular dependence is only contained in the spherical harmonics function.

As the basis functions Ξ_{jlm} are orthonormal on $\mathbb{R}^3$, we use Eq. (2) to estimate the coefficients c_n from the entire $\mathbf{q}$-space data consisting of N_{data} points. The coefficients are cast into an N_{coef}-dimensional vector $\mathbf{c}$ and the signal values are placed in an N_{data}-dimensional vector $\mathbf{y}$. Design matrix $\mathbf{Q} \in \mathbb{R}^{N_{\text{data}} \times N_{\text{coef}}}$ then has elements $\mathbf{Q}_{ij} = \Xi_i(u_0, \mathbf{q}_j)$. With these definitions, Eq. (2) turns into the matrix equation $\mathbf{y} = \mathbf{Q}\mathbf{c}$. The coefficients $\mathbf{c}$ are found by solving the least squares problem $\mathbf{c} = \text{argmin}_{\mathbf{c}} \|\mathbf{y} - \mathbf{Q}\mathbf{c}\|^2 = (\mathbf{Q}^{\mathsf{T}}\mathbf{Q})^{-1}\mathbf{Q}^{\mathsf{T}}\mathbf{y}$. Note that $\mathbf{Q}$ needs to be recomputed for every voxel as u_0 is data dependent. The EAP can then be sampled at specific positions $\mathbf{r}$ using the matrix equation $\mathbf{r} = \mathbf{K}\mathbf{c}$, where matrix $\mathbf{K} \in \mathbb{R}^{N_{\text{sample}} \times N_{\text{coef}}}$ has elements $\mathbf{K}_{ij} = \Upsilon_i(u_0, \mathbf{r}_j)$ [15]. The basis fitting can then be regularized in different ways, which we explain in the next section.

2.1 Regularization

2.1.1 Laplacian Regularization

We propose to compute the Laplacian regularization term for the fitting procedure. In this case we want to minimize the quantity $\mathbf{c} = \text{argmin}_{\mathbf{c}} \|\mathbf{y} - \mathbf{Q}\mathbf{c}\|^2 + \lambda_\Delta U(\mathbf{c})$ where λ_Δ weights the regularization functional

$$U(\mathbf{c}) = \int_{\mathbb{R}^3} \|\Delta E_{\mathbf{c}}(\mathbf{q})\|^2 d\mathbf{q} \tag{5}$$

with $E_{\mathbf{c}}(\mathbf{q}) = \sum_i c_i \Xi_i(\mathbf{q})$ the reconstructed signal and Δ is the Laplacian operator. We can then express $E_{\mathbf{c}}(\mathbf{q})$ in a summation of SHORE basis functions

$$U(\mathbf{c}) = \int_{\mathbb{R}^3} \left(\sum_i c_i \Delta \Xi_i(\mathbf{q}) \right)^2 d\mathbf{q} = \sum_i \sum_k c_i c_k \int_{\mathbb{R}^3} \Delta \Xi_i(\mathbf{q}) \cdot \Delta \Xi_k(\mathbf{q})\, d\mathbf{q} \tag{6}$$

where the subscripts i and k indicate the radial and angular order of the ith or kth basis function $\Xi_i(\mathbf{q}) = \Xi_{j(i)l(i)m(i)}(\mathbf{q})$. We can write the summations in quadratic form such that $U(\mathbf{c}) = \mathbf{c}^{\mathsf{T}}\mathbf{R}\mathbf{c}$ where regularization matrix $\mathbf{R}$ has elements

$$\mathbf{R}_{ik} = \int_{\mathbb{R}^3} \Delta \Xi_i(\mathbf{q}) \cdot \Delta \Xi_k(\mathbf{q}) d\mathbf{q}. \tag{7}$$

The equation for the elements of $\mathbf{R}$ can be solved by using the general differential equation whose solutions form the functional basis functions Ξ_{jlm} of the SHORE basis

$$\left(-\frac{\Delta}{(2\pi u_0)^2} + (2\pi u_0)^2 q^2 \right) \Xi_{jlm}(\mathbf{q}) = \Lambda_{jlm} \Xi_{jlm}(\mathbf{q}) \tag{8}$$

with $\Lambda_{jlm} = 2l + 4j - 1$ [15]. By inverting this equation we can show that

$$\Delta \Xi_{jlm}(\mathbf{q}) = 4\pi^2 u_0^2 (4\pi^2 q^2 u_0^2 - \Lambda_{jlm}) \Xi_{jlm}(\mathbf{q}). \tag{9}$$

Inserting Eq. (9) into Eq. (7), using the fact that Y_l^m is an orthonormal basis with respect to the dot product on S^2 and $L_n^\alpha(x)$ is orthonormal with respect to the weighting function $x^\alpha e^{-x}$ on $[0, \infty)$, we find the general equation for $\mathbf{R}$ as

$$\mathbf{R}_{ik} = \delta_{(l(i),l(k))} \delta_{(m(i),m(k))} R\,(j(i), j(k), l) \tag{10}$$

where we define the intermediate function R as

$$R\left(j(i), j(k), l\right) = \begin{cases} \delta_{(j(i),j(k)+2)} \frac{2^{2-l}\pi^2 u_0 \Gamma\left(\frac{5}{2}+j(k)+l\right)}{\Gamma(j(k))} \\ \delta_{(j(i),j(k)+1)} \frac{2^{2-l}\pi^2 u_0 (-3+4j(i)+2l)\Gamma\left(\frac{3}{2}+j(k)+l\right)}{\Gamma(j(k))} \\ \delta_{(j(i),j(k))} \frac{2^{-l}\pi^2 u_0 \left(3+24j(i)^2+4(-2+l)l+12j(i)(-1+2l)\right)\Gamma\left(\frac{1}{2}+j(i)+l\right)}{\Gamma(j(i))} \\ \delta_{(j(i),j(k)-1)} \frac{2^{2-l}\pi^2 u_0 (-3+4j(k)+2l)\Gamma\left(\frac{3}{2}+j(i)+l\right)}{\Gamma(j(i))} \\ \delta_{(j(i),j(k)-2)} \frac{2^{2-l}\pi^2 u_0 \Gamma\left(\frac{5}{2}+j(i)+l\right)}{\Gamma(j(i))} \end{cases} \tag{11}$$

with δ the Dirac delta function. Note that regularization matrix $\mathbf{R}$ is symmetric, mostly sparse and its elements depend only on the ordering of the basis functions and their radial and angular indices j, l and m. Using this formulation we can compute $\mathbf{R}$ up to a given $n_{\max}$ and obtain the SHORE coefficients using penalized least squares with unique minimum

$$\mathbf{c} = (\mathbf{Q}^\mathsf{T}\mathbf{Q} + \lambda_\Delta \mathbf{R})^{-1}\mathbf{Q}^\mathsf{T}\mathbf{y}. \tag{12}$$

2.1.2 Separated Regularization

In [2] a regularization method was proposed involving a separated angular Laplace Beltrami functional $\mathbf{L}$ and a radial low pass filter $\mathbf{N}$. In this case the penalized least squares equation has unique minimum

$$\mathbf{c} = (\mathbf{Q}^\mathsf{T}\mathbf{Q} + \lambda_n \mathbf{N}^\mathsf{T}\mathbf{N} + \lambda_l \mathbf{L}^\mathsf{T}\mathbf{L})^{-1}\mathbf{Q}^\mathsf{T}\mathbf{y} \tag{13}$$

with regularization weights λ_n and λ_l. Note that separated regularization has two weighting parameters, whereas our Laplacian regularization only has one, making our approach easier to tune. In the next section we explain the methods to quantify the reconstruction quality of the signal and EAP.

3 Materials and Methods

To quantify the reconstruction quality of the signal and EAP we simulate two types of data. First we generate the restricted intra-axonal diffusion signal of a single white matter (WM) bundle. On this data we quantify reconstruction quality based on the similarity to the ground truth signal and EAP and on the estimation of a microstructural measure known as the Return-to-Axis Probability (RTAP). Secondly we compute fiber crossings using a multiple compartments Gaussian model on which we quantify signal and EAP reconstruction quality.

3.1 Microstructural Data Generation and Quantification

We first generate synthetic data using a recently introduced analytical model for intra-axonal diffusion [21]. Assuming axon diameters are Gamma-distributed, this model describes the restricted intra-axonal signal perpendicular to a WM bundle as

$$E_{\text{perp}}(q_\perp;\alpha,\beta) = {}_3F_2\left(\frac{3}{2},\frac{\alpha}{2}+1,\frac{\alpha}{2}+\frac{3}{2};2,3;-16\pi^2\beta^2q_\perp^2\right) \tag{14}$$

where ${}_3F_2$ is a generalized hypergeometric function, α and β are the shape and scale parameters of the Gamma distribution and $q_\perp$ is the norm of $\mathbf{q}$ perpendicular to the fiber path. We assume axial symmetry of the diffusion signal and free diffusion along the fiber path, i.e. $E_{\text{par}}(q_\parallel, D) = \exp(-4\pi^2 q_\parallel^2 D_\parallel)$ with $q_\parallel$ the parallel component of $\mathbf{q}$ and $D_\parallel$ the parallel free water diffusivity. We simulate the intra-axonal signal similar as in [3] to be

$$E_{\text{intra}}(\mathbf{q}) = E_{\text{perp}}(q_\perp;\alpha,\beta)E_{\text{par}}(q_\parallel, D_\parallel). \tag{15}$$

Using this model the restricted intra-axonal diffusion signal in the whole $\mathbf{q}$-space can be readily obtained for any Gamma distributed axon diameter distribution. Rician noise is then added with noise variance σ such that SNR $= 1/\sigma$.

To quantify signal reconstruction based on the microstructure we use two measures known as the Return-To-Axis and Return-To-Origin probability (RTAP and RTOP) [15]. These values are known to be sensitive to the anisotropy of WM tissue. RTAP is computed as the integral of the diffusion signal on the plane perpendicular to the fiber direction and RTOP is integral of the whole 3D diffusion signal.

$$RTAP = \int_{\mathbb{R}^2} E(\mathbf{q}_\perp)d\mathbf{q}_\perp \qquad RTOP = \int_{\mathbb{R}^3} E(\mathbf{q})d\mathbf{q} \tag{16}$$

Moreover, in the case of restricted intra-axonal diffusion in a single fiber path RTAP is related to the reciprocal of the mean cross-sectional area of the axons, i.e. $\langle A\rangle = 1/RTAP$ [13].

The computations of RTOP and RTAP rely on integrals of the complete q-space, which depend highly on the extrapolation of the signal beyond the $\mathbf{q}$-space truncation. To quantify the accuracy of the extrapolation we simulate the intra-axonal signal on three equispaced shells in $\mathbf{q}$-space with 90 samples each for 22 realistic axon diameter distributions [1]. We consider two scenarios: (1) varying the maximum q-value $q_{\max}$ included in the measurements while keeping the signal-to-noise ratio (SNR) constant and (2) varying SNR while keeping $q_{\max}$ constant. In both cases we fit SHORE to the signal with different regularization methods with $n_{\max} = 6$. We quantify the accuracy of RTAP by estimating $\langle A\rangle$ and comparing the results with the ground truth $\langle A\rangle_{gt}$, which can be computed using the parameters of the Gamma distribution as $\langle A\rangle_{gt} = \alpha(\alpha+1)\beta^2$. For RTOP we directly compare the estimated values with the 3D integrals of Eq. (15).

3.2 Fiber Crossing Data Generation

To further quantify the quality of both signal and EAP reconstruction we generate synthetic fiber crossing data. The signal is simulated using a multi-compartment Gaussian model

$$E(\mathbf{q}) = \sum_{m=1}^{M} f_m \exp(-2\pi^2 \mathbf{q}^\mathsf{T} \mathbf{D}_m \mathbf{q}) \tag{17}$$

where M is the number of compartments, f_m is the relative compartment size with $\sum_{m=1}^{M} f_m = 1$ and $\mathbf{D}_m$ the corresponding diffusion tensor. We use acquisition parameters from the Human Connectome Project (HCP) where three shells with b-values $\in [1{,}000, 2{,}000, 3{,}000]\,\mathrm{s/mm^2}$ are sampled 90 times each with 5 b_0 samples per shell. A cross-section of the ground truth of the signal and EAP of an $M = 2, 72$ degree crossing with $f_1 = 0.6$ and $f_2 = 0.4$ is shown in Fig. 1. Again, Rician noise is added with noise variance σ such that SNR $= 1/\sigma$. Figure 2 shows the signal from Fig. 1a for three different noise levels. We then fit SHORE using separated and Laplacian regularization and compare signal and EAP reconstruction using the metrics given in the next section.

3.3 Error Metrics

We define two error metrics to quantify the reconstruction quality of the signal and EAP in the single WM bundle data and the multiple compartment Gaussian model. For the signal we use the L_2 metric

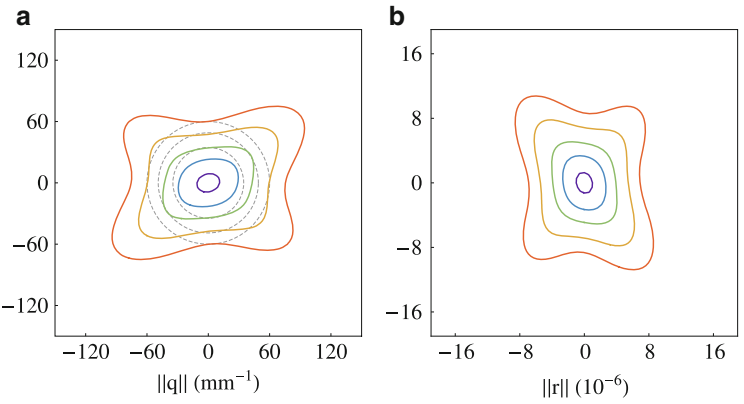

Fig. 1 Isocontour representations of the ground truth of the signal as a function of **q** (**a**) and the EAP as a function of **r** (**b**). The isocontours are color-labeled from *dark blue* (0.95 of maximum value) to *red* (0.1 of maximum value). The *dashed grey circles* in the signal represent the measured shells in **q**-space. (**a**) Ground truth signal. (**b**) Ground truth EAP

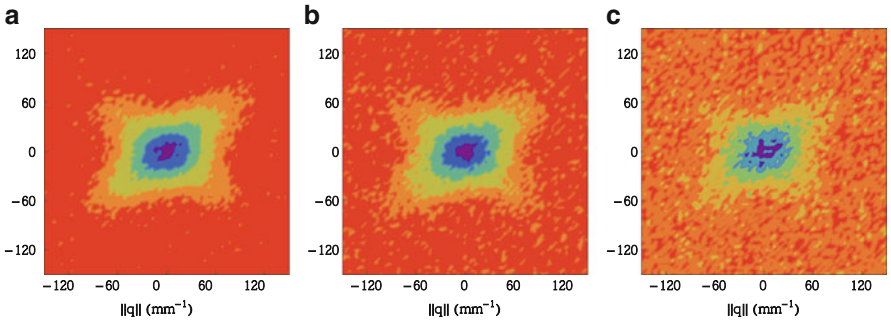

Fig. 2 The signal from Fig. 1a corrupted by Rician Noise. (**a**) SNR=30; (**b**) SNR=20; (**c**) SNR=10

$$\mathrm{L}_2(\mathbf{c}) = \int_{\mathbb{R}^3} (E_{\mathrm{GT}}(\mathbf{q}) - E_{\mathbf{c}}(\mathbf{q}))^2 d\mathbf{q} \tag{18}$$

where $E_{\mathrm{GT}}(\mathbf{q})$ is the ground truth signal and $E_{\mathbf{c}}(\mathbf{q})$ is the reconstructed signal with coefficients $\mathbf{c}$. For the EAP we use the Bhattacharyya distance (BD) [5] as it is a real metric between probability densities

$$\mathrm{BD}(\mathbf{c}) = -\ln\left(\int_{\mathbb{R}^3} \sqrt{P_{\mathrm{GT}}(\mathbf{r}) P_{\mathbf{c}}(\mathbf{r})} d\mathbf{r}\right) \tag{19}$$

where $P_{\mathrm{GT}}(\mathbf{r})$ and $P_{\mathbf{c}}(\mathbf{r})$ are the ground truth and reconstructed probability density functions of the EAP. We use these metrics to analyze the reconstruction quality for different regularization methods in the next section.

3.4 Optimal Weighting Parameter Choice

To fairly compare EAP reconstructions, we use the Generalized Cross Validation (GCV) algorithm [8] to obtain optimal regularization parameters λ_n, λ_l and λ_Δ. GCV is based on an N_{data}-fold cross validation. Fortunately, the estimation of λ as the minimum argument of the GCV function can be calculated as

$$GCV(\lambda, \mathbf{y}) = \frac{\|\mathbf{y} - \hat{\mathbf{y}}_\lambda\|}{N_{\mathrm{data}} - Tr(\mathbf{S}_\lambda)} \tag{20}$$

where $\mathbf{S}_\lambda = \mathbf{Q}(\mathbf{Q}^{\mathsf{T}}\mathbf{Q} + \lambda\mathbf{R})^{-1}\mathbf{Q}^{\mathsf{T}}$ is the smoother matrix and $\hat{\mathbf{y}}_\lambda = \mathbf{S}_\lambda\mathbf{y}$. Here $\mathbf{R}$ can contain multiple regularization functionals that can be optimized.

4 Results

4.1 Microstructure Experiments

To compare signal and EAP reconstruction quality on a single WM bundle between separated and Laplacian regularization we simulated the intra-axonal signal on three equispaced shells in **q**-space with 90 samples each for 22 realistic axon diameter distributions [1] as outlined in Eq. (14). We only generate the intra-axonal diffusion signal for two scenarios: in the first we vary $q_{\max}$ from 10 to 310 mm^{-1} in steps of 30 mm^{-1} while keeping $SNR = 20$. In the second we vary SNR between noiseless and $SNR = 5$ while keeping $q_{\max}$ at 200 mm^{-1}. In both cases we regenerate the noise 100 times per $q_{\max}$ or SNR and average the results over all axon diameter distributions and noise generations. For both datasets we compute the averaged absolute error between the estimated mean cross-sectional area $\langle A \rangle$ and ground truth $\langle A \rangle_{\mathrm{gt}}$ (Fig. 5b and c) and the values for RTOP with the ground truth (Fig. 5d and e). We do not show the results for the least squares solution as the extrapolation of the signal without regularization is completely unreliable (see Fig. 5a). It should be noted that using separated regularization approximately 2–3 % of all RTAP and RTOP estimates yield negative values, while this is only 0.03 % for Laplacian regularization.

4.2 Fiber Crossing Experiment

To quantify general fitting of the signal and EAP, the SHORE basis was fitted on a 72 degree crossing using separated and Laplacian regularization. In Fig. 3 we show the average L_2 and BD metrics for the reconstruction of the signal and EAP for 300 repetitions for every SNR. It is seen that Laplacian regularization has the lowest metrics and standard deviation for both the signal and the EAP. Furthermore, in Table 1 we show the variances for the weighting parameters,

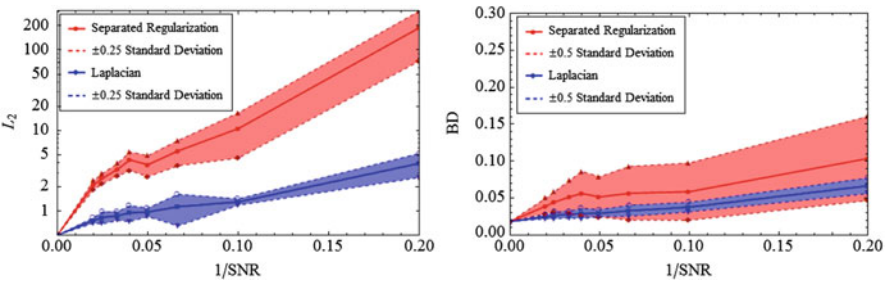

Fig. 3 The error metrics for the reconstruction of (*left*) the signal (L_2) and (*right*) the EAP (DB) as a function of 1/SNR. The L_2 plot for the signal is on a logarithmic scale. It can be seen that the Laplacian better and more reliably approximates the signal and EAP for all SNR

Table 1 Weighting parameter variances as a function of SNR

	1/SNR	0	0.02	0.025	0.033	0.040	0.050	0.067	0.100	0.200
Separated	Var(λ_n)	0	0.033	0.015	0.043	0.058	0.116	0.078	0.107	0.135
	Var(λ_l)	0	0.040	0.050	0.078	0.073	0.089	0.081	0.035	0.17
	Corr(λ_n,λ_l)	0	−0.461	−0.456	−0.633	−0.728	−0.797	−0.785	−0.727	−0.708
Laplacian	Var(λ_Δ)	0	0.027	0.028	0.030	0.026	0.026	0.031	0.057	0.031

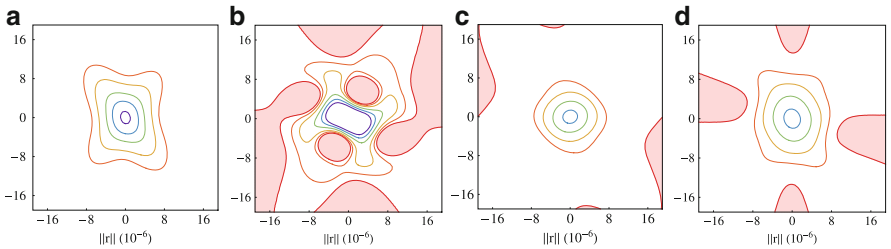

Fig. 4 A section of the ground truth of the EAP (**a**) with EAP reconstructions using no (**b**), separated (**c**) and Laplacian regularization (**d**). Noise was added such that $1/SNR = 0.1$. The *red* areas indicate negative values. The Laplacian best preserves the angular shape of the ground truth among the given methods. (**a**) EAP GT; (**b**) EAP LS; (**c**) EAP Sep; (**d**) EAP Lap

together with the Pearson correlation between λ_n and λ_l for every SNR. It can be seen that the variance for the Laplacian is much lower than those of the separated regularization. Finally, to give a visual interpretation to the graphs in Fig. 3 we show EAP reconstructions with different regularization methods at $1/SNR = 0.1$ together with the ground truth in Fig. 4. It can be seen that Laplacian regularization maintains the best angular characteristics of the ground truth, given that the signal is severely distorted (see Fig. 2c).

4.3 Human Connectome Project

In our last experiment we use the Human Connectome Project data, which was sampled on three shells with b-values $\in [1{,}000, 2{,}000, 3{,}000]\,\mathrm{s/mm^2}$, with 90 directions per shell. We selected a section in the brain near the Corpus Callosum (see Fig 6). In order to highlight reconstruction differences in the case of more noisy images we add noise to the data such that SNR = 20. We used GCV to obtain optimal weighting parameters for every voxel and we fit SHORE using $n_{\max} = 6$. In Fig. 6 we visualize the EAP at a radius of 10 and 20 μm and the ODFs using separated and our Laplacian regularization. The spherical representation of the EAP $P(\mathbf{r})$ at a certain radius $\mathbf{r}$ shows the relative probability of particles traveling this distance in the given diffusion time. It can be seen that the Laplacian attenuates spurious behaviour in the lower radius of the EAP (yellow box), though this effect is not as prominent in the ODF.

5 Discussion and Conclusion

In this paper we proposed and derived the full 3D Laplacian functional as a regularization for the fitting of the SHORE basis. We compared our proposed regularization with the previously proposed separated Laplace–Beltrami and radial low-pass filtering [2]. In our first experiment we show that Laplacian regularization

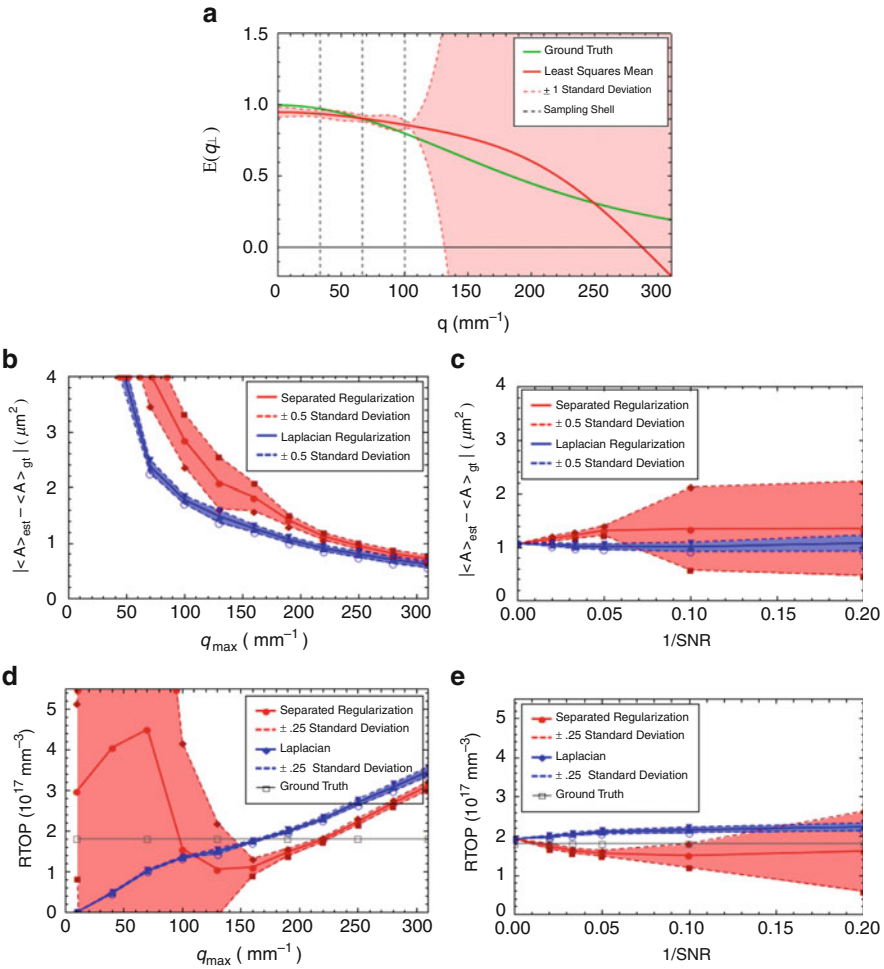

Fig. 5 (**a**) shows the Least Squares signal approximation. The *red area* indicates one standard deviation of the approximation. It can be seen that after the last sampling shell (the *grey dashed line*) the extrapolation is unreliable. (**b**) and (**c**) show the error in $\langle A \rangle$ for different regularization methods as a function of $q_{\max}$ and SNR. (**d**) and (**e**) show the values of RTOP with the ground truth. Both (**b**) and (**c**) show lower average error and lower standard deviations with Laplacian regularization under all $q_{\max}$ and SNR. (**d**) shows that with Laplacian regularization the estimated RTOP approaches the ground truth at $q_{\max}$ near 160 mm^{-1} but continues to grow as $q_{\max}$ increases. Moreover, it can be seen that RTOP for separated regularization has very unreliable estimates for low $q_{\max}$. Only after a $q_{\max}$ of 160 mm^{-1} the estimation stabilizes and a similar trend is seen of increasing RTOP as $q_{\max}$ increases. In (**e**) it can be seen that the mean RTOP becomes slightly higher than the ground truth for Laplacian regularization and slightly lower for separated regularization as SNR becomes lower. Again the Laplacian benefits from much lower standard deviations

of the SHORE basis provides more reliable estimates of microstructural features compared to separated regularization (Fig. 5). When comparing the mean and

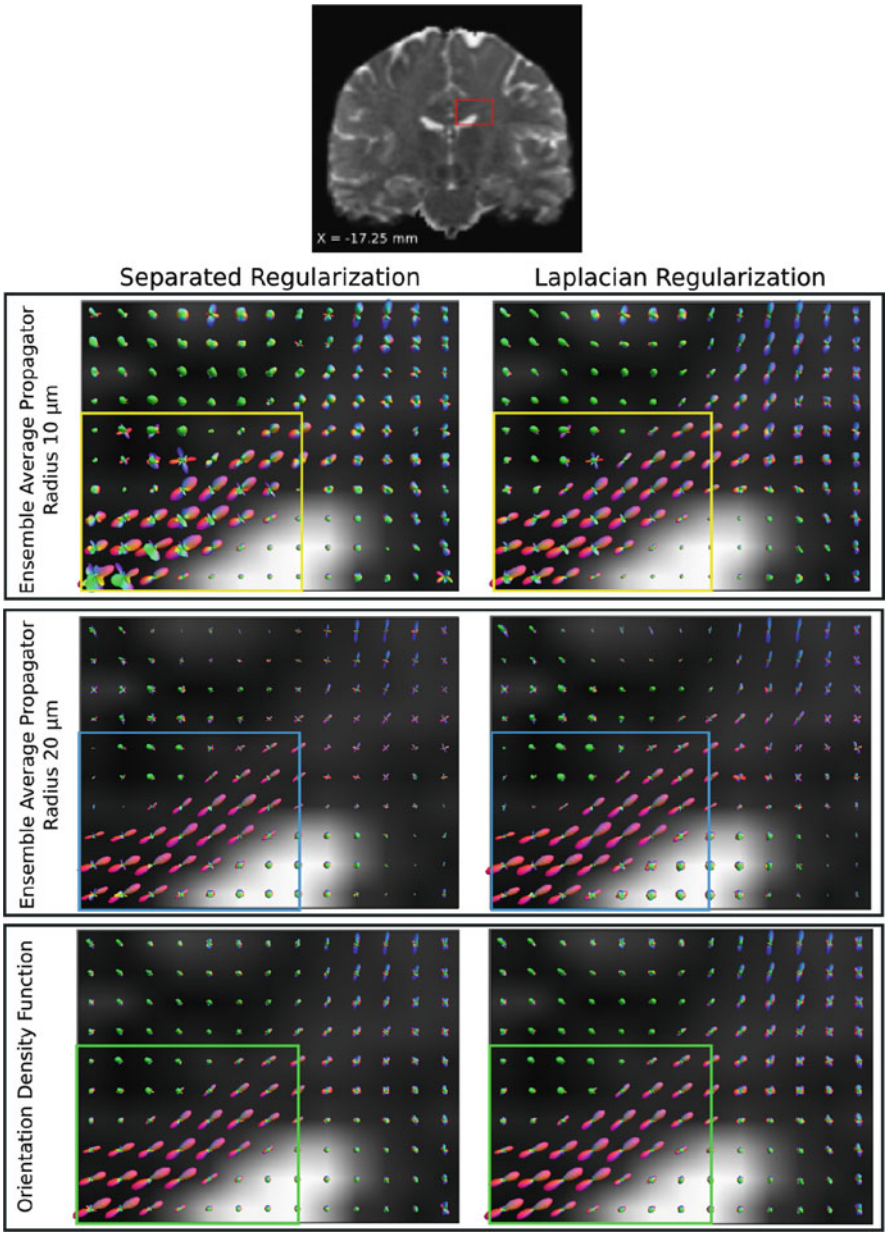

Fig. 6 Reconstructions of the EAP and ODF in an area near the Corpus Callosum of the Human Connectome Project using separated regularization (*left column*) and Laplacian regularization (*right column*). The EAP is reconstructed for two EAP radii (*top two rows*) and ODFs is given on the *bottom*. The Laplacian regularization stops spurious behaviour in the EAP compared to separated regularization (*yellow and blue rectangles*), though this effect is not as noticeable in the ODFs (*green rectangles*)

standard deviation of RTAP and RTOP between regularization methods, it can be seen that Laplacian regularization greatly improves signal extrapolation and robustness to noise at lower **q**-values and low SNR levels. The fact that almost no negative values for microstructural values were found using the Laplacian further underlines this result.

Moreover, in our second experiment we show that Laplacian regularization enables better and more reliable approximation of the signal and EAP in crossings (Fig. 3) and that the angular features of the EAP are better maintained under high levels of noise compared to separated regularization (Fig. 4). We also show that the estimation of the optimal weighting parameter is more stable for the Laplacian than for the separated implementation (Table 1), which suggests that our approach is better suited for this type of data. Finally, we provide visualization of the EAP and ODF on the Human Connectome Project dataset (Fig. 6). It can be seen that the influence of the regularization, while visible in the EAP, is not as noticeable on the ODFs.

Nonetheless, combined with the results of the other experiments in this work, we believe that the accurate approximation of the signal and EAP is essential to understanding the underlying microstructure, and appropriate regularization such as our Laplacian approach is therefore fundamental.

Acknowledgements Data were provided [in part] by the Human Connectome Project, WU-Minn Consortium (Principal Investigators: David Van Essen and Kamil Ugurbil; 1U54MH091657) funded by the 16 NIH Institutes and Centers that support the NIH Blueprint for Neuroscience Research; and by the McDonnell Center for Systems Neuroscience at Washington University.

References

1. Alexander, D.C.: A general framework for experiment design in diffusion MRI and its application in measuring direct tissue-microstructure features. Magn. Reson. Med. **60**, 439–448 (2008)
2. Assemlal, H.E., et al.: Efficient and Robust Computation of PDF features from diffusion MR signal. Med. Image. Anal. **13**(5), 715–729 (2009)
3. Avram, L., et al.: Three-dimensional water diffusion in impermeable cylindrical tubes: theory versus experiments. NMR Biomed. **21**(8), 888–898 (2008)
4. Basser, P.J., et al.: Estimation of the effective self-diffusion tensor from the NMR Spin Echo. J. Magn. Reson. Ser. B **103**(3), 247–254 (1994)
5. Bhattacharyya, A.: On a measure of divergence between two statistical populations defined by their probability distributions. Bull. Calcutta Math. Soc. **35**, 99–109 (1943)
6. Callaghan, P.T., et al.: High-resolution q-space imaging in porous structures. J. Magn. Reson. **90**(1), 177–182 (1990)
7. Caruyer, E., et al.: Diffusion MRI signal reconstruction with continuity constraint and optimal regularization. Med. Image. Anal. **16**(6), 1113–1120 (2012)
8. Craven, P., et al.: Smoothing noisy data with spline functions. Numer. Math. **31**(4), 377–403 (1978)
9. Descoteaux, M., et al.: Regularized, fast, and Robust analytical Q ball imaging. Magn. Reson. Med. **58**(3), 497–510 (2007)

10. Descoteaux, M., et al.: Multiple Q-shell diffusion propagator imaging. Med. Image. Anal. **15**(4), 603–621 (2011)
11. Merlet, S., et al.: Continuous diffusion signal, EAP and ODF estimation via compressive sensing in diffusion MRI. Med. Image. Anal. **17**(5), 556–572 (2013)
12. Özarslan, E., et al.: Simple harmonic oscillator based reconstruction and estimation for three-dimensional Q-space MRI (2009)
13. Özarslan, E., et al.: Nuclear magnetic resonance characterization of general compartment size distributions. New J. Phys. **13**(1), 015010 (2011)
14. Özarslan, E., et al.: Temporal scaling characteristics of diffusion as a new MRI contrast: findings in rat hippocampus. Neuroimage **60**(2), 1380–1393 (2012)
15. Özarslan, E., et al.: Mean apparent propagator (MAP) MRI: a novel diffusion imaging method for mapping tissue microstructure. NeuroImage **78**, 16–32 (2013)
16. Stejskal, E.O.: Use of spin echoes in a pulsed magnetic-field gradient study anisotropic restricted diffusion flow. J. Chem. Phys. **43**(10), 3597–3603 (1965)
17. Tournier, J., et al.: Robust determination of the fibre orientation distribution in diffusion MRI: non-negativity constrained super-resolved spherical deconvolution. NeuroImage **35**(4), 1459–1472 (2007)
18. Tuch, D.S.: Q-ball imaging. Magn. Reson. Med. **52**(6), 1358–1372 (2004)
19. Walter, G.G.: Properties of Hermite series estimation of probability density. Ann. Stat. **5**, 1258–1264 (1977)
20. Wedeen, V.J., et al.: Mapping complex tissue architecture with diffusion spectrum magnetic resonance imaging. Magn. Reson. Med. **54**(6), 1377–1386 (2005)
21. Sanguinetti, G., Deriche, R.: Mapping average axon diameters under long diffusion time. ISBI (2014)

Part V
Post-processing

Motion Is Inevitable: The Impact of Motion Correction Schemes on HARDI Reconstructions

Shireen Elhabian, Yaniv Gur, Clement Vachet, Joseph Piven, Martin Styner, Ilana Leppert, G. Bruce Pike, and Guido Gerig

Abstract Diffusion weighted imaging (DWI) is known to be prone to artifacts related to motion originating from subject movement, cardiac pulsation and breathing, but also to mechanical issues such as table vibrations. Given the necessity for rigorous quality control and motion correction, users are often left to use simple heuristics to select correction schemes, but do not fully understand the consequences of such choices on the final analysis, moreover being at risk to introduce con-

[*] The NIH funded Autism Centers of Excellence Infant Brain Imaging Study (ACE-IBIS) Network: Clinical Sites: University of North Carolina: J. Piven (IBIS Network PI), H.C. Hazlett, C. Chappell; University of Washington: S. Dager, A. Estes, D. Shaw; Washington University: K. Botteron, R. McKinstry, J. Constantino, J. Pruett; Children's Hospital of Philadelphia: R. Schultz, S. Paterson; University of Alberta: L. Zwaigenbaum; Data Coordinating Center: Montreal Neurological Institute: A.C. Evans, D.L. Collins, G.B. Pike, V. Fonov, P. Kostopoulos; Samir Das; Image Processing Core: University of Utah: G. Gerig; University of North Carolina: M. Styner; Statistical Analysis Core: University of North Carolina: H. Gu.

S. Elhabian (✉) • Y. Gur • C. Vachet • G. Gerig
Scientific Computing and Imaging Institute, Salt Lake City, UT, USA
e-mail: shireen@sci.utah.edu; yanivg@sci.utah.edu; cvachet@sci.utah.edu; gerig@sci.utah.edu

J. Piven
Department of Psychiatry, University of North Carolina, Wilmington, NC, USA
e-mail: jpiven@med.unc.edu

M. Styner
Department of Psychiatry and Department of Computer Science, University of North Carolina, Wilmington, NC, USA
e-mail: styner@unc.edu

I. Leppert
Department of Neurology and Neurosurgery, Montreal Neurological Institute, Montreal, QC, Canada
e-mail: ilana@bic.mni.mcgill.ca

G. Bruce Pike
Department of Neurology and Neurosurgery, Montreal Neurological Institute, Montreal, QC, Canada

Department of Radiology, University of Calgary, Calgary, AB, Canada
e-mail: bruce.pike@mcgill.ca

L. O'Donnell et al. (eds.), *Computational Diffusion MRI*, Mathematics and Visualization, DOI 10.1007/978-3-319-11182-7_15

founding factors in population studies. This paper reports work in progress towards a comprehensive evaluation framework of HARDI motion correction to support selection of optimal methods to correct for even subtle motion. We make use of human brain HARDI data from a well controlled motion experiment to simulate various degrees of motion corruption. Choices for correction include exclusion or registration of motion corrupted directions, with different choices of interpolation. The comparative evaluation is based on studying effects of motion correction on three different metrics commonly used when using DWI data, including similarity of fiber orientation distribution functions (fODFs), global brain connectivity via Graph Diffusion Distance (GDD), and reproducibility of prominent and anatomically defined fiber tracts. Effects of various settings are systematically explored and illustrated, leading to the somewhat surprising conclusion that a best choice is the alignment and interpolation of all DWI directions, not only directions considered as corrupted.

1 Introduction

In today's clinical diffusion-weighted (DW)-MRI acquisitions, subject motion is considered one of the most relevant sources of noise artifacts [1], ranging from physiological motion such as cardiac pulsation, to physical (voluntary or involuntary) movement by the patient. While physiological motion can be controlled by gating or in the sequence design, the physical patient movement during the diffusion-encoding gradient pulses leads to severe signal perturbation which results in a significant signal phase shift, or signal loss [2].

During a scanning session, the degree of patient's cooperation may vary. For example, elderly people who may become uncomfortable during large scanning sessions, patients in pain who become restless and agitated during a scan and unsedated pediatric subjects who will not cooperate long enough to be imaged without motion artifacts, to name a few. As such, it is safe to assume that there are always motion artifacts in any given DW-MRI acquisition, a proof-of-concept of this hypothesis being presented in Sect. 2.1.1.

Motion effects can be reduced by real-time motion detection [3, 4], where the acquisition and the source of motion are synchronized so that the data is never corrupted. However, this prospective approach for motion correction might affect the acquisition time. Further there is no guarantee that the head will ever move back to the original position. Alternatively, the exclusion of one or more gradients

bearing strong motion artifacts can be exercised [5], a.k.a motion scrubbing in functional MRI, however, this limits the ability to reconstruct crossing fibers especially at small separation angles. As such, post-acquisition motion correction is imperative to guarantee voxel-wise correspondence between different DWIs referring to the same anatomical structure. A common practice is to heuristically select transformation parameter thresholds for detection of motion outliers, where registration and interpolation is applied to gradient directions that are claimed to be corrupted.

To mitigate motion artifacts, raw DWIs are usually co-registered to the least diffusion-weighted images using rigid transformation. Software packages for image-based registration of DWIs are becoming readily available, e.g. FSL-MCFLIRT [6], the Advanced Normalization Tools (ANTS) [7], TORTOISE [8] and DTIPrep [9]. Nonetheless, the interpolation step of a typical registration approach has been shown to significantly change the noise properties of DWIs [10].

The optimal pre-processing pipeline for HARDI sequences remains an open question and a challenge on real data. For example, is there a threshold that would identify a motion-corrupted volume? How sensitive are HARDI reconstructions to such a pre-defined threshold? What is the impact of various motion-correction schemes on subsequent HARDI-based reconstructions and tractography? So far, these issues have received, surprisingly, little attention in various DW-MRI studies of clinical populations.

This study does not focus on the closeness of HARDI-based reconstructions to an existing truth, but on the effect of pre-processing schemes, in particular motion correction, commonly deployed as a post-acquisition step, on succeeding steps. In this paper, we propose a comprehensive experimental framework (see Fig. 1) that enables making use of human brain HARDI data from a well controlled motion experiment to simulate various degrees of motion corruption. Choices for correction include scrubbing or registration of motion corrupted directions, with different choices of interpolation, and also the option of registration/interpolation of all directions. The comparative evaluation covers three different metrics, including similarity of fiber orientation distribution functions (fODFs) via Jensen-Shannon divergence (JSD), global brain connectivity via Graph Diffusion Distance (GDD), and reproducibility of four anatomically-defined fiber pathways via Cohen's Kappa statistics.

On the basis of our findings, we recommend assuming there is always motion, even subtle, in the acquired scans. As such, motion correction needs to be applied to all gradient directions without relying heuristically on a threshold which determines a gradient direction to be claimed as motion corrupted.

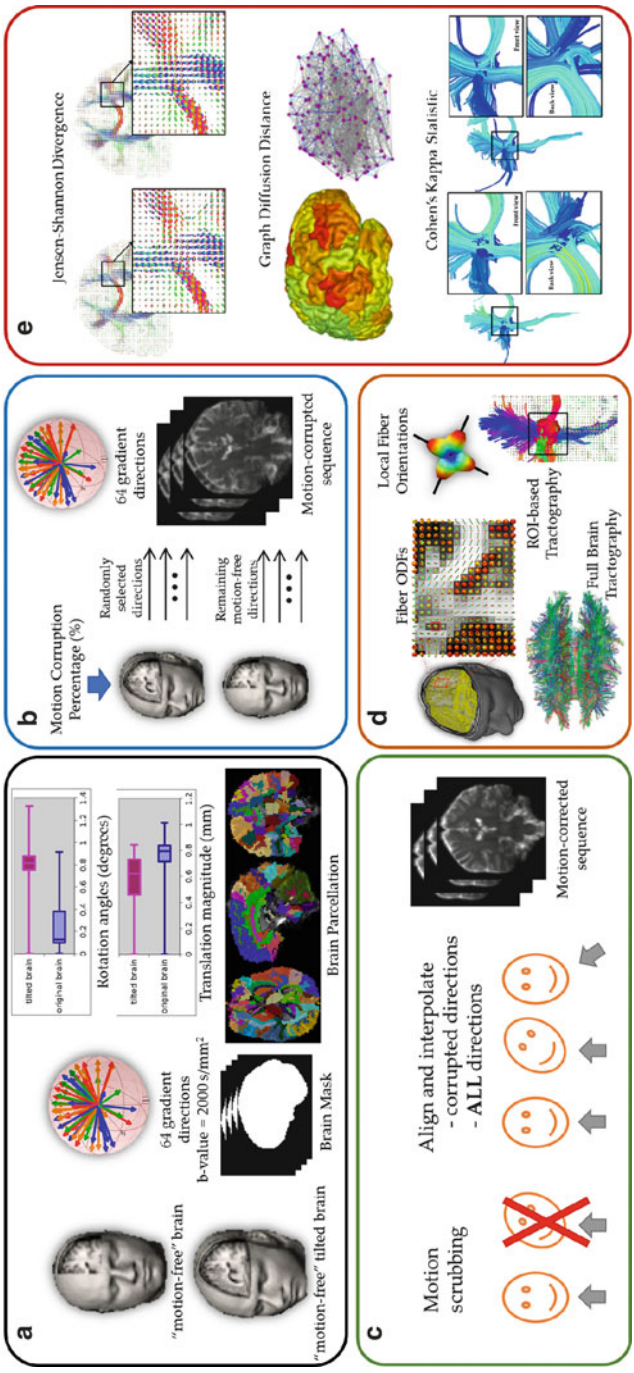

Fig. 1 Experimental framework for subject motion simulation and HARDI-based reconstructions evaluation. (**a**) Data acquisition/preprocessing. (**b**) Motion simulation. (**c**) Motion correction schemes. (**d**) Reconstruction. (**e**) Evaluation

2 Materials and Methods

2.1 Phantom Acquisition

2.1.1 Proof-of-Concept

To backup our assumption that motion is omnipresent, we analyze data from three healthy human volunteers (males 30–40 years-old) visiting four clinical sites where they signed a generic consent form at each site agreeing to be scanned for research purposes. Each subject was scanned twice on a 3T Siemens Tim Trio scanner with a strict calibration of image acquisition parameters. The scanning environment was well controlled, a comfortable padding was used to minimize head motion while urging participants to remain without movement. Eddy current was compensated by using a Twice-refocused Spine Echo (TRSE) protocol, with FoV = 209 mm, 76 transversal slices, thickness = 2 mm, $(2\,\text{mm})^3$ voxel resolution, matrix size = 106^2, TR = 11,100 ms, TE = 103 ms, one baseline image with zero *b*-value and 64 DWI with b-value at 2,000 s/mm^2, with total scan time of 12.5 min.

FSL-MCFLIRT [6] was then used to provide the rigid transformation matrix (6 DOF) for each image volume having the baseline image as the reference for motion correction and normalized mutual information as the cost function. To quantify motion, we used the magnitude of the translation vector (in mm) as well as the axis-angle rotation representation (in degrees). The boxplots in Fig. 2 show the rotational and translational components of the motion being detected from a total of 24 DWI datasets. This shows an experimental proof of the existence of quantifiable motion (on average 0.39° rotation and 0.61 mm translation), even subtle, in the acquired HARDI data. The graphs in Fig. 2 illustrate the arbitrariness of common calculation of percentage of motion corruption, here shown as a function of thresholding on the estimated motion parameters.

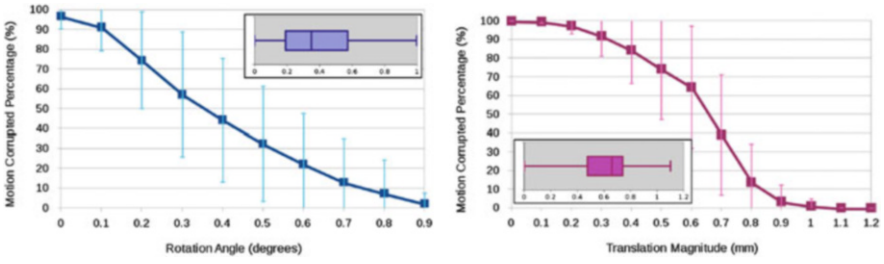

Fig. 2 Average and standard deviation of the percentage of motion-corrupted gradient directions as a function of thresholding on the estimated rotation angle in degrees (*left*) and the estimated translation magnitude in mm (*right*) for three human phantoms scanned twice at four clinical sites. The *boxplots* show the overall statistics of estimated motion parameters

2.1.2 Atlas-Guided White Matter Parcellation

For automated placement of 3D region-of-interests (ROIs) defining seeds for tractography and connectivity, we used the publicly available JHU-DTI-SS (a.k.a. "Eve") atlas described in [11], which includes 176 core and peripheral ROIs. To reduce variability introduced by individual parcellation in subject space, we defined a common reference for our population (multiple acquisitions of the same phantom). This is achieved by generating an unbiased average and diffeomorphic deformations from the sets of images (using tensor maps extracted from HARDI). The "Eve" Fractional Anisotropy (FA) atlas was registered to FA images of the phantom-specific atlases using the ANTS [7] tool, along with mapping of the "Eve" white matter labels. Finally, "Eve" labels were mapped back to coordinates of original HARDI data by inverse diffeomorphic transforms.

2.1.3 Human Motion Simulation

As a pilot, one human phantom was asked to be re-scanned while having the head tilted to simulate noticeable motion. The two datasets were then used to construct motion-corrupted sequences. Based on alignment of the baseline images of the two scans (original and tilted) using FSL-MCLFIRT, 12° rotation and 7 mm translation were detected, while less than 1° of rotation and 0.8 mm of translation were found when aligning individual DWIs to their corresponding baseline image. We arbitrarily considered the first out of the two scans as the "motion-free" sequence and used it as a reference for performance evaluation of different motion correction schemes. A random percentage of DW images (10, 30, 50, 70 and 90 %, each with ten different random sets of gradient directions) drawn from the second scan (tilted brain) were mixed with the first scan to construct 50 motion-corrupted datasets (10 experiments times 5 corruption percentages).

2.1.4 Motion Correction Schemes

We explored three motion correction schemes. In the first approach, we follow the motion scrubbing approach, usually deployed in functional MRI, where we exclude the affected gradient directions from subsequent computations (i.e., diffusion profile reconstruction and tractography). In the second approach, we only align and interpolate the corrupted gradient directions. This mimics the situation where a pre-defined motion parameter threshold is used to claim whether a DWI volume is motion-corrupted. Note that the diffusion gradient vectors corresponding to the corrupted volumes are re-oriented to incorporate the rotational component of subject motion. In the third approach, assuming there is always motion, we force the alignment and interpolation of all DWI volumes while the respective gradient vectors are re-oriented accordingly. The interpolation step in the second and

third approaches was performed using FSL-MCFLIRT [6] with nearest neighbor, trilinear, sinc and spline interpolants.

2.2 Reconstruction and Tractography

We employed the constrained spherical deconvolution (CSD) technique [12] to reconstruct fODFs using the DiPy library [13]. We used spherical harmonics representation of order 8 which was kept constant for all our experiments. Full brain tractography was performed using the EuDX deterministic tracking technique [14] (implemented in the DiPy library), using random seeding inside the brain region and a turning-angle threshold of 30° between two connected voxels. The fODFs and tractography were computed for the 450 motion corrected sequences (50 datasets times 9 correction schemes), as well as the motion-free sequence.

Further, a multi-ROI approach was used to reconstruct four prominent and previously well-described fiber pathways using the Template ROI set (TRS) defined in [15] which exploits the existing anatomical knowledge of track trajectories. The TRS (pass through and not-pass through) of four fundamental fiber bundles (left and right hemispheres) were defined based on "Eve" atlas-based parcellation of the original DWI images. We report the matching results from the four bundles as defined in [15]: the cortical spinal track (CST), the inferior fronto-occipital track (IFO), the inferior longitudinal fasciculus (ILF), and the uncinate fasciculus (UNC).

2.3 Evaluation Metrics

2.3.1 Voxel-Based Metric

Similarities between the original motion-free fODFs and the fODFs corresponding to the motion corrected images were measured using the Jensen-Shannon divergence (JSD), which has been used to quantify differences between ODFs in various studies [16].

2.3.2 Global Connectivity-Based Metric

We used the 176 core and peripheral ROIs defined in the white matter parcellation (see Sect. 2.1.2) to compute weighted connectivity graphs from the full brain tractography result. The edge weights were inversely proportional to the tracts lengths giving a higher connection strength to short tracts to compensate for signal attenuation. The brain connectivity graphs were then compared by means of the recently proposed graph diffusion distance (GDD) metric [17], which takes into account the graph structure in addition to the edge weights.

2.3.3 Track-Based Metric

The spatial matching between motion-free and motion-corrected tracts was examined using Cohen's Kappa statistic [18]. The Kappa statistic measures the level of agreement of the tracking results (determined by cross-tabulating track detection for two given tracking results) and corrects for agreement that would be expected by chance (determined by the marginal frequencies of each tracking result).

3 Results and Discussion

The average JSD metric was computed using the fODF reconstruction from the raw dataset not corrupted by mixing DWI directions from the tilted-brain scan as a reference (i.e. only presenting subtle motion inherent to a scan). We differentiated between regions where multiple fibers were detected versus single fiber regions. Figure 3 shows the average JSD values for single and multiple fiber regions as a function of motion corrupted percentage. As anticipated, heterogeneous regions are more affected (showing larger average JSD) by the interpolation step of motion correction in general when compared to that of single fiber regions, regardless of the interpolation scheme employed. It can be observed that the impact of motion scrubbing (removing gradient directions) becomes more pronounced when compared to interpolation. The JSD values indicate minimal deformations in fODFs reconstructed after forcing the alignment and interpolation of all gradient directions.

Figure 4(left) shows the average GDD metric computed based on the weighted connectivity graphs from tractography result based on raw scan reconstructions versus that of motion-corrected ones. One may observe consistent findings when compared to the JSD metric; the global brain connectivity is least affected by the motion correction step when forcing the alignment and interpolation of all gradient directions without setting a pre-defined threshold to claim corrupted volumes. Although excluding corrupted gradients might seem an alternative choice for motion correction, the connectivity graphs show high deviations (larger GDD) especially when the percentage of directions being corrupted is increased.

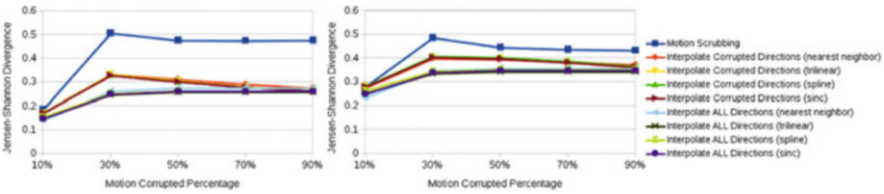

Fig. 3 The average Jensen-Shannon divergence (*JSD*) values for single fiber regions (*left*) and for multiple fiber regions (*right*)

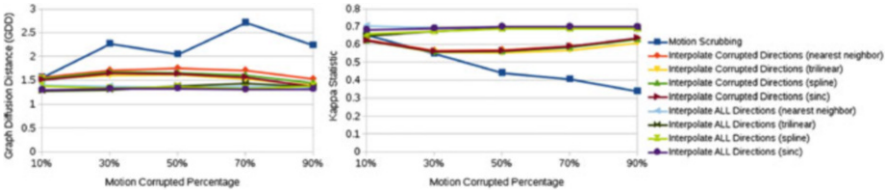

Fig. 4 *Left*: average graph diffusion distance (*GDD*). *Right*: average Cohen's Kappa statistic for the cortical spinal track (*CST*) for the left hemisphere

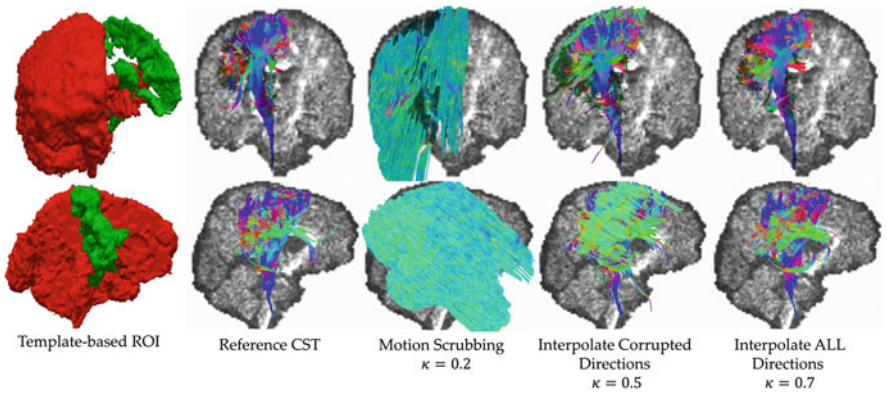

Fig. 5 Sample tractography result for the cortical spinal track (*CST*) (*left hemisphere*) with 50 % motion corruption

Figure 4(right) shows the average Kappa statistic computed from the CST track in the left hemisphere (other fiber tracts showed similar trends, yet their graphs were omitted due to space limitation). Being consistent with the results from JSD and GDD metrics, motion scrubbing shows a significant decrease in the degree of track agreement when increasing percentage of motion corruption which in turn yields discarding more gradient directions. Nonetheless, the maximal agreement is achieved when aligning and interpolating all gradient directions to correct for motion, even if considered subtle, see Fig. 5 for a sample tractography result. One can observe that the detected tracts when corrupted gradients are excluded deviate from being anatomically realistic. This is due to insufficient number of gradients and unbalanced sampling of the q-space.

4 Conclusion

Although there is excellent theoretical work on DWI acquisition parameters and ODF reconstruction schemes, as well as its effects on the quality and crossing fiber resolution, standard users lack clear guidelines and recommendations on the

best ways to approach and correct for motion in practical settings. This work investigates motion correction using transformation and interpolation of affected DWI directions versus the exclusion of subsets of DWIs, and its impact on the reconstructed fODFs, on brain connectivity and on the detection of fiber tracts. The various effects are systematically explored and illustrated via living phantom data, leading to the conclusion that motion, even subtle, exists in every acquired DW scan while subsequent reconstructions are least affected by the motion correction step when forcing the alignment and interpolation of all gradient directions without setting pre-defined thresholds to claim corrupted volumes.

Acknowledgements This work is supported by NIH grants ACE RO1 HD 055741 and NA-MIC Roadmap U54 EB005149 and the cocaine infant project (CAMID NIDA DA022446-01).

References

1. Pierpaoli, C.: Artifacts in diffusion MRI. In: Jones, D.K. (ed.) Diffusion MRI: Theory, Methods and Applications, pp. 303–318. Oxford University Press, New York (2010)
2. Tournier, J.D., Mori, S., Leemans, A.: Diffusion tensor imaging and beyond. Magn. Reson. Med. **65**(6), 1532–1556 (2011)
3. Caruyer, E., Aganj, I., Lenglet, C., Sapiro, G., Deriche, R.: Motion detection in diffusion MRI via online odf estimation. Int. J. Biomed. Imaging **2013**, 849363 (2013)
4. Kober, T., Gruetter, R., Krueger, G.: Prospective and retrospective motion correction in diffusion magnetic resonance imaging of the human brain. Neuroimage **59**(1), 389–398 (2012)
5. Liu, Z., Wang, Y., Gerig, G., Gouttard, S., Tao, R., Fletcher, T., Styner, M.: Quality control of diffusion weighted images. In: SPIE Medical Imaging, International Society for Optics and Photonics, pp. 76280J–76280J (2010)
6. Jenkinson, M., Bannister, P., Brady, M., Smith, S.: Improved optimization for the robust and accurate linear registration and motion correction of brain images. Neuroimage **17**(2), 825–841 (2002)
7. Avants, B.B., Epstein, C.L., Grossman, M., Gee, J.C.: Symmetric diffeomorphic image registration with cross-correlation: evaluating automated labeling of elderly and neurodegenerative brain. Med. Image Anal. **12**(1), 26–41 (2008)
8. Pierpaoli, C., Walker, L., Irfanoglu, M., Barnett, A., Basser, P., Chang, L., Koay, C., Pajevic, S., Rohde, G., Sarlls, J., et al.: Tortoise: an integrated software package for processing of diffusion MRI data. Proc. Int. Soc. Magn. Reson. Med. **18**, 1597 (2010)
9. Oguz, I., Farzinfar, M., Matsui, J., Budin, F., Liu, Z., Gerig, G., Johnson, H.J., Styner, M.A.: Dtiprep: quality control of diffusion-weighted images. Front. Neuroinform. **8**, 4 (2014)
10. Rohde, G.K., Barnett, A.S., Basser, P.J., Pierpaoli, C.: Estimating intensity variance due to noise in registered images: applications to diffusion tensor MRI. Neuroimage **26**(3), 673–684 (2005)
11. Oishi, K., Faria, A., Jiang, H., Li, X., Akhter, K., Zhang, J., Hsu, J.T., Miller, M.I., van Zijl, P., Albert, M., et al.: Atlas-based whole brain white matter analysis using large deformation diffeomorphic metric mapping: application to normal elderly and alzheimer's disease participants. Neuroimage **46**(2), 486–499 (2009)
12. Tournier, J., Yeh, C.H., Calamante, F., Cho, K.H., Connelly, A., Lin, C.P., et al.: Resolving crossing fibres using constrained spherical deconvolution: validation using diffusion-weighted imaging phantom data. Neuroimage **42**(2), 617–625 (2008)

13. Garyfallidis, E., Brett, M., Amirbekian, B., Rokem, A., Van Der Walt, S., Descoteaux, M., Nimmo-Smith, I.: Dipy, a library for the analysis of diffusion MRI data. Front. Neuroinform. **8**(8) (2014)
14. Garyfallidis, E.: Towards an accurate brain tractography. Ph.D. thesis, University of Cambridge (2012)
15. Zhang, Y., Zhang, J., Oishi, K., Faria, A.V., Jiang, H., Li, X., Akhter, K., Rosa-Neto, P., Pike, G.B., Evans, A., et al.: Atlas-guided track reconstruction for automated and comprehensive examination of the white matter anatomy. Neuroimage **52**(4), 1289–1301 (2010)
16. Cohen-Adad, J., Descoteaux, M., Wald, L.L.: Quality assessment of high angular resolution diffusion imaging data using bootstrap on q-ball reconstruction. J. Magn. Reson. Imaging **33**(5), 1194–1208 (2011) 1194–1208
17. Hammond, D.K., Gur, Y., Johnson, C.R.: Graph diffusion distance: a difference measure for weighted graphs based on the graph laplacian exponential kernel. In: Global Conference on Signal and Information Processing (GlobalSIP), 2013 IEEE, Austin, Dec 2013, pp. 419–422
18. Landis, J.R., Koch, G.G., et al.: The measurement of observer agreement for categorical data. Biometrics **33**(1), 159–174 (1977)

Joint Super-Resolution Using Only One Anisotropic Low-Resolution Image per q-Space Coordinate

Vladimir Golkov, Jonathan I. Sperl, Marion I. Menzel, Tim Sprenger, Ek Tsoon Tan, Luca Marinelli, Christopher J. Hardy, Axel Haase, and Daniel Cremers

Abstract Recently, super-resolution methods for diffusion MRI capable of retrieving high-resolution diffusion-weighted images were proposed, yielding a resolution beyond the scanner hardware limitations. These techniques rely on acquiring either *one isotropic* or *several anisotropic* low-resolution versions of each diffusion-weighted image. In the present work, a variational formulation of joint super-resolution of all diffusion-weighted images is presented which takes advantage of interrelations between similar diffusion-weighted images. These interrelations allow to use only *one anisotropic* low-resolution version of each diffusion-weighted image and to retrieve its missing high-frequency components from other images which have a similar q-space coordinate but a different resolution-anisotropy orientation. An acquisition scheme that entails complementary resolution-anisotropy among neighboring q-space points is introduced. High-resolution images are recovered at reduced scan time requirements compared to state-of-the-art anisotropic super-resolution methods. The introduced principles of joint super-resolution thus have the potential to further improve the performance of super-resolution methods.

V. Golkov (✉) • T. Sprenger
GE Global Research, Garching, Germany

Technische Universität München, Garching, Germany
e-mail: golkov@in.tum.de; sprenger@ge.com

J.I. Sperl • M.I. Menzel
GE Global Research, Garching, Germany
e-mail: menzel@ge.com; sperl@ge.com

E.T. Tan • L. Marinelli • C.J. Hardy
GE Global Research, Niskayuna, NY, USA
e-mail: ek.tan@ge.com; marinell@research.ge.com; hardycj@ge.com

A. Haase • D. Cremers
Technische Universität München, Garching, Germany
e-mail: axel.haase@tum.de; cremers@tum.de

L. O'Donnell et al. (eds.), *Computational Diffusion MRI*, Mathematics and Visualization, DOI 10.1007/978-3-319-11182-7_16

1 Introduction

Diffusion MRI allows measuring the molecular self-diffusion of water in biological tissue, and provides unique information on tissue microstructure unavailable to other non-invasive imaging techniques. Diffusion MRI has the potential to improve the diagnosis of, inter alia, multiple sclerosis [11], traumatic brain injury [26], and many kinds of cancer [19]. This potential stems from its ability to determine the macroscopic orientation and "bulk statistics" of diffusion within the underlying microscopic cellular architecture. This is done by acquiring diffusion-weighted images for different diffusion directions and diffusion weightings (constituting a three-dimensional diffusion space, the q-space), and fitting a diffusion model to the measurements. For details, please refer to [12, 13].

A major challenge in diffusion MRI is balancing between acquisition duration, image resolution and signal-to-noise ratio (SNR). Numerous denoising methods were proposed to increase SNR by incorporating prior knowledge into postprocessing [15, 28] or directly into image reconstruction [10].

Another approach to improve the balance between scan time, resolution and SNR is to increase image resolution via super-resolution techniques.

1.1 Non-diffusion MRI Super-Resolution

Numerous super-resolution methods are available for non-diffusion MRI [20, 29]. Notably, the total generalized variation (TGV) [2, 14] regularizer, which prevents staircasing artifacts by modeling higher-order derivatives of the image, was applied to super-resolution of isotropic low-resolution MRI volumes [17].

1.2 Diffusion MRI Super-Resolution

In contrast to conventional diffusion MRI techniques, super-resolution methods for diffusion MRI exceed the scanner hardware limitations on image resolution.

Fiber-based methods reconstruct super-resolution information on nerve fiber bundles from conventional diffusion MRI [4–6, 18], or enhance the resolution of diffusion-weighted images by using estimated underlying nerve fiber orientations for the super-resolution model [31].

Patch-based super-resolution [8] uses *one isotropic* low-resolution version of a diffusion-weighted image, and performs super-resolution using self-similarity [3, 16, 24] of the image. In *collaborative* patch-based super-resolution [8], a high-resolution non-diffusion-weighted image is used to retrieve high-frequency information for the isotropic low-resolution diffusion-weighted image, in addition to the self-similarity prior.

The methods introduced by Scherrer et al. [25] and Poot et al. [22] use *several anisotropic* low-resolution versions of each diffusion-weighted image with complementary resolution-anisotropy orientations. Resolution anisotropy is achieved by anisotropic k-space sampling, meaning that high frequencies are not sampled for all directions equally. Subsequently, each high resolution diffusion-weighted image is reconstructed independently by using the complementary high-frequency information from the anisotropic low-resolution acquisitions. Several anisotropic low-resolution acquisitions with different distortions are used in [23] for joint susceptibility artifact correction and super-resolution.

Model-based super-resolution [27] introduces a framework to estimate high-resolution parameter maps for an arbitrary diffusion model from *several anisotropic* low-resolution versions of each diffusion-weighted image. As a proof of concept, the authors use the ball-and-stick model [1] and apply the method to an in silico phantom. Model-based super-resolution uses information from the entire q-space simultaneously, and is shown to outperform independent super-resolution of individual diffusion-weighted images. However, information on high frequencies is still completely acquired for every q-space coordinate—several acquisitions per q-space coordinate are used.

Three different combination schemes of q-space coordinates and resolution-anisotropy orientations were proposed for tomographic reconstruction of diffusion tensors [7]. However, the scheme that uses only *one anisotropic* acquisition per q-space coordinate restricts the resolution-anisotropy orientation exactly to the respective diffusion gradient direction.

We propose a super-resolution method for diffusion MRI that jointly recovers high frequencies of all diffusion-weighted images, but requires only *one anisotropic* low-resolution acquisition per q-space coordinate. The resolution-anisotropy orientations are chosen such that neighbors in q-space possess complementary high-frequency information, and regularization along q-space allows them to propagate this information to each other.

2 Methods

Two formulations for joint super-resolution of five-dimensional data (2-D image space and 3-D q-space) are introduced, relying on two respective imaging models: the formation of low-resolution images from high-resolution images, or the formation of acquired subsampled k-space raw data from underlying high-resolution images.

2.1 Image Formation Model

In the following, five-dimensional data are considered. The 5-D low-resolution images $\mathbf{y}$ are formed from the high-resolution images $\boldsymbol{\rho}$ in the following way:

$$\mathbf{y} = \mathbf{D}\rho + \boldsymbol{\epsilon}_{\mathbf{y}} \,, \tag{1}$$

where $\mathbf{D}$ is the blur and downsampling operator [8,27], and $\boldsymbol{\epsilon}_{\mathbf{y}}$ is the residual noise. The model for the acquired k-space data $\mathbf{d}$ is

$$\mathbf{d} = \mathbf{U}\mathscr{F}_{\mathrm{x}\to\mathrm{k}}\boldsymbol{\rho} + \boldsymbol{\epsilon}_{\mathbf{d}} \,, \tag{2}$$

where $\mathscr{F}_{\mathrm{x}\to\mathrm{k}}$ is the Fourier transform from image space (x-space) to k-space along two of the five data dimensions, $\mathbf{U}$ is the undersampling operator in k-space (omitting high frequencies in a certain orientation), and $\boldsymbol{\epsilon}_{\mathbf{d}}$ is complex-valued i.i.d. Gaussian noise.

2.2 k-q Acquisition Scheme

For the present purpose, coordinates in q-space are sampled on a regular Cartesian grid up to a maximum diffusion weighting $b_{\max}$, as in diffusion spectrum imaging (DSI) [30]. For each q-space point, only *one anisotropic* low-resolution image is acquired by omitting high frequencies in k-space in one direction, see Fig. 1. The resolution-anisotropy directions are chosen such that neighboring points in q-space contain complementary high-frequency information. For an image lacking vertical high frequencies, all of its six Cartesian-grid q-space neighbors contain vertical high frequencies but lack horizontal high frequencies—and vice versa. Figure 2 illustrates this relationship.

2.3 Joint Super-Resolution

We perform super-resolution for all diffusion-weighted images jointly. The data in our formulation is thus five-dimensional (2-D image space and 3-D q-space). TGV [2, 14] along all five data dimensions is applied as a regularization term. This regularization has a threefold effect:

- Regularization along q-space propagates complementary high-frequency information between q-space-neighboring diffusion-weighted images of different resolution-anisotropy orientations (Fig. 2).

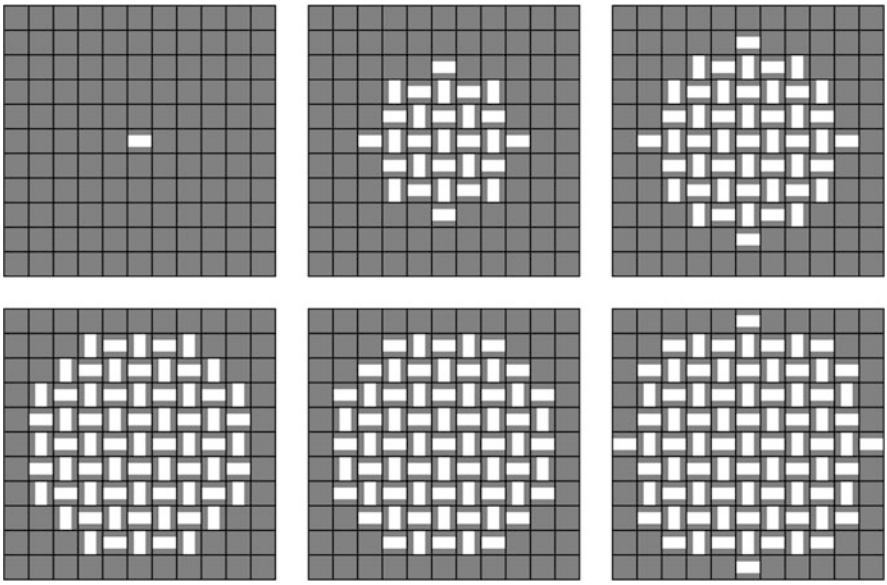

Fig. 1 Sampling scheme in joint k-q space. The *six large squares* correspond to q-space DSI coordinates $q_z = -5\ldots0$ (coordinates $q_z = 1\ldots5$ analogous to $q_z = -1\ldots-5$ not depicted). The *small squares within each large square* correspond to coordinates $q_x = -5\ldots5$, $q_y = -5\ldots5$. The *small squares* depict sampled (*white*) and unsampled (*gray*) k-space points for each q-space coordinate. Sampling anisotropy in k-space results in resolution anisotropy in image space, and the anisotropy orientations are chosen such that neighbors in q-space have complementary high-frequency information in horizontal and vertical directions (cf. Fig. 2)

- The image model of TGV introduces prior knowledge capable of retrieving missing high frequencies when regularizing along image space in a super-resolution framework [17].
- TGV regularization along five dimensions reconstructs missing information in 5-D space and reduces noise [9].

Second-order TGV is a piecewise-smooth image model, formulated [2, 14] as

$$\mathrm{TGV}(\boldsymbol{\rho}) = \min_{\mathbf{v}} \int_{\Omega} \alpha_1 |\nabla \boldsymbol{\rho} - \mathbf{v}| \mathrm{d}\, x + \alpha_0 \int_{\Omega} |\mathscr{E}(\mathbf{v})| \mathrm{d}\, x \ , \tag{3}$$

where $\mathscr{E}(\mathbf{v}) = \frac{1}{2}\left(\nabla \mathbf{v} + \nabla \mathbf{v}^T\right)$ is the symmetrized derivative, α_1 and α_0 are regularization parameters, and Ω is the image domain (field of view). TGV balances the first and second derivatives of the image via the vector field $\mathbf{v}$, allowing both affine regions and edges.

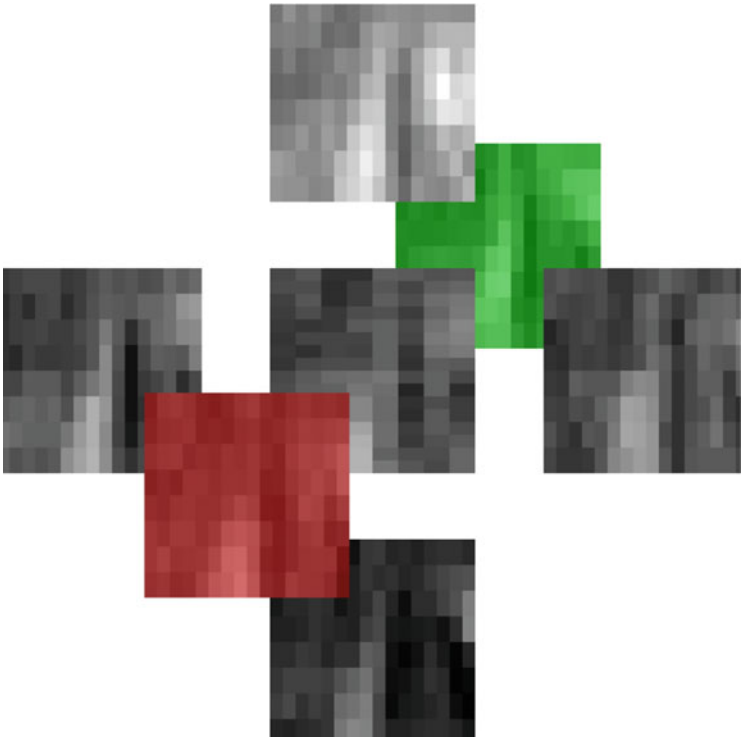

Fig. 2 Detail of a low-resolution image (*middle*) and its six neighbors in Cartesian q-space along q_x (*left*, *right*), along q_y (*bottom*, *top*) and along q_z (*red*, *green*). The *middle image* lacks horizontal resolution, but its six q-space neighbors all have high horizontal resolution, and the information they contain is propagated to the middle image in iterative joint super-resolution via regularization along q-space. The same principle analogously applies to images lacking vertical resolution. Middle image taken from DSI q-space coordinate $(q_x, q_y, q_z) = (0, -3, 1)$

Joint super-resolution is formulated in a variational framework. To estimate high-resolution images $\hat{\boldsymbol{\rho}}$ from low-resolution images $\mathbf{y}$ formed according to the model in Eq. (1), the following optimization problem is solved:

$$\hat{\boldsymbol{\rho}} = \arg\min_{\boldsymbol{\rho}} \|\mathbf{D}\boldsymbol{\rho} - \mathbf{y}\|_2^2 + \mathrm{TGV}(\boldsymbol{\rho}) \; . \tag{4}$$

To obtain high-resolution 5-D image estimates $\hat{\boldsymbol{\rho}}$ from raw k-space data $\mathbf{d}$ formed according to the imaging model in Eq. (2), the following optimization problem is solved:

$$\hat{\boldsymbol{\rho}} = \arg\min_{\boldsymbol{\rho}} \|\mathbf{U}\mathscr{F}_{\mathrm{x}\to\mathrm{k}}\boldsymbol{\rho} - \mathbf{d}\|_2^2 + \mathrm{TGV}(\boldsymbol{\rho}) \; . \tag{5}$$

In both cases, solutions are obtained with a first-order primal-dual algorithm [21].

2.4 Experiments

As a proof of concept, the resolution of a healthy volunteer scan was retrospectively reduced according to the scheme described in Sect. 2.2. In this way, comparison to the original high-resolution data was possible. The scan was performed using a single coil on a 3T GE MR750 clinical MR scanner (GE Healthcare, Milwaukee, WI, USA) with the following imaging parameters: $T_R = 2535\,\text{ms}$, $T_E = 93.3\,\text{ms}$, 515 DSI q-space coordinates within the sphere inscribed in a $11 \times 11 \times 11$ Cartesian grid, $b_{\max} = 2000\,\text{s/mm}^2$, voxel size $1.875 \times 1.875 \times 4\,\text{mm}$. Thus, the artificially downsampled resolution was $1.875 \times 3.75 \times 4\,\text{mm}$ and $3.75 \times 1.875 \times 4\,\text{mm}$, depending on q-space coordinate, cf. Fig. 1. Informed consent was obtained.

Joint super-resolution from low-resolution image space, Eq. (4), and from low-resolution (undersampled) k-space data, Eq. (5), was performed.

3 Results

Joint super-resolution results are shown in Fig. 3. Joint super-resolution, especially from k-space data $\mathbf{d}$, largely removes low-resolution artefacts which manifest themselves as underestimations and overestimations (blue and red in the bottom rows of Fig. 3) of the true signal around salient image features.

Six of the acquired 515 q-space coordinates, namely $(q_x, q_y, q_z) = (\pm 5, 0, 0)$, $(0, \pm 5, 0)$ and $(0, 0, \pm 5)$, have only one neighbor in q-space. We observed that low-resolution artefacts remained at these coordinates (not shown). Due to this issue, but also for the sake of optimization of the entire protocol, adaptive regularizers and/or further development of the sampling scheme might be beneficial for joint super-resolution.

Peak signal to noise ratio (PSNR) was calculated, which is defined as

$$\text{PSNR} = 20 \log_{10}(\text{MAX}/\text{RMSE}) \,, \tag{6}$$

where MAX is the maximal intensity of the image and RMSE is the root mean squared error of the image compared to the high-resolution original. PSNR was 40.69 dB for low-resolution images, which could be improved to 41.33 dB for joint super-resolution images reconstructed from low-resolution images via the optimization problem (4), and 41.37 dB for joint super-resolution from k-space data by solving (5). Since the original high-resolution image is noisy, its noise is also captured in the calculation of PSNR, preventing the distinction between noise and low-resolution artifact removal. However, artifacts are visibly removed by the joint super-resolution method, cf. Fig. 3.

Besides, the denoising effect [9] of regularization of the five-dimensional data can also be observed in our results (joint super-resolution results contain less noise than the original high-resolution images, and a great part of the incoherent noise in

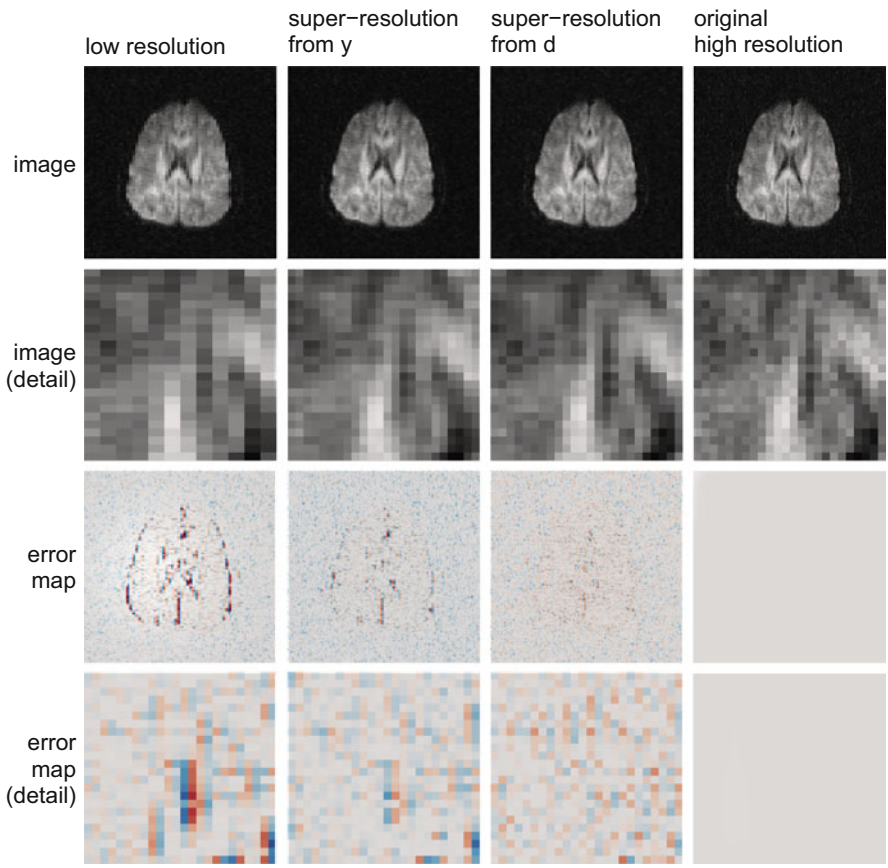

Fig. 3 Comparison of low-resolution images, high-resolution images retrieved by joint super-resolution, and original high-resolution images with full k-space coverage. Error maps compared to the high-resolution original are shown in the *third* and *fourth row*. DSI q-space coordinate $(q_x, q_y, q_z) = (0, -3, 1)$ is shown

the error maps, Fig. 3, is caused by noise in the original high-resolution image). This indicates that the improved stability to noise when using TGV for super-resolution as reported in [17] also benefits *joint* super-resolution.

4 Discussion and Conclusions

Two formulations for joint super-resolution of 5-D data were introduced along with a k-q acquisition scheme. Joint super-resolution from k-space, Eq. (5), outperformed joint super-resolution from low-resolution image space, Eq. (4), in terms of PSNR and visual image quality. This result can be attributed inter alia to an imperfect

approximation of **D** in the image space model, cf. [8, 22, 25, 27]. Both joint super-resolution formulations were able to enhance fine details in diffusion-weighted images.

All in all, acquiring only one anisotropic image per q-space point strongly reduces the imaging time compared to state-of-the-art super-resolution techniques. We demonstrated that it is feasible to retrieve missing high-resolution information using an appropriate regularization and complementary resolution-anisotropy orientations among q-space neighbors.

With this scan time reduction in prospect, future work may focus on optimizing the protocol in terms of motion and distortion compensation [22, 25], q-space coordinates, maximal b-value, anisotropy orientations and downsampling factors in order to match a realistic clinical setting and compare the performance of joint super-resolution to state-of-the-art super-resolution methods. From the discussed results we conclude that the introduced principles of joint super-resolution have the potential to further improve the performance of super-resolution methods.

Acknowledgements Grant support: Deutsche Telekom Foundation.

References

1. Behrens, T.E.J., Woolrich, M.W., Jenkinson, M., Johansen-Berg, H., Nunes, R.G., Clare, S., Matthews, P.M., Brady, J.M., Smith, S.M.: Characterization and propagation of uncertainty in diffusion-weighted MR imaging. Magn. Reson. Med. **50**, 1077–1088 (2003). doi:10.1002/mrm.10609
2. Bredies, K., Kunisch, K., Pock, T.: Total generalized variation. SIAM J. Imaging Sci. **3**, 492–526 (2010). doi:10.1137/090769521
3. Buades, A., Coll, B., Morel, J.M.: A review of image denoising algorithms, with a new one. Multiscale Model. Simul. **4**, 490–530 (2005). doi:10.1137/040616024
4. Calamante, F., Tournier, J.-D., Jackson, G.D., Connelly, A.: Track-density imaging (TDI): super-resolution white matter imaging using whole-brain track-density mapping. NeuroImage **53**, 1233–1243 (2010). doi:10.1016/j.neuroimage.2010.07.024
5. Calamante, F., Tournier, J.-D., Heidemann, R.M., Anwander, A., Jackson, G.D., Connelly, A.: Track density imaging (TDI): validation of super resolution property. NeuroImage **56**, 1259–1266 (2011). doi:10.1016/j.neuroimage.2011.02.059
6. Calamante, F., Tournier, J.-D., Kurniawan, N.D., Yang, Z., Gyengesi, E., Galloway, G.J., Reutens, D.C., Connelly, A.: Super-resolution track-density imaging studies of mouse brain: comparison to histology. NeuroImage **59**, 286–296 (2012). doi:10.1016/j.neuroimage.2011.07.014
7. Cheryauka, A.B., Lee, J.N., Samsonov, A.A., Defrise, M., Gullberg, G.T.: MRI diffusion tensor reconstruction with PROPELLER data acquisition. Magn. Reson. Imaging **22**, 139–148 (2004). doi:10.1016/j.mri.2003.08.001
8. Coupé, P., Manjón, J.V., Chamberland, M., Descoteaux, M., Hiba, B.: Collaborative patch-based super-resolution for diffusion-weighted images. NeuroImage **83**, 245–261 (2013). doi:10.1016/j.neuroimage.2013.06.030
9. Golkov, V., Menzel, M.I., Sprenger, T., Souiai, M., Haase, A., Cremers, D., Sperl, J.I.: Direct reconstruction of the average diffusion propagator with simultaneous compressed-sensing-accelerated diffusion spectrum imaging and image denoising by means of total generalized

variation regularization. In: Proceedings of Joint Annual Meeting ISMRM-ESMRMB, Milan, Italy, 10–16 May 2014, p. 4472
10. Haldar, J.P., Wedeen, V.J., Nezamzadeh, M., Dai, G., Weiner, M.W., Schuff, N., Liang, Z.-P.: Improved diffusion imaging through SNR-enhancing joint reconstruction. Magn. Reson. Med. **69**, 277–289 (2013). doi:10.1002/mrm.24229
11. Inglese, M., Bester, M.: Diffusion imaging in multiple sclerosis: research and clinical implications. NMR Biomed. **23**, 865–872 (2010). doi:10.1002/nbm.1515
12. Johansen-Berg, H., Behrens, T.E.J. (eds.): Diffusion MRI: From Quantitative Measurement to In-vivo Neuroanatomy, 2nd edn. Academic, New York (2013)
13. Jones, D.K. (ed.): Diffusion MRI: Theory, Methods and Applications. Oxford University Press, Oxford (2010)
14. Knoll, F., Bredies, K., Pock, T., Stollberger, R.: Second order total generalized variation (TGV) for MRI. Magn. Reson. Med. **65**, 480–491 (2011). doi:10.1002/mrm.22595
15. Lam, F., Babacan, S.D., Haldar, J.P., Weiner, M.W., Schuff, N., Liang, Z.-P.: Denoising diffusion-weighted magnitude MR images using rank and edge constraints. Magn. Reson. Med. **71**, 1272–1284 (2014). doi:10.1002/mrm.24728
16. Manjón, J. V, Coupé, P., Buades, A., Fonov, V., Louis Collins, D., Robles, M.: Non-local MRI upsampling. Med. Image Anal. **14**, 784–792 (2010). doi:10.1016/j.media.2010.05.010
17. Martín, A., Marquina, A., Hernández-Tamames, J.A., García-Polo, P., Schiavi, E.: MRI TGV based super-resolution. In: Proceedings of the ISMRM 21st Annual Meeting, Salt Lake City, 20–26 Apr 2013, p. 2696
18. Nedjati-Gilani, S., Alexander, D.C., Parker, G.J.M.: Regularized super-resolution for diffusion MRI. In: 5th IEEE International Symposium on Biomedical Imaging: From Nano to Macro, Paris, 14–17 May 2008, pp. 875–878
19. Padhani, A.R., Liu, G., Mu-Koh, D., Chenevert, T.L., Thoeny, H.C., Ross, B.D., Cauteren, M. Van, Collins, D., Hammoud, D.A., Rustin, G.J.S., Taouli, B.: Diffusion-weighted magnetic resonance imaging as a cancer biomarker: consensus and recommendations. Neoplasia **11**, 102–125 (2009). doi:10.1593/neo.81328
20. Plenge, E., Poot, D.H.J., Bernsen, M., Kotek, G., Houston, G., Wielopolski, P., van der Weerd, L., Niessen, W.J., Meijering, E.: Super-resolution methods in MRI: can they improve the trade-off between resolution, signal-to-noise ratio, and acquisition time? Magn. Reson. Med. **68**, 1983–1993 (2012). doi:10.1002/mrm.24187
21. Pock, T., Cremers, D., Bischof, H., Chambolle, A.: An algorithm for minimizing the Mumford–Shah functional. In: 12th International Conference on Computer Vision (ICCV). pp. 1133–1140. IEEE, Kyoto (2009)
22. Poot, D.H.J., Jeurissen, B., Bastiaensen, Y., Veraart, J., Van Hecke, W., Parizel, P.M., Sijbers, J.: Super-resolution for multislice diffusion tensor imaging. Magn. Reson. Med. **69**, 103–113 (2013). doi:10.1002/mrm.24233
23. Ruthotto, L., Mohammadi, S., Weiskopf, N.: A new method for joint susceptibility artefact correction and super-resolution for dMRI. In: Proceedings of SPIE 9034, Medical Imaging 2014: Image Processing, San Diego, 15 Feb 2014
24. Rousseau, F.: A non-local approach for image super-resolution using intermodality priors. Med. Image Anal. **14**, 594–605 (2010). doi:10.1016/j.media.2010.04.005
25. Scherrer, B., Gholipour, A., Warfield, S.K.: Super-resolution reconstruction to increase the spatial resolution of diffusion weighted images from orthogonal anisotropic acquisitions. Med. Image Anal. **16**, 1465–1476 (2012). doi:10.1016/j.media.2012.05.003
26. Shenton, M.E., Hamoda, H.M., Schneiderman, J.S., Bouix, S., Pasternak, O., Rathi, Y., Vu, M., Purohit, M.P., Helmer, K., Koerte, I., Lin, A.P., Westin, C.-F., Kikinis, R., Kubicki, M., Stern, R.A., Zafonte, R.: A review of magnetic resonance imaging and diffusion tensor imaging findings in mild traumatic brain injury. Brain Imaging Behav. **6**, 137–192 (2012). doi:10.1007/s11682-012-9156-5
27. Tobisch, A., Neher, P.F., Rowe, M.C., Maier-Hein, K.H., Zhang, H.: Model-based super-resolution of diffusion MRI. In: Schultz, T., Nedjati-Gilani, G., Venkataraman, A., O'Donnell,

L., Panagiotaki, E. (eds.) Computational Diffusion MRI and Brain Connectivity, MICCAI Workshops, pp. 25–34. Springer International Publishing, Berlin (2014)
28. Tristán-Vega, A., García-Pérez, V., Aja-Fernández, S., Westin, C.-F.: Efficient and robust nonlocal means denoising of MR data based on salient features matching. Comput. Methods Programs Biomed. **105**, 131–144 (2012). doi:10.1016/j.cmpb.2011.07.014
29. Van Reeth, E., Tham, I.W.K., Tan, C.H., Poh, C.L.: Super-resolution in magnetic resonance imaging: a review. Concepts Magn. Reson. Part A **40**, 306–325 (2012). doi:10.1002/cmr.a.21249
30. Wedeen, V.J., Hagmann, P., Tseng, W.-Y.I., Reese, T.G., Weisskoff, R.M.: Mapping complex tissue architecture with diffusion spectrum magnetic resonance imaging. Magn. Reson. Med. **54**, 1377–1386 (2005). doi:10.1002/mrm.20642
31. Yap, P.-T., An, H., Chen, Y., Shen, D.: Fiber-driven resolution enhancement of diffusion-weighted images. NeuroImage **84**, 939–950 (2014). doi:10.1016/j.neuroimage.2013.09.016

Bilateral Filtering of Multiple Fiber Orientations in Diffusion MRI

Ryan P. Cabeen and David H. Laidlaw

Abstract We present and evaluate a bilateral filter for smoothing diffusion MRI fiber orientations with preservation of anatomical boundaries and support for multiple fibers per voxel. Two challenges in the process are the geometric structure of fiber orientations and the combinatorial problem of matching multiple fibers across voxels. To address these issues, we define distances and local estimators of weighted collections of multi-fiber models and show that these provide a basis for an efficient bilateral filtering algorithm for orientation data. We evaluate our approach with experiments testing the effect on tractography-based reconstruction of fiber bundles and response to synthetic noise in computational phantoms and clinical human brain data. We found this to significantly reduce the effects of noise and to avoid artifacts introduced by linear filtering. This approach has potential applications to diffusion MR tractography, brain connectivity mapping, and cardiac modeling.

1 Introduction

In this paper, we present and evaluate a method for smoothing orientation image data that preserves edges and supports multiple orientations per voxel. We apply this to diffusion MR imaging, a technique for measuring patterns of water molecule diffusion with clinical applications to the in-vivo characterization of tissue. While many of properties of tissue microstructure can be measured, we consider fiber orientations, which are a feature of most diffusion models. In brain white matter imaging, fiber orientations provide the basis for the reconstruction of fiber bundles and mapping of brain connectivity [2], and in cardiac imaging, fiber orientations aid the understanding of myocardial structure and the electrical and mechanical function of the heart [22]. A common issue with diffusion imaging is the presence of noise, which can lead to errors in fiber orientation estimation. We examine a model-based approach to regularization that extends the bilateral filter to single and multiple orientation data.

R.P. Cabeen (✉) • D.H. Laidlaw
Brown University, Providence, RI, USA
e-mail: cabeen@cs.brown.edu; dhl@cs.brown.edu

L. O'Donnell et al. (eds.), *Computational Diffusion MRI*, Mathematics and Visualization, DOI 10.1007/978-3-319-11182-7_17

Standard approaches for diffusion MR filtering either operate the diffusion-weighted signal measured in each voxel and gradient encoding direction [27] or incorporate robust statistics when fitting diffusion models [3]. Alternatively, model-based image processing has the potential advantage of greater efficiency and the ability to incorporate anatomical knowledge [17]. However, one challenge is that the geometric structure of diffusion models must be incorporated. There has been much success in developing such model-based frameworks with differential manifolds, such as with the tensor model [17] and orientation distribution functions [11]. For multi-compartment models, an additional combinatorial problem arises, where correspondence must be made between fibers in different voxels. Local estimators that incorporate clustering are one solution and have been applied to multi-tensors [25] and orientations [6]. Other more global approaches for orientation regularization have also been studied for single [8, 19, 28] and multi-fiber models [10, 23].

In this paper, we derive a bilateral filter that extends previous work on local linear filters for fiber orientations [6]. Such bilateral filters are well-studied for scalar and vector images [26] and are closely related to normalized convolution [14], anisotropic diffusion, and kernel regression [15]. Model-based bilateral filters have been developed for the regularization of single diffusion tensor [12] and functional [21] MR images. Related data-adaptive filters for 2D image orientations have also been proposed for 2D smoothing [18] and hair modeling [16] applications. Our work's distinguishing features are the handling of 3D orientations, support for multiple fibers per voxel, and a computationally efficient formulation.

In the rest of the paper, we first discuss computational analysis of single and multi-fiber orientations and derive the bilateral filter. We then evaluate our approach with computational phantoms and human brain data, measuring the effect on tractography-based reconstruction of fiber bundles and the voxelwise response to synthetic noise. We show that the proposed filter improves bundle reconstructions, significantly reduces the effects of noise, and offers an improvement over linear filtering at anatomical boundaries.

2 Methods

In this section, we first describe models of fiber orientations in diffusion MRI and discuss the computation of distances and averages of single and multiple orientations. We then apply these results to derive the proposed bilateral filter.

2.1 Fiber Orientation Modeling

Many methods exist for estimating fiber orientations. In this paper, we use the multi-direction ball-and-stick compartment model to obtain both fiber orientations and their volume fractions. This is a parametric mixture model consisting of an isotropic ball compartment and multiple tensor sticks that are constrained to be completely anisotropic [4]; our focus in this paper is on fiber orientations. These orientations have no preferred direction, so they are typically considered axial or line data and can be represented by unit vectors with no associated sign. For the case of multiple fibers, we consider a model M to be a weighted combination of N fiber volume-fraction and orientation pairs $M = \{(f_i, v_i)\}_{i=1}^{N}$ that lie in a single voxel. To perform analysis of these models, we need suitable distances, weighted averages, and related efficient computational routines. In the following sections, we'll discuss such ideas for both individual fiber orientations and their weighted combinations.

2.2 Single Fiber Analysis

We measure the distance $d_f(a, b)$ between single fiber orientations a and b by the sine of their angle. Although the angle between axes may seem more natural, the sine angle distance allows for a desirable representation and offers robustness to outliers [5]. This distance can be found by considering the representation $\phi(v) = vv^T$, known as the Veronese–Whitney embedding, the dyadic product, or Knutsson mapping [13,20]. This representation induces the sine angle fiber distance d_f^2 via the Euclidean distance d_e^2 in the embedding ϕ:

$$d_f^2(a, b) = d_e^2(\phi(a), \phi(b)) = \|\phi(a) - \phi(b)\|^2 \tag{1}$$

$$= \mathrm{Tr}((\phi(a) - \phi(b))^T(\phi(a) - \phi(b)) \tag{2}$$

$$= 2(1 - (a \cdot b)^2) = 2sin^2(\theta) \tag{3}$$

Weighted averages can then be computed with respect to this distance by $\mu = \sum_i w_i \phi(v_i)$. As this is an extrinsic mean, the result may no longer lie in the embedding, so it must be projected to the nearest point $\mathrm{argmin}_v d_e^2(\phi(v), \mu)$. A closed form expression for this is given by the principal eigenvector of the matrix μ [5]. This formulation also has a statistical interpretation, as the fiber distance is equivalent to the Bregman divergence between Watson distributions [7], and the weighted average of fibers is the maximum likelihood estimate of the direction of a Watson distribution [24]. We also note that both the fiber distance and the embedding provide a computationally efficient approach for optimization with orientations.

2.3 Multi-Fiber Analysis

In addition to measuring distances between fibers, we also wish to measure a distance $d_m(M, \hat{M})$ between weighted combinations of fibers:

$$d_m^2(M, \hat{M}) = \min_{\pi} \sum_j f_j \, d_f^2(v_j, \hat{v}_{\pi(j)}) \tag{4}$$

which is selected across all possible mappings π from left to right fibers. Intuitively, this finds the weighted sum of squared fiber distances from each of the left fibers to its nearest right fiber. Similar combinatorial distances have been applied to multi-fiber analyses by [23, 25]. We note that d_m^2 is asymmetric with respect to its inputs and invariant to the specific order of fiber compartments in M. Of course, when one fiber per voxel is present, this distance reduces to the single fiber distance d_f^2. We also need to compute the weighted average $\hat{M}$ under this distance, which can be defined and simplified as follows:

$$\hat{M} = \operatorname*{argmin}_M \sum_i^C w_i \, d_m^2(M_i, M) = \operatorname*{argmax}_{M,\pi} \sum_i^C \sum_j^{N_i} w_i \, f_{ij} (v_{ij} \cdot v_{\pi(ij)})^2 \tag{5}$$

For a fixed number of fibers in $\hat{M}$, this objective can be minimized by an iterative Expectation Maximization procedure similar to k-means clustering. In fact, this is equivalent to the procedure for hard Mixture of Watsons clustering of Sra et al. [24]. With this in mind, we now move to the task of defining bilateral filtering for multi-fiber models.

2.4 Bilateral Filtering

Perhaps one of the most basic smoothing filters is the Gaussian blur, where a weighted average of pixel intensities is found based on spatial proximity to a given voxel. While this approach can remove noise, it also tends to smooth features that we'd rather preserve. In contrast, bilateral filtering is a non-linear technique that has been found to smooth images while preserving edges [26]. This is achieved by computing weights based on both spatial proximity and intensity similarity. For multi-fiber models, we can make a similar extension to the linear multi-fiber filter proposed in [6] by including weights for directional similarity of fiber models. We

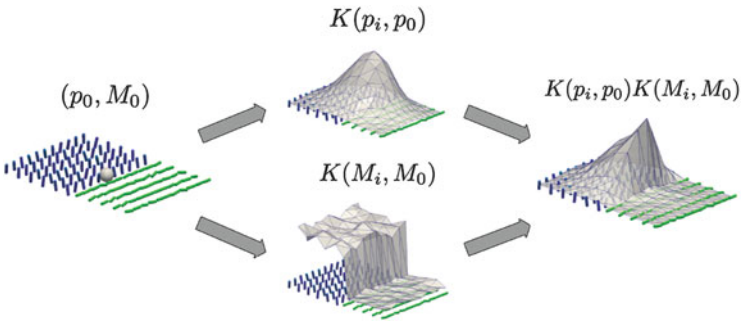

Fig. 1 An example of bilateral filter weights computed for a single voxel p_0 with associated fiber model M_0 (*left*), located near a boundary in a noisy phantom. For each voxel p_i and associated model M_i in a neighborhood of p_0, the bilateral weights (*right*) are given by the product of the linear Gaussian weights $K(p_i, p_0)$ (*top*) and data-adaptive weights $K(M_i, M_0)$ (*bottom*)

define such a filter on a per-voxel basis with a local estimation framework [15] as follows. Given an input voxel position and model (p_0, M_0) and local neighborhood $\{(p_i, M_i)\}_{i=1}^{C}$, with $M_i = \{(f_{ij}, v_{ij})\}_{j=1}^{N_i}$, the filtered model $\hat{M}$ is:

$$\hat{M} = \underset{M}{\operatorname{argmin}} \sum_{i=0}^{C} K\left(\frac{d_e^2(p_i, p_0)}{h_p^2}\right) K\left(\frac{d_m^2(M_i, M_0)}{h_m^2}\right) d_m^2(M_i, M) \tag{6}$$

given bandwidth parameters h_p and h_m and a kernel functions K, which we take to be the exponential $K(x) = \exp(-x)$. This defines non-linear filter weights that depend on M_0, as illustrated in Fig. 1. Each voxel may be processed separately by recomputing weights and solving Eq. 5 with the related Expectation Maximization procedure [24]. Two additional concerns are the number of fibers and the resulting volume fractions, which we estimate with standard bilateral filtering. The number of fibers is then a weighted average, which is rounded to the nearest integer, and the volume fractions are also weighted averages, but within groups defined by the optimal fiber correspondences π. Multiple passes through the volume may have some benefit, but we only consider a single pass.

3 Experiments

We performed evaluation with two experiments: the first applies tractography-based fiber bundle reconstructions in the human brain data, and the second measures the response to noise in computational phantoms and human brain data. We compared to the linear filtering approach [6] in both experiments.

3.1 Datasets

3.1.1 Computational Phantom Data

Two computational phantoms were constructed with single and double fiber models. The first represents the interface between two bundles, such as the corpus callosum/cingulum boundary. The second represents a similar interface with an additional bundle crossing both, such as the corpus callosum/corona radiata/superior longitudinal fasciculus juncture. These are represented by single and double fiber models, respectively, and both include fanning and curving to represent features of real data.

3.1.2 Human Brain Data

Diffusion MRIs were acquired from a healthy volunteer with a GE 1.5T scanner with a voxel size of 2 mm^3, dimensions 128x128x72, seven T_2-weighted volumes, and 64 gradient encoding directions with b-value 1,000 s/mm^2. Three repeated acquisitions of a single subject were concatenated to produce a high signal-to-noise volume. The repeated scans (high SNR) and a single acquisition (low SNR) were each processed with FSL to correct for motion, extract the brain, and fit single and multi-fiber models with Xfibres [4].

3.2 Design

The first experiment tested the effect of filtering on streamline tractography of the superior longitudinal fasciculus I [9], as shown in Fig. 2. We compared bundles with the Dice coefficient, fiber count, and volume, taking the high SNR acquisition as a reference and applying filtering to the low SNR scan. The second experiment tested the response to noise by randomly perturbing fiber orientations in the phantom and real data, as shown in Fig. 3. We measured error by the volume-fraction weighted minimum angular difference in degrees between models across all one-to-one pairings (the same metric used in [6]) and estimated the error rates by a Monte Carlo simulation with 1,000 noise iterations with $h_p = 3.0$ and $h_m = 0.75$. We tested for a reduction in error by a one-sided paired t-test at each voxel, where samples were paired by noise iteration. We measured the per-voxel effect size by a paired Cohen's d-score. In both experiments, we compared linear and bilateral filtering.

	Reference 3x64 directions	Unfiltered 64 directions	Linear Filtered 64 directions	Bilateral Filtered 64 directions
Dice	1.0	0.32	0.47	0.53
Count	130	36	312	125
Volume	2320 mm^3	608 mm^3	5288 mm^3	2432 mm^3

Fig. 2 Filtering effects on tractography of the left superior longitudinal fasciculus I, which runs anterior-posterior through dorsal frontal and parietal white matter. The high SNR (3x64 dir) taken as a reference, the low SNR scan (64 dir) was taken as a test case, and linear and bilateral filtering were applied to the test case. Using TrackVis, two spherical regions were manually chosen to delineate the bundle consistently across cases, and agreement of bundles with the reference was computed with the Dice coefficient, fiber count, and volume. We found bilateral filtering to be most similar to the reference, while linear filtering inflated both volume and count

3.3 Results

In the first experiment, we found bilateral filtering to produce more similar bundles to the reference than either the source or linear filtered volumes, as shown by an increased Dice score and similar fiber counts and volumes. In the second experiment, we found bilateral filtering to significantly reduce noise-induced error in all voxels ($d > 1.0$, $p < 0.05$) and found linear filtering to reduce noise in most areas, though not near some boundaries. Near these boundaries, the bilateral error was significantly lower with a large effect size ($d > 1.0$, $p < 0.05$). We also measured error as a function of adaptive bandwidth h_m and found a nonlinear trend that varied between high error as $h_m \to 0$ and the linear filtering error as $h_m \to \infty$ with a single global minimum between. On a 1.3 GHz Intel Core i5, our implementation ran in two minutes for a full brain volume.

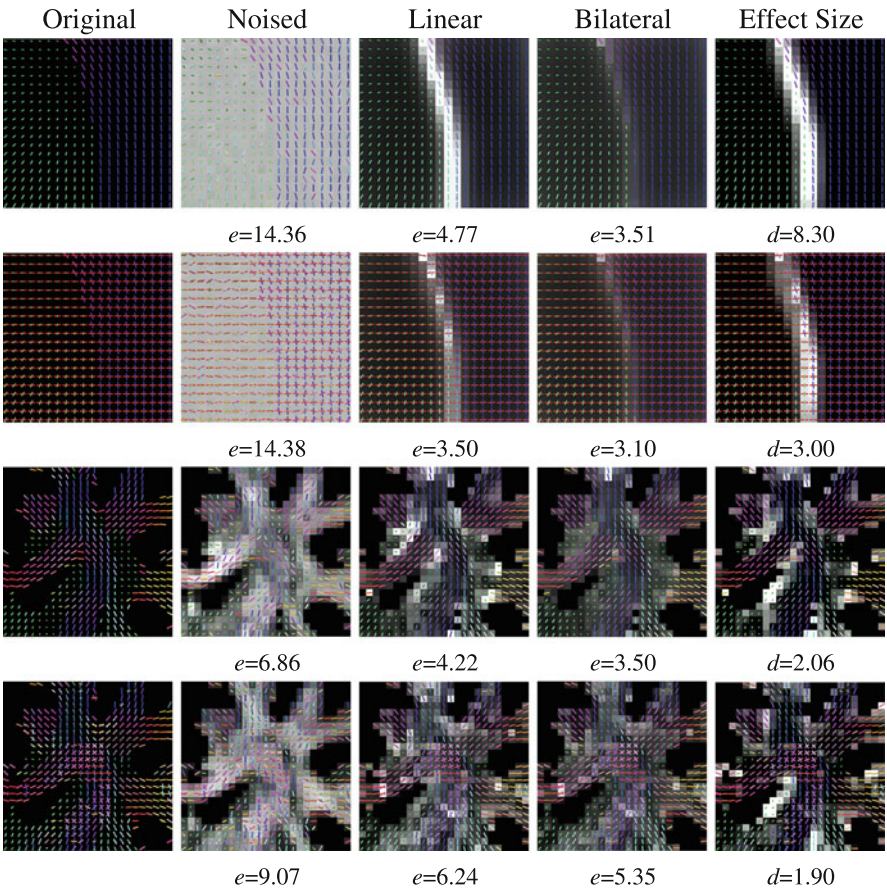

Fig. 3 Filter response to synthetic noise in two phantoms and two human brain cases. Orientation color-coded fiber models are superimposed on grayscale renderings of estimated voxel-wise error (*e*) and effect size (*d*) of the error reduction of bilateral vs. linear filtering (described in Sect. 2). Rows show (*top* to *bottom*): single and double fiber phantom, and coronal slices of single and double human brain data. Columns show (*left* to *right*): original fibers, noisy fibers, linear filtering error, bilateral filtering error, and significant improvements over linear filtering. We found both filters to significantly reduce noise-induced error, with linear filtering having higher error near junctions and boundaries but bilateral filtering showing reduced errors in these regions

4 Conclusion

In this paper, we presented a bilateral filter for fiber orientation data. Our experiments suggest this approach is valuable for regularization and improving fiber bundle reconstruction. Other practical applications include brain connectivity mapping [2], heart modeling [22], and texture analysis [1]. Open problems include incorporation of microstructure properties, testing performance with partial volume

effects, comparison with diffusion-weighted image smoothing techniques, and evaluation for clinical study. In conclusion, we found this approach to offer an efficient way to improve fiber-based modeling in diffusion MR images, as demonstrated with our experiments on synthetic phantom and real human brain datasets.

References

1. Aach, T., Mota, C., Stuke, I., Muhlich, M., Barth, E.: Analysis of superimposed oriented patterns. IEEE Trans. Image Process. **15**(12), 3690–3700 (2006)
2. Basser, P.J., Pajevic, S., Pierpaoli, C., Duda, J., Aldroubi, a.: In vivo fiber tractography using DT-MRI data. Magn. Reson. Med. **44**(4), 625–32 (2000)
3. Basu, S., Fletcher, T., Whitaker, R.: Rician noise removal in diffusion tensor mri. In: Medical Image Computing and Computer-Assisted Intervention - MICCAI 2006. Lecture Notes in Computer Science, vol. 4190, pp. 117–125. Springer, Berlin (2006)
4. Behrens, T.E.J., Berg, H.J., Jbabdi, S., Rushworth, M.F.S., Woolrich, M.W.: Probabilistic diffusion tractography with multiple fibre orientations: What can we gain? NeuroImage **34**(1), 144–155 (2007)
5. Bhattacharya, R., Patrangenaru, V.: Large sample theory of intrisic sample means on manifolds I. Ann. Stat. **31**(1), 1–29 (2013)
6. Cabeen, R.P., Bastin, M.E., Laidlaw, D.H.: Estimating constrained multi-fiber diffusion mr volumes by orientation clustering. In: Medical Image Computing and Computer-Assisted Intervention - MICCAI 2013. Lecture Notes in Computer Science, vol. 8149, pp. 82–89. Springer, Berlin (2013)
7. Cabeen, R.P., Laidlaw, D.H.: White matter supervoxel segmentation by axial dp-means clustering. In: Medical Computer Vision. Large Data in Medical Imaging. Lecture Notes in Computer Science, pp. 95–104. Springer, Switzerland (2014)
8. Coulon, O., Alexander, D., Arridge, S.: Diffusion tensor magnetic resonance image regularization. Med. Image Anal. **8**(1), 47–67 (2004)
9. De Schotten, M.T., Dell'Acqua, F., Forkel, S.J., Simmons, A., Vergani, F., Murphy, D.G., Catani, M.: A lateralized brain network for visuospatial attention. Nat. Neurosci. **14**(10), 1245–1246 (2011)
10. Demiralp, C., Laidlaw, D.H.: Generalizing diffusion tensor model using probabilistic inference in Markov random fields. In: Proceedings of MICCAI CDMRI Workshop (2011)
11. Goh, A., Lenglet, C., Thompson, P., Vidal, R.: A nonparametric riemannian framework for processing high angular resolution diffusion images (hardi). In: IEEE Conference on Computer Vision and Pattern Recognition, CVPR. pp. 2496–2503 (2009)
12. Hamarneh, G., Hradsky, J.: Bilateral filtering of diffusion tensor magnetic resonance images. IEEE Trans. Image Process. **16**(10), 2463–2475 (2007)
13. Knutsson, H.: Representing local structure using tensors. In: Proceedings of the 6th Scandinavian Conference on Image Analysis (1989)
14. Knutsson, H., Westin, C.F.: Normalized and differential convolution. In: IEEE Computer Society Conference on Computer Vision and Pattern Recognition, pp. 515–523 (1993)
15. Milanfar, P., Takeda, H., Farsiu, S.: Kernel regression for image processing and reconstruction. IEEE Trans. Image Process. **16**(2), 349–66 (2007)
16. Paris, S., Briceño, H.M., Sillion, F.X.: Capture of hair geometry from multiple images. ACM Trans. Graph. **23**(3), 712–719 (2004)
17. Pennec, X., Fillard, P., Ayache, N.: A Riemannian framework for tensor computing. Int. J. Comput. Vis. **66**, 41–66 (2006)
18. Perona, P.: Orientation diffusions. IEEE Trans. Image Process. **7**(3), 457–67 (1998)

19. Poupon, C., Clark, C., Frouin, V., Régis, J., Bloch, I., Le Bihan, D., Mangin, J.F.: Regularization of diffusion-based direction maps for the tracking of brain white matter fascicles. NeuroImage **12**(2), 184–195 (2000)
20. Rieger, B., van Vliet, L.: Representing orientation in n-dimensional spaces. In: Computer Analysis of Images and Patterns, pp. 1–8. Springer, Berlin (2003)
21. Rydell, J., Knutsson, H., Borga, M.: Bilateral filtering of fMRI data. IEEE J. Sel. Top. Sign. Process. **2**(6), 891–896 (2008)
22. Scollan, D., Holmes, A., Zhang, J., Winslow, R.: Reconstruction of cardiac ventricular geometry and fiber orientation using magnetic resonance imaging. Ann. Biomed. Eng. **28**(8), 934–944 (2000)
23. Sigurdsson, G., Prince, J.: Smoothing fields of weighted collections with applications to diffusion MRI processing. In: Proceedings of SPIE Medical Imaging (2014)
24. Sra, S., Jain, P., Dhillon, I.: Modeling data using directional distributions: Part II. In: Technical Report TR-07–05, Department of CS, University of Texas at Austin (2007)
25. Taquet, M., Scherrer, B., Commowick, O.: A mathematical framework for the registration and analysis of multi-fascicle models for population studies of the brain microstructure. IEEE Trans. Med. Imaging **33**(2), 1–14 (2013)
26. Tomasi, C., Manduchi, R.: Bilateral filtering for gray and color images. In: 6th International Conference on Computer Vision, pp. 839–846 (1998)
27. Tristán-Vega, A., Aja-Fernández, S.: Dwi filtering using joint information for dti and hardi. Med. Image Anal. **14**(2), 205–218 (2010)
28. Tschumperlé, D., Deriche, R.: Orthonormal vector sets regularization with PDE's and applications. Int. J. Comput. Vis. **50**(3), 237–252 (2002)

Dictionary Based Super-Resolution for Diffusion MRI

Burak Yoldemir, Mohammad Bajammal, and Rafeef Abugharbieh

Abstract Diffusion magnetic resonance imaging (dMRI) provides unique capabilities for non-invasive mapping of fiber tracts in the brain. It however suffers from relatively low spatial resolution, often leading to partial volume effects. In this paper, we propose to use a super-resolution approach based on dictionary learning for alleviating this problem. Unlike the majority of existing super-resolution algorithms, our proposed solution does not entail acquiring multiple scans from the same subject which renders it practical in clinical settings and applicable to legacy data. Moreover, this approach can be used in conjunction with any diffusion model. Motivated by how functional connectivity (FC) reflects the underlying structural connectivity (SC), we quantitatively validate our results by investigating the consistency between SC and FC before and after super-resolving the data. Based on this scheme, we show that our method outperforms traditional interpolation strategies and the only existing single image super-resolution method for dMRI that is not dependent on a specific diffusion model. Qualitatively, we illustrate that fiber tracts and track-density maps reconstructed from super-resolved dMRI data reveal exquisite details beyond what is achievable with the original data.

1 Introduction

Diffusion magnetic resonance imaging (dMRI) based tractography provides a powerful non-invasive in vivo tool for localizing white matter tracts in the brain. Accurate mapping of white matter fiber tracts is important in gaining insights into the brain function since fiber tracts act as a substrate enabling communication between brain regions [8]. However, accuracy of the reconstructed fiber tracts is often hampered by the inherently low resolution of dMRI data. Currently achievable spatial dMRI resolution is around $2 \times 2 \times 2\,\mathrm{mm}^3$, while the actual neuronal fiber diameter is on the order of 1 μm [18]. A voxel can thus comprise several distinct fiber bundles with differing orientations, leading to partial volume averaging

B. Yoldemir (✉) • M. Bajammal • R. Abugharbieh
Biomedical Signal and Image Computing Laboratory, The University of British Columbia, Vancouver, BC, Canada
e-mail: buraky@ece.ubc.ca; bajammal@ece.ubc.ca; rafeef@ece.ubc.ca

L. O'Donnell et al. (eds.), *Computational Diffusion MRI*, Mathematics and Visualization, DOI 10.1007/978-3-319-11182-7_18

[2]. At such locations, diffusion information typically becomes ambiguous, and tractography is often falsely terminated. Therefore, increasing the spatial resolution in dMRI holds great promise towards more accurate delineation of fiber tracts. There are practical limitations in increasing the resolution of the acquired data directly, such as reduced signal-to-noise ratio (SNR) and prolonged scanning time [13]. Such limitations motivate the search for post-processing solutions for increasing the spatial resolution, such as super-resolution techniques.

Super-resolution techniques have been previously adopted to increase the spatial detail in dMRI. In the literature, the term super-resolution is used for two distinct classes of methods which follow different paradigms. The first class of methods are based on performing multiple low-resolution acquisitions, followed by the fusion of the information in these images to generate high-resolution images. To this end, fusing images spatially shifted at sub-voxel level [16], as well as fusing multiple anisotropic images with high resolution only along one axis [17, 18] have been explored. In a fairly similar spirit, combining diffusion-weighted (DW) images acquired at two different resolutions to infer high-resolution diffusion parameters using a Bayesian model has also been proposed [20]. The inherent drawback of these approaches is the dependence on a specific acquisition protocol, limiting their usability in general settings. The second class of methods do not require multiple acquisitions, and these are typically based on examples or priors about the correspondence between low and high resolution images. Falling in this category, an approach to reconstruct diffusion tensors at a resolution higher than the underlying DW images using a single dMRI acquisition has been recently proposed [7]. Even though this method eliminates the need for multiple acquisitions, it is only geared towards estimating diffusion tensors, and cannot be easily extended to higher order diffusion models such as orientation distribution functions (ODFs). To the best of our knowledge, the only previous work that tackled the problem of super-resolving dMRI data from a single acquisition independent of the diffusion model was by Coupé et al. [4]. Specifically, the authors showed that super-resolving $b = 0$ (non-diffusion-weighted) image using a locally adaptive patch-based strategy, and using this high-resolution $b = 0$ image to drive the reconstruction of DW images outperforms upsampling of dMRI data using classical interpolation methods. Beyond these two classes, a new perspective to gain spatial resolution in dMRI has been proposed which is termed as super-resolution track-density imaging (TDI) [3]. This approach is fundamentally different than the aforementioned super-resolution methods in the sense that the aim is to generate high resolution track density maps through counting the number of tracts present in each element of a sub-voxel grid, rather than super-resolving the DW volumes prior to tractography.

In this paper, we employ a super-resolution approach [23] for dMRI that does not require more than a single acquisition per subject. Importantly, we apply this method on DW images before the diffusion modeling step, removing the limitation of applicability to a specific model such as diffusion tensors. The technique is based on sparse coding of DW images via dictionary learning [23]. We note that

similar methods following the sparse coding principle have been investigated before for natural images [6, 22], however the applicability of such an approach on DW images and its added value remain unknown. Given a set of training images, we start with constructing an over-complete dictionary representing the data. Another over-complete dictionary is then constructed from the downsampled versions of these training images. Notably, these two dictionaries are constructed such that the coding vectors modeling downsampled and original data as sparse linear combinations of the learned dictionary atoms are the same, hence the correspondence between low and high resolution images are automatically captured. We then exploit this correspondence between the two dictionaries to super-resolve a new input image to a higher resolution. The advantage of this method is three-fold. First, the super-resolved DW images can be used with any diffusion model as permitted by the number of gradient directions in the original dataset. Second, this method does not rely on repeated acquisitions from the same subject, allowing it to be used with legacy data and under various clinical acquisition schemes. Third, this method may still be readily applied when the imaging protocol involves multiple acquisitions, as an additional step after reconstructing a single image from multiple low resolution acquisitions [16–18].

We qualitatively validate our proposed approach by comparing the fiber tracts and track-density maps reconstructed from the original and super-resolution data. In the absence of ground truth connectivity information, in order to provide a meaningful basis for quantitative comparison, we use the consistency between intra-subject structural connectivity (SC) and functional connectivity (FC) estimates inferred from dMRI and resting state functional MRI (RS-fMRI) data, respectively. Our rationale is that FC is inherently shaped by the wiring of the brain [8, 19]. Therefore, a more accurate estimate of SC would presumably increase the SC-FC correlation. In addition, we also examine the number of fiber tracts for more insight into the observed differences in the SC-FC correlation values.

2 Methods

We start by presenting our assumed data acquisition model (Sect. 2.1). Given a set of acquired DW volumes, we form a training set that includes the original volumes and a set of corresponding downsampled volumes at double the voxel size. We then construct two over-complete dictionaries from the original and downsampled set of volumes (Sect. 2.2). For a previously unseen input DW volume, we obtain the super-resolution data in two steps. First, we sparsely code the volume against the dictionary learned from the downsampled volumes in the training set. We finally apply the generated sparse code to the dictionary learned from the original resolution set to obtain the super-resolution data (Sect. 2.3).

2.1 Acquisition Model

Let v_L be an acquired volume and v_H be the corresponding unobserved higher resolution volume. We assume that the relationship between these two volumes is modeled by [23]:

$$v_L = \mathbf{S}\,\mathbf{B}\,v_H + n \tag{1}$$

where $\mathbf{S}$ is a downsampling operator, $\mathbf{B}$ is a blurring operator and n is additive white Gaussian noise. We aim to invert this acquisition model to approximate the unobserved higher resolution volume through super-resolution. The maximum-likelihood solution to this problem involves the minimization of $||\mathbf{S}\,\mathbf{B}\,\hat{v_H} - v_L||_2$, where $\hat{v_H}$ is the estimated high resolution volume. However, the inversion of $\mathbf{S}\,\mathbf{B}$ is ill-posed [23], hence infinitely many maximum-likelihood solutions exist. We thus cast the problem in a dictionary learning framework instead, as explained in the following sections.

2.2 Dictionary Construction

We model each 3D patch in dMRI volumes as a sparse linear combination of atoms from a learned dictionary $\mathbf{D}$. In the proposed approach, we use two dictionaries to capture the correspondence between low and high resolution dMRI volumes. These two dictionaries are learned from the original training dataset and its downsampled version, respectively.

Let $\mathbf{v}_O$ be the set of original training volumes concatenated across scans and $\mathbf{v}_D$ be the corresponding set of downsampled volumes. We extract all overlapping patches in these two sets of volumes, denoted by $\mathbf{p}_O$ and $\mathbf{p}_D$, respectively. Using $\mathbf{p}_O$ and $\mathbf{p}_D$, we construct two over-complete dictionaries as follows:

$$\min_{\mathbf{D}_O,\mathbf{D}_D,\mathbf{y}} \sum \|\mathbf{p}_D - \mathbf{D}_D\mathbf{y}\|_2^2 + \sum \|\mathbf{p}_O - \mathbf{D}_O\mathbf{y}\|_2^2 + \psi(\mathbf{y}) \tag{2}$$

where $\mathbf{y} = \{\mathbf{y}_{(i,j,k)}\}$ is the set of sparse coding vectors for each image location (i, j, k), and $\mathbf{D}_D$ and $\mathbf{D}_O$ are the generated over-complete dictionaries of the downsampled and original volumes, respectively [23]. $\psi(\mathbf{y})$ is a regularization term which we set to be $\psi(\mathbf{y}) = ||\mathbf{y}||_1$, inducing sparsity on the generated coding vector [21]. We note that the same set of coding vectors $\mathbf{y}$ is used for both dictionaries. In other words, the learned atoms of the two dictionaries represent matched pairs. We set the number of atoms in each dictionary to 1,000 and the patch size to $3 \times 3 \times 3$ voxels, which were empirically chosen to strike a balance between representation accuracy and overfitting.

2.3 Super-Resolved Volume Generation

Let $\mathbf{p}_I$ be the set of low resolution overlapping patches obtained from a previously unseen input volume that we wish to super-resolve. We code $\mathbf{p}_I$ with respect to $\mathbf{D}_D$ as:

$$\min_{\mathbf{y}_I} \; ||\mathbf{p}_I - \mathbf{D}_D \mathbf{y}_I||_2^2 + \psi(\mathbf{y}_I) \tag{3}$$

where $\mathbf{y}_I$ is the set of coding vectors for $\mathbf{p}_I$, with $\psi(\mathbf{y}_I)$ again being the l_1 norm of $\mathbf{y}_I$, enforcing sparsity on the coefficients. Once the input volume is sparsely coded using $\mathbf{D}_D$, we generate a new set of super-resolved patches, $\mathbf{p}_S$, by applying the sparse coding vector $\mathbf{y}_I$ to $\mathbf{D}_O$ previously constructed from the training data:

$$\mathbf{p}_S = \mathbf{D}_O \mathbf{y}_I. \tag{4}$$

We note that this process results in a patch being generated for each voxel. We then reconstruct the super-resolved volume by averaging neighboring overlapping patches.

We used K-singular value decomposition (K-SVD) [1] to construct the dictionaries and orthogonal matching pursuit [15] to sparsely code the 3D patches. Theoretically, $\mathbf{p}_O$, $\mathbf{p}_D$ and $\mathbf{p}_I$ can be extracted at once from the volumes of all gradient directions in the DW images. However, we opt to apply super-resolution for each gradient direction separately. This helps circumvent computational limitations that might arise, especially with the increasingly large number of gradient directions acquired in practice.

3 Materials

We validated our method on the publicly available multimodal Kirby 21 dataset.[1] Along with other imaging modalities, this dataset comprises dMRI and RS-fMRI scans of 21 subjects with no history of neurological disease (11 men, 10 women, 32±9.4 years old). We summarize the key acquisition parameters in Sects. 3.1 and 3.2. Further details on data acquisition can be found in [10]. In our experiments, we used 10 subjects for dictionary training, and 10 other subjects for testing.

[1]This dataset is available online at: http://www.nitrc.org/projects/multimodal.

3.1 RS-fMRI Data

The RS-fMRI data of 7 min duration were collected with a TR of 2 s and a voxel size of 3 mm (isotropic). The data were preprocessed using in-house software written in MATLAB, and the steps followed included motion correction, bandpass filtering at 0.01 and 0.1 Hz, and removal of white matter and cerebrospinal fluid confounds. We divided the brain into 150 parcels by applying Ward clustering [12] on the voxel time courses, which were temporally concatenated across subjects. Parcel time courses were then found by averaging the voxel time courses within each parcel.

3.2 dMRI Data

The dMRI data had 32 diffusion-weighted images with a b-value of 700 s/mm^2 in addition to a single $b = 0$ image, with a voxel size of $0.83 \times 0.83 \times 2.2$ mm^3. Since anisotropic voxels were previously shown to be suboptimal for fiber tractography [14], we resampled each volume to 2 mm isotropic resolution prior to any analysis. We also applied a Rician-adapted denoising filter [11] to eliminate nonstationary noise commonly observed in DW images, since our acquisition model described in Sect. 2.1 assumes Gaussian noise. We then warped our functionally derived group parcellation map to the $b = 0$ volume of each subject using FSL [9] to facilitate the computation of fiber count.

4 Results and Discussion

We first present a qualitative comparison between the fiber tracts reconstructed from the original (2 mm isotropic) and super-resolved (1 mm isotropic) dMRI data. For ease of interpretation, we chose to employ deterministic streamline tractography with the diffusion tensor model, which is by far the most popular tractography approach to date. However, we highlight that our super-resolution approach can be used with any diffusion model and any tractography method. Tractography was carried out using Dipy [5], with 750,000 seed points for both the original and super-resolution data. We generated the track-density maps by calculating the total number of fiber tracts present in each voxel. Figure 1a,c and b,d show sample track-density maps with the original and super-resolved dMRI data, respectively. As observed from these figures, the track-density maps generated from the super-resolution data clearly convey more spatial information. Figure 1e,f and g,h show the corticospinal tracts extracted using a region of interest (ROI) placed on the brain stem for two representative subjects. It can be observed that fiber tracts reconstructed from the super-resolution data can capture the fan-shape configuration of the corticospinal track more fully.

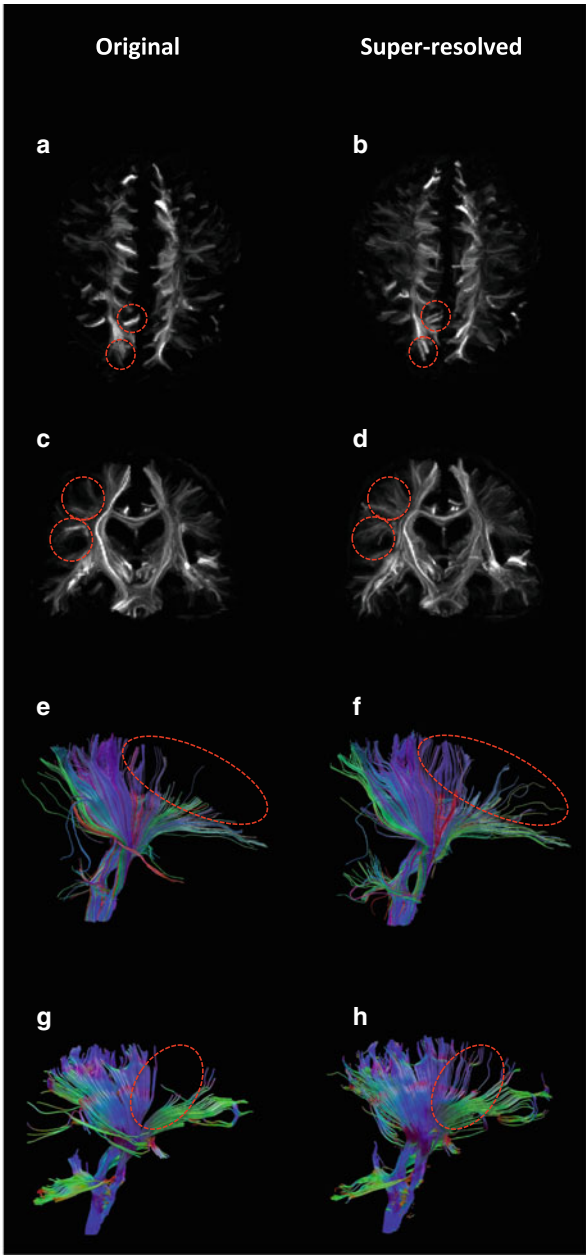

Fig. 1 Qualitative comparison between the track-density maps and fiber tracts reconstructed from the original (*left*) and super-resolved (*right*) dMRI data. Original dataset has 2 mm isotropic resolution which is super-resolved to 1 mm isotropic resolution. Each row corresponds to a different test subject. Track-density maps of super-resolved data ((**b**) and (**d**)) show markedly improved spatial detail compared to those of original data ((**a**) and (**c**)). Corticospinal tracts reconstructed from super-resolved data ((**f**) and (**h**)) can capture the fan-shape configuration more accurately than those generated from original data ((**e**) and (**g**))

To quantify the improvement in tractography with the suggested approach, we analyzed the consistency between measures of intra-subject SC and FC. We estimated SC using the fiber counts between brain region pairs, and FC using Pearson's correlation between parcel time courses. For each subject, SC and FC are vectors of size $d(d-1)/2 \times 1$ comprising the corresponding connectivity estimates between each region pair, where d is the number of brain regions. We then calculated Pearson's correlation between intra-subject SC and FC to quantify the consistency between the two connectivity estimates. Using this correlation measure, we compared the proposed super-resolution approach with trilinear and spline interpolation in addition to an alternative super-resolution method; collaborative and locally adaptive super-resolution (CLASR) [4]. To the best of our knowledge, CLASR is the only existing single image super-resolution method for dMRI which is independent of the diffusion model employed. Figure 2 shows the SC-FC correlation for each subject tested. Taking the average SC-FC correlation across the group when using the original data as a baseline, the improvement was 5.7 % with spline interpolation, 13.6 % with CLASR, and 27.1 % with our proposed method. On the other hand, there was a 6.3 % decrease in the correlation when trilinear interpolation was used. The difference in the performance of our method and every other method tested was found to be statistically significant at $p < 0.01$ based on the Wilcoxon signed-rank test, showing its potential for enhanced structural connectivity assessment. Our results thus suggest that low spatial resolution of dMRI data can partially account for the low SC-FC correlation, and statistically significant improvements can be achieved using super-resolved dMRI data.

To investigate why trilinear interpolation resulted in a lower SC-FC correlation compared to the original data, we calculated the number of tracts reconstructed with each method. The local intra-parcel connections were excluded since they have no effect on SC-FC correlation. Figure 3 shows the number of inter-parcel tracts averaged across the group along with the corresponding standard deviations. As observed from this figure, performing tractography on volumes upsampled with trilinear interpolation resulted in a lower number of tracts compared to the original volumes, even though the same number of seed points were used to initiate tracking for all of the methods we compared. We speculate that the reason of this phenomenon is the additional partial volume effects introduced by the blurring of the data during trilinear interpolation, which hamper the tractography quality. Spline interpolation, however, is known to cause less blurring compared to trilinear interpolation, and our results suggest that upsampling dMRI data using spline interpolation can be beneficial for tractography. The overall trend of inter-parcel track counts closely resembles to that of the SC-FC correlation, with our proposed method outperforming all other methods tested. This shows that dictionary based super-resolution is a viable post-processing solution for dMRI that can help in mapping the white matter brain architecture more accurately.

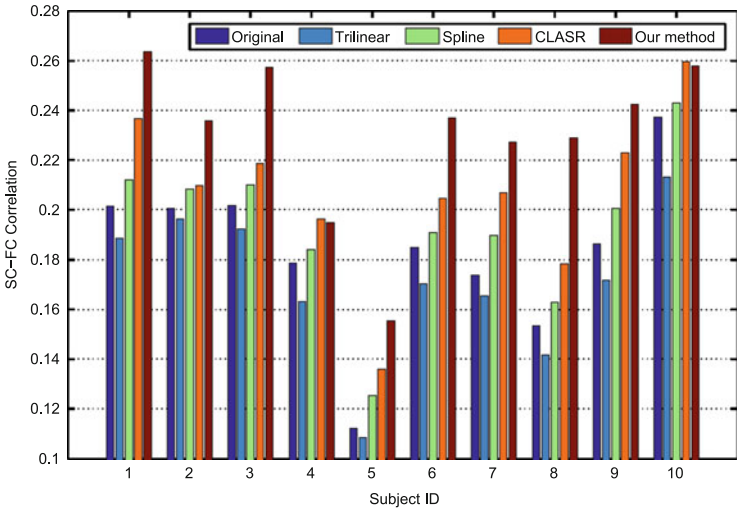

Fig. 2 SC-FC correlation for 10 subjects with SC estimated from the data at its original resolution (2 mm isotropic), and high-resolution data (1 mm isotropic) obtained using trilinear interpolation, spline interpolation, CLASR and the proposed method. Our method outperforms all other methods tested for eight of the subjects, and performs comparable to CLASR for two subjects (subjects 4 and 10)

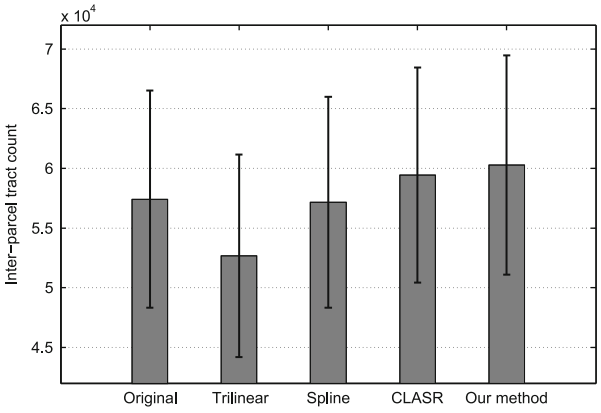

Fig. 3 Number of inter-parcel tracts reconstructed from the data at its original resolution (2 mm isotropic), and high-resolution data (1 mm isotropic) obtained using trilinear interpolation, spline interpolation, CLASR and the proposed method. Intra-parcel tracts are not included here since they do not contribute to SC-FC correlation. We emphasize that tractography is initiated with the same number of seeds (750,000) for each method

5 Conclusions and Future Work

Low spatial resolution is a known limitation of dMRI, which often hinders the performance of tractography significantly. We proposed the use of a simple yet very effective super-resolution technique in dMRI to capture a more accurate portrayal of the white matter architecture. This approach does not require multiple dMRI acquisitions and is applicable to legacy data. Quantitatively, we demonstrated that SC-FC consistency can be markedly increased with the use of our approach in estimating SC. We also qualitatively illustrated that the gain in spatial resolution remarkably improves the fiber tracts and track-density maps generated. Taken collectively, our results suggest that dictionary based super-resolution holds great promise in enhancing the spatial resolution in dMRI, without requiring additional scans or any modifications of the acquisition protocol.

It is important to acknowledge that the performance of the proposed method inherently depends on the training dataset, as in any machine learning method that involves training or prior information. The age span of the subjects we used in our experiments was 23–61, showing that the method can generalize to a large range of ages. However, how well abnormalities such as tumor and edema can be modeled with dictionary learning is currently unclear and warrants further research.

Acknowledgements The authors wish to thank Dr. Pierrick Coupé for assisting in the comparative assessment of our method with CLASR.

References

1. Aharon, M., Elad, M., Bruckstein, A.: K-SVD: an algorithm for designing overcomplete dictionaries for sparse representation. IEEE Trans. Signal Process. **54**(11), 4311–4322 (2006)
2. Alexander, A., Hasan, K., Lazar, M., Tsuruda, J., Parker, D.: Analysis of partial volume effects in diffusion-tensor MRI. Magn. Reson. Med. **45**(5), 770–780 (2001)
3. Calamante, F., Tournier, J.D., Jackson, G.D., Connelly, A.: Track-density imaging (TDI): super-resolution white matter imaging using whole-brain track-density mapping. NeuroImage **53**(4), 1233–1243 (2010)
4. Coupé, P., Manjón, J.V., Chamberland, M., Descoteaux, M., Hiba, B.: Collaborative patch-based super-resolution for diffusion-weighted images. NeuroImage **83**, 245–261 (2013)
5. Garyfallidis, E., Brett, M., Amirbekian, B., Rokem, A., Van Der Walt, S., Descoteaux, M., Nimmo-Smith, I.: Dipy, a library for the analysis of diffusion MRI data. Front. Neuroinform. **8**(8) (2014)
6. Glasner, D., Bagon, S., Irani, M.: Super-resolution from a single image. In: Proc. IEEE 12th International Conference on Computer Vision, pp. 349–356 (2009)
7. Gupta, V., Ayache, N., Pennec, X.: Improving DTI resolution from a single clinical acquisition: a statistical approach using spatial prior. In: Mori, K., Sakuma, I., Sato, Y., Barillot, C., Navab, N. (eds.) MICCAI, LNCS, vol. 8151, pp. 477–484. Springer, Heidelberg (2013)
8. Honey, C., Thivierge, J.P., Sporns, O.: Can structure predict function in the human brain? NeuroImage **52**(3), 766–776 (2010)
9. Jenkinson, M., Beckmann, C., Behrens, T., Woolrich, M., Smith, S.: FSL. NeuroImage **62**(2), 782–790 (2012)

10. Landman, B., Huang, A., Gifford, A., Vikram, D., Lim, I., Farrell, J., Bogovic, J., Hua, J., Chen, M., Jarso, S., Smith, S., Joel, S., Mori, S., Pekar, J., Barker, P., Prince, J., van Zijl, P.: Multi-parametric neuroimaging reproducibility: a 3-T resource study. NeuroImage **54**(4), 2854–2866 (2011)
11. Manjón, J.V., Coupé, P., Buades, A., Collins, D.L., Robles, M.: New methods for MRI denoising based on sparseness and self-similarity. Med. Image Anal. **16**(1), 18–27 (2012)
12. Michel, V., Gramfort, A., Varoquaux, G., Eger, E., Keribin, C., Thirion, B.: A supervised clustering approach for fMRI-based inference of brain states. Pattern Recogn. **45**(6), 2041–2049 (2012)
13. Mori, S., Zhang, J.: Principles of diffusion tensor imaging and its applications to basic neuroscience research. Neuron **51**(5), 527–539 (2006)
14. Neher, P., Stieltjes, B., Wolf, I., Meinzer, H., Maier-Hein, K.: Analysis of tractography biases introduced by anisotropic voxels. In: Proc. Annual Meeting ISMRM (2013)
15. Pati, Y., Rezaiifar, R., Krishnaprasad, P.S.: Orthogonal matching pursuit: recursive function approximation with applications to wavelet decomposition. In: Proc. Asilomar Conference on Signals, Systems and Computers, pp. 40–44 (1993)
16. Peled, S., Yeshurun, Y.: Super-resolution in MRI: application to human white matter fiber track visualization by diffusion tensor imaging. Magn. Reson. Med. **45**(1), 29–35 (2001)
17. Poot, D., Jeurissen, B., Bastiaensen, Y., Veraart, J., Van Hecke, W., Parizel, P., Sijbers, J.: Super-resolution for multislice diffusion tensor imaging. Magn. Reson. Med. **69**(1), 103–113 (2013)
18. Scherrer, B., Gholipour, A., Warfield, S.: Super-resolution in diffusion-weighted imaging. In: Fichtinger, G., Martel, A., Peters, T. (eds.) MICCAI, LNCS, vol. 6892, pp. 124–132. Springer, Heidelberg (2011)
19. Skudlarski, P., Jagannathan, K., Calhoun, V., Hampson, M., Skudlarska, B., Pearlson, G.: Measuring brain connectivity: diffusion tensor imaging validates resting state temporal correlations. NeuroImage **43**(3), 554–561 (2008)
20. Sotiropoulos, S.N., Jbabdi, S., Andersson, J.L., Woolrich, M.W., Ugurbil, K., Behrens, T.E.J.: RubiX: combining spatial resolutions for Bayesian inference of crossing fibers in diffusion MRI. IEEE Trans. Med. Imaging **32**(6), 969–982 (2013)
21. Tibshirani, R.: Regression shrinkage and selection via the Lasso. J. R. Stat. Soc. Ser. B **58**, 267–288 (1994)
22. Yang, J., Wright, J., Huang, T., Ma, Y.: Image super-resolution as sparse representation of raw image patches. In: Proc. IEEE Conference on Computer Vision and Pattern Recognition, pp. 1–8 (2008)
23. Zeyde, R., Elad, M., Protter, M.: On single image scale-up using sparse-representations. In: Boissonnat, J.D., Chenin, P., Cohen, A., Gout, C., Lyche, T., Mazure, M.L., Schumaker, L. (eds.) Curves and Surfaces, LNCS, vol. 6920, pp. 711–730. Springer, Heidelberg (2012)

Index

L. O'Donnell et al. (eds.), *Computational Diffusion MRI*, Mathematics and Visualization, DOI 10.1007/978-3-319-11182-7